Acta Pharmacologica Sinica (2011) 32: 139–140
 1671-4083/11 $32.00
www.nature.com/aps

Research Highlight

Ubiquitination/deubiquitination and acetylation/deacetylation: Making DNMT1 stability more coordinated

Qi HONG, Zhi-ming SHAO*

Acta Pharmacologica Sinica (2011) 32: 139–140; doi: 10.1038/aps.2011.3

In mammals, DNA methylation plays a crucial role in the regulation of gene expression, telomere length, cell differentiation, X chromosome inactivation, genomic imprinting and tumorigenesis[1]. DNA methylation patterns are established *de novo* by DNA methyltransferases (DNMTs) 3a and 3b, whereas DNMT1 maintains the parent-specific methylation from parental cells to their progeny[2]. After DNA replication, the new DNA strand is unmethylated. Thus with the mother methylated strand, the DNA is hemimethylated. The protein UHRF1 (ubiquitin-like, containing PHD and RING finger domains 1) recognizes and binds to the hemimethylated sites by its SRA domain. Then DNMT1 is recruited to the sites by the same domain, thereby it methylates the newly synthesized DNA strand[3, 4]. Increased DNMT1 abundance has been seen in many human cancers, and the roles of DNMT1 in tumorigenesis have been shown by some genetic knockout and RNA interference-mediated knockdown studies[5, 6]. Seeing that the mRNA abundance of DNMT1 contributes less to DNMT1 abundance, the stability of DNMT1 protein therefore plays an important role in human cancers[7, 8].

Department of Breast Surgery, Breast Cancer Institute, Cancer Hospital, Institutes of Biomedical Science, Shanghai Medical College, Fudan University, Shanghai 200032, China
Correspondence: Zhi-ming SHAO (zhimingshao@yahoo.com)

Ubiquitin-proteasome pathway is significant in the stability of DNMT1[8], but ubiquitin-mediated protein degradation can be enhanced or attenuated by some modifications like acetylation/deacetylation, protein methylation/demethylation, phosphorylation and *S*-nitrosylation[9–11]. Estève *et al* demonstrated that SET7-mediated lysine methylation of DNMT1 decreased DNMT1 level by ubiquitin-mediated degradation[10]. Furthermore, an early study[12] showed that HDAC inhibitors could induce degradation of DNMT1. These suggest that DNMT1-associated proteins may play key roles in DNMT1 stability. In a recent issue of *Science Signaling*, Du *et al* reported[13] that some DNMT1-associated proteins can ubiquitinate/deubiquitinate and acetylate/deacetylate DNMT1. These modifications make the regulation of DNMT1 stability more coordinated (Figure 1).

They identified deubiquitinase HAUSP (herpesvirus-associated ubiquitin specific protease) as a DNMT1-associated protein. Knockout or knockdown of HAUSP increased DNMT1 ubiquitination and reduced its abundance, then they demonstrated the direct deubiquitination of DNMT1 *in vitro* by purified HAUSP recombinant proteins. They also found that overexpression of DNMT1-associated E3 ligase UHRF1 led to increased ubiquitination of DNMT1 and decreased abundance of DNMT1 mutant lacking the HAUSP interaction domain, but not the full-length protein. These results show the coordination between ubiquitination of DNMT1 by UHRF1 and deubiquitination by HAUSP. Furthermore, they found that knockdown of HDAC1 increased DNMT1 acetylation, and reduced DNMT1 abundance. Additionally, acetyltransferase Tip60 which was found to acetylate DNMT1 promoted its ubiquitination, then destabilized it. At last, Tip60 and HAUSP were found to regulate DNMT1 protein stability during the cell cycle. The following clinical samples of human colon cancer also revealed the correlation between the abundance of HAUSP and the abundance of DNMT1.

Drugs targeting epigenetic modifications have been edging toward anti-cancer therapies. DNMT1 also provides a candidate anti-cancer target[14]. Although global genomic DNA hypomethylation and tumor suppressor genes hypermethylation have been frequently observed in different human cancers, this methylation change is not caused simply by increased levels of DNMT1[15]. This paper shows that DNMT1, HAUSP, UHRF1, Tip60, HDAC1, and PCNA (proliferating cell nuclear antigen) can interact with each other, thus they regulate DNMT1 stability and activity by a more coordinated way. Consequently, the current or future epigenetic drugs

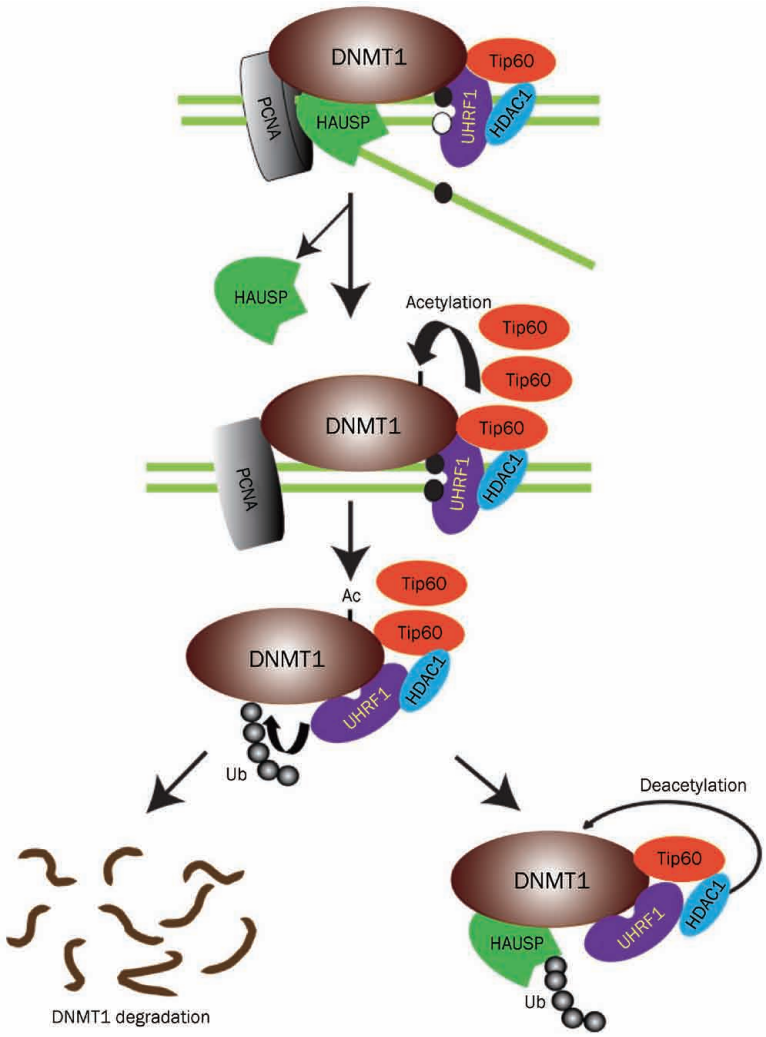

Figure 1. A model of posttranslational regulation of DNMT1 stability[13]. DNMT1 physically interacts with HAUSP, Tip60, UHRF1, HDAC1, and PCNA on chromatin. After the completion of DNA methylation in S phase, HAUSP dissociates from DNMT1 to enable DNMT1 degradation. Moreover, increased abundance of Tip60 results in increased acetylation of DNMT1, which in turn triggers the ubiquitination of DNMT1 by UHRF1. This sequence of events results in proteasomal degradation of DNMT1. In contrast, HAUSP and HDAC1 protect DNMT1 from degradation through deubiquitination and deacetylation, respectively. Reprinted with permission from AAAS: Science Signaling, copyright 2010.

such as 5-aza CdR (DNMT1 inhibitor), HDAC inhibitors, HAUSP inhibitors, and UHRF1 inhibitors may have a potential combination for effective cancer therapy. And equally, the drug interactions and side effects should be taken into account, as one of the inhibitors may affect the other targets.

1 Goll MG, Bestor TH. Eukaryotic cytosine methyltransferases. Annu Rev Biochem 2005; 74: 481–514.
2 Ooi SK, Bestor TH. Cytosine methylation: remaining faithful. Curr Biol 2008; 18: R174–6.
3 Bostick M, Kim JK, Estève PO, Clark A, Pradhan S, Jacobsen SE. UHRF1 plays a role in maintaining DNA methylation in mammalian cells. Science 2007; 317: 1760–4.
4 Sharif J, Muto M, Takebayashi S, Suetake I, Iwamatsu A, Endo TA, *et al*. The SRA protein Np95 mediates epigenetic inheritance by recruiting Dnmt1 to methylated DNA. Nature 2007; 450: 908–12.
5 Robert MF, Morin S, Beaulieu N, Gauthier F, Chute IC, Barsalou A, *et al*. DNMT1 is required to maintain CpG methylation and aberrant gene silencing in human cancer cells. Nat Genet 2003; 33: 61–5.
6 Brown KD, Robertson KD. DNMT1 knockout delivers a strong blow to genome stability and cell viability. Nat Genet 2007; 39: 289–90.
7 De Marzo AM, Marchi VL, Yang ES, Veeraswamy R, Lin X, Nelson WG. Abnormal regulation of DNA methyltransferase expression during colorectal carcinogenesis. Cancer Res 1999; 59: 3855–60.
8 Agoston AT, Argani P, Yegnasubramanian S, De Marzo AM, Ansari-Lari MA, Hicks JL, *et al*. Increased protein stability causes DNA methyltransferase 1 dysregulation in breast cancer. J Biol Chem 2005; 280: 18302–10.
9 Kruse JP, Gu W. Modes of p53 regulation. Cell 2009; 137: 609–22.
10 Estève PO, Chin HG, Benner J, Feehery GR, Samaranayake M, Horwitz GA, *et al*. Regulation of DNMT1 stability through SET7-mediated lysine methylation in mammalian cells. Proc Natl Acad Sci USA 2009; 106: 5076–81.
11 Azad N, Iyer A, Vallyathan V, Wang L, Castranova V, Stehlik C, *et al*. Role of oxidative/nitrosative stress-mediated Bcl-2 regulation in apoptosis and malignant transformation. Ann N Y Acad Sci 2010; 1203: 1–6.
12 Zhou Q, Agoston AT, Atadja P, Nelson WG, Davidson NE. Inhibition of histone deacetylases promotes ubiquitin-dependent proteasomal degradation of DNA methyltransferase 1 in human breast cancer cells. Mol Cancer Res 2008; 6: 873–83.
13 Du Z, Song J, Wang Y, Zhao Y, Guda K, Yang S, *et al*. DNMT1 stability is regulated by proteins coordinating deubiquitination and acetylation-driven ubiquitination. Sci Signal 2010; 3: ra80.
14 Karberg S. Switching on epigenetic therapy. Cell 2009; 139: 1029–31.
15 Szyf M. Towards a pharmacology of DNA methylation. Trends Pharmacol Sci 2001; 22: 350–4.

Acta Pharmacologica Sinica (2011) 32: 141–151
 1671-4083/11 $32.00
www.nature.com/aps

Review

Active ingredients in Chinese medicines promoting blood circulation as Na^+/K^+-ATPase inhibitors

Ronald JY CHEN[1], Tzyy-rong JINN[2], Yi-ching CHEN[1], Tse-yu CHUNG[1], Wei-hung YANG[1, 2], Jason TC TZEN[1, 2, 3, *]

[1]*Graduate Institute of Biotechnology, National Chung Hsing University, Taichung 40227, Taiwan, China;* [2]*School of Chinese Medicine, China Medical University, Taichung 40402, Taiwan, China;* [3]*Agricultural Biotechnology Research Center, Academia Sinica, Taipei 11529, Taiwan, China*

The positive inotropic effect of cardiac glycosides lies in their reversible inhibition on the membrane-bound Na^+/K^+-ATPase in human myocardium. Steroid-like compounds containing a core structure similar to cardiac glycosides are found in many Chinese medicines conventionally used for promoting blood circulation. Some of them are demonstrated to be Na^+/K^+-ATPase inhibitors and thus putatively responsible for their therapeutic effects via the same molecular mechanism as cardiac glycosides. On the other hand, magnesium lithospermate B of danshen is also proposed to exert its cardiac therapeutic effect by effectively inhibiting Na^+/K^+-ATPase. Theoretical modeling suggests that the number of hydrogen bonds and the strength of hydrophobic interaction between the effective ingredients of various medicines and residues around the binding pocket of Na^+/K^+-ATPase are crucial for the inhibitory potency of these active ingredients. Ginsenosides, the active ingredients in ginseng and sanqi, substantially inhibit Na^+/K^+-ATPase when sugar moieties are attached only to the C-3 position of their steroid-like structure, equivalent to the sugar position in cardiac glycosides. Their inhibitory potency is abolished, however, when sugar moieties are linked to C-6 or C-20 position of the steroid nucleus; presumably, these sugar attachments lead to steric hindrance for the entrance of ginsenosides into the binding pocket of Na^+/K^+-ATPase. Neuroprotective effects of cardiac glycosides, several steroid-like compounds, and magnesium lithospermate B against ischemic stroke have been accordingly observed in a cortical brain slice-based assay model, and cumulative data support that effective inhibitors of Na^+/K^+-ATPase in the brain could be potential drugs for the treatment of ischemic stroke.

Keywords: cardiac glycoside; ginsenoside; magnesium lithospermate B; neuroprotection; Na^+/K^+-ATPase inhibitors; blood circulation; steroid-like compound; traditional Chinese medicine

Acta Pharmacologica Sinica (2011) 32: 141–151; doi: 10.1038/aps.2010.197

Introduction

In an aging population cardiovascular diseases, such as congestive heart failure, have gradually become serious health challenges. Congestive heart failure, generally defined as incapability of the heart to supply sufficient blood flow to meet the body's needs, frequently leads to significantly adverse influences on physical and mental health, resulting in a markedly decreased quality of life and even death[1]. While cardiac glycosides, such as digoxin, digitoxin and ouabain, have been a cornerstone of the treatment of congestive heart failure for more than two centuries, severe side effects have been reported for these steroid-like compounds[2, 3]. The narrow therapeutic index (the margin between effectiveness and toxicity) of cardiac glycosides further limits their clinical applications[4]. The limited benefit with certain side effects of the existing remedies has prompted investigators to search for complementary and alternative therapies and drugs.

Many traditional Chinese medicines have long been used in the treatment of various cardiovascular diseases, such as coronary heart disease, heart stroke and myocardial infarction, and some of them are effective in promoting blood circulation, removing blood stasis and supplementing vital energy[5, 6]. Although these medicines display considerable therapeutic effects with low toxicity, little is known about their primary active ingredients and detailed pharmaceutical mechanisms. Nevertheless, these traditional Chinese medicines, dating back 2000 years, have been regarded as valuable sources to screen potential drugs for the treatment of cardiovascular diseases.

With the rapid development of technology, numerous constituents in traditional Chinese medicines have been isolated and structurally determined[7]. Abundant steroid-like compounds, structurally similar to cardiac glycoside, have been found in many Chinese medicines used for promoting blood circulation[8, 9]. It is likely that these steroid-like compounds

* To whom correspondence should be addressed.
E-mail TCTZEN@dragon.nchu.edu.tw
Received 2010-09-03 Accepted 2010-10-28

are responsible for the therapeutic effects of these medicines via the same molecular mechanism triggered by effective inhibition of Na^+/K^+-ATPase. On the other hand, no appreciable contents of steroid-like compounds are found in danshen (*Salvia miltiorrhiza*), a well-known Chinese herb traditionally regarded as an effective medicine for promoting blood circulation[10]. Instead, magnesium lithospermate B (MLB), the major soluble ingredient in danshen, is assumed to be responsible for the therapeutic effect by inhibiting Na^+/K^+-ATPase in a manner comparable to that of cardiac glycosides.

This review summarizes recent research on Na^+/K^+-ATPase inhibitory potency of some active ingredients identified in the Chinese medicines used for promoting blood circulation. Molecular modeling and docking of these compounds to Na^+/K^+-ATPase resolve at molecular level the difference in their inhibitory potency. Potential usage of these active ingredients as inhibitors of Na^+/K^+-ATPase in the brain for the treatment of ischemic stroke is also discussed.

Structure and function of Na^+/K^+-ATPase

Na^+/K^+-ATPase, a P-type ATPase also known as sodium pump, is an active transport system of sodium and potassium ions that is highly conserved in all animal cells. It commonly consumes 20%–30% of the adenosine triphosphate (ATP) energy generated in animal cells at rest to actively transport three Na^+ out of and two K^+ into cells[11]. The X-ray crystal structure of Na^+/K^+-ATPase recently resolved[12–14] shows that it is composed of three subunits (α, β and γ subunits) with distinct properties[15-17]; and the α catalytic subunit, a 112 kDa protein, contains sites important for ATP binding and phosphorylation as well as ion occlusion (Figure 1A) and an ouabain-binding site (Figure 1B), the primary binding site for many pharmacological agents, such as cardiac glycosides, that affect pump activity[18].

Physiological functions of Na^+/K^+-ATPase have been deduced from its role as an ion pump. Specifically, the ability of Na^+/K^+-ATPase to establish and maintain ion gradients makes it essential for the generation and maintenance of electrical membrane potentials, which are necessary for neuronal excitability, transmission[19] and cardiac muscle contraction[20]. Na^+/K^+-ATPase also generates the Na^+ gradient that is critical for the reabsorption of sodium ion and water from the glomerular filtrate in the nephron[21] and absorption of fluid from the lungs and intestine[22]. It can also drive secondary active co-/countertransporters, which are coupled to the gradient of extracellular to intracellular Na^+ concentration, such as the sodium glucose cotransporter and the Na^+/Ca^{2+} exchanger[23]. In addition, recent findings have suggested additional signaling modes of action of Na^+/K^+-ATPase[24–26], implicating its regulation of several important cellular processes and highlighting potential therapeutic roles of its inhibitors (such as cardiac glycosides) in various diseases.

Inhibition of Na^+/K^+-ATPase by cardiac glycosides leading to a positive inotropic effect

Cardiac glycosides, such as ouabain and digoxin, are a diverse

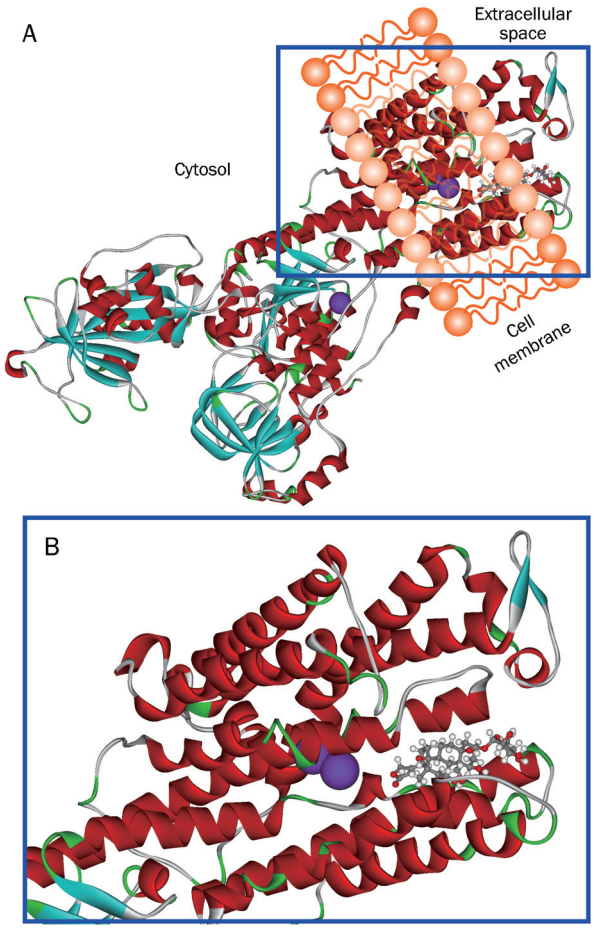

Figure 1. (A) Crystal structure of ouabain binding to the extracellular pocket of shark rectal gland Na^+/K^+-ATPase (PDB code 3A3Y) α subunit[17]. Amino acid residues of Na^+/K^+-ATPase α subunit are shown in ribbon structure, and ouabain in scaled ball and stick. K^+ binding sites are shown in purple balls. (B) Enlarged diagram without the membrane bilayer shown in the blue box of (A).

family of naturally derived compounds that bind to and inhibit Na^+/K^+-ATPase. While they show considerable structural diversity, all members of this family share a common steroidal framework, regarded as the pharmacophoric moiety responsible for the activity of these compounds[27]. Generally, this steroid core is double-substituted with an unsaturated lactone ring at position 17 and a sugar portion at position 3; and this lactone moiety of cardiac glycosides is critical for their potent inhibition of Na^+/K^+-ATPase. Although the sugar moiety does not greatly influence their biological activity, the addition of sugars to the steroid core affects the pharmacodynamic and pharmacokinetic profile of each glycoside[28].

Cardiac glycosides have been in clinical use for many years for the treatment of congestive heart failure and cardiac arrhythmia, and the mechanism of their positive inotropic effect is well characterized. According to the most widely accepted molecular mechanism responsible for the therapeutic effect of cardiac glycosides, they act through reversible inhibition of Na^+/K^+-ATPase in the membrane of heart muscle

cells[29, 30]. In human heart, inhibition of the Na^+/K^+-ATPase leads to the accumulation of intracellular sodium ion, which decreases the sodium gradient across the membranes of cardiac muscle cells. This reduced sodium gradient in turn limits the activity of the Na^+/Ca^{2+} exchanger in the cell membrane, which normally uses the sodium gradient for energy in the extrusion of calcium ion[31]. Each cardiac action potential is thus followed by elevated levels of residual intracellular calcium ion, and the net effect of which is to strengthen successive heart contractions[32]. In this way, inhibition of the Na^+/K^+-ATPase by cardiac glycosides produces beneficial effects in patients with congestive heart failure. However, severe side effects and narrow therapeutic index of cardiac glycosides have apparently limited their clinical applications[29].

Steroid-like compounds in Chinese medicines for promoting blood circulation and their inhibitory potency on Na^+/K^+-ATPase

Many Chinese medicinal products traditionally used in the treatment of cardiovascular diseases seem to achieve their therapeutic effects via promotion of blood circulation. A number of steroid-like compounds, such as triterpenoids, steroids and saponins, have been found in Chinese medicinal products used for promoting blood circulation (Table 1), and regarded as the active ingredients responsible for their therapeutic effects[33–64]. In light of the structural similarity between the core structure of these steroid-like compounds and the steroidal framework of cardiac glycosides, we propose that some of these medicines may possess therapeutic effects via inhibition of Na^+/K^+-ATPase by their steroid-like compounds[65]. Some of the steroid-like compounds listed in Table 1 are commercially available and thus subjected to Na^+/K^+-ATPase inhibition assay (Figure 2). The results show that all examined steroid-like compounds found in Chinese medicines for promoting blood circulation displayed more or less inhibitory potency on Na^+/K^+-ATPase. Among these steroid-like compounds, bufalin (structurally almost equivalent to ouabain) exhibits significantly higher inhibitory potency (IC_{50} value around 1 μmol/L) than the others while ginsenoside Rh2, ursolic acid and oleanolic acid are relatively moderate inhibitors of Na^+/K^+-ATPase with IC_{50} values around 50–100 μmol/L. Based on the experimental observation of inhibitory potency of steroid-like compounds on Na^+/K^+-ATPase, the therapeutic effects of many cardiac Chinese medicines may be partly attributed to various steroid-like compounds that promote blood circulation via the same molecular mechanism triggered by cardiac glycosides, that is, accentuating the force of myocardial contraction by elevating calcium concentration via the inhibition of Na^+/K^+-ATPase.

Inhibition of Na^+/K^+-ATPase by MLB, a non-steroid compound, leading to the therapeutic effect of danshen

Danshen, the dried roots of medicinal plant *Salvia miltiorrhiza*, is one of the most popular Chinese medicines widely used in many medicinal preparations and formulae taken by people in several Asian countries. Traditionally it is regarded as an effective herb for promoting blood circulation, removing blood stasis, relieving pain, stimulating menstrual discharge, and relaxing the mind. Therefore, danshen has also been extensively used in the treatment of coronary heart disease, myocardial infarction, heart failure, menstrual disorders, and

Table 1. Steroid-like compounds in Chinese medicines used for the promotion of blood circulation.

Compound	Chinese medicinal sources	References
Bufalin	The dried venom of *Bufo bufo gargarizans* Cantor or *B bufo melanostictua* Schneider	33, 34
Ginsenoside Rh2	The dry root of *Panax ginseng* or *P notoginseng* F H Chen	35–37
Ursolic acid	Whole plant of *Prunella vulgaris* L with dry flowers	38, 39
Oleanolic acid	Whole plant of *Prunella vulgaris* L with dry flowers	38, 39
Saikosaponin A	The dry root of *Bupleurum chinense* DC or *B scorzonerifolium* Willd	40, 41
Cholic acid	The dried bile of *Ursus arctos* Linnaeus or *Selenarctos thibetanus* G Cuvier	42, 43
Sarsasapogenin	The dry root of *Anemarrhena asphodeloides* Bge	44
Polygalacic acid	The dry root of *Platycodon grandiflorum* (Jacq) A DC	45
Jujuboside B	The mature seeds of *Ziziphus jujube* Mill var *spinosa* (Bunge) Hu ex H F Chou	46
Glycyrrhizin	The root of *Glycyrrhiza uralensis* Fisch - *G inflata* Bat or *G glabra* L	47, 48
Astragaloside III	The dry root of *Astragalus membranaceus* (Fisch) Bge or var *mongholicus* (Bge) Hsiao	49
Betulinic acid	The dried root cortex of *Paeonia suffruticosa*	50
Inokosterone	The dry root of *Achyranthes bidentata* Blume	51
Dehydrocorydaline	The tuber of *Corydalis yanhusuo* W T Wang	52, 53
Rhynchophylline	The hook of *Uncaria rhynchophylla* (Miquel) Jacks	54, 55
Hirsutine	The hook of *Uncaria rhynchophylla* (Miquel) Jacks	56–58
Cucurbitacin D	The fruit of *Trichosanthes kirilowii* Maxim or *T rosthornii* Harms	59, 60
β-Boswellic acid	The oleogum resin of *Boswellia carterii* Birdwood	61
Isolimonoic acid	The fruit of *Citrus aurantium* L	62
β-Sitosterol	The rhizome of *Sparganium stoloniferum* Buch-Ham	63
Pachymic acid	The sclerotium of *Poria cocos* (Schw) Wolf	64

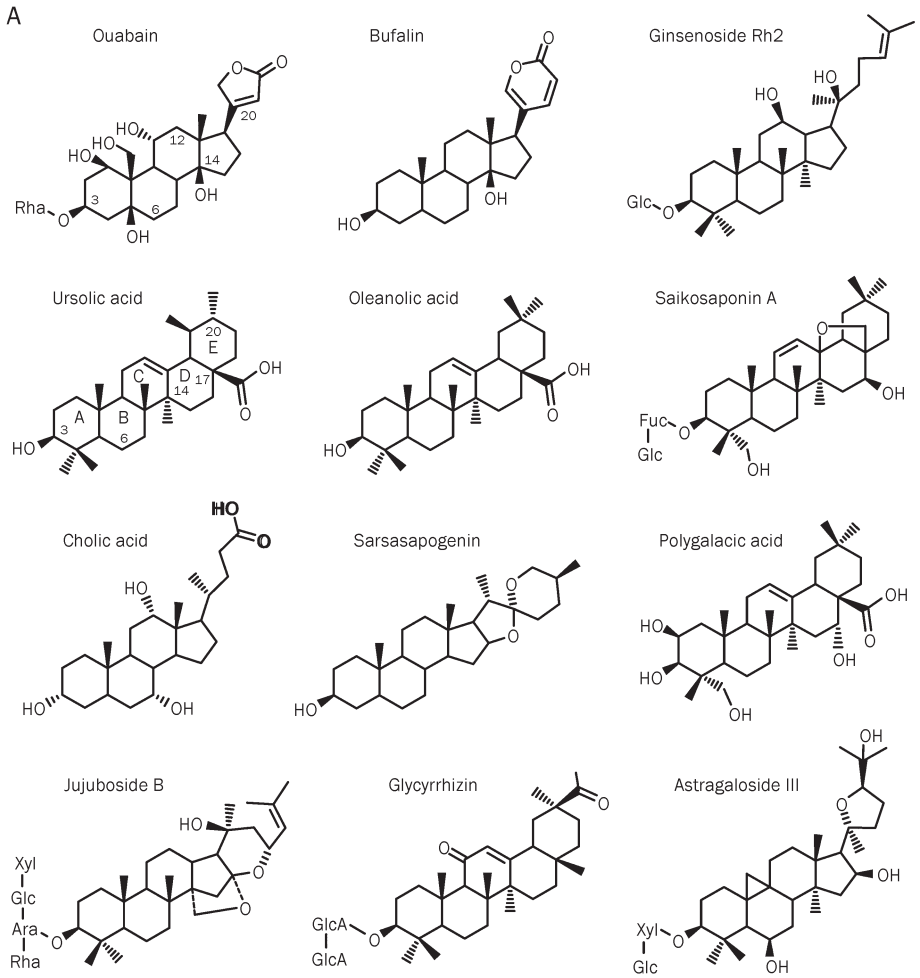

Figure 2. (A) Chemical structures of ouabain and 11 steroid-like compounds found in Chinese medicinal products used for the promotion of blood circulation. (B) Inhibition of porcine Na^+/K^+-ATPase by 0.1 mmol/L of ouabain and the selected 11 steroid-like compounds. Data represent mean±SEM of 5 replicates. $^bP<0.05$, $^cP<0.01$ *vs* control group (CON: deionized water only). (Adopted and modified from Figures 1 and 2 of Chen *et al*, Acta Pharmacol Sin 2010; 31: 696–702).

other cerebrovascular diseases[66]. Ingredients in danshen are mainly divided into water-soluble and lipid-soluble compounds. Although some lipid-soluble constituents in this herb, such as tanshinones, have been conventionally considered the active ingredients[67, 68], the major water-soluble component MLB, a derivative of caffeic acid tetramer, recently has also been demonstrated to possess several medicinal effects, such as vasodilating, antihypertensive, antioxidative, and free radical scavenging activities[69–73]. MLB possesses a relatively rigid structure due to the formation of salt bridges between Mg^{2+} and the four oxygen atoms of carboxyl groups from the four caffeic acid fragments.

In spite of being a non-steroid compound, MLB possesses potent inhibition on Na^+/K^+-ATPase *in vitro*[74]. The molecular organization and configuration of MLB in the 3D structure is somewhat similar to ouabain, a cardiac glycoside with a rigid steroid backbone (Figure 3A), although they are totally different compounds with distinct molecular weights (584.65 for ouabain and 740.67 for MLB). Based on experimental observation and theoretical modeling, we propose that MLB acts as the active component responsible for the cardiac therapeutic effect of danshen by the same molecular mechanism triggered by cardiac glycosides, *ie*, inhibition of Na^+/K^+-ATPase (Figure 3B). In agreement with this proposal, the intracellular Ca^{2+}

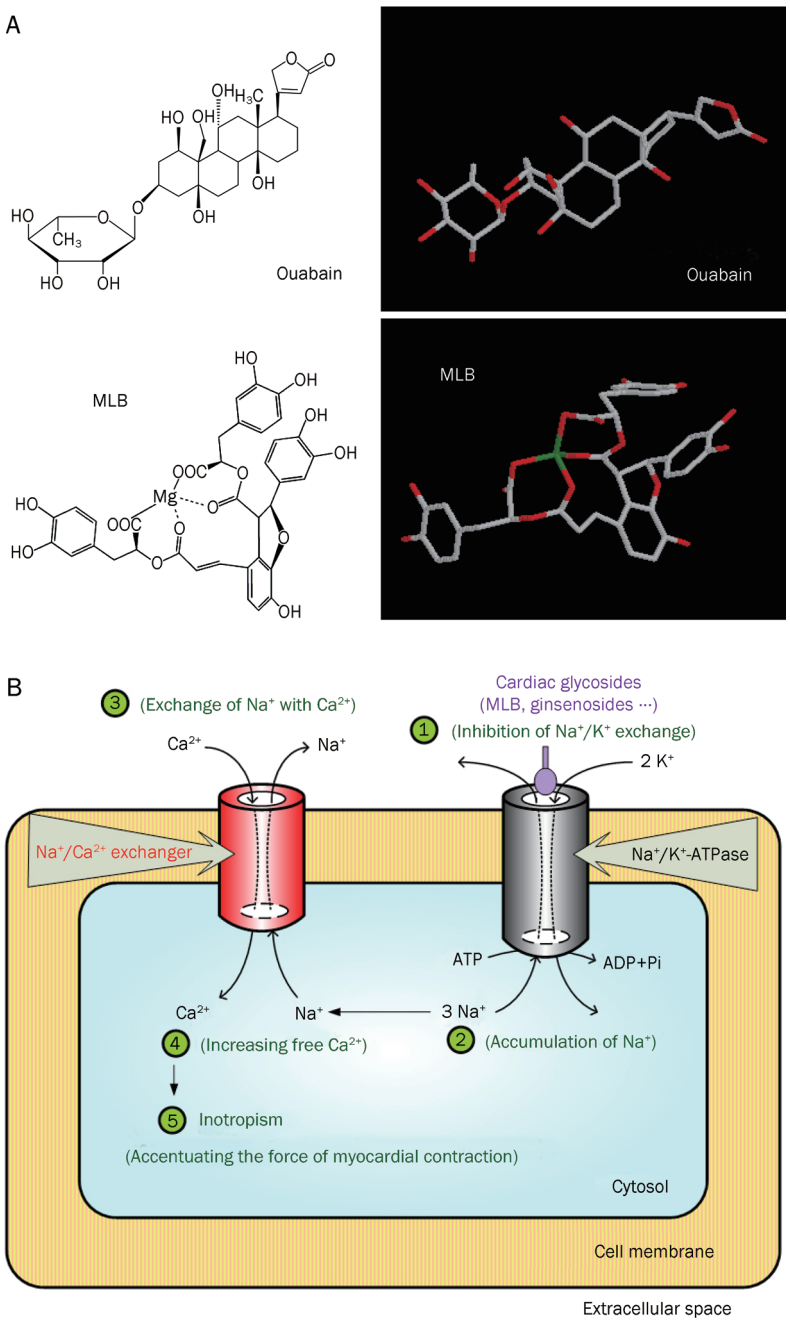

Figure 3. (A) Chemical structures of ouabain and MLB. The 3D structures of ouabain and MLB (in dark background) were displayed using RasWin Molecular Graphics Windows Version 2.6. Gray, red, and green colors represent C, O, and Mg^{2+} atoms, respectively. (B) Proposed molecular mechanism responsible for the therapeutic effects of cardiac glycosides, ginsenosides, MLB, and other steroid-like compounds in cardiac cells. Step 1: Inhibiting the cellular exchange of Na^+ and K^+ by drugs binding to Na^+/K^+-ATPase. Step 2: Accumulation of Na^+ in the intracellular space due to the inhibition of Na^+/K^+-ATPase activity. Step 3: Promotion of the cellular exchange of Na^+ and Ca^{2+} via the Na^+/Ca^{2+} exchanger system. Step 4: Increasing the intracellular Ca^{2+} concentration owing to the activation of the Na^+/Ca^{2+} exchanger system. Step 5: The elevated intracellular Ca^{2+} concentration leads to an increased inotropism and accentuates the force of myocardial contraction. (Adopted from Figure 1 and the cover page of Tzen *et al*, Acta Pharmacol Sin 2007; 28: 609–15).

levels of SH-SY5Y neuroblastoma cells treated with MLB are substantially elevated in a manner similar to that observed in cells treated with ouabain[75]. The elevated Ca^{2+} levels seem to be supplied by both extracellular influx through the Na^+/Ca^{2+} exchanger and intracellular release from endoplasmic reticulum.

Cell toxicity caused by cardiac glycosides at high concentrations has been noticed and blamed to their putative triggering of several signaling cascade responses that lead to cell death[76]. In contrast, MLB is generally regarded as an antioxidant without notable toxicity[74]. Similar results were found in our studies: severe cell toxicity accompanied with dendritic shrink was observed in SH-SY5Y cells treated with ouabain, but not in those treated with MLB[75]. Therefore, we surmise that MLB has a great potential, with extensive clinical trials, to become a safer drug than cardiac glycosides.

Molecular modeling: the binding mode of potential inhibitors to Na^+/K^+-ATPase

Molecular modeling and docking of steroid-like compounds and MLB to the α subunit of Na^+/K^+-ATPase revealed the observed difference in their Na^+/K^+-ATPase inhibition at molecular level. The drastic difference observed in the inhibitory potency of these active ingredients is ascribed mainly to the number of hydrogen bonds (H-bonds) and partially to the strength of hydrophobic interaction between the com-

pounds and residues around the deep cavity close to the two K^+ binding sites of Na^+/K^+-ATPase (Figure 4). As expected from structural similarity, the interaction of bufalin with the binding pocket of Na^+/K^+-ATPase nearly matched to that of ouabain reported previously[16] with the unique lactone ring penetrating deeply into the cavity close to two K^+ binding sites. For ouabain, three H-bonds are formed between the lactone ring and Ile328 and Ala330 of Na^+/K^+-ATPase, and two H-bonds between the hydroxyl group at C-14 and Thr804 of Na^+/K^+-ATPase. In contrast, one H-bond is formed between the lactone ring of bufalin and Ala330 of Na^+/K^+-ATPase, and two H-bonds between the hydroxyl group at C-14 of bufalin and Thr804 of Na^+/K^+-ATPase. Two H-bonds are formed between the hydroxyl groups at C-12 and C-20 of ginsenoside Rh2 and Asn129 and Thr804 of Na^+/K^+-ATPase, respectively. Strong hydrophobic interaction is found between the lactone ring of ouabain or bufalin and six hydrophobic residues (Ile327, Ile328, Val329, Ile787, Phe790, and Ile807) around the deep cavity of Na^+/K^+-ATPase. A hydrophobic interaction between the alkyl group of ginsenoside Rh2 and the same six hydrophobic residues of Na^+/K^+-ATPase is also found. Only one H-bond is formed between the carboxyl group of ursolic acid and Ile322 of Na^+/K^+-ATPase, and a moderate hydrophobic interaction is found between the ring E of ursolic acid and four hydrophobic residues (Ile327, Val329, Phe790, and Ile807) of Na^+/K^+-ATPase. On the whole, no H-bond is formed between those steroid-like compounds with weak inhibitory potency and the binding pocket of Na^+/K^+-ATPase[65]. However, hydrophobic interaction of similar strength is observed between the hydrophobic steroidal core of all 12 steroid-like compounds examined and 8 other hydrophobic residues (Leu132, Tyr315, Ile322, Phe323, Ile325, Phe793, Ile794, and Leu802 located in the upper portions of the figures) around the binding pocket of Na^+/K^+-ATPase.

Three H-bonds are formed between the hydroxyl group at C-4 position of MLB and Lys912 (forming two H-bonds) and Glu915 (forming one H-bond) of Na^+/K^+-ATPase, one H-bond between the carbonyl group at C-9 position of MLB and Thr804 of Na^+/K^+-ATPase, and one H-bond between the hydroxyl group at C-4 position of MLB and Leu110 of Na^+/K^+-ATPase. Similar to the hydrophobic steroidal core of ouabain, the four aromatic rings of MLB form strong hydrophobic interaction with hydrophobic residues (Leu132, Tyr315, Ile322, Phe323, Ile325, Phe793, Ile794, and Leu802) around the binding pocket of Na^+/K^+-ATPase.

Effects of different sugar attachments to ginsenosides on Na^+/K^+-ATPase inhibitory potency

Ginsenosides are triterpenoidal saponins that have a common four ring hydrophobic steroid-like structure with various sugar moieties attached mostly at the C-3, C-6, or C-20 position (Figure 5). To date, more than 80 ginsenosides have been isolated from over ten *Panax taxa*, and most of them are derived from four types of aglycones: protopanaxadiol, protopanaxatriol, oleanolic acid, and ocotillol[77]. Several biological activities, such as neuroprotective effects, antitumour activity, and cardiac therapeutic effects, have been documented for many ginsenosides[78, 79]. Ginsenosides have also been regarded as the active ingredients in many Chinese herbs, for instance, ginseng and sanqi (the roots of *Panax ginseng* and *Panax notoginseng*), two well-known traditional Chinese herbs commonly used for the treatment of coronary heart disease and cerebral vascular disease[80–82].

Based on experimental observation and theoretical modeling, the therapeutic effects of ginseng and sanqi in promoting blood circulation should be at least partly attributed to the effective inhibition of Na^+/K^+-ATPase by ginsenosides[83], such as ginsenoside Rh2. However, different sugar moieties in ginsenosides affect their inhibitory potency on Na^+/K^+-ATPase. In our study, ginsenosides with sugar moieties attached only to the C-3 position of the steroid-like structure, equivalent to the sugar position in cardiac glycosides, possess inhibitory potency on Na^+/K^+-ATPase. However, their inhibitory potency is significantly reduced or completely abolished when a monosaccharide was linked to the C-6 or C-20 position of the steroid-like structure; the inhibitory potency is lost completely when the monosaccharide is replaced by a disaccharide molecule at either positions. Molecular modeling and docking show that sugar attachment to the C-6 or C-20 position of the steroid-like structure apparently causes steric hindrance to the entrance of ginsenosides into the extracellular binding pocket of the Na^+/K^+-ATPase α subunit, and thus greatly reduces or completely abolishes their inhibitory potency.

Paradoxically, most ginsenosides found in ginseng and sanqi do not seem to be competent inhibitors of Na^+/K^+-ATPase due to their sugar attachment to the C-6 or C-20 position of the steroid-like structure. Nevertheless, ginsenosides might act as prodrugs, as they tend to be metabolized to their active forms by intestinal bacterial deglycosylation after oral administration[84]. Generally, the metabolites, easily absorbed by the intestines due to an increase of hydrophobicity after deglycosylation, might display the same or different pharmacological actions in comparison with their parent compounds[85]. Therefore, the cardiac therapeutic effects of ginseng and sanqi could very possibly be attributed to the effective inhibition of Na^+/K^+-ATPase by the metabolized ginsenosides, with sugar moieties attached only to the C-3 position of the steroid-like structure.

Combinational usage of danshen and sanqi for the treatment of cardiovascular diseases

In contrast with Western medicines, combinational usage of traditional Chinese medicines with similar or different therapeutic effects is a common practice. Currently, several commercial products for cardiovascular diseases comprise mainly danshen and sanqi in variable ratios, mostly with danshen as the major and sanqi the minor constituents[86]. The active ingredients in danshen and sanqi for cardiac therapeutic effects are MLB and ginsenosides, respectively. MLB, a polyphenolic compound, is metabolized within a few hours after consumption[87]. In contrast, it takes a couple of days to metabolize the steroid-like ginsenosides in human body[88, 89].

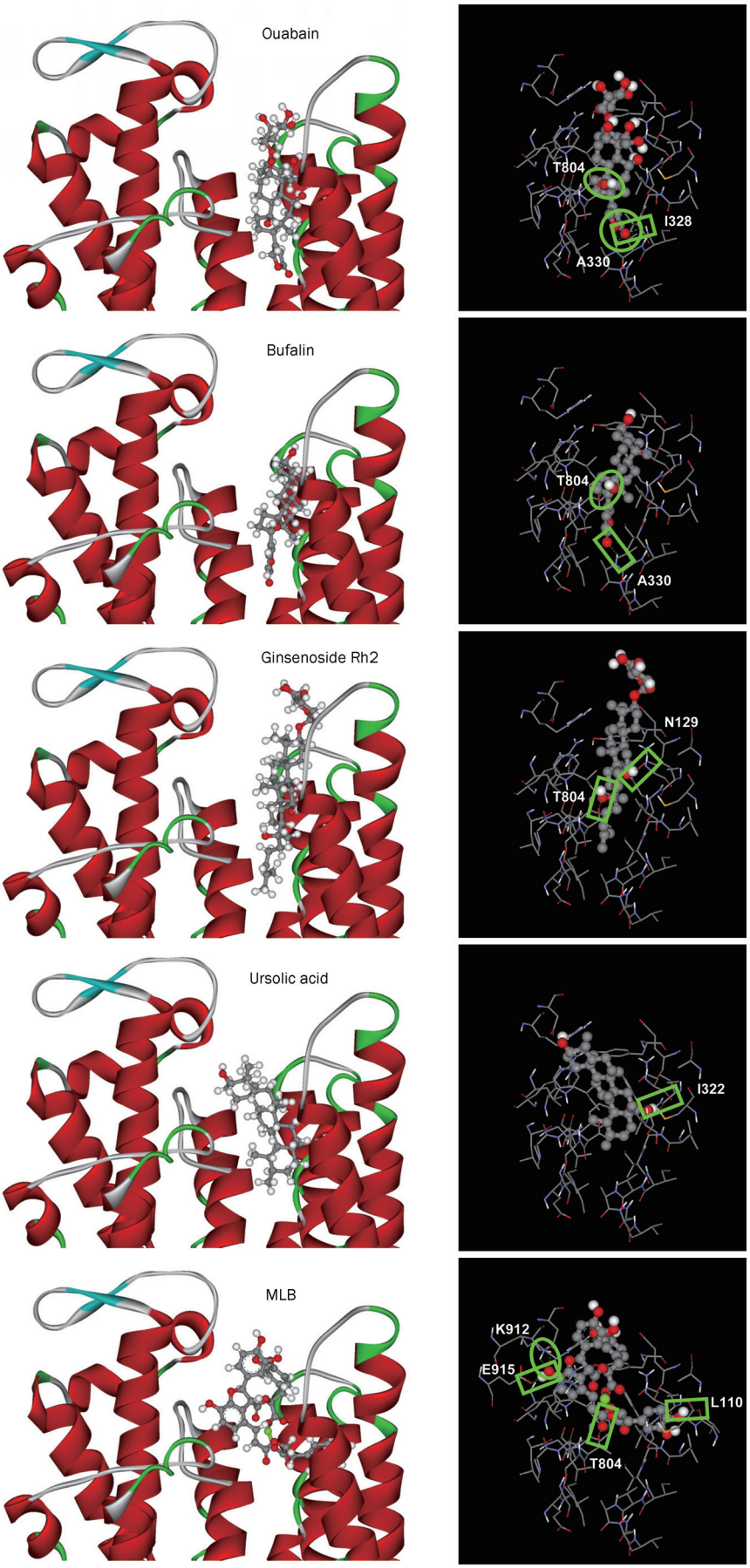

Figure 4. Detailed molecular interactions between the extracellular binding pocket of Na^+/K^+-ATPase and ouabain, bufalin, ginsenoside Rh2, ursolic acid, or MLB. (Left panels) Modeling is displayed for ligand compounds, ouabain, bufalin, ginsenoside Rh2, ursolic acid, and MLB binding to the extracellular pocket of Na^+/K^+-ATPase α subunit. Amino acid residues around the binding pocket of Na^+/K^+-ATPase are shown in ribbon structure, and ligand compounds in stick structure. (Right panels) Amino acid residues of Na^+/K^+-ATPase close to ligand compounds (ball-and-stick structure) are shown in line structure. Green box or oval represents one or two hydrogen bonds formed between Na^+/K^+-ATPase and ligand compounds. (Adopted and modified from Figure 6 of Chen *et al*, Acta Pharmacol Sin 2010; 31: 696–702 and Figure 5 of Chen *et al*, Acta Pharmacol Sin 2010; 31: 923–9).

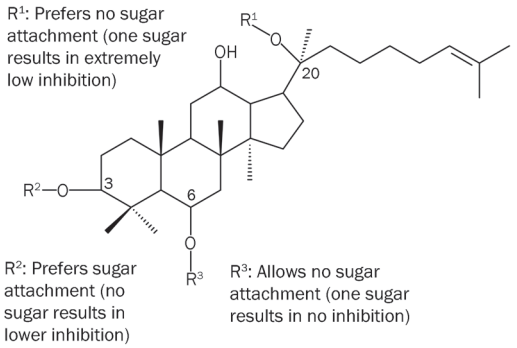

Figure 5. A summarized diagram for the effects of sugar attachments in three different positions of the steroid nucleus of ginsenosides. Detailed 3D diagrams are shown in Figures 4, 5, and 6 of Chen *et al*, Acta Pharmacol Sin 2009; 30: 61–9.

In light of our recent studies, we rationalize that the combinational usage of danshen and sanqi for the treatment of cardiovascular diseases takes the advantages of the non-toxic and yet strong Na^+/K^+-ATPase inhibitory potency of MLB to relieve the symptoms promptly and the moderate Na^+/K^+-ATPase inhibitory potency of ginsenosides to provide a relatively long-term basal therapeutic effect.

Inhibition of Na^+/K^+-ATPase and its potential neuroprotection

In brain cells, approximately half of all energy is spent for the active exchange of cytosolic sodium for extracellular potassium, a process carried out by Na^+/K^+-ATPase for the maintenance of transmembrane ionic gradients for all mammalian cells[90–92]. As the brain's primary consumer of ATP, Na^+/K^+-ATPase is particularly vulnerable to ATP depletion commonly observed in ischemic stroke. This vulnerability suggests that pharmacological inhibition of the Na^+/K^+-ATPase in brain cells should further compromise ATP-depleted neurons. Indeed, there is accumulating evidence that inhibiting the brain Na^+/K^+-ATPase can actually provide neuroprotection in the context of ischemia[93].

Cardiac glycosides, being potent inhibitors of Na^+/K^+-ATPase, have been demonstrated to provide neuroprotection against ischemic stroke in a cortical brain slice-based compound screening platform[94]. Moreover, it has been hypothesized that blockade of Na^+/K^+-ATPase may provide neuroprotective effect in ischemia-reperfusion through ATP conservation and modulating intracellular calcium levels just as the cardiac glycosides do in the heart contraction cycle[93]. Similar neuroprotective effects have also been documented for ginsenosides against ischemic stroke, and some of the results were observed using the same brain slice assay model[95–99]. Oleanolic acid, a steroid-like compound and moderate inhibitor of Na^+/K^+-ATPase, also displayed neuroprotective effect against focal cerebral ischemic injury[100]. Furthermore, the same phenomenon was observed when we examined the neuroprotective effect of MLB against ischemic stroke in a similar brain slice assay model[74]. Taken together, these experimental data support that inhibiting Na^+/K^+-ATPase may provide neuroprotection in the context of ischemia as well as other neurodegenerative conditions. It is more than likely that effective inhibitors of Na^+/K^+-ATPase in the brain are potential drugs for the treatment of ischemic stroke.

Conclusions and perspectives

With a history of at least 2000 years, traditional Chinese medicines have long been regarded as precious resources for screening new drugs. Our recent studies have shown that steroid-like compounds in many Chinese medicines used for promoting blood circulation display more or less inhibitory potency on Na^+/K^+-ATPase, and may thus provide the therapeutic effects of corresponding medicines via the same molecular mechanism triggered by cardiac glycosides. Except bufalin in ChanSu, steroid-like compounds in traditional Chinese medicines used for promoting blood circulation are expected to exert less severe side effects than cardiac glycosides. Nevertheless, side effects have to be expected of a continuous consumption of these steroid-like compounds for a long period of time. In contrast, MLB, the non-steroid active ingredient responsible for the cardiac therapeutic effect of danshen by effective inhibition of Na^+/K^+-ATPase, is generally regarded as a non-toxic antioxidant without apparent adverse effects. Therefore, we believe that MLB is of great potential to replace cardiac glycosides for the treatment of congestive heart failure, provided it undergoes necessary clinical trials. Moreover, searching from traditional Chinese medicines for additional antioxidant polyphenolic compounds possessing inhibitory potency on Na^+/K^+-ATPase may lead to the discovery of novel drugs for the treatment of cardiovascular diseases without side effects.

Acknowledgements

Project supported by a grant to Jason TC TZEN from the National Science Council, Taiwan, China (No 96-2752-B-005-008-PAE).

We thank Prof Chih-ning SUN (Department of Entomology, National Chuang Hsing University, China) for critical reading of the manuscript.

References

1 Boxer R, Yang SX, Hager WD. Congestive heart failure and the elderly. Conn Med 2003; 67: 497–503.
2 Haustein KO. Cardiotoxicity of digitalis. Arch Toxicol Suppl 1986; 9: 197–204.
3 Koren G, Woodland C, Ito S. Toxic digoxin-drug interactions: the major role of renal P-glycoprotein. Vet Hum Toxicol 1998; 40: 45–6.
4 Vivo RP, Krim SR, Perez J, Inklab M, Tenner T Jr, Hodgson J. Digoxin: current use and approach to toxicity. Am J Med Sci 2008; 336: 423–8.
5 Gong X, Sucher NJ. Stroke therapy in traditional Chinese medicine (TCM): prospects for drug discovery and development. Phytomedicine 2002; 9: 478–84.
6 Liang H, Chen S, Shen S. Clinical observation on influence of Chinese medicines for promoting blood circulation to remove blood stasis on FIB and DD in plasma of patients with cerebral thrombosis.

J Tradit Chin Med 2002; 22: 256–9.
7 Yang M, Sun J, Lu Z, Chen G, Guan S, Liu X, *et al*. Phytochemical analysis of traditional Chinese medicine using liquid chromatography coupled with mass spectrometry. J Chromatogr A 2009; 1216: 2045–62.
8 Liu XX, Wang L, Chen XQ, Deng XT, Cao Y, Wang Q. Simultaneous quantification of both triterpenoid and steroidal saponins in various Yunnan Baiyao preparations using HPLC-UV and HPLC-MS. J Sep Sci 2008; 31: 3834–46.
9 Zhang Q, Ye M. Chemical analysis of the Chinese herbal medicine Gan-Cao (licorice). J Chromatogr A 2009; 1216: 1954–69.
10 Wang X, Morris-Natschke SL, Lee KH. New developments in the chemistry and biology of the bioactive constituents of Tanshen. Med Res Rev 2007; 27: 133–48.
11 Skou JC, Esmann M. The Na, K-ATPase. J Bioenerg Biomembr 1992; 24: 249–61.
12 Shinoda T, Ogawa H, Cornelius F, Toyoshima C. Crystal structure of the sodium-potassium pump at 2.4 Å resolution. Nature 2009; 459: 446–50.
13 Morth JP, Pedersen BP, Toustrup-Jensen MS, Sorensen TL, Petersen J, Andersen JP, *et al*. Crystal structure of the sodium-potassium pump. Nature 2007; 450: 1043–9.
14 Ogawa H, Shinoda T, Cornelius F, Toyoshima C. Crystal structure of the sodium-potassium pump (Na^+,K^+-ATPase) with bound potassium and ouabain. Proc Natl Acad Sci USA 2009; 106: 13742–7.
15 O'Brien WJ, Lingrel JB, Wallick ET. Ouabain binding kinetics of the rat alpha two and alpha three isoforms of the sodium-potassium adenosine triphosphate. Arch Biochem Biophys 1994; 310: 32–9.
16 Morris JF, Ismail-Beigi F, Butler VP, Gati I, Lichtstein D. Ouabain-sensitive Na^+,K^+-ATPase activity in toad brain. Comp Biochem Physiol A Physiol 1997; 118: 599–606.
17 Lebovitz RM, Takeyasu K, Fambrough DM. Molecular characterization and expression of the (Na^+, K^+)-ATPase alpha-subunit in *Drosophila melanogaster*. EMBO J 1989; 8: 193–202.
18 Rose AM, Valdes R Jr. Understanding the sodium pump and its relevance to disease. Clin Chem 1994; 40: 1674–85.
19 Gillis RA, Quest JA. The role of the nervous system in the cardiovascular effects of digitalis. Pharmacol Rev 1979; 31: 19–97.
20 Blanco G, Mercer RW. Isozymes of the Na-K-ATPase: heterogeneity in structure, diversity in function. Am J Physiol 1998; 275: F633–50.
21 Lingrel JB. Na,K-ATPase: isoform structure, function, and expression. J Bioenerg Biomembr 1992; 24: 263–70.
22 Lingrel JB. The physiological significance of the cardiotonic steroid/ouabain-binding site of the Na,K-ATPase. Annu Rev Physiol 2010; 72: 395–412.
23 Blaustein MP. Physiological effects of endogenous ouabain: control of intracellular Ca^{2+} stores and cell responsiveness. Am J Physiol 1993; 264: C1367–87.
24 Xie Z, Xie J. The Na/K-ATPase-mediated signal transduction as a target for new drug development. Front Biosci 2005; 10: 3100–9.
25 Xie Z, Cai T. Na^+/K^+-ATPase-mediated signal transduction: from protein interaction to cellular function. Mol Interv 2003; 3: 157–68.
26 Zhang L, Zhang Z, Guo H, Wang Y. Na^+/K^+-ATPase-mediated signal transduction and Na^+/K^+-ATPase regulation. Fundam Clin Pharmacol 2008; 22: 615–21.
27 Schonfeld W, Weiland J, Lindig C, Masnyk M, Kabat MM, Kurek A, *et al*. The lead structure in cardiac glycosides is 5 beta, 14 beta-androstane-3 beta 14-diol. Naunyn Schmiedebergs Arch Pharmacol 1985; 329: 414–26.
28 Melero CP, Medarde M, San Feliciano A. A short review on cardiotonic steroids and their aminoguanidine analogues. Molecules 2000; 5: 51–81.
29 Li-Saw-Hee FL, Lip GY. Digoxin revisited. QJM 1998; 91: 259–64.
30 Lin SC, Way EL. A high affinity Ca^{2+}-ATPase in enriched nerve-ending plasma membranes. Brain Res 1982; 235: 387–92.
31 Blaustein MP. The interrelationship between sodium and calcium fluxes across cell membranes. Rev Physiol Biochem Pharmacol 1974; 70: 33–82.
32 Ferrandi M, Barassi P, Molinari I, Torielli L, Tripodi G, Minotti E, *et al*. Ouabain antagonists as antihypertensive agents. Curr Pharm Des 2005; 11: 3301–5.
33 Yang Z, Luo H, Wang H, Hou H. Preparative isolation of bufalin and cinobufagin from Chinese traditional medicine ChanSu. J Chromatogr Sci 2008; 46: 81–5.
34 Bick RJ, Poindexter BJ, Sweney RR, Dasgupta A. Effects of ChanSu, a traditional Chinese medicine, on the calcium transients of isolated cardiomyocytes: cardiotoxicity due to more than Na, K-ATPase blocking. Life Sci 2002; 72: 699–709.
35 Lee E, Kim S, Chung KC, Choo MK, Kim DH, Nam G, *et al*. 20(S)-ginsenoside Rh2, a newly identified active ingredient of ginseng, inhibits NMDA receptors in cultured rat hippocampal neurons. Eur J Pharmacol 2006; 536: 69–77.
36 Jia WW, Bu X, Philips D, Yan H, Liu G, Chen X, *et al*. Rh2, a compound extracted from ginseng, hypersensitizes multidrug-resistant tumor cells to chemotherapy. Can J Physiol Pharmacol 2004; 82: 431–7.
37 Chen Y, Zhan E, Chen H, Duan X, Guo L. Saponins with low sugar chain from the leaves of *Panax notoginseng* (Burk) F H Chen. Zhong Yao Cai 2002; 25: 176–8.
38 Lee IK, Kim DH, Lee SY, Kim KR, Choi SU, Hong JK, *et al*. Triterpenoic acids of *Prunella vulgaris* var lilacina and their cytotoxic activities *in vitro*. Arch Pharm Res 2008; 31: 1578–83.
39 Ryu SY, Oak MH, Yoon SK, Cho DI, Yoo GS, Kim TS, *et al*. Anti-allergic and anti-inflammatory triterpenes from the herb of *Prunella vulgaris*. Planta Med 2000; 66: 358–60.
40 Tan LL, Cai X, Hu ZH, Ni XL. Localization and dynamic change of saikosaponin in root of *Bupleurum chinense*. J Integr Plant Biol 2008; 50: 951–7.
41 Zhou QL, Zhang ZQ, Nagasawa T, Hiai S. The structure activity relationship of saikosaponins and glycyrrhizin derivatives for Na^+, K^+-ATPase inhibiting action. Yao Xue Xue Bao 1996; 31: 496–501.
42 Wang FS, Xu LX, Zhao YJ, Liu AR, Jin LZ, Zhang XQ. Determination of bile acids in bear gall drainage by thin layer chromatographic scanning. Yao Xue Xue Bao 1989; 24: 397–400.
43 Kurozumi K, Harano T, Yamasaki K, Ayaki Y. Studies on bile acids in bear bile. J Biochem 1973; 74: 489–95.
44 Liu Y, Chen W, Qiao C, Zhao N. Determination of sarsasapogenin in *Anemarrhena asphodeloides* Bunge by GC. Zhongguo Zhong Yao Za Zhi 1999; 24: 554–5, 75.
45 Fu WW, Hou WB, Dou DQ, Hua HM, Gui MH, Fu R, *et al*. Saponins of polygalacic acid type from *Platycodon grandiflorum*. Yao Xue Xue Bao 2006; 41: 358–60.
46 Zhang M, Zhang Y, Xie J. Simultaneous determination of jujuboside A, B and betulinic acid in semen *Ziziphi spinosae* by high performance liquid chromatography-evaporative light scattering detection. J Pharm Biomed Anal 2008; 48: 1467–70.
47 Hennell JR, Lee S, Khoo CS, Gray MJ, Bensoussan A. The determination of glycyrrhizic acid in *Glycyrrhiza uralensis* Fisch ex DC (Zhi Gan Cao) root and the dried aqueous extract by LC-DAD. J Pharm Biomed Anal 2008; 47: 494–500.
48 Sun ZR, Zhai MP, Wang WQ, Li YR. Effects of density on seedling growth and glycyrrhizinic acid content in *Glycyrrhiza uralensis*. Zhongguo Zhong Yao Za Zhi 2007; 32: 2222–6, 81. Chinese.

49 Xu Q, Ma X, Liang X. Determination of astragalosides in the roots of *Astragalus spp* using liquid chromatography tandem atmospheric pressure chemical ionization mass spectrometry. Phytochem Analysis 2007; 18: 419–27.
50 Lin HC, Ding HY, Wu YC. Two novel compounds from *Paeonia suffructicosa*. J Nat Prod 1998; 61: 343–6.
51 Zhu TT, Liang H, Zhao YY, Wang B. Isolation and structure identification of C-25 epimers of inokosterone from *Achyranthes bidentata* Blume. Yao Xue Xue Bao 2004; 39: 913–6. Chinese.
52 Hu T, Zhang X, Ma S, Cheng Y, Yao X. Chemical constituents from *Corydalis yanhusuo*. Zhongguo Zhong Yao Za Zhi 2009; 34: 1917–20. Chinese.
53 Zhang J, Jin Y, Liu Y, Xiao Y, Feng J, Xue X, *et al*. Purification of alkaloids from *Corydalis yanhusuo* W T Wang using preparative 2-D HPLC. J Sep Sci 2009; 32: 1401–6.
54 Zhang WB, Chen CX, Sim SM, Kwan CY. *In vitro* vasodilator mechanisms of the indole alkaloids rhynchophylline and isorhynchophylline, isolated from the hook of *Uncaria rhynchophylla* (Miquel). Naunyn Schmiedebergs Arch Pharmacol 2004; 369: 232–8.
55 Shi JS, Yu JX, Chen XP, Xu RX. Pharmacological actions of *Uncaria* alkaloids, rhynchophylline and isorhynchophylline. Acta Pharmacol Sin 2003; 24: 97–101.
56 Nakazawa T, Banba K, Hata K, Nihei Y, Hoshikawa A, Ohsawa K. Metabolites of hirsuteine and hirsutine, the major indole alkaloids of *Uncaria rhynchophylla*, in rats. Biol Pharm Bull 2006; 29: 1671–7.
57 Horie S, Yano S, Aimi N, Sakai S, Watanabe K. Effects of hirsutine, an antihypertensive indole alkaloid from *Uncaria rhynchophylla*, on intracellular calcium in rat thoracic aorta. Life Sci 1992; 50: 491–8.
58 Ozaki Y. Vasodilative effects of indole alkaloids obtained from domestic plants, *Uncaria rhynchophylla* Miq and *Amsonia elliptica* Roem et Schult. Nippon Yakurigaku Zasshi 1990; 95: 47–54. Japanese.
59 Oh H, Mun YJ, Im SJ, Lee SY, Song HJ, Lee HS, *et al*. Cucurbitacins from *Trichosanthes kirilowii* as the inhibitory components on tyrosinase activity and melanin synthesis of B16/F10 melanoma cells. Planta Med 2002; 68: 832–3.
60 Takahashi N, Yoshida Y, Sugiura T, Matsuno K, Fujino A, Yamashita U. Cucurbitacin D isolated from *Trichosanthes kirilowii* induces apoptosis in human hepatocellular carcinoma cells *in vitro*. Int Immunopharmacol 2009; 9: 508–13.
61 Badria FA, Mikhaeil BR, Maatooq GT, Amer MM. Immunomodulatory triterpenoids from the oleogum resin of *Boswellia carterii* Birdwood. Z Naturforsch C 2003; 58: 505–16.
62 Jayaprakasha GK, Mandadi KK, Poulose SM, Jadegoud Y, Nagana Gowda GA, Patil BS. Novel triterpenoid from *Citrus aurantium* L. possesses chemopreventive properties against human colon cancer cells. Bioorg Med Chem 2008; 16: 5939–51.
63 Zhang S. Chemical constituents of the *Sparganium stoloniferum* Buch.-Ham. Zhongguo Zhong Yao Za Zhi 1995; 20: 486–7. Chinese.
64 Zheng Y, Yang XW. Two new lanostane triterpenoids from *Poria cocos*. J Asian Nat Prod Res 2008; 10: 323–8.
65 Chen RJY, Chung TY, Li FY, Yang WH, Jinn TR, Tzen JTC. Steroid-like compounds in Chinese medicines promote blood circulation via inhibition of Na^+/K^+-ATPase. Acta Pharmacol Sin 2010; 31: 696–702.
66 Li XC, Yu C, Sun WK, Liu GY, Jia JY, Wang YP. Pharmacokinetics of magnesium lithospermate B after intravenous administration in beagle dogs. Acta Pharmacol Sin 2004; 25: 1402–7.
67 Shigematsu T, Tajima S, Nishikawa T, Murad S, Pinnell SR, Nishioka I. Inhibition of collagen hydroxylation by lithospermic acid magnesium salt, a novel compound isolated from *Salviae miltiorrhizae* Radix. Biochim Biophys Acta 1994; 1200: 79–83.
68 Lu Y, Foo LY. Polyphenolics of *Salvia* — a review. Phytochemistry 2002; 59: 117–40.
69 Wu XJ, Wang YP, Wang W, Sun WK, Xu YM, Xuan LJ. Free radical scavenging and inhibition of lipid peroxidation by magnesium lithospermate B. Acta Pharmacol Sin 2000; 21: 855–8.
70 Kasimu R, Tanaka K, Tezuka Y, Gong ZN, Li JX, Basnet P, *et al*. Comparative study of seventeen *Salvia* plants: aldose reductase inhibitory activity of water and MeOH extracts and liquid chromatography-mass spectrometry (LC-MS) analysis of water extracts. Chem Pharm Bull 1998; 46: 500–4.
71 Yokozawa T, Chung HY, Dong E, Oura H. Confirmation that magnesium lithospermate B has a hydroxyl radical-scavenging action. Exp Toxicol Pathol 1995; 47: 341–4.
72 Yokozawa T, Lee TW, Oura H, Nonaka G, Nishioka I. Effect of magnesium lithospermate B in rats with sodium-induced hypertension and renal failure. Nephron 1992; 60: 460–5.
73 O K, Lynn EG, Vazhappilly R, Au-Yeung KK, Zhu DY, Siow YL. Magnesium tanshinoate B (MTB) inhibits low density lipoprotein oxidation. Life Sci 2001; 68: 903–12.
74 Tzen JT, Jinn TR, Chen YC, Li FY, Cheng FC, Shi LS, *et al*. Magnesium lithospermate B possesses inhibitory activity on Na^+,K^+-ATPase and neuroprotective effects against ischemic stroke. Acta Pharmacol Sin 2007; 28: 609–15.
75 Chen YC, Jinn TR, Chung TY, Li FY, Fan RJ, Tzen JT. Magnesium lithospermate B extracted from *Salvia miltiorrhiza* elevates intracellular Ca^{2+} level in SH-SY5Y cells. Acta Pharmacol Sin 2010; 31: 923–9.
76 Kulikov A, Eva A, Kirch U, Boldyrev A, Scheiner-Bobis G. Ouabain activates signaling pathways associated with cell death in human neuroblastoma. Biochim Biophys Acta 2007; 1768: 1691–702.
77 Zhu S, Zou K, Cai S, Meselhy MR, Komatsu K. Simultaneous determination of triterpene saponins in ginseng drugs by high-performance liquid chromatography. Chem Pharm Bull 2004; 52: 995–8.
78 Dan M, Su MM, Gao XF, Zhao T, Zhao AH, Xie GX, *et al*. Metabolite profiling of *Panax notoginseng* using UPLC-ESI-MS. Phytochemistry 2008; 69: 2237–44.
79 Hasegawa H. Proof of the mysterious efficacy of ginseng: basic and clinical trials: metabolic activation of ginsenoside: deglycosylation by intestinal bacteria and esterification with fatty acid. J Pharmacol Sci 2004; 95: 153–7.
80 Sengupta S, Toh SA, Sellers LA, Skepper JN, Koolwijk P, Leung HW, *et al*. Modulating angiogenesis: the yin and the yang in ginseng. Circulation 2004; 110: 1219–25.
81 Lei XL, Chiou GC. Cardiovascular pharmacology of *Panax notoginseng* (Burk) F H Chen and *Salvia miltiorrhiza*. Am J Chin Med 1986; 14: 145–52.
82 Cicero AF, Vitale G, Savino G, Arletti R. *Panax notoginseng* (Burk) effects on fibrinogen and lipid plasma level in rats fed on a high-fat diet. Phytother Res 2003; 17: 174–8.
83 Chen RJY, Chung TY, Li FY, Lin NH, Tzen JTC. Effect of sugar positions in ginsenosides and their inhibitory potency on Na^+/K^+-ATPase activity. Acta Pharmacol Sin 2009; 30: 61–9.
84 Nah SY, Kim DH, Rhim H. Ginsenosides: are any of them candidates for drugs acting on the central nervous system? Cns Drug Rev 2007; 13: 381–404.
85 Tawab MA, Bahr U, Karas M, Wurglics M, Schubert-Zsilavecz M. Degradation of ginsenosides in humans after oral administration. Drug Metab Dispos 2003; 31: 1065–71.
86 Shang HC, Gao XM, Guo LP. The optimization of different combinations and distributions between Danshen and Sanqi along with syn-

thetical information evaluation. Drug Evaluation 2005; 2: 209–11. Chinese.

87 Li XC, Yu C, Cai YB, Liu GY, Jia JY, Wang YP. Simultaneous determination of six phenolic constituents of danshen in human serum using liquid chromatography/tandem mass spectrometry. J Chromatogr B 2005; 820: 41–7.

88 Tawab MA, Bahr U, Karas M, Wurglics M, Schubert-Zsilavecz M. Degradation of ginsenosides in humans after oral administration. Drug Metab Dispos 2003; 31: 1065–71.

89 Oian TX, Cai ZW, Wong RNS, Jiang ZH. Liquid chromatography mass spectrometric analysis of rat samples for *in vivo* metabolism and pharmacokinetic studies of ginsenoside Rh2. Rapid Commun Mass Sp 2005; 19: 3549–54.

90 Clausen T, Van Hardeveld C, Everts ME. Significance of cation transport in control of energy metabolism and thermogenesis. Physiol Rev 1991; 71: 733–74.

91 Friberg H, Wieloch T. Mitochondrial permeability transition in acute neurodegeneration. Biochimie 2002; 84: 241–50.

92 Astrup J. Energy-requiring cell functions in the ischemic brain. Their critical supply and possible inhibition in protective therapy. J Neurosurg 1982; 56: 482–97.

93 Annunziato L, editor. New strategies in stroke intervention. New York: Springer; 2009.

94 Wang JK, Portbury S, Thomas MB, Barney S, Ricca DJ, Morris DL, *et al*. Cardiac glycosides provide neuroprotection against ischemic stroke: discovery by a brain slice-based compound screening platform. Proc Natl Acad Sci USA 2006; 103: 10461–6.

95 Zhang YG, Liu TP. Influences of ginsenosides Rb1 and Rg1 on reversible focal brain ischemia in rats. Zhongguo Yao Li Xue Bao 1996; 17: 44–8.

96 Tian J, Fu F, Geng M, Jiang Y, Yang J, Jiang W, *et al*. Neuroprotective effect of 20(S)-ginsenoside Rg3 on cerebral ischemia in rats. Neurosci Lett 2005; 374: 92–7.

97 Zhou XM, Cao YL, Dou DQ. Protective effect of ginsenoside Re against cerebral ischemia/reperfusion damage in rats. Biol Pharm Bull 2006; 29: 2502–5.

98 Yuan QL, Yang CX, Xu P, Gao XQ, Deng L, Chen P, *et al*. Neuroprotective effects of ginsenoside Rb1 on transient cerebral ischemia in rats. Brain Res 2007; 1167: 1–12.

99 Chen LM, Zhou XM, Cao YL, Hu WX. Neuroprotection of ginsenoside Re in cerebral ischemia-reperfusion injury in rats. J Asian Nat Prod Res 2008; 10: 439–45.

100 Cho SO, Ban JY, Kim JY, Ju HS, Lee IS, Song KS, *et al*. Anti-ischemic activities of *Aralia cordata* and its active component, oleanolic acid. Arch Pharm Res 2009; 32: 923–32.

Acta Pharmacologica Sinica (2011) 32: 152–159
 1671-4083/11 $32.00
www.nature.com/aps

Review

Embryonic stem cell application in drug discovery

Yi-jia LOU*, Xing-guang LIANG

Institute of Pharmacology, Toxicology and Biochemical Pharmaceutics, Zhejiang University, Hangzhou 310058, China

Embryonic stem (ES) cells and their differentiated progeny offer tremendous potential for regenerative medicine, even in the field of drug discovery. There is an urgent need for clinically relevant assays that make use of ES cells because of their rich biological utility. Attention has been focused on small molecules that allow the precise manipulation of cells *in vitro*, which could allow researchers to obtain homogeneous cell types for cell-based therapies and discover drugs for stimulating the regeneration of endogenous cells. Such therapeutics can act on target cells or their niches *in vivo* to promote cell survival, proliferation, differentiation, and homing. In the present paper, we reviewed the use of ES cell models for high-throughput/content drug screening and toxicity assessment. In addition, we examined the role of stem cells in large pharmaceutical companies' R&D and discussed a novel subject, nicheology, in stem cell-related research fields.

Keywords: embryonic stem cells; induced pluripotent stem (iPS) cells; differentiation; small molecules; high-throughput/content screening; drug discovery; toxicity assessment; nicheology

Acta Pharmacologica Sinica (2011) 32: 152–159; doi: 10.1038/aps.2010.194; published online 10 Jan 2011

Introduction

Stem cell research promises to make significant progress in regenerative medicine to replace damaged tissues and organs. An outstanding landmark in the past decade has been the development between stem cell biology and chemistry[1–6]. The combination of the two fields will likely provide an impetus for revealing intricate molecular interactions and functions under complex cellular differentiation, which offers systems for drug discovery and sources for potential cell therapy[7–10].

Embryonic stem (ES) cells can mimic embryogenesis and differentiate into cells of the three embryonic germ layers (endoderm, mesoderm, and ectoderm) from which various specialized cell types of the entire organism are produced[11]. Human ES (hES) cells can also differentiate into all terminal cell types of the human body. Small molecules with inducing ability *in vitro* are expected to possess their own mechanism of promoting differentiation *in vivo*. This makes them potentially valuable for pharmaceutical development and safety assessment. Indeed, small molecules can be screened using hES cell models to find new chemical entities that modulate the fate of adult stem cells, or they could be used directly in cell therapies[4, 8, 10, 11].

Mouse ES (mES) cells have been in use for several years in drug discovery to develop genetically modified mice for target validation, target selectivity, model development and toxicity evaluation[12–17]. Combined with advances in hES cell technology, the drug discovery community may soon have a physiologically relevant screening tool (with limitless availability) that shows normal growth and genetic structure.

Understanding molecular mechanisms that determine stem cell fate (*ie*, self-renewal or differentiation) will significantly promote the realization of the therapeutic potential of stem cells[16, 18–22]. To date, much attention has been paid to signal transduction and the related molecular events during ES cell differentiation. ES cells probably had some novel drug targets, especially in a definite differentiation medium containing low-molecular-weight compound(s). Studies have suggested that a stem cell niche is dynamic, not static, and can be modified or even created[23–27]. Therefore, the stem cell niches regulated by small molecules can control the cell fate, which offers a suitable microenvironment to screen drugs.

A chemical approach of differentiation by small molecules has currently been developed. This review will address ES cell lines that could potentially be used to discover low-molecular-weight agents for the control of differentiation and drugs for the treatment of degenerative diseases. In addition, small molecules could participate in producing induced pluripotent stem (iPS) cells for lower oncogenic and higher reprogramming efficiency by small-molecule hitting.

ES cell models for drug screening

The development of new drugs is costly and time-consuming.

* To whom correspondence should be addressed.
E-mail yijialou@zju.edu.cn
Received 2010-06-10 Accepted 2010-10-12

In particular, the initial stages of research and development (R&D) require *in vitro* models to screen the activity and toxicity of a large number of compounds. Thus, a suitable model that can be used for both effects and safety assessment is extremely important. Cell-based *in vitro* assays with high human relevance are urgently needed for pre-clinical activities. Previous studies have suggested that ES cells could serve as a screening platform to identify low-molecular-weight compounds that affect endogenous stem cell populations and repair damaged tissue[4, 8, 10, 11, 28, 29], and a set of screening protocols is available (*ie*, the primary screen and the secondary assay). In addition, several cell lines, such as D3 mES cells and H1, H7, and H9 hES cells, are available for drug screening[12, 30, 31]. Table 1 lists some characteristics of ES cell and other cell types and their respective advantages and disadvantages.

High-throughput/content screening (primary screen)

Small-molecule libraries can contain millions of compounds. Thus, screens must be employed to effectively eliminate molecules that are toxic or do not have any biological activity. High-throughput screening (HTS) technologies already allow the rapid testing of thousands of compounds. Studies have suggested, however, that screening against a defined molecular target usually exploits a protein's function and results in expression or transcription of differentiation-related genes[29, 32, 33]. For instance, HTS assays usually use 96- or 384-well plates, and the assays can be performed on chemical compounds in various formats.

Generally, enzymatic activity, signal transduction, or molecular interactions with partners that contain reporter systems have been used to assess whether compounds activate particular signaling pathways of interest[34]. Recently, a notable report demonstrated an image-based, high-content assay for detecting compounds that affect hES cell survival or pluripotency[35]. In that study, 1040 compounds were screened using an hES cell colony-based assay. The assay was designed to detect changes in the phenotype of hES cell colonies by quantifying multiple parameters, including the number of cells in a colony, colony area and shape, intensity of nuclear staining, the percentage of cells in the colony that expressed a marker of pluripotency, and the number of colonies per well. As a result, several steroids that promoted hES cell differentiation were identified, and the antihypertensive drug pinacidil was shown to affect hES cell survival. Phenotypic screens can be advantageous because they can be carried out in cells by examining multiple markers and functional changes (for example, cell morphology and behavior) using automated high-content imaging technologies in a high-throughput manner [1, 4, 36, 37].

HTS based on receptors in ES cell-derived neurons have also been reported[38]. That study described an mES cell-based screen of a library of 2.4×10^6 compounds, as well as the identification of novel chemical "hits" for alpha-amino-3-hydroxyl-5-methyl-4-isoxazolepropionate-subtype glutamate receptors, structure–function relationships of compounds and receptors, and validation of lead compounds. The emergence of automated cellular systems has allowed rapid visualization of large groups of cells and phenotypic analysis in a quantitative manner.

Primary screens can also be directly evaluated under a contrast-phase microscope to examine cell differentiation into terminal cells. One protocol for hES cell differentiation into neuroepithelial cells has been recommended, and evaluation

Table 1. Advantages and disadvantages of different cells available for drug screening.

Cell types	Advantages	Disadvantages
Immortalized cell lines	• Homogeneous cell population • Growth and maintenance cheap • Time- and labor-saving	• Lack important aspects of native function • Genetic mutations that cause permanent and heritable change in the phenotype
Primary cells	• Close approximation of native function • Reflect *in vivo* physiological or pathological condition	• Require fresh preparation • Difficult to procure in sufficient quantity • prone to batch-to-batch variability in quality
Stem cells	• Continuously propagated *in vitro* and retain the potential to generate all the cell types of the body (ES cell). • Compounds can modulate more than one target to achieve a desired biological effect. • High quantity • Readily available source of all cell types • Both develop-dependent and fully differentiated cell types	• Limited potential for expansion and are lineage restricted (adult stem cells), • Growth and maintenance expensive • A lot of time needed to obtain fully differentiated cell types • Require more effort to achieve purified populations
iPS cells	• With genetic information of the patients • Reflect *in vivo* physiological or pathological condition • Mimic both develop-dependent and fully differentiated cell types	• Very low efficacy for harvest, (≤1%), expensive for preparations, • Growth and maintenance expensive • A lot of time needed to obtain fully differentiated cell types • Require more effort to achieve purified populations

under a contrast-phase microscope has been described[39]. Recent studies in hES cells have identified a novel neural stem cell stage (*ie*, the rosette stage). In this stage, cells exhibit plasticity by generating a broad range of neuronal cell types in response to appropriate developmental signals. Such rosette-stage neural stem cells can also be distinguished from other neural stem cell populations with a contrast-phase microscope because of their specific rosette cytoarchitecture ("morphology")[40]. The striking cytoarchitecture of rosettes could become a powerful tool for translational medicine and applications in HTC assays that require large numbers of homogeneous cell populations. Recently, a study reported that light microscopy could be used to evaluate embryoid body (EB) structure and size, and the number of wells containing contracting cardiomyocytes was determined[41]. In addition, hepatocytes containing two morphologically distinct populations, a mononuclear population and a binuclear population, were clearly identified under light microscopy. Another study used immunohistochemical analysis to confirm that albumin-positive cells (*ie*, hepatocytes) were present in the outgrowths of EBs with binuclear cells[42]. Examining differentiation into terminal cells under a contrast-phase microscope can save both time and labor during a primary screen. Indeed, this approach has been shown to be helpful for successful screening[14].

More recently, a screen for chemical mediators of reprogramming has been reported[39]. So far, most studies of direct reprogramming have been performed with lentiviruses/retroviruses, which encode the reprogramming factors. This represents a major limitation to therapeutic applications because viral integration in the host genome increases the risk of tumorigenicity. Low-level residual expression of reprogramming factors may alter the differentiation potential of human induced pluripotent stem (iPS) cells. Indeed, both the viral vectors used for gene transfer and the encoded reprogramming factors are probably oncogenic and possess low transduction efficiency[43]. Some small molecules can replace transcription factors, and the combined activity of transcription factors can reprogram adult cells into iPS cells. For example, one study using a high-throughput/content screen showed that a TGF-β inhibitor replaced Sox2 in reprogramming and produced unmodified iPS cell lines[44]. Therefore, small-molecule replacement of transcription factors may be one potential solution to lower the oncogenic potential and increase the reprogramming efficiency[39, 43, 44].

Another valuable report demonstrated a strategy to adapt hES cells to HTS conditions, which resulted in an assay that is suitable for the discovery of small molecules that drive the self-renewal or differentiation of hES cells[45]. Use of this new assay (*ie*, global gene expression analysis) has led to the identification of several marketed drugs and natural compounds that promote short-term hES cell maintenance and direct early lineage choice during differentiation. Desbordes *et al* demonstrated the feasibility of hES cell-based HTS and enhanced the repertoire of chemical compounds that can manipulate hES cell fate.

A series of secondary assays

It has also been recommended that, in general, hit compounds identified from a primary screen be further confirmed using a series of more functional secondary assays and analyzed using informatics tools[29, 45, 46]. Before a compound enters mechanistic studies, it is normally optimized through structure-activity relationship studies to improve its properties, such as increasing its potency and specificity and enhancing its pharmacokinetic properties. All these data can be expected to be obtained via secondary assays.

To identify the molecular targets and pathways of an unknown compound, biochemical and cellular or sub-cellular experiments are commonly used. One study reported that phosphoserine (P-Ser) increased neurogenesis in hES cell-derived neural progenitors[1]. It also confirmed that the effects of P-Ser are mediated by the group III metabotropic glutamate receptor 4 (mGluR4). Saxe and colleagues highlighted the tremendous potential of developing effective small-molecule drugs for use in regenerative medicine or transplantation therapy.

Similarly, protein interactions can be mapped in ES cells to enable systematic discovery of regulatory pathways[47, 48]. Indeed, a method for defining the proteome of stem cell populations using isobaric tags for relative and absolute quantitation has been developed. This allows simultaneous analysis of samples to be analyzed simultaneously, which can give relative quantification for hundreds of proteins from a relatively small (1–5 million) cell number. It is a rapid secondary assay system that precedes more-focused, hypothesis-driven research. The available techniques to study translational regulation of protein levels have decreased the reliance on proteomic confirmation of mRNA-based analyses. In addition, these techniques offer opportunities to develop new quantitative biological approaches to investigate stem cell self-renewal or differentiation, which increase the probability of discovering proteins that regulate development.

During the early stage of development, differentiation-related gene expression or transcriptomics can be regulated, and a genome-wide transcriptional analysis has been used as a powerful assay[32, 33, 49]. For example, genome-wide transcriptional analysis has shown more than just the effects of *Mesp*1 dramatically accelerates and enhances multipotent cardiovascular progenitor specification through an intrinsic and cell-autonomous mechanism. In addition, analysis at various time points identified 1355 genes that were significantly regulated, and the differentiation track was described in a principal component analysis[33]. Differentiation cultures exposed to monobutyl phthalate or 6-aminonicotinamide (from the EB stage onward) for 24 or 96 h showed RNA expression patterns that deviated from the differentiation track. Studies like these demonstrate that secondary assays can be used as informatics tools and are involved in further functional evaluation.

ES cell models for drug toxicity assessment

Stem cells have been used to evaluate cardiotoxicity for more than 10 years. ES cells are an important *in vitro* model to test drugs, and they have the potential to predict toxicity in human[32, 33, 50]. For example, a stem cell-based reporter assay was developed to detect drug-induced alterations in the canonical Wnt/β-catenin signaling pathway, which is involved in the regulation of early embryonic development. The so-called ReProGlo assay allows simultaneous determination of cell viability and luciferase reporter activity in a high throughput 96-well microtiter format[50]. Several test chemicals were analyzed in the new assay system, and known embryo toxicants like retinoic acid and lithium chloride induced concentration-dependent increases in reporter activity. The potency of valproic acid and a series of structural analogs that activate the Wnt pathway correlated well with their reported teratogenic activity in the mouse. The new test may help to predict embryotoxic potential of chemicals in drug discovery.

Studies have also utilized differentiated fibroblastic progenies of hES cells for *in vitro* toxicological screening[51]. These cells were generated through random spontaneous differentiation within standard culture media over several passages. The cytotoxic response of the differentiated hES cell fibroblastic progenies to mitomycin C was observed to be more sensitive than the L929 cell line. Therefore, ES cell tests represent reliable, scientifically validated *in vitro* systems for the detection and classification of compounds according to their teratogenic potency[41, 51–57].

Using contrast-phase microscope is a simple way to examine cell differentiation into terminal cells. One study used light microscopy to determine the number of wells containing contracting cardiomyocytes and evaluate EB structure and size[41]. The results indicated that a decrease in the pH may be the mechanism by which the alkoxyacetic acid metabolites of glycol ethers cause embryotoxicity. Interestingly, scientists have developed a new molecular approach based on an analysis of the expression of certain marker proteins specific for developing heart tissue[52]. The approach involves a combination of quantitative flow cytometry, to measure marker proteins (*ie*, sarcomeric myosin heavy chain and α-actinin) in mES cells on day 7, and concurrent cell viability analysis. This approach was subsequently referred to as a molecular fluorescence-activated cell sorting (FACS)-ES cell test, which offered the same sensitivity as the validated protocol, but did not require as much time. This new molecular method has the potential to be a sensitive, rapid and reproducible screening tool, which is highly suited to predict developmental toxicity *in vivo* from *in vitro* data. This protocol was also suitable for *in vitro* embryotoxicity assays by measuring the disturbance of the differentiation of ES cells into endothelial cells (*ie*, the reduction in the expression of platelet/endothelial cell adhesion molecule-1, *ie* PECAM-1 and vascular endothelial cadherin)[53]. High-content image analysis was used to assess the utility of dissociated humen N2TM (HN2TM) cultures as an *in vitro* model for neurite outgrowth[54]. In addition, the molecular phenotype of these cells was examined using immunocytochemical staining. The hN2TM cultures are amenable for examining morphological changes and effects on neural outgrowth in high-to-medium-throughput developmental neurotoxicity screening because they possess cellular homogeneity, a rapid rate of neurite outgrowth, and low inter-experiment variability in automated morphological counting by FACS[54, 55]. The hepatocyte-like cells derived by analysis of the expression of certain marker proteins specific for development method may prove to be useful as an *in vitro* model of hepatotoxicity[14], which would provide a novel and promising alternative for obtaining large numbers of functional hepatocyte-like cells for *in vitro* drug metabolism and hepatotoxicity screening of potential drug candidates[56].

The applications of extracellular matrix are relevant to the evaluation of drug efficacy and drug toxicity. To promote both *in vitro* and *in vivo* growth, healthy cellularized 3-D tissues are summarized as follows. Primary cells and cell lines, including ES cells constitute a new 3-D method for rapid evaluation of hepatotoxicity *in vitro*[57]. In addition to addressing the roles and advantages of ES cells in the aforementioned toxicity models, this review also examined how genetic selection has been employed to overcome major limitations to the implementation of stem cell-based *in vitro* models for toxicology.

ES cells with novel drug targets result in “hits” by small-molecular probes

ES cell differentiation, which involves modulation of the transcription and translation of a vast number of genes and proteins, respectively, offers a desirable model for screening small-molecular probes. This system, which is modeled as a network of regulatory circuits that direct multiple steps of gene expression and mediate spatiotemporal control of a cell’s proteome, can determine both cellular phenotype and plasticity[21, 27, 39, 49, 58, 59]. Commitment to developmental lineages has been considered to be a stepwise process. To guide stem cells towards defined fates, researchers will need to know how these changes are regulated so that they can manipulate cells to change in a predictable and reproducible way[60]. To address this, it is necessary to identify the molecular target(s) bound by the drug leads, which may be responsible for their pharmacological activity. Direct approaches, such as affinity chromatography, expression cloning and protein microarrays, have analyzed compounds bound to their targets. Indirect approaches are based on a comparison of the genome-wide activity profile of the compound with databases of the activity profiles of other compounds with known targets or activity profiles following specific genetic changes. A variety of technologies and approaches have been explored for target identification after phenotypic screening[1, 44, 50]. Here, we would like to describe our recent work, which took advantage of chemical probing to identify signaling pathways involved in the differentiated state of ES cells (Figure 1). In the schematic drawing, we have reported at least six events initiated by small-molecule compounds (icariin, icaritin, and partly unpublished).

Differentiation is accompanied by a global increase in both transcript levels and efficiency of protein translation. Mul-

tiple vital genes have been identified where protein levels are exclusively regulated at the translational level during differentiation[13, 16, 17]. For example[1], high-throughput identification of small molecules revealed that the orphan ligand phosphoserine (P-Ser) was an enhancer of neurogenesis. Saxe *et al* selectively modulated molecular, cellular, and system-level properties of the mammalian brain. Phosphoserine has been shown to inhibit neural stem cell/progenitor proliferation and self-renewal, enhance neurogenic fate commitment, and improve neuronal survival. Another group[4] described a chemical screening platform to investigate hES cell differentiation and identified a small molecule, (–)-indolactam V, which specifically works at one stage of pancreatic development to induce pancreatic progenitors from the definitive endoderm. These examples have shown that small molecules that target these regulatory processes are valuable tools for probing and manipulating the molecular mechanisms by which stem cells self-renew, differentiate, and arise from somatic cell reprogramming.

Niche-mediated control of stem cell fate

Complexity in the spatial organization of ES cell cultures creates heterogeneous microenvironments (niches) that influence ES cell fate. Studies have demonstrated that[23] the rate and trajectory of hES cell differentiation can be controlled by engineering hES cell niche properties. ES cells provide an *in vitro* system that closely resembles what would occur *in vivo*[23–26]. Significant advances in defining adult stem cell niches and understanding how they regulate stem cell function *in vivo* have provided new strategies for controlling cell fate (*ie*, by pharmacologically manipulating the niches). Typically, homogeneous and functional cell types generated

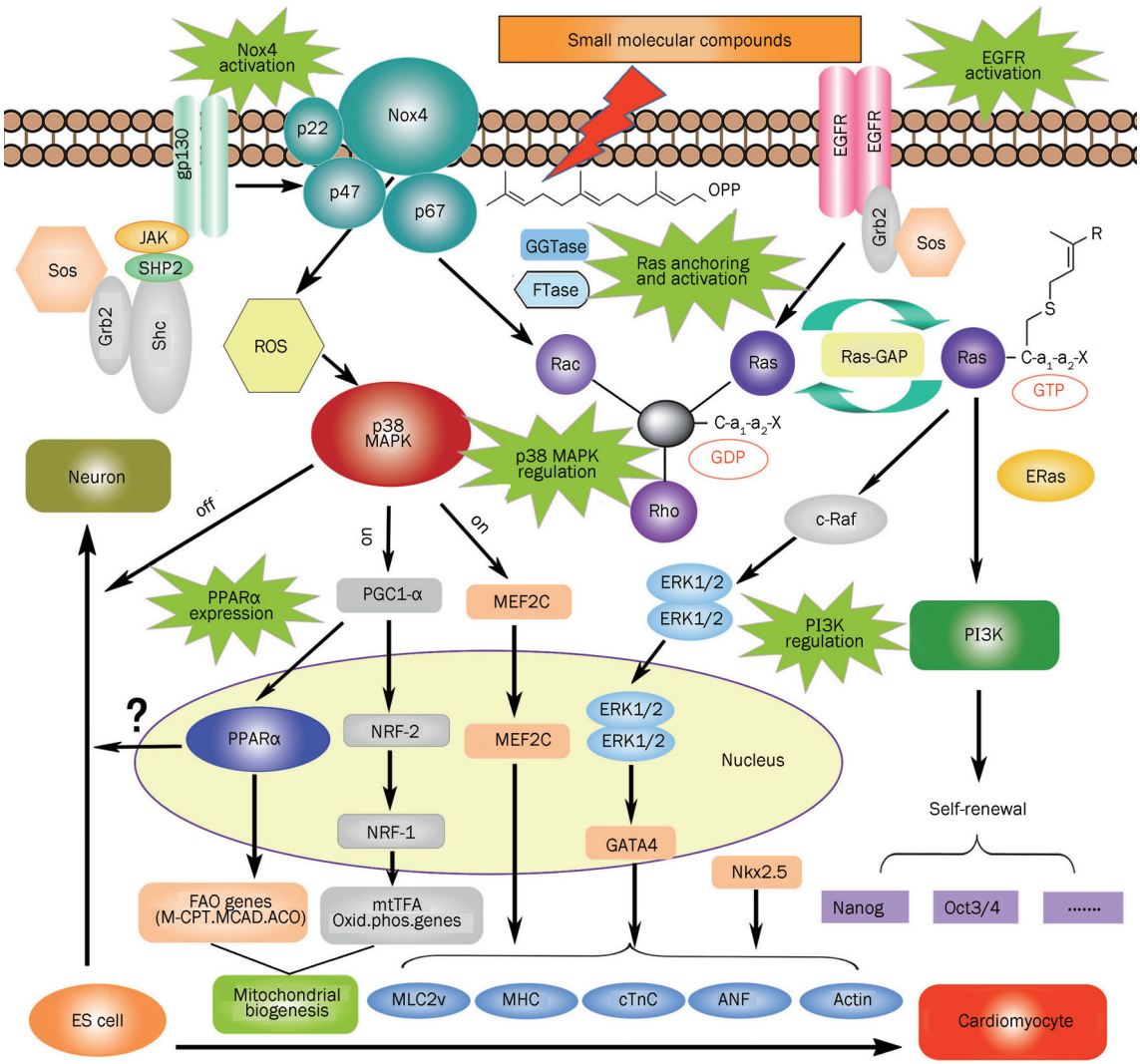

Figure 1. Schematic drawing with proposed mechanisms by which small molecules from a screening library can probe signal transduction and molecular events during stem cell differentiation. The drawing compiles the conclusions of signaling transduction and the possible molecular events. Green stars represent supposed targets for small molecular probe hits. NOX: NADPH oxidases; EGFR: epidermal growth factor receptor; MAPK: mitogen-activated protein kinase; PPAR: peroxisome proliferator-activated receptor; PI3K: phosphatidylinositol 3-kinase.

in chemically defined conditions can be used for cell-based therapy. Alternatively, conventional chemical and biological therapeutics can be developed to target patients' own cells or their niches to stimulate regeneration *in vivo*.

Therefore, the creation of "nicheology" in stem cells is a completely novel concept. Niche originally referred to the maintenance of nearby stem cells in a self-renewing state. Cells without direct contact with the niche were shown to differentiate *in vivo*[60]. The state of stem cell differentiation can be accomplished by supplying outside signals and extracellular factors instead of genetic manipulation[60]. The suffix "-ology" is used to describe the study of a specific science subject. Therefore, we defined nicheology as a branch of chemical biology or basic medicine that deals with heterogeneous microenvironments for stem cell fate, regenerative medicine, and drug discovery.

Chemically defined medium conditions for controlling hES cell fate will facilitate the practical application of hES cells in research and therapy. In addition, defined medium conditions will provide an excellent system for studying the molecular mechanisms underlying self-renewal and differentiation without the multiple unknown and variable factors associated with feeder cells and serum. From an *in vivo* nicheology point of view, these outside signals and the micro-environment constitute a niche in which adult stem cells are present and compete for limiting concentrations of growth factors or drugs, which maintains a balance between self-renewal and differentiation of the cells[23].

Role of stem cells in large pharmaceutical companies

The development of new drugs is costly and requires a tremendous amount of resources. The large pharmaceutical companies are currently facing increasing developmental costs and a lower success rate of bringing new compounds to the market. Lowering costs and increasing the success rate can be accomplished by increasing the predictability of the candidate drugs in the pipeline and lowering the number of drugs that fail in later stages of testing.

The use of stem cells amongst the top 20 pharmaceutical and top 10 biotech companies was 70% (64% with hES cells) and 50% (20% with hES cells), respectively[61, 62]. The screening of small molecules will be the predominate and most exciting approach for developing new therapeutics. The pharmaceutical industry has identified the use of stem cells for drug screening as a new and imminently necessary resource. To date, three European pharmaceutical companies, Roche Holding AG, GlaxoSmithKline and AstraZeneca, have announced that they are starting to develop ways to use stem cells for drug screening.

Prospects

Although it seems like there are extensive opportunities to use hES cells in combination with HTS systems for elucidation of differentiation pathways, there are essential complexities in these biological systems that need to be taken into consideration. For example, automated high-content analysis can provide information about multiple properties and quantitative data of individual cells, and these analyses are well suited to study non-homogenous cell populations. From a pharmaceutical perspective, the identification of small-molecule compounds regulating cellular differentiation may provide chemical tools that can be translated into clinical applications. Small molecules can replace transcription factors and/or enhance efficiency during somatic cell reprogramming[63]. They are also expected to be one potential solution for decreasing the oncogenic potential of iPS cells.

Endogenous adult stem cells exist in multiple tissues throughout the human body. Small molecules with inducing ability *in vitro* are expected to possess their own promoting differentiation nature *in vivo*. A novel regenerative medicine approach for tissue repair is focused on direct manipulation of these stem cell pools *in situ* using drugs from hES cell-based HTS to stimulate regeneration.

Acknowledgements

This work was supported by the National Natural Science Foundation of China (NSFC No 30973600 and 90813026).

References

1 Saxe JP, Wu H, Kelly TK, Phelps ME, Sun YE, Kornblum HI, *et al*. A phenotypic small-molecule screen identifies an orphan ligand-receptor pair that regulates neural stem cell differentiation. Chem Biol 2007; 14: 1019–30.
2 Sharma NS, Wallenstein EJ, Novik E, Maguire T, Schloss R, Yarmush ML. Enrichment of hepatocyte-like cells with upregulated metabolic and differentiated function derived from embryonic stem cells using S-NitrosoAcetyl Penicillamine. Tissue Eng Part C Methods 2009; 15: 297–306.
3 Christie VB, Barnard JH, Batsanov AS, Bridgens CE, Cartmell EB, Collings JC. Synthesis and evaluation of synthetic retinoid derivatives as inducers of stem cell differentiation. Org Biomol Chem 2008; 6: 3497–507.
4 Chen S, Borowiak M, Fox JL, Maehr R, Osafune K, Davidow L, *et al*. A small molecule that directs differentiation of human ESCs into the pancreatic lineage. Nat Chem Biol 2009; 5: 258–65.
5 Lee J, Wu X, Magliano MP, Peters EC, Wang Y, Hong J, *et al*. A small-molecule antagonist of the hedgehog signaling pathway. Chembiochem 2007; 8: 1916–9.
6 Wu X, Ding S, Ding Q, Gray NS, Schultz PG. Small molecules that induce cardiomyogenesis in embryonic stem cells. J Am Chem Soc 2004; 126: 1590–1.
7 Chen S, Do JT, Zhang Q, Yao S, Yan F, Peters EC. Self-renewal of embryonic stem cells by a small molecule. Proc Natl Acad Sci USA 2006; 103: 17266–71.
8 Harding SE, Ali NN, Brito-Martins M, Gorelik J. The human embryonic stem cell-derived cardiomyocyte as a pharmacological model. Pharmacol Ther 2007;113: 341–53.
9 Stummann TC, Hareng L, Bremer S. Embryotoxicity hazard assessment of methylmercury and chromium using embryonic stem cells. Toxicology 2007; 242: 130–43.
10 Agarwal S, Holton KL, Lanza R. Efficient differentiation of functional hepatocytes from human embryonic stem cells. Stem Cells 2008; 26: 1117–27.
11 Klimanskaya I, Rosenthal N, Lanza R. Derive and conquer: sourcing and differentiating stem cells for therapeutic applications. Nat Rev

Drug Discov 2008; 7: 131–42.
12 Zhu DY, Lou YJ. Inducible effects of icariin, icaritin, and desmethylicaritin on directional differentiation of embryonic stem cells into cardiomyocytes *in vitro*. Acta Pharm Sin 2005; 26: 477–85.
13 Zhu DY, Lou YJ. Icariin-mediated expression of cardiac genes and modulation of nitric oxide signaling pathway during differentiation of mouse embryonic stem cells into cardiomyocytes *in vitro*. Acta Pharm Sin 2006; 27: 311–20.
14 Zhu DY, Du Y, Huang X, Guo MY, Ma KF, Lou YJ. *et al*. MAPEG expression in murine embryonic stem cell-derived hepatic tissue system. Stem cell Dev 2008; 17: 775–84.
15 Hao JJ, Daleo MA, Murphy CK, Yu PB, Ho JN, Hu J, *et al*. Dorsomorphin, a selective small molecule inhibitor of BMP signaling, promotes cardiomyogenesis in embryonic stem cells. Plos One 2008; 3: 1–8.
16 Ogawa K, Saito A, Matsui H, Suzuki H, Ohtsuka S, Shimosato D, *et al*. Activin-Nodal signaling is involved in propagation of mouse embryonic stem cells. J Cell Sci 2007; 120: 55–65.
17 Peters AK, Steemans M, Hansen E, Mesens N, Verheyen GR, Vanparys P. Evaluation of the embryotoxic potency of compounds in a newly revised high throughput embryonic stem cell test. Toxicol Sci 2008; 105: 342–50.
18 Elkabetz Y, Panagiotakos G, Shamy GA, Socci ND, Tabar V, Studer L. Human ES cell-derived neural rosettes reveal a functionally distinct early neural stem cell stage. Gene Dev 2008; 22: 152–65.
19 Hakuno D, Takahashi T, Lammerding J, Lee RT. Focal adhesion kinase signaling regulates cardiogenesis of embryonic stem cells. J Biol Chem 2005; 280: 39534–44.
20 Pan G, Thomson JA. Nanog and transcriptional networks in embryonic stem cell pluripotency. Cell Res 2007; 17: 42–9.
21 Sampath P, Pritchard DK, Pabon L, Reinecke H, Schwartz SM, Morris DR, *et al*. A hierarchical network controls protein translation during murine embryonic stem cell self-renewal and differentiation. Cell Stem Cell 2008; 2: 448–60.
22 Babale Y, Herwig R, Greber B, Brink TC, Wruck W, Groth D, *et al*. Analysis of Oct4-dependent transcriptional networks regulating self-renewal and pluripotency in human embryonic stem cells. Stem Cells 2007; 25: 500–10.
23 Peerani R, Rao BM, Bauwens C, Yin T, Wood GA, Nagy A, *et al*. Niche-mediated control of human embryonic stem cell self-renewal and differentiation. EMBO J 2007; 26: 4744–55.
24 Morag H. Stewart MH, Bendall SC, Bhatia M. Deconstructing human embryonic stem cell cultures: niche regulation of self-renewal and pluripotency. J Mol Med 2008; 86: 875–86.
25 Yao S, Chen S, Clark J, Hao E, Beattie GM, Hayek A, *et al*. Long-term self-renewal and directed differentiation of human embryonic stem cells in chemically defined conditions. Proc Natl Acad Sci USA 2006; 103: 6907–12.
26 Bouhona IA, Kato H, Chandran S, Allen ND. Neural differentiation of mouse embryonic stem cells in chemically defined medium. Brain Res Bull 2005; 68: 62–75.
27 Firestone AJ, Chen JK. Controlling destiny through chemistry: small-molecule regulators of cell fate. ACS Chem Biol 2010; 5: 15–34.
28 Krencik R, Zhang SC. Stem cell neural differentiation: a model for chemical biology. Curr Opin Chem Biol 2006; 10: 592–7.
29 Xu Y, Shi Y, Ding S. A chemical approach to stem-cell biology and regenerative medicine. Nature 2008; 453: 338–44.
30 Harding SE, Ali NN, Brito-Martins M, Gorelik J. The human embryonic stem cell-derived cardiomyocyte as a pharmacological model. Pharmacol Ther 2007; 113: 341–53.
31 Brito-Martins M, Harding SE, Ali NN. β1- and 2-adrenoceptor responses in cardiomyocytes derived from human embryonic stem cells: comparison with failing and non-failing adult human heart. Br J Pharmacol 2008; 153: 751–9.
32 van Dartel DA, Pennings JL, de la Fonteyne LJ, van Herwijnen MH, van Delft JH, van Schooten FJ, *et al*. Monitoring developmental toxicity in the embryonic stem cell test using differential gene expression of differentiation-related genes. Toxicol Sci 2010; 116: 130–9.
33 Dartel DAM, Penning JLA, Schooten FJ, Aldert H. Piersma AH. Transcriptomics-based identification of developmental toxicants through their interference with cardiomyocyte differentiation of embryonic stem cells. Toxicol Appl Pharmacol 2010; 243: 420–8.
34 Starkuviene V, Pepperkok R. The potential of high-content high-throughput microscopy in drug discovery. Br J Pharmacol 2007; 152: 62–71.
35 Barbaric I, Gokhale PJ, Jones M, Glen A, Baker D, Andrews PW. Novel regulators of stem cell fates identified by a multivariate phenotype screen of small compounds on human embryonic stem cell colonies. Stem Cell Res 2010; 5: 104–19.
36 Noggle SA, James D, Brivanlou AH. A molecular basis for human embryonic stem cell pluripotency. Stem Cell Rev 2005; 111–8.
37 Chen WLK, Likhitpanichkul M, Ho A, Simmons CA. Integration of statistical modeling and high-content microscopy to systematically investigate cell-substrate interactions. Biomaterials 2010; 31: 2489–97.
38 McNeish J, Roach M, Hambor J, Mather RJ, Weibley L, Lazzaro J. *et al*. High-throughput screening in embryonic stem cell-derived neurons identifies potentiators of alpha-amino-3-hydroxyl-5-methyl-4-isoxazolepropionate-type glutamate receptors. J Biol Chem 2010; 285: 17209–27.
39 Ichida JK, Blanchard J, Lam K, Son EY, Chung JE, Egli D, *et al*. A small-molecule inhibitor of Tgf-beta signaling replaces Sox2 in reprogramming by inducing nanog. Cell Stem Cell 2009; 5: 491–503.
40 Elkabetz Y, Studer L. Human ESC-derived neural rosettes and neural stem cell progression. Cold Spring Harb Symp Quant Biol 2008; 73: 377–87.
41 Louisse J, Bai Y, Verwei M, Sandt JJMV, Blaauboer BJ, Rietjens IM. Decrease of intracellular pH as possible mechanism of embryotoxicity of glycol ether alkoxyacetic acid metabolites. Toxicol Appl Pharmacol 2010; 245: 236–43.
42 Ogawa S, Tagawa Y, Kamiyoshi A, Suzuki A, Nakayama J, Hashikura Y, *et al*. Crucial roles of mesodermal cell lineages in a murine embryonic stem cell-derived *in vitro* liver organogenesis system. Stem Cells 2005; 23: 903–13.
43 Sakurai K, Shimoji M, Tahimic CGT, Aiba K, Kawase E, Hashikura Y.*et al*. Efficient integration of transgenes into a defined locus in human embryonic stem cells. Nucleic Acids Res 2010; 38: e96.
44 Ebert AD, Svendsen CN. Human stem cells and drug screening: opportunities and challenges. Nat Rev Drug Discov 2010; 9: 1–6.
45 Desbordes SC, Placantonakis DG, Ciro A, Socci ND, Lee G, Djaballah H, *et al*. High-throughput screening assay for the identification of compounds regulating self-renewal and differentiation in human embryonic stem cells. Cell Stem Cell 2008; 2: 602–12.
46 Zanella F, Lorens JB, Link W. High content screening: seeing is believing. Trends Biotechnol 2010;28:237–45.
47 Williamson AJ, Smith DL, Blinco D, Unwin RD, Pearson S, Wilson C, *et al*. Quantitative proteomics analysis demonstrates post-transcriptional regulation of embryonic stem cell differentiation to hematopoiesis. Mol Cell Proteomics 2008; 7: 459–72.
48 Yocum AK, Gratsch TE, Leff N, StrahlerJR, Hunter CL, Walker AK, *et al*. Coupled global and targeted proteomics of human embryonic stem cells during induced differentiation. Mol Cell Proteomics 2008; 7:

750–67.

49 Bondue A, Lapouge G, Paulissen C, Semeraro C, Iacovino M, Kyba M, *et al*. Mesp1 acts as a master regulator of multipotent cardiovascular progenitor specification. Cell Stem Cell 2008; 3: 69–84.

50 Uibel F, Mühleisen A, Köhle C, Weimer M, Stummann TC, Bremer S. A new stem cell-based reporter assay aimed to predict embryotoxic potential of drugs and chemicals. Reprod Toxicol 2010; 30: 103–12.

51 Cao T, Lu K, Fu X, Heng BC. Differentiated fibroblastic progenies of human embryonic stem cells for toxicology screening. Cloning Stem Cells 2008; 10: 1–9.

52 Buesen R, Genschow E, Slawik B, Visan A, Spielmann H, Luch A, *et al*. Embryonic stem cell test remastered: comparison between the validated EST and the new molecular FACS-EST for assessing developmental toxicity *in vitro*. Toxicol Sci 2009; 108: 389–400.

53 Festag M, Viertel B, Steinberg P, Sehner C. An *in vitro* embryotoxicity assay based on the disturbance of the differentiation of murine embryonic stem cells into endothelial cells. II. Testing of compounds. Toxicol in Vitro 2007; 21: 1631–40.

54 Harrill JA, Freudenrich TM, Machacek DW, Stice SL, Mundy WR. Quantitative assessment of neurite outgrowth in human embryonic stem cell-derived hN2TM cells using automated high-content image analysis. Neurotoxicology 2010; 31: 277–90.

55 Theunissena PT, Schulpen SHW, Dartela DAMV, Hermsen SAB, Schooten SJV, Piersma AH. An abbreviated protocol for multilineage neural differentiation of murine embryonic stem cells and its perturbation by methyl mercury. Reprod Toxicol 2010; 29: 383–92.

56 Kulkarni JS, Khanna A. Functional hepatocyte-like cells derived from mouse embryonic stem cells: a novel *in vitro* hepatotoxicity model for drug screening. Toxicol in Vitro 2006; 20: 1014–22.

57 Prestwich GD. Evaluating drug efficacy and toxicology in three dimensions: using synthetic extracellular matrices in drug discovery. Accounts Chem Res 2008; 41: 139–48.

58 Pan G, Thomson JA. Nanog and transcriptional networks in embryonic stem cell pluripotency. Cell Res 2007; 17: 42–9.

59 Babaie Y, Herwig R, Greber B, Brink TC, Wruck W, Groth D, *et al*. Analysis of Oct4-dependent transcriptional networks regulating self-renewal and pluripotency in human embryonic stem cells. Stem Cells 2007; 25: 500–10.

60 Roel Nusse. Wnt signaling and stem cell control. Cell Res 2008; 18: 523–7.

61 Kochegarov A. Small molecules for stem cells. Expert Opin Ther Pat 2009; 19: 275–81.

62 Jensen J, Hyllner J, Björquist P. Human embryonic stem cell technologies and drug discovery. J Cell Physiol 2009; 219: 513–9.

63 Tenzen T, Zembowicz F, Cowan CA. Genome modification in human embryonic stem cells. J Cell Physiol 2010; 222: 278–81.

Acta Pharmacologica Sinica (2011) 32: 160–166
 1671-4083/11 $32.00
www.nature.com/aps

Original Article

Enhanced NMDA receptor NR1 phosphorylation and neuronal activity in the arcuate nucleus of hypothalamus following peripheral inflammation

Jian-ming PENG[1, #], Long-sheng XU[1, #], Qi ZHU[1], Shan GONG[1], Xian-min YU[2], Shi-yu GUO[1], Gen-cheng WU[3], Jin TAO[1], Xing-hong JIANG[1, *]

[1]*Key Laboratory of Pain Basic Research & Clinical Therapy, Department of Neurobiology and Institute of Neuroscience, Medical College of Soochow University, Suzhou 215123, China;* [2]*Department of Biomedical Sciences, College of Medicine, Florida State University, Florida 32306, USA;* [3]*State Key Laboratory of Medical Neurobiology, Fudan University, Shanghai 200032, China*

Aim: To investigate the role of glutamate and *N*-methyl-*D*-aspartate (NMDA) receptors in central sensitization following peripheral inflammation in the arcuate nucleus (ARC) of the mediobasal hypothalamus.
Methods: Mediobasal hypothalamic slices were prepared from rats undergoing peripheral inflammation, which was induced by a unilateral injection of complete Freund's adjuvant (CFA) into hind paw. Neuronal activation levels in the ARC were monitored by recording extracellular unit discharges. The NMDA receptor NR1 subunit (NR1) was measured using Western blot analysis.
Results: Enhanced NR1 phosphorylation was observed in the ARC of CFA-inflamed rats. Compared with the control rats, the firing rate of spontaneous discharges in ARC neurons of inflamed rats was significantly higher, and it was significantly reduced both by an NMDA receptor antagonist (MK-801, 300 μmol/L) and by a non-NMDA receptor antagonist (CNQX, 30 μmol/L). Application of exogenous glutamate (200 μmol/L) or NMDA (25 μmol/L) resulted in increased neuronal discharges for ARC neurons, which was enhanced to a greater extent in inflamed rats than in control rats.
Conclusion: Glutamate receptor activation in the hypothalamic ARC plays a crucial role in central sensitization associated with peripheral inflammation.

Keywords: arcuate nucleus (ARC); NMDA receptor; NR1 phosphorylation; inflammation; central sensitization; MK-801; CNQX

Acta Pharmacologica Sinica (2011) 32: 160–166; doi: 10.1038/aps.2010.190

Introduction

Glutamate is a major excitatory neurotransmitter in the central nervous system (CNS). The receptors for glutamate comprise two large families: the ionotropic glutamate receptors (iGluRs) and the metabotropic glutamate receptors (mGluRs). The iGluRs are classified into the following receptor subtypes: *N*-methyl-*D*-aspartate (NMDA), kainate (KA) and alpha-amino 3-hydroxy-5-methyl-4-isoxazole propionate (AMPA). KA and AMPA receptor subtypes are collectively classified as non-NMDA receptors. Molecular studies have indicated that functional NMDA receptors contain a heteromeric combination of NR1 subunits (essential for channel-formation) and one or more NR2A to D subunits[1–3].

NMDA receptors have been shown to play an important role in several physiological processes, such as long-term potentiation, learning and memory, as well as in some pathological conditions, including neurodegenerative diseases, ischemia and persistent nociception. The NMDA receptor has also been shown to be involved in the development of central sensitization, which is believed to underlie hyperalgesia during inflammatory pain and neuropathic pain[2, 3]. The majority of the data describing central sensitization were derived from studies in the dorsal horn of spinal cord, which is the first station to receive and integrate nociceptive information in the CNS[3–9]. However, studies investigating the molecular mechanisms of central sensitization in the supraspinal centers of nociceptive regulation remain elusive[10, 11].

Previous studies have demonstrated that the arcuate nucleus (ARC) of mediobasal hypothalamus, which exhibits large clusters of β-endorphinergic neurons, is one of the critical structures in the modulation of nociception. Electrical

# These two authors contributed equally to this work.
* To whom correspondence should be addressed.
E-mail jiangxinghong@suda.edu.cn
Received 2010-05-26 Accepted 2010-10-12

or chemical stimulation of ARC can elicit antinociceptive effects[12–14], while electrolytic or chemical lesioning of ARC attenuates the morphine-induced analgesia, acupuncture-induced analgesia and stress-induced analgesia[12, 15, 16]. Furthermore, peripheral noxious stimulation modulates the spontaneous discharges of neurons in ARC, indicating that peripheral nociceptive information is sent to the hypothalamic nucleus and can result in neuronal activation in ARC[17]. In addition, glutamate and glutamate receptors, such as NMDA receptors, are highly expressed in the nuclei of the medial hypothalamus, including ARC[18–24].

Based on these observations, we hypothesized that hypothalamic ARC, a supraspinal center in pain modulation, might be a locus for central sensitization induced by injuries in peripheral tissues. We investigated the function of the NR1 subunit of the NMDA receptor and neuronal activation in ARC in mediobasal hypothalamic slices from rats suffering from peripheral inflammatory injury. We found that peripheral inflammation enhanced NR1 phosphorylation and increased neuronal activation in ARC. These findings provide new insights into how noxious signals are centrally processed during persistent nociception, which may be important in the development of novel analgesic strategies.

Materials and methods

Animals

Adult male Wistar rats (180 to 220 g) were housed in a light- (lights on 06.00–18.00 h) and temperature- (22±1 °C) controlled room and were fed rat chow and tap water *ad libitum*. All experiments were approved by the Institutional Animal Care and Use Committee at the Medical College, Soochow University and were in accordance with the ethical standards of the Helsinki Declaration and the guidelines of the International Association for the study of Pain for pain research in animals.

Drugs and reagents

In this study *L*-glutamic acid (glutamate), NMDA, MK-801 (a non-competitive NMDA receptor antagonist), CNQX (a non-NMDA receptor antagonist), rabbit anti-mouse NR1 antibody and rabbit anti-serine-897-phosphorylated-NR1 (pNR1) antibody were purchased from Sigma Chemical Co. The avidin-biotin complex and the biotinylated goat anti-rabbit IgG secondary antibody were purchased from Vector Laboratories Inc. All other chemical reagents were purchased from Sinopharm Chemical Reagent Co, Ltd.

Inflammatory pain model

Inflammatory pain was induced by injecting complete Freund's adjuvant (CFA, 50% in saline, with 5 mg/mL heat-killed *Mycobacterium tuberculosis*, 0.1 mL) into the plantar surface of the left hind paw. Western blotting and electrophysiological experiments were conducted one week after CFA injection, when symptoms of inflammatory pain were evident, such as redness, swelling of the ankle joint, hyperalgesia and impairment in motor activity. Normal rats injected with an equal volume of saline were prepared as a control.

Western blot analysis

One week after CFA injection, rats (including control rats) were deeply anesthetized and decapitated to quickly isolate the ARC region. Three (anterior, middle and posterior) ARC slices (500 μm thick) were isolated from each animal and transferred into the ice-cold artificial cerebrospinal fluid (ACSF). The ARC slices were then homogenized in the presence of protease and phosphatase inhibitors. The homogenate was centrifuged twice at 13 000×*g* for 10 min at 4 °C. The supernatant was used for Western blot analyses. The concentration of protein in the homogenate was measured using a bicinchoninic acid (BCA) kit and was used to calculate volume for equal protein loading in the gel. Proteins were separated and were transferred onto PVDF membranes (Invitrogen) by SDS-PAGE using Criterion XT Precast 6% Bis-Tris gels (Bio-Rad, Hercules, CA) in standard transfer buffer (25 mmol/L Tris, 192 mmol/L glycine, 10% *v/v* methanol, pH 8.3) for 1.5 h at room temperature. After being blocked with 5% milk in Tris-buffered saline and 0.1% Tween 20 (TBS-T) for 1 h, the membranes were incubated in specific antibodies against NR1 (1:2000, rabbit affinity-purified polyclonal antibody, Sigma), pNR1-Ser897 (1:500, rabbit affinity-purified polyclonal antibody, Upstate) and β-actin (1:20 000, mouse monoclonal, Sigma) overnight at 4 °C. After extensive washing in TBST, the membranes were incubated in goat anti-rabbit horseradish peroxidase (HRP) secondary antibody (1:5000, Jackson Immunoresearch Co) for 1 h at room temperature. After extensive washing, signals were detected by Western Lightning ECL and were quantified relative to a β-actin control by densitometry on Image-Pro Plus 6.0.

Mediobasal hypothalamus slice preparation

Hypothalamic slices (400 μm) were prepared as described previously[25, 26]. In brief, hypothalamus slices containing ARC in a recording chamber were continuously perfused with ACSF (3 mL/min) saturated with 5% CO_2 and 95 % O_2 at 33±1 °C. The ACSF media (pH 7.35–7.40) contained the following reagents: NaCl (124 mmol/L), $NaHCO_3$ (26 mmol/L), KCl (5 mmol/L), $CaCl_2$ (2.4 mmol/L), $MgSO_4$ (1.3 mmol/L), NaH_2PO_4 (1.24 mmol/L), and *D*-glucose (10 mmol/L). After 1 h of ACSF perfusion, extracellular single unit recordings were collected.

Electrophysiological recording

The spontaneous unit discharges from the ARC were recorded extracellularly with glass microelectrodes containing 0.5 mol/L sodium acetate and 2% pontamine sky blue (10–20 MΩ). Using a stereomicroscope and a microelectrode manipulator, the glass microelectrode was lowered into the ARC, which was located anatomically with respect to the third ventricle (3V) and medium eminence (Figure 1). The electrical signals were amplified (microelectrode amplifier, MEZ-8201, Nihon Kohden, Japan) and sent to a dual-beam oscilloscope (VC-10, Nihon Kohden, Japan). Neuronal unit discharges were continuously recorded online. The firing rate and interspike interval of neuronal discharges were analyzed with

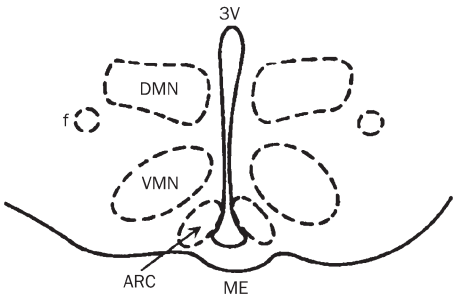

Figure 1. Schematic drawing of a mediobasal hypothalamic slice that contains the ARC. Dashed lines indicate the boundaries of the nucleus, as indicated. DMN: dorsomedial nucleus; VMN: ventromedial nucleus; ME: medium eminence; 3V: third ventricle; f: fornix.

Powerlab/4SP (AD Instruments, Australia).

Drug application

All the drugs used in our experiments were freshly prepared, dissolved in ACSF saturated with 5% CO_2 and 95% O_2, and perfused hypothalamic slices via a three-way stopcock near the recording chamber. The baseline activity of neuronal discharges was recorded for 5 to 10 min as control. After establishing a good baseline, glutamate receptor agonists (glutamate 200 μmol/L, NMDA 25 μmol/L) or antagonists (MK-801 300 μmol/L, CNQX 30 μmol/L) were applied. The drug effects were observed continuously for 8 min after application.

Statistical analysis

The ARC neuron responses to glutamate or NMDA were determined according to the critical ratio criterion (CR), using the following formula: $CR=(E-S)/(S+E)^{1/2}$ (where E is discharge frequency after drug application and S is discharge frequency before drug application). The response was considered excitatory, if the ratio exceeded 1.96[27]. All data are presented as mean±SD. Statistical comparisons were performed using one-way ANOVA or student's *t*-test. $P<0.05$ was considered statistically significant.

Results

Expression of NMDA receptor in ARC

NMDA receptors are composed of NR1 subunits, which are essential, and one of the NR2 subunits (NR2A, NR2B, NR2C, or NR2D). In the present study, we used Western blotting to measure the relative amounts of NR1 and pNR1 in ARC isolated from control and inflamed animals. Figure 2 illustrates that the relative amount of pNR1 in CFA-induced inflamed rats was significantly increased as compared with control rats ($n=6$, $P<0.01$, Figure 2A and 2B). Meanwhile the relative amounts of NR1 in inflamed and control rats were not statistically different ($n=6$, $P>0.05$, Figure 2A, 2C). These data suggest that peripheral inflammation increased NR1 phosphorylation in ARC, but it had no effect on NR1 subunit upregulation.

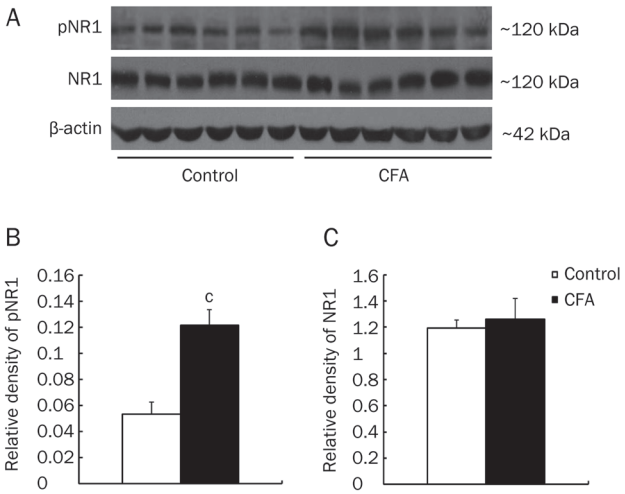

Figure 2. Enhanced pNR1 but not NR1 expression in the ARC from CFA-inflamed rats. (A) Immunoblots of phosphorylated NR1 (pNR1) and NR1 in the ARC of control and CFA-inflamed rats. β-actin was as control. (B) The relative density of pNR1 protein was significantly increased in the ARC of CFA-inflamed rats ($n=6$) compared to control rats ($n=6$; $^cP<0.01$, unpaired *t*-test). (C) There was no significant difference in NR1 protein expression between control ($n=6$) and CFA-inflamed ($n=6$) rats.

The discharge patterns of ARC neurons

We also measured the neuronal discharge activity in ARC. We found that the spontaneous discharges of ARC neurons in the slices could be divided into three firing patterns: regular, irregular and burst firing (Figure 3). Irregular discharges were observed in the majority of recorded neurons. As indicated in Table 1, the number of neurons exhibiting regular, irregular and burst firing was similar across control and inflamed rats (Table 1).

Discharge frequency in ARC neurons

The frequency of spontaneous discharge in ARC neurons was calculated for each discharge pattern, as well as for the mean of the three discharge patterns. The mean firing rate and the

Table 1. Frequency of spontaneous discharges of ARC neurons from control and inflamed rats. $^bP<0.05$, $^cP<0.01$ *vs* control. The number of neurons in each firing pattern is indicated in parenthesis.

	Regular firing (Hz)	Irregular firing (Hz)	Burst firing (Hz)	Mean (Hz)
Control	1.59±0.34 (21)	1.07±0.13 (86)	1.54±0.29 (16)	1.22±0.24 (123)
CFA-inflamed	2.36±0.38^b (14)	1.52±0.11^c (95)	1.94±0.36^b (33)	1.70±0.27^b (142)

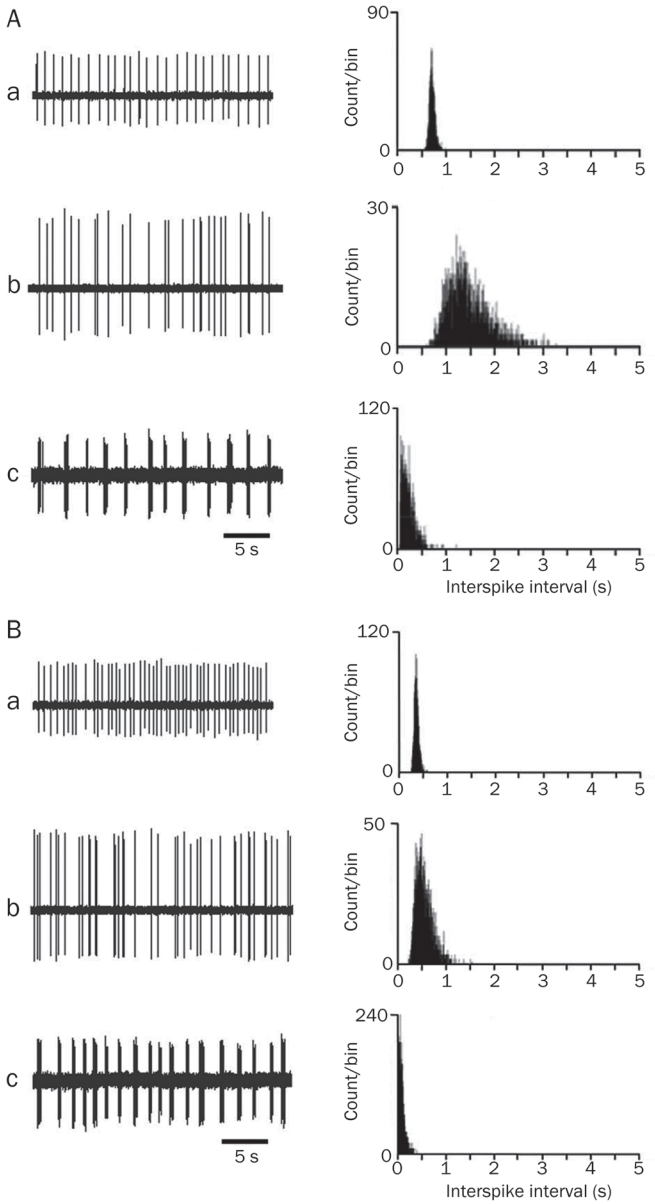

Figure 3. The discharge patterns of arcuate neurons. Examples of electrical signals (left) and their inter-spike interval histograms (right) recorded from arcuate neurons in control and inflamed rats are shown in A and B, respectively. a, b, and c show examples of regular, irregular and burst firing, respectively.

firing rate of each discharge pattern in ARC neurons from inflamed rats were significantly elevated as compared with the normal group (P<0.05, Table 1). This significant difference was also observed for the inter-spike interval histograms. As shown in Figure 3, as the firing rate increased, the inter-spike intervals shifted to the left in the inflamed animals.

Effect of glutamate on the electrophysiological activities of ARC neurons

We investigated the response of ARC neurons to application of exogenous glutamate (200 μmol/L) to monitor their electric activities. In control animals, neuronal discharges increased significantly following glutamate application with a latency of 28.5±5.9 s (n=26). The firing rate increased by 44.5%±9.9%, and this increase persisted for up to (152.5±15.3) s. In inflamed rats, the glutamate-induced excitatory response was more rapid, with a latency of (19.8±2.8) s (n=23), and was more long lasting (188.5 s±20.1 s). The firing rate increased by 84.0%±32.7%. These results indicate that the glutamate-induced excitatory response in ARC neurons from inflamed rats exhibited a shorter latency (P<0.05), longer duration (P<0.05) and an enhanced firing rate (P<0.01) as compared with control rats (Figure 4).

Effect of NMDA on the electric activities of ARC neurons

Similar to application of exogenous glutamate, application of an NMDA receptor agonist, NMDA (25 μmol/L), also induced an excitatory response in ARC neurons in both the control and inflamed rats. In inflamed rats (n=24), the excitatory response exhibited a shorter latency, larger increment and longer duration, all of which were significantly different (P<0.05) from

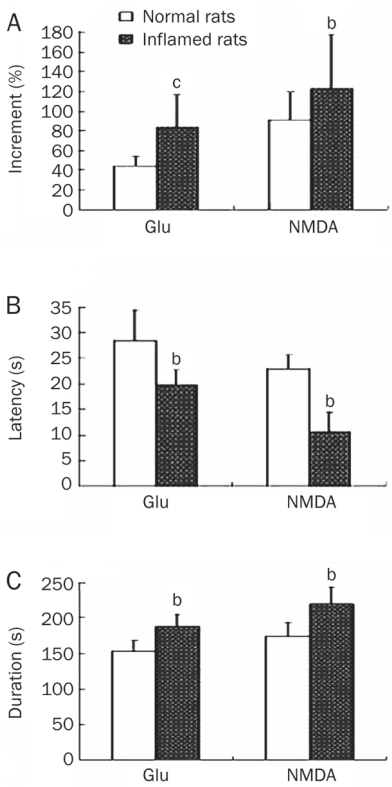

Figure 4. Effects of exogenous glutamate and NMDA on neuronal discharges in the ARC. Relative increases in neuronal discharge frequency following glutamate (200 μmol/L, n=26 in control rats, n=23 in inflamed rats) or NMDA (25 μmol/L, n=29 in control rats, n=24 in inflamed rats) application are shown in A. The baseline discharge frequency before glutamate application in control and inflamed rats were 1.26±0.31 Hz and 1.58±0.22 Hz, respectively; before NMDA application they were 1.27±0.22 Hz and 1.69±0.34 Hz, respectively. The latency and duration of glutamate or NMDA-induced increases in neuronal discharges are shown in B and C, respectively. ^bP<0.05, ^cP<0.01 as compared with control rats.

ARC neurons in control animals (n=29, Figure 4). These results indicate that both NMDA and glutamate could induce a stronger excitatory response in inflamed rats than in control rats.

Effects of MK-801 and CNQX on the spontaneous discharge of ARC neurons

It is well known that the increased excitability of nociceptive neurons in the spinal cord during persistent inflammation is mediated by glutamate receptors, including NMDA and non-NMDA receptor subtypes. To examine the role of glutamate receptors in the neuronal activation of ARC neurons during peripheral inflammation, we tested the effects of MK-801 (NMDA receptor antagonist) and CNQX (non-NMDA receptor antagonist) on the increased spontaneous discharges of ARC neurons from inflamed rats. Application of either MK-801 (300 μmol/L) or CNQX (30 μmol/L) resulted in a significant reduction in the discharge frequency of ARC neurons from inflamed rats. After MK-801 application, the discharge frequency was reduced from (2.32±0.29) Hz to (1.23±0.17) Hz (n=11, P<0.01, Figure 5A). After CNQX application, the discharge frequency decreased from (2.17±0.25) Hz to (1.32±0.15) Hz (n=11, P<0.01, Figure 5B). In control rats neither antagonist induced a significant reduction in the discharge frequency of ARC neurons (Figure 5A, 5B). These results suggest that the increase in spontaneous discharges of ARC neurons from inflamed rats was mediated by NMDA and non-NMDA receptors.

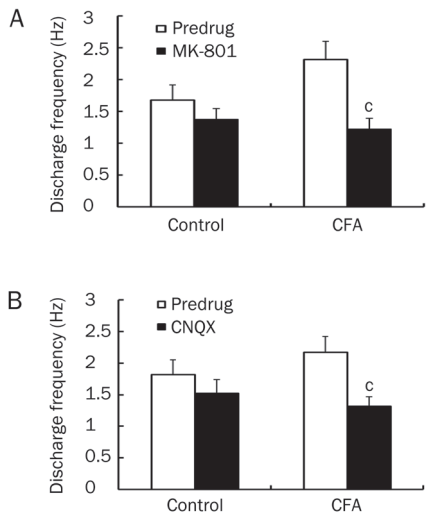

Figure 5. MK-801 (NMDA receptor antagonist) and CNQX (non-NMDA receptor antagonist) inhibit spontaneous discharge of ARC neurons in inflamed rats. (A) A significant decrease in neuronal discharge frequency was observed following MK-801 application (300 μmol/L) in inflamed rats (n=11; P<0.01, unpaired t-test) but not in control rats (n=12). (B) A significant decrease in neuronal discharge frequency was observed following CNQX application (30 μmol/L) in inflamed rats (n=11; ^cP<0.01, unpaired t-test), but not in control rats (n=10).

Discussion

The results of this study were threefold: 1) CFA-inflamed rats exhibited elevated levels of phosphorylated NR1 but not unphosphorylated NR1; 2) ARC neurons from CFA-inflamed rats exhibited a higher frequency of neuronal discharges, which was both NMDA and non-NMDA receptor dependent; and 3) ARC neurons from CFA-inflamed rats exhibited enhanced responses to exogenous glutamate and NMDA.

NMDA receptors in spinal dorsal horn have been shown to play a critical role in nociceptive transmission[2, 3]. Peripheral tissue injury dramatically enhances the function of spinal NMDA receptor that is involved in the initiation and maintenance of central sensitization, a persistent increase in the excitability of nociceptive neurons[2, 3, 28, 29]. The hyperfunction of the NMDA receptor could result from phosphorylation, upregulation, or a combination of both[30, 31]. Our western blot analysis indicated that the NMDA receptor NR1 subunit was phosphorylated but not upregulated in the ARC, and this effect was enhanced in inflamed rats. These results are consistent with previous studies. Yang *et al* found that CFA treatment in mice did not affect total NR1 levels, but it did result in a marked increase in NR1 phosphorylation[32]. Bird *et al* demonstrated that mono-arthritis induced by an injection of a kaolin suspension with carrageenan into the knee joint in rats resulted in increased NR1 phosphorylation rather than receptor upregulation in the amygdala[33]. Similarly, Maneepak *et al* reported that dural stimulation by topical application of an inflammatory soup enhanced phosphorylation but not expression of NR1 in the trigeminal nucleus caudalis of the spinal cord in rats[34].

Phosphorylation of NR1 has been shown to induce NMDA receptor trafficking from storage sites in the endoplasmic reticulum to the synaptic plasma membrane, leading to a hyperactivation state of NMDA receptor in nociceptive transmission[35, 36]. Furthermore, NR1 phosphorylation has been correlated with hyperalgesia and allodynia, which are characteristic behavioral manifestations of central sensitization[31, 37]. Previous investigations have demonstrated that the blockage of NR1 phosphorylation could reverse allodynia[37]. These data indicate that NR1 phosphorylation plays an important role in the initiation and maintenance of central sensitization. In the present study, NR1 phosphorylation was enhanced in ARC neurons from inflamed rats, thereby suggesting that central sensitization during peripheral inflammation might also occur in this supraspinal center.

Many studies have demonstrated that increased excitability of nociceptive neurons in the spinal dorsal horn is an important manifestation of central sensitization[38]. In addition, central sensitization has been shown to result from glutamate-induced activation of multiple signaling pathways in dorsal horn neurons, which involve both ionotropic (NMDA and non-NMDA) receptors and metabotropic receptors[38, 39]. In present study we also observed increased excitability of ARC neurons from CFA-inflamed rats, as evidenced by the increased frequency of spontaneous discharges that was

NMDA and non-NMDA receptor dependent. The enhanced responsiveness of ARC neurons from inflamed rats by glutamate and NMDA application indicates that the excitability of ARC neurons increased following peripheral inflammation.

In the present study, hypothalamic ARC neurons from CFA-inflamed rats exhibited enhanced NR1 phosphorylation, increased excitability and increased responsiveness. These data suggest that the hypothalamic ARC may be important in the development of central sensitization associated with inflammatory injuries.

Acknowledgements

This work was supported by Funding from State Key Laboratory of Medical Neurobiology (09-09, Fudan University, Shanghai, China), the National Natural Science Foundation of China (No 30900437), Natural Science Funding for Colleges and Universities in Jiangsu Province (No 09KJB180008), Natural Science Funding of Jiangsu Province (No BK2009118), and Doctoral Funding of Ministry of Education of China (No 20093201110018).

Author contribution

Xing-hong JIANG, Xian-min YU, and Gen-cheng WU designed the experiments; Long-sheng XU, Jian-ming PENG, Qi ZHU, and Shan GONG performed all experiments; Shi-yu GUO and Jin TAO analyzed data; Xing-hong JIANG and Jin TAO wrote the manuscript.

References

1 Dingledine K, Borges K, Bowie D, Traynelis S. The glutamate receptor ion channels. Pharmacol Rev 1999; 51: 7–61.
2 Fundytus ME. Glutamate receptors and nociception: implications for the drug treatment of pain. CNS Drugs 2001; 15: 29–58.
3 Petrenko AB, Yamakura T, Baba H, Shimoji K. The role of *N*-methyl-*D*-aspartate (NMDA) receptors in pain: a review. Anesth Analg 2003; 97: 1108–16.
4 Rygh LJ, Svendsen F, Hole K, Tjolsen A. Natural noxious stimulation can induce long-term increase of spinal nociceptive responses. Pain 1999; 82: 305–10.
5 Sandkuhler J, Liu X. Induction of long-term potentiation at spinal synapse by noxious stimulation or nerve injury. Eur J Neurosci 1998; 10: 2476–80.
6 Ji RR, Woolf CJ. Neuronal plasticity and spinal transduction in nociceptive neurons: implications for the initiation and maintenance of pathological pain. Neurobiol Dis 2001; 8: 1–10.
7 Willis WD. Role of neurotransmitters in sensitization of pain responses. Ann NY Acad Sci 2001; 933: 142–56.
8 Salter MW. Cellular neuroplasticity mechanism mediating pain persistence. J Orofac Pain 2004; 18: 318–24.
9 Gao X, Kim HK, Chung JM, Chung K. Reactive oxygen species (ROS) are involved in enhancement of NMDA-receptor phosphorylation in animal models of pain. Pain 2007; 131: 262–71.
10 Urban MO, Gebhart GF. Supraspinal contributions to hyperalgesia. Proc Natl Acad Sci USA 1999; 96: 7687–92.
11 Coutinho SV, Urban MO, Gebhart GF. Role of glutamate receptors and nitric oxide in the rostral ventromedial medulla in visceral hyperalgesia. Pain 1998; 78: 59–69.
12 Guo SY, Yin WP, Zhang HQ, Yin QZ. Role of hypothalamic arcuate region in lip-acupuncture analgesia in rats. Acta Physiol Sin 1982; 34: 71–7.
13 Zhang N, Yin QZ. Involvement of rat locus coeruleus in the analgesic effect induced by monosodium glutamate injection into the hypothalamic arcuate nucleus area. Acta Physiol Sin 1988; 40: 529–38.
14 Wang Q, Mao LM, Han JS. Characterization of inhibition of spinal nociceptive reflex by stimulation of the arcuate nucleus of the hypothalamus in the pentobarbital-anesthetized rat. Pain 1990; 41: 101–8.
15 Guo SY, Yin WP, Yin QZ. Effects of neonatal administration of monosodium glutamate on morphine-, acupuncture- and stress-analgesia in adult rats. Acta Pharmacol Sin 1983; 4: 14–6.
16 Zhu MY, Wang XY, Zhang DX, Wan XX. Effects of lesion of hypothalamic arcuate nucleus region on brain β-endorphin, 5-hydroxytryptamine and norepinephrine content and acupuncture analgesia in rats. Acta Physiol Sin 1984; 36: 42–8.
17 Yu XM, Yin QZ. Changes in unit discharge of hypothalamic arcuate nucleus area during noxious stimulation or acupuncture in rats. Acta Physiol Sin 1984; 36: 33–41.
18 Palkovits M, Láng T, Patthy A, Elekes I. Distribution and stress-induced increase of glutamate and aspartate levels in discrete brain nuclei of rats. Brain Res 1986; 373: 252–7.
19 Kiss J, Csaba Z, Csáki A, Halász B. Glutamatergic innervation of growth hormone-releasing hormone-containing neurons in the hypothalamic arcuate nucleus and somatostatin-containing neurons in the anterior periventricular nucleus of the rat. Brain Res Bull 2006; 70: 278–88.
20 Hrabovszky E, Deli L, Turi GF, Kalló I, Liposits Z. Glutamatergic innervation of the hypothalamic median eminence and posterior pituitary of the rat. Neuroscience 2007; 144: 1383–92.
21 Kiss J, Csaba Z, Csáki A, Halász B. Glutamatergic innervation of neuropeptide Y and pro-opiomelanocortin-containing neurons in the hypothalamic arcuate nucleus of the rat. Eur J Neurosci 2005; 21: 2111–9.
22 MacDonald MC, Robertson HA, Wilkinson M. Expression of c-fos protein by *N*-methyl-*D*-aspartic acid in hypothalamus of immature female rats: blockade by MK-801 or neonatal treatment with monosodium glutamate. Brain Res Dev Brain Res 1990; 56: 294–7.
23 Hu L, Fernstrom JD, Goldsmith PC. Exogenous glutamate enhances glutamate receptor subunit expression during selective neuronal injury in the ventral arcuate nucleus of postnatal mice. Neuroendocrinology 1998; 68: 77–88.
24 Khan AM, Stanley BG, Bozzetti L, Chin C, Stivers C, Currás-Collazo MC. *N*-methyl-*D*-aspartate receptor subunit NR2B is widely expressed throughout the rat diencephalon: an immunohistochemical study. J Comp Neurol 2000; 428: 428–49.
25 Liu YL, Yu GD, Jiang XH, Yin QZ. Effects of serotonin on circadian rhythm of electric activity of suprachiasmatic neurons in rat hypothalamic slice. Acta Acad Med Suzhou 1999; 18: 897–900.
26 Zhou XJ, Jiang XH, Yu GD, Yin QZ. Modulation of circadian rhythm of discharge of suprachiasmatic nucleus neurons in rat hypothalamic slices by melatonin. Acta Physiol Sin 2000; 52: 215–9.
27 Feldman S, Dafny N. Effects of cortisol on unit activity in the hypothalamus of the rats. Exp Neurol 1970; 27: 375–87.
28 Ren K, Hylden JLK, Williams GM, Ruda MA, Dubner R. The effects of a non-competitive NMDA receptor antagonist, MK-801, on behavioral hyperalgesia and dorsal horn neuronal activity in rats with unilateral inflammation. Pain 1992; 50: 331–44.
29 Coderre TJ, Melzack R. The contribution of excitatory amino acids to central sensitization and persistent nociception after formalin-induced tissue injury. J Neurosci 1992; 12: 3665–70.

30 Wu LJ, Toyoda H, Zhao MG, Lee YS, Tang J, Ko SW, *et al*. Upregulation of forebrain NMDA NR2B receptors contributes to behavioral sensitization after inflammation. J Neurosci 2005; 25: 11107–16.
31 Zou X, Lin Q, Willis WD. Enhanced phosphorylation of NMDA receptor 1 subunits in spinal cord dorsal horn and spinothalamic tract neurons after intradermal injection of capsaicin in rats. J Neurosci 2000; 20: 6989–97.
32 Yang X, Yang HB, Xie QJ, LiuXH, Hu XD. Peripheral inflammation increased the synaptic expression of NMDA receptors in spinal dorsal horn. Pain 2009; 144: 162–9.
33 Bird GC, Lash LL, Han JS, Zou XJ, Willis WD, Neugebauer V. Protein kinase A-dependent enhanced NMDA receptor function in pain-related synaptic plasticity in rat amygdala neurones. J Physiol 2005; 564: 907–21.
34 Maneepak M, le Grand S, Srikiathachorn A. Serotonin depletion increases nociception-evoked trigeminal NMDA receptor phosphorylation. Headache 2009; 49: 375–82.
35 Carroll RC, Zukin RS. NMDA-receptor trafficking and targeting: implication for synaptyic transmission and plasticity. Trends Neurosci 2002; 25:571–7.
36 Scott DB, Blanpied TA, Ehlers MD. Coordinated PKA and PKC phosphorylation suppresses RXR-mediated ER retention and regulates the surface delivery of NMDA receptors. Neuropharmacology 2003; 45: 755–67.
37 Gao X, Kim HK, Chung JM, Chung K. Enhanncement of NMDA receptor phosphorylation of the spinal dorsal horn and nucleus gracilis neurons in neuropathic rats. Pain 2005; 116: 62–72.
38 Ji RR, Kohno T, Moore KA, Woolf CJ. Central sensitization and LTP: do pain and memory share similar mechanisms? Trends Neurosci 2003; 26: 696–705.
39 Kawasaki Y, Kohno T, Zhuang ZY, Brenner GJ, Wang HB, van der Meer C, *et al*. Ionotropic and metaboteropic receptors, protein kinase A, protein kinase C, and Src contribuite to C-fiber-induced ERK activation and cAMP response element-binding protein phosphorylation in dorsal horn neurons, leading to central sensitization. J Neurosci 2004; 24: 8310–21.

Acta Pharmacologica Sinica (2011) 32: 167–174
 1671-4083/11 $32.00
www.nature.com/aps

Original Article

Kynurenic acid attenuates multiorgan dysfunction in rats after heatstroke

Yi-chang HSIEH[1], Ruei-feng CHEN[2], Yi-shian YEH[3], Mao-tsun LIN[4], Jui-hsiang HSIEH[1], Sheng-hsien CHEN[5, *]

[1]Institute of Biomedical Engineering, Chung Yuan Christian University, Chung Li, Taiwan, China; [2]Department of Life Science and Institute of Zoology, National Taiwan University, Taiwan, China; [3]Department of Neurosurgery, Taipei Medical University-Shuang Ho Hospital, Taipei, Taiwan, China; [4]Department of Medical Research, Chi Mei Medical Center, Tainan, Taiwan, China; and Graduate Institute of Disease Prevention and Control, Taipei Medical University, Taipei, Taiwan, China; [5]Department of Biotechnology, Southern Taiwan University, and Department of Obstetrics and Gynecology, Chi Mei Medical Center, Tainan, Taiwan, China

Aim: To assess whether systemic delivery of kynurenic acid improves the outcomes of heatstroke in rats.
Methods: Anesthetized rats were divided into 2 major groups and given vehicle solution (isotonic saline 0.3 mL/kg rat weight) or kynurenic acid (30–100 mg in 0.3 mL saline/kg) 4 h before the start of thermal experiments. They were exposed to an ambient temperature of 43 °C for 68 min to induce heatstroke. Another group of rats were exposed to room temperature (26 °C) and used as normothermic controls. Their core temperatures, mean arterial pressures, serum levels of systemic inflammatory response molecules, hypothalamic values of apoptotic cells and neuronal damage scores, and spleen, liver, kidney and lung values of apoptotic cells were determined.
Results: The survival time values during heatstroke for vehicle-treated rats were decreased from the control values of 475–485 min to new values of 83–95 min. Treatment with KYNA (30–100 mg/kg, iv) 4 h before the start of heat stress significantly and dose-dependently decreased the survival time to new values of 152–356 min ($P<0.05$). Vehicle-treated heatstroke rats displayed hypotension, hypothalamic neuronal degeneration and apoptosis, increased serum levels of tunor necrosis factor-α (TNF-α), intercellular adhesion molecule-1 (ICAM-1), and interleukin-10 (IL-10), and spleen, liver, kidney, and lung apoptosis. KYNA preconditioning protected against hypotension but not hyperthermia and attenuated hypothalamic neuronal degeneration and apoptosis during heatstroke. KYNA preconditioning attenuated spleen, kidney, liver, and lung apoptosis and up-regulated serum IL-10 levels but down-regulated serum TNF-α and ICAM-1 levels during heatstroke.
Conclusion: Our results suggest that systemic delivery of kynurenic acid may attenuate multiorgan dysfunction in rats after heatstroke.

Keywords: heatstroke; tumor necrosis factor-α; interleukin-10; intercellular adhesion molecule-1; *N*-methyl-*D*-aspartate receptor; kynurenic acid; hypothalamus; spleen; kidney; liver

Acta Pharmacologica Sinica (2011) 32: 167–174; doi: 10.1038/aps.2010.191

Introduction

Heatstroke is defined as a form of excessive hyperthermia (>40 °C) associated with a systemic inflammatory response that leads to multi-organ dysfunction in which central nervous system (CNS) disorders such as delusion, convulsion and coma predominate[1]. Our recent results have demonstrated that heatstroke rodents display hypotension, systemic inflammatory responses, hypothalamic ischemia and neuronal damage, and multi-organ dysfunction[2–4].

Kynurenic acid (KYNA) or its metabolic precursor *L*-kynurenine may be of therapeutic value in neurodegenerative diseased models[5, 6]. For example, systemically administered high doses of KYNA had a neuroprotective effect in the gerbil model of global ischemia[7]. Both the homocysteine-induced impairment of endothelial cells[8] and the motility and inflammatory activation in the early phase of acute experimental colitis in the rat[9] were significantly reduced by administration of KYNA.

The aim of this study was to investigate whether the heatstroke induced hypotension, systemic inflammatory responses, hypothalamic ischemia and damage, and multiorgan dysfunction could be attenuated by KYNA preconditioning. Accordingly, the temporal profiles of the apoptotic cell numbers of spleen, kidney, liver, lung, and hypothalamus,

* To whom correspondence should be addressed.
E-mail 891201@mail.chimei.org.tw
Received 2010-06-14 Accepted 2010-09-27

the serum levels of systemic inflammatory response molecules (*eg*, tumor necrosis factor-α [TNF-α], intracellular adhesion molecule-1 [ICAM-1], and interleukin-10 [IL-10]), body core temperature (Tco), and mean arterial pressure (MAP) during heatstroke were assessed in rats treated with or without KYNA (3–30 mg/kg of body weight, intravenously, 4 h before the start of thermal experiments).

Materials and methods

Animals

Adult male Sprague-Dawley rats (weight 263±15 g) were obtained from the Animal Resource Center of the National Science Council of China (Taipei, Taiwan). The animals were housed 4 in a group at an ambient temperature of 22±1 °C, with a 12-h light/dark cycle. Pellet rat chow and tap water were available *ad libitum*. All protocols were approved by the Animal Ethics Committee of the Chi Mei Medical Center (Tainan, Taiwan, China) in accordance with the Guide for the Care and Use of Laboratory Animals of the National Institutes of Health, as well as the guidelines of the Animal Welfare Act. Adequate anesthesia was maintained to abolish the corneal reflex and pain reflexes induced by tail pinching throughout all experiments (approximately 6 h) by a single intraperitoneal dose of urethane (1.4 g/kg body weight). At the end of the experiments, control rats that had survived heatstroke were killed with an overdose of urethane.

Surgery and physiological parameter monitoring

The right femoral artery and vein of rats were cannulated with polyethylene tubing (PE50), under urethane anesthesia, for blood pressure monitoring and drug administration. The Tco was monitored continuously by a thermocouple, while MAP and heart rate (HR) were monitored continuously with a pressure transducer.

Induction of heatstroke

The Tco of the anesthetized animals were maintained at about 37 °C with an infrared light lamp, except during the heat stress experiments. Heatstroke was induced by placing the animals in a folded heating pad maintained at 43 °C by circulating hot water. Survival time values (interval between the start of heat stress and animal death) were determined.

Experimental groups

Animals were assigned randomly to one of three groups. One group of rats, treated with an intravenous dose of vehicle solution (0.3 mL normal saline per rat) was exposed to 26 °C for up to 480 min (or to the end of the experiments). This group of rats was used as normothermic controls. The second group was treated with the same dose of vehicle solution 4 h before the initiation of heat exposure (43 °C for 68 min) and was used as vehicle-treated heatstroke animals. The third group of rats was intravenously treated with KYNA (30–100 mg/kg of body weight in 0.3 mL saline; Sigma Chemical Co, St Louis, MO, USA) 4 h before the start of thermal experiments. The last two groups of rats were exposed to heat stress (43 °C) for exactly 68 min to induce heatstroke and were then allowed to recover at 26 °C. Physiological parameters and survival time were observed for up to 480 min (or to the end of the experiments). In Experiment 1, the survival time values for normothermic rats, vehicle-treated heatstroke rats, and KYNA-treated heatstroke rats were determined randomly.

In Experiment 2, values of both Tco and MAP for normothermic rats (NT), vehicle-treated heatstroke rats (VEH+HS), and KYNA-treated heatstroke rats (KYNA+HS) were determined at 0 min, 68 min, or 85 min after the initiation of heat exposure in heatstroke rats or the equivalent times in NT group. All heatstroke groups had heat exposure (43 °C) withdrawn exactly at 68 min and were then allowed to recover at 26 °C temperature.

In Experiment 3, values of neuronal damage score, apoptolic cell numbers of hypothalamus, spleen, kidney, liver, and lung, and serum levels of TNF-α, ICAM-1, and IL-10 were determined at 85 min after the initiation of heat exposure in heatstroke rats or the equivalent time in normothermic controls.

Neuronal damage score

Eighty-five minutes after the start of heat stress, animals were killed by an overdose of urethane, and the brains were fixed in 10% neutral-buffered formalin for at least 24 h. The brain was removed and embedded in paraffin blocks. Serial sections (10 μm thick) through the hypothalamus were stained with hematoxylin and eosin for microscopic evaluation. The extent of neuronal damage was scored on a scale of 0–3, modified from the grading system of Pulsinelli *et al*[10], in which 0 is normal, 1 indicates approximately 30% of the neurons are damaged, 2 indicates that approximately 60% of the neurons are damaged, and 3 indicates that 100% of the neurons are damaged. Each hemisphere was evaluated independently by an examiner blinded to the experimental conditions.

The terminal deoxynucleotidyl transferase-mediated and dUTP-biotin nickened-labeling, TUNEL, staining

The TUNEL assay was performed using the apoptotic cells in different tissue samples including the spleen, kidney, liver, lung and hypothalamus. Color was developed using 3,3′-diaminobenzidine tetrachloride (Sigma chemical Co, St Louis, MO, USA). Sections were treated with xylene and ethanol to remove paraffin and for dehydration. They were then washed with phosphate buffered saline (PBS) and incubated in 3% hydrogen peroxide solution for 20 min. The sections were treated with 5 μg/mL proteinase k for 2 min at room temperature, and rewashed in PBS (0.1 mol/L, pH 7.4). The sections were then treated with a TUNEL reaction mixture (terminal deoxynucleotidyl transferase nucleotide mixture, Roche, Mannheim, Germany) at 37 °C for 1 h, and the sections were washed with distilled water. They were then incubated in anti-fluorescein antibody conjugated with horseradish peroxidase at room temperature for 30 min, washed and visualized using the avadinbiotin complex technique and 0.05% 3,3′-diaminobenzidine tetrachloride as a chromogen. The numbers of TUNEL-positive cells were counted by a patholo-

gist at 200× magnification, 30 fields per section. Blinding was performed for the pathologist's grading of results.

Measurement of serum TNF-α, ICAM-1, and IL-10 levels

Eighty-five minutes after the start of heat stress, blood samples were collected, immediately separated, and stored at -80 °C until they could be assayed. We used commercially available ELISA kits for the determination of serum TNF-α, ICAM-1, and IL-10 levels (Quantikine, R&D Systems Inc, Minneapolis, MN, USA) according to the manufacturer's instructions.

Statistical analysis

All data are expressed as means±standard deviation. One-way analysis of variance with Tukey's multiple comparisons test was used for serum markers, Tco, MAP, survival time, and apoptotic cell numbers. The Wilcoxon test was used for histological assessment. Significant differences were established at $P<0.05$. For all statistical analyses, SPSS software version 10.0 (SPSS Inc, Chicago, IL, USA) was used.

Results

KYNA prolonged survival time values during heatstroke

As depicted in Figure 1, body Tco and MAP increased to values of about 41 °C and about 140 mmHg, respectively at 68 min after the start of heat exposure (43 °C). However, 85 min after the start of heat stress, the Tco and MAP reached new values of about 41 °C and about 40 mmHg, respectively. The instant (85 min after heat exposure) in which Tco rose above 41 °C and MAP dropped about 40 mmHg was arbitrarily defined as the time point for the onset of heatstroke[3, 11, 12]. At 68 min, the heating pad was removed, and the animals were allowed to recover at room temperature (26 °C). The survival time values during heatstroke for vehicle-treated rats were decreased from the control values of 475–485 min (n=6) to new values of 83-95 min (n=6). Treatment with KYNA (30–100 mg per kg of body weight, intravenously) 4 h before the start of heat stress significantly ($P<0.05$) and dose-dependently decreased the survival time to new values of 152–356 min compared with normothermic rats (Table 1).

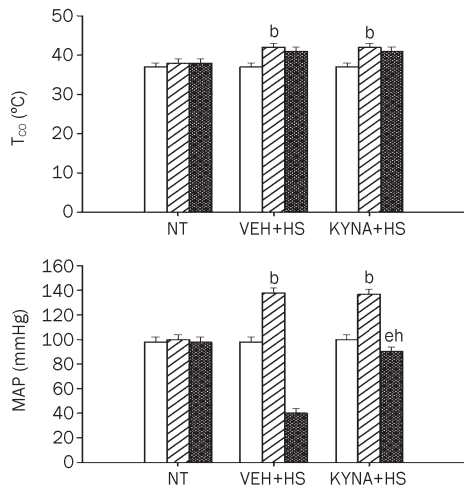

Figure 1. Values of both core temperature (Tco) and mean arterial pressure (MAP) for normothermic controls (NT), heatstroke (HS) rats treated with vehicle solution (VEH+HS) and HS rats treated with KYNA (KYNA+HS). The values were obtained at 0 (empty bar), 68 (diagonally shaded bar), or 85 (cross-hatched bar) min after the initiation of heat exposure in heatstroke rats or the equivalent times in NT. $^bP<0.05$ in comparison with NT group; $^eP<0.05$ in comparison with time "0" group; $^hP<0.05$ in comparison with (VEH+HS) group. All HS groups had heat exposure (43 °C) withdrawn exactly at 68 min and were then allowed to recover at room temperature (26 °C). Bars were the mean±SD of six rats for each group.

Table 1. The survival time values for normothermic rats, vehicle-treated rats, and KYNA-treated rats. Data were mean±SD. n=6. $^bP<0.05$, in comparison with group 1; $^eP<0.05$, in comparison with group 2.

Treatment groups	Survival time (min)
Normothermic rats	480±5
Vehicle-treated heatstroke rats	89±6^b
KYNA (10 mg/kg, iv)-treated heatstroke rats	152±7^e
KYNA (30 mg/kg, iv)-treated heatstroke rats	191±9^e
KYNA (100 mg/kg, iv)-treated heatstroke rats	356±17^e

All heatstroke rats which had heat exposure (43 °C) were withdrawn exactly at 68 min and then allowed to recover at room temperature (26 °C). Heatstroke rats were killed 85 min after the start of heat stress, where as the normothermic rats were killed about 480 min after the start of experiment (or at the experiment end). Vehicle or KYNA was injected 4 h before the start of experiments.

KYNA protected against hypotension but not hyperthermia during heatstroke

As shown in this Figure 1, heat stress induced significant ($P<0.05$) increase in both Tco and MAP in vehicle-treated heatstroke rats at 68 min. However, 17 min after termination of heat stress (or 85 min after the initiation of heat exposure), the values of MAP but not Tco were significantly ($P<0.05$) lower than those of the normothermic rats (40 mmHg *vs* 98 mmHg; Figure 1). The heat-induced hypotension, but not hyperthermia, was significantly ($P<0.05$) reduced by KYNA preconditioning.

KYNA attenuated hypothalamic neuronal degeneration and apoptosis during heatstroke

As shown in Table 2, after the onset of heatstroke, the hypothalamic neuronal damage scores were higher in animals treated vehicle compared with the normothermic controls. Histopathologic verification revealed that heatstroke caused cell body shrinkage, pyknosis of the nucleus, loss of Nissl substance, and disappearance of the nucleus in the hypothalamus of vehicle-treated rats (Figure 2). The figure also showed that the heat-induced hypothalamic neuronal degeneration were greatly reduced in KYNA-treated heatstroke rats ($P<0.05$).

Figure 3 showed the effects of heat exposure on the number of TUNEL-positive cells in the hypothalamus of normothermic

Table 2. The neuronal damage scores for normothermic rats, vehicle-treated heatstroke rats, and KYNA-treated heatstroke rats. [b]$P<0.05$, compared with group 1; [e]$P<0.05$, compared with group 2.

Treatment groups	Neuronal damage score (0–3)
Normothermic rats	0 (0, 0)
Vehicle-treated heatstroke rats	2 (2, 2)[b]
KYNA (30 mg/kg, iv)-treated heatstroke rats	1 (0.25, 0.75)[e]
KYNA (100 mg/kg, iv)-treated heatstroke rats	0 (0, 0)[e]

Values represented the median with the first and third quartile in parentheses of 6 rats per group. For determination of neuronal damage score, heatstroke rats were killed 85 min after the start of heat stress, whereas the normothermic rats were killed 480 min after the start of heat exposure (or at the experiment end). All heatstroke rats which had heat exposure (43 ºC) were withdrawn exactly at 68 min and then allowed to recover at room temperature (26 ºC). The data were evaluated by a Wilcoxon signed rank test followed by the Duncan test when appropriate.

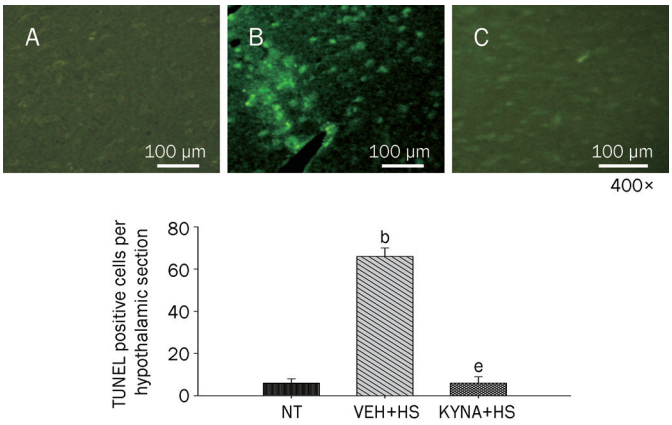

Figure 3. Mean number of TUNEL-positive cells per hypothalamic section for normothermic controls (NT), vehicle-treated heatstroke rats (VEH+HS), and KYNA-treated heatstroke rats (KYNA+HS). The values were obtained 85 min after the start of heat exposure for heatstroke groups or the equivalent time period for normothermic group. [b]$P<0.05$, in comparison with NT group. [e]$P<0.05$, in comparison with (VEH+HS) group. All heatstroke groups had heat exposure (43 ºC) withdrawn exactly at 68 min and were then allowed to recover at room temperature (26 ºC). Bars were the mean±SD or six rats per group. Top panels showed the hypothalamic staining for a NT rat (A), a (VEH+HS) rat (B), and a (KYNA+HS) rat (C).

controls, vehicle-treated heatstroke rats, and KYNA-treated heatstroke rats. After the onset of heatstroke (or 85 min after the start of heat stress), the number of TUNEL-positive cells of the hypothalamus was greater ($P<0.05$) in vehicle-treated heatstroke rats than in the normothermic controls. However, increase of TUNEL-positive cells in the hypothalamus of heatstroke rats was greatly attenuated by KYNA. A typical example of TUNEL staining of the hypothalamus was shown in the top panel of Figure 3.

KYNA attenuated spleen, kidney, liver, and lung apoptosis during heatstroke

Figures 4–7 summarized the effects of heat exposure on the number of TUNEL-positive cells in the spleen, the kidney, the liver, and the lung, respectively, of normothermic controls, vehicle-treated heatstroke rats, and KYNA-treated heatstroke rats. After the onset of heatstroke, the number of TUNEL-positive cells of these organs were greater ($P<0.05$) in vehicle-treated heatstroke rats than in the normothermic controls. However, increase of TUNEL-positive cells in these organs of heatstroke rats was greatly ($P<0.05$) attenuated by KYNA preconditioning. The typical examples of TUNEL stainings of these organs were shown in the top panel of Figures 4–7, respectively.

KYNA up-regulated serum IL-10 levels but down-regulated serum TNF-α and ICAM-1 levels during heatstroke

Figure 8 showed the serum levels of ICAM-1, TNF-α, and IL-10 among the three experimental groups. Compared with the normothermic controls, vehicle-treated heatstroke rats had higher levels ($P<0.05$) of ICAM-1 and TNF-α after the onset of heatstroke. The increase in the serum levels of these two markers caused by heatstroke were significantly reduced by KYNA preconditioning. However, compared with the vehicle-treated rats, KYNA-treated rats had higher ($P<0.05$) serum levels of IL-10 after the onset of heatstroke.

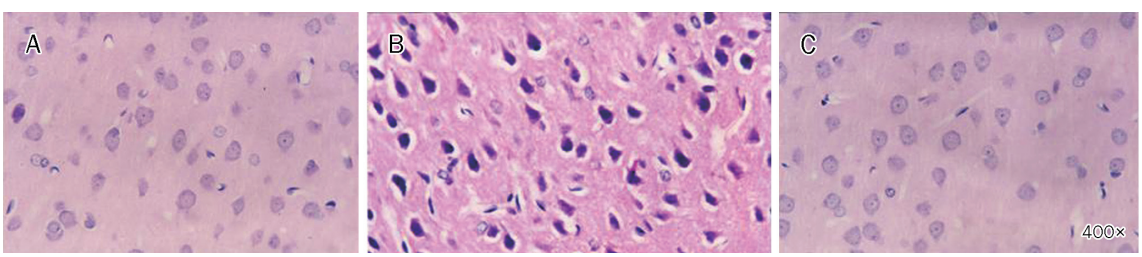

Figure 2. Histological examination of neuronal damage. The photomicrograph of the hypothalamus for a normothermic rat (A), a heatstroke rats treated with vehicle solution (B), or a heatstroke rat treated with KYNA (C). Heatstroke rats were killed 85 min after the start of heat stress, whereas the normothermic rats were killed at the equivalent time period. The hypothalamus of the vehicle-treated rats showed cell body shrinkage, pyknosis of the nucleus, loss of Nissl substance, and disappearance of the nucleolus (B). However, heat-induced neuronal damage was reduced in group "C". Magnification ×400

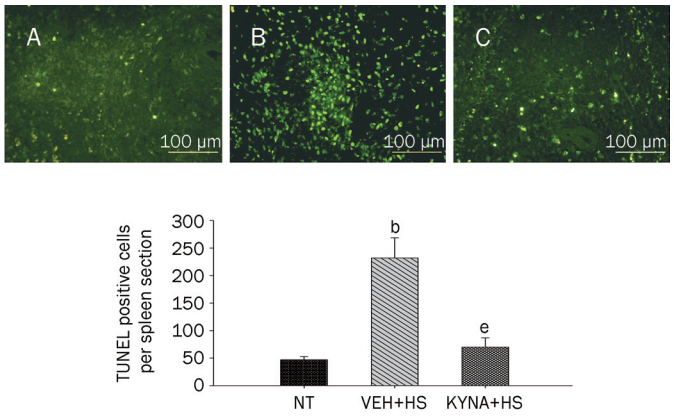

Figure 4. Values of renal TUNEL-positive cells for NT rats, (VEH+HS) rats, and (KYNA+HS) rats. The values were obtained at 85 min after the initiation of heat exposure in heatstroke rats or the equivalent times in NTs. $^{b}P<0.05$ in comparison with (NT) group; $^{e}P<0.05$ in comparison with (VEH+HS) group. All HS groups had heat exposure (43 °C) withdrawn exactly at 68 min and were then allowed to recover at room temperature (26 °C). Bars were the mean±SD of six rats for each group. Top panels depicted the kidney TUNEL-positive cells for a NT rat (A), a (VEH+HS) rat (B), and a (KYNA+HS) rat (C).

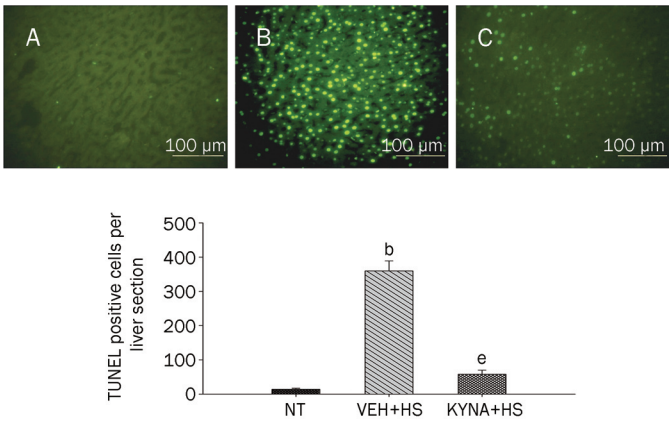

Figure 6. Values of liver TUNEL-positive cells for NT rats, (VEH+HS) rats, and (KYNA+HS) rats. The values were obtained at 85 min after the initiation of heat exposure in heatstroke rats or the equivalent times in NTs. $^{b}P<0.05$ in comparison with NT group; $^{e}P<0.05$ in comparison with (VEH+HS) group. All HS groups had heat withdrawn exactly at 68 min and were then allowed to recover at room temperature (26 °C). Bars were the mean±SD of six rats for each group. Top panels depicted the TUNEL stainings for a NT rat (A), a (VEH+HS) rat (B), and a (KYNA+HS) rat (C).

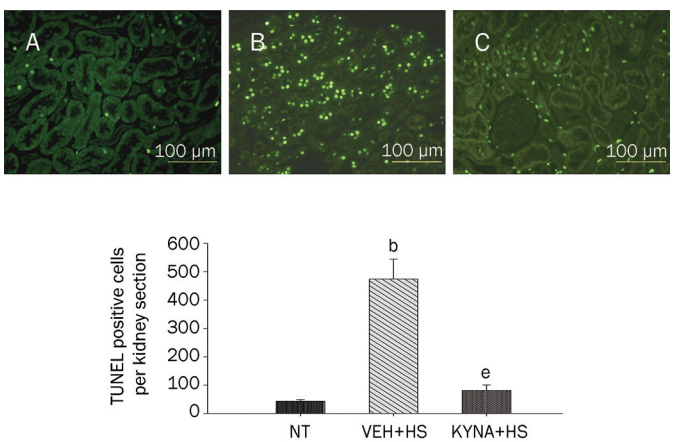

Figure 5. Values of spleen TUNEL-positive cells for NT rats, (VEH+HS) rats, and (KYNA+HS) rats. The values were obtained at 85 min after the initiation of heat exposure in heatstroke rats or the equivalent times in NTs. $^{b}P<0.05$ in comparison with (NT) group; $^{e}P<0.05$ in comparison with (VEH+HS) group. All HS group had heat withdrawn exactly at 68 min and were then allowed to recover at room temperature (26 °C). Bars were the mean±SD of six rats for each group. Top panels depicted the TUNEL stainings for a NT rat (A), a (VEH+HS) rat (B), and a (KYNA+HS) rats (C).

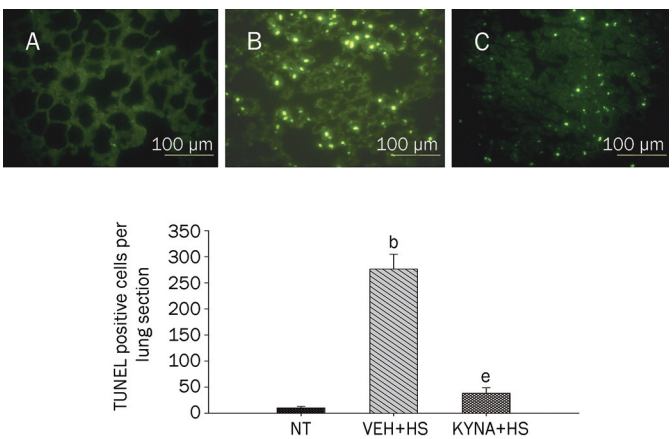

Figure 7. Values of lung TUNEL-positive cells for NT rats, (VEH+HS) rats, and (KYNA+HS) rats. The values were obtained at 85 min after the initiation of heat exposure in heatstroke rats or the equivalent times in NTs. $^{b}P<0.05$ in comparison with NT group; $^{e}P<0.05$ in comparison with (VEH+HS) group. All HS groups had heat withdrawn exactly at 68 min and were then allowed to recover at room temperature (26 °C). Bars were the mean±SD of six rats for each group. Top panels depicted the TUNEL stainings for a NT rat (A), a (VEH+HS) rat (B), and a (KYNA+HS) rat (C).

Discussion

A hypothesis of how heat stress leads to multi-organ dysfunction has been proposed[2, 13]. Heat stress stimulates metabolism and progressively reduces blood flow to critical splanchnic and brain tissues. Increased metabolic demand coupled with reduced splanchnic and brain blood flow generates cellular hypoxia, compromises cellular energy production, and produces derangements in intracellular Ca^{2+} homeostasis. As heat stress continues, hypoxic cells can produce multiorgan dysfunction and inflammation. Although the severity of heatstroke depends on the degree of hyperthermia and its duration[14], normal volunteers can passively endure a core temperature of about 42 °C with none or minimal tissue injury[15, 16]. Indeed, as demonstrated in the present results, KYNA treatment significantly prevented the occurrence of heat-induced multi-organ damage and inflammation without

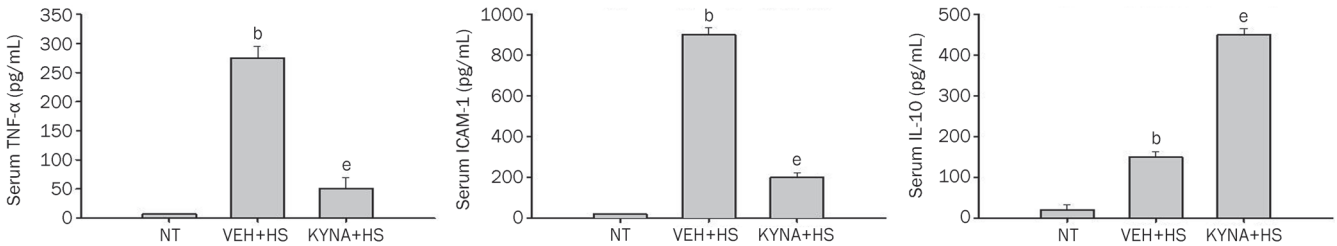

Figure 8. Serum levels of tumor necrosis factor-α (TNF-α), intercellular adhesion molecule-1 (ICAM-1), and interleukin-10 (IL-10) for NT rats, (VEH+HS) rats, and (KYNA+HS) rats. The samples were obtained at 85 min after the initiation of heat exposure in heatstroke rats or the equivalent times in NTs group. $^{b}P<0.05$, in comparison with NT group; $^{e}P<0.05$ in comparison with (VEH+HS) group. All heatstroke group had heat exposure (43 °C) withdrawn exactly at 68 min and were then allowed to recover at room temperature (26 °C). Bars were the mean±SD of six rats for each group.

affecting the induced hyperthermia. It should be mentioned that, in the present study, all these heatstroke animals were under the general anesthesia of urethane. Although the survival time values of these heatstroke animals were prolonged by KYNA preconditioning, but all the animals died. To determine whether there was durable improvement in survival, unanesthetized and unrestrained animals with or without KYNA should be exposed to heat stress in future studies.

Recent findings have documented that unanesthetized, unrestrained rodents display thermoregulatory deficits (*eg*, the heatstroke animals showed hypothermia when exposed to room temperature, 26 °C) 4 h after the initiation of heat stress[17, 18]. The heatstroke-induced thermoregulatory deficits may have resulted from neuronal apoptosis and cell degeneration in the hypothalamus (as demonstrated in the current study). The current results further showed that the hypothalamic apoptosis and neuronal degeneration that occurred during heatstroke in rats could be significantly ameliorated by KYNA treatment.

KYNA is a tryptophan metabolite formed as part of the kynurenine pathway. It has been shown that KYNA is an antagonist of the glycine site of NMDA and of the α-7 nicotinic acetylcholine receptors[19, 20] as well as a ligand for the orphan G-protein coupled receptor, GPR 35[21]. Excessive or persistent activation of glutamate receptors in the mammalian central nervous system results in neuronal death, contributing to brain damage in stroke, trauma, epilepsy[22] or other neurodegenerative disorders[23]. Most glutamate effects are mediated by the *N*-methyl-*D*-aspartate (NMDA) receptor, although α-amino-3-hydroxy-5-methyl-4-isoxazole-propionic acid (AMPA) or kainite[24] receptors, and metabotropic G-protein-coupled receptors[25] may also be involved. Only high doses of KYNA proved to be neuroprotective in neonatal rats by reducing anoxia-[26] or hypoxia-ischemia-induced[27] brain edema and in adult rats[28] and gerbils[7] given before ischemia induction. For example, KYNA exerted a neuroprotective effect at very high doses (1000–1200 mg/kg, ip), which induced a marked increase in the whole brain concentration of KYNA in gerbils subjected to transient forebrain ischemia[7]. Based on these observations together, KYNA might cause the attenuation of heat-induced multiple organ dysfunction via the mechanisms of the glycine site of NMDA and of the α-7 nicotinic acetylcholine receptors as well as a ligand for the orphan G-protein coupled receptor, GPR35. Altered blood-brain-barrier (BBB) permeability and brain injury occurred during heatstroke in rats[29]. In addition, human umbilical cord derived $CD34^{+}$ cells were found to be able to pass into the hyperthermic brain to attenuate heat-induced brain injury and damage in rats[30]. It could be derived from the foregoing statements that systemic delivery of KYNA might ameliorate multiorgan dysfunction that occurred during heatstroke via both the central and peripheral components of inhibition. In particular, KYNA might have achieved its central action via passing through the disrupted blood-brain-barrier.

It is generally believed that activation of the excitatory amino acid receptors plays an important role in neuronal death in stroke[31], as well as in the grey matter ischemia[32]. Kynurenic acid is one of the few known endogenous NMDA receptor inhibitors[33]. Our data and theoretical consideration suggest that KYNA or its metabolic precursor *L*-kynurenine may be of therapeutic value in heatstroke syndromes. However, the use of KYNA as a neuroprotective agent can be excluded because it is barely able to cross the BBB, whereas L-kynurenine is transported much more readily across the BBB[34].

In additional to inducing neuronal damage to brain tissues, heatstroke caused severe damage to the lung, kidney, liver, and spleen[2–4]. The current results further demonstrated that heat-induced multi-organ damage could be significantly ameliorated by KYNA preconditioning in the rat. In fact, the glutamate receptors are also present in pancreas, gut, kidney, liver, lung, spleen, and testis[35, 36]. Experiments performed on bovine aorta endothelial cell cultures showed that KYNA exerted a protective activity against the homocysteine-induced impairment of endothelial cells[8]. The addition of KYNA significantly increased endothelial cell migration and proliferation, which was diminished by homocysteine. KYNA also protected cells against homocysteine-induced cytotoxicity. KYNA was also shown to decrease motility and inflammatory activation in the early phase of acute experimental colitis in the rat[9].

A high affinity glutamate/aspartate transport system exists in pancreatic islets of langerhans and that this system contributes to a glutamatergic signaling pathway that can modulate

glucose-inducible insulin secretion[35]. Our previous results[37] showed that, after the onset of heatstroke in the rat, hypotension accompanied by no change in blood levels of glucose were observed.

It has been documented that the pathophysiological responses exerted during heatstroke are the results of a systemic inflammatory response that ensues following thermal injury rather than a direct effect of hyperthermia[1]. The serum TNF-α and ICAM-1 levels can be regarded as markers for the systemic inflammatory response as they indirectly reflect the whole body production of both TNF-α and ICAM-1 in various organs[38–41]. The expression of adhesion molecules can be induced by TNF-α[38]. The adhesion molecule ICAM-1 mediates firm adhesion between leukocytes and endothelial cells and contributes to the migration of leukocytes from postcapillary venues into the reperfused tissue[42, 43]. ICAM-1 initiates adhesion and transendothelial migration of circulating leukocytes[42]. Evidence has also suggested that IL-10 may have a therapeutic potential in acute and chronic inflammatory disease[44]. Exogenous administration of recombinant IL-10 protects mice from lethal endotoxemia by reducing TNF-α release[44]. In the present study, we showed that KYNA preconditioning increased the serum levels of IL-10 and decreased the serum levels of both TNF-α and ICAM-1, and prolonged the survival time during heatstroke. These observations suggested that KYNA might improve survival of heatstroke rats via reducing systemic inflammatory response in the rat.

In summary, the present data indicated that KYNA might exert a protective role on multiple organs during heatstroke through the following mechanisms: (A) Anti-inflammation: KYNA inhibited the up-regulation of systemic inflammatory response molecules such as TNF-α and ICAM-1 but enhanced the up-regulation of IL-10: (B) Anti-hypotension: KYNA reduced heat-induced splanchnic and brain ischemia; (C) Anti-apoptosis: KYNA inhibited heat-induced hypothalamic neuronal apoptosis and degeneration and multi-organ dysfunction.

Acknowledgements

This work was supported in part by the National Science Council (Taipei, Taiwan, China) NSC96-2314-B-384-002 and NSC96-2314-B-384-003-MY3 and DOH99-TD-B-111-003, Center of Excellence for Clinical Trail and Research in Neuroscience.

Author contribution

Yi-chang HSIEH and Sheng-hsien CHEN designed research; Yi-chang HSIEH and Ruei-feng CHEN performed research; Yi-shian YEH contributed new analytical tools and reagents; Sheng-hsien CHEN and Jui-hsiang HSIEH analyzed data; Mao-tsun LIN and Sheng-hsien CHEN wrote the paper.

References

1 Bouchama A, Knochel JP. Heat stroke. N Engl J Med 2002; 346: 1978–88.
2 Chang CK, Chang CP, Chiu WT, Lin MT. Prevention and repair of circulatory shock and cerebral ischemia/injury by various agents in experimental heatstroke. Curr Med Chem 2006; 13: 3145–54.
3 Liu WS, Chen CT, Foo NH, Huang HR, Wang JJ, Chen SH, *et al*. Human umbilical cord blood cells protect against hypothalamic apoptosis and systemic inflammation response during heatstroke in rats. Pediatr Neonatol 2009; 50: 208–16.
4 Yang HH, Chang CP, Cheng JT, Lin MT. Inhibition of acute lung inflammation and injury is a target of brain cooling after heatstroke injury. J Trauma 2010; in press.
5 Nemeth H, Robotka H, Toldi J, Vecsei L. Kynurenines in the central nervous system: recent developments. Centr Nerv Sys Agents Med Chem 2007; 7: 45–56.
6 Salvati P, Ukmar G, Dho L, Rosa B, Cini M, Marconi M, *et al*. Brain concentrations of kynurenic acid after a systemic neuroprotective dose in the gerbil model of global ischemia. Prog Neuropsychopharmacol Biol Psychiatry 1999; 23: 741–52.
7 Wejksza K, Rzeski W, Turski WA. Kynurenic acid protects against the homocysteine-induced impairment of endothelial cells. Pharmacol Rep 2009; 61: 751–6.
8 Varga G, Erces D, Fazekas B, Fulop M, Kovacs T, Kaszaki J, *et al*. *N*-Methyl-*D*-aspartate receptor antagonism decreases motility and inflammatory activation in the early phase of acute experimental colitis in the rat. Neurogastroenterol Motil 2010; 22: 217–25.
9 Pulsinelli WA, Levy DE, Duffy TE. Regional cerebral blood flow and glucose metabolism following transient forebrain ischemia. Ann Neurol 1982; 11: 499–509.
10 Chen SH, Chang FM, Tsai YC, Huang KF, Lin MT. Resuscitation from experimental heatstroke by transplantation of human umbilical cord blood cells. Crit Care Med 2005; 33: 1377–83.
11 Chen SH, Chang FM, Tsai YC, Huang KF, Lin CL, Lin MT. Infusion of human umbilical cord blood cells protect against cerebral ischemia and damage during heatstroke in the rat. Exp Neurol 2006; 199: 67–76.
12 Hall DM, Buettner GR, Oberley LW, Xu L, Matthes RD, Gisolfi CV. Mechanisms of circulatory and intestinal barrier dysfunction during whole body hyperthermia. Am J Physiol Heart Circ Physiol 2001; 280: H509–21.
13 Dematte JE, O'Mara K, Buescher J, Whitney CG, Forsythe S, McNamee T, *et al*. Near-fatal heat stroke during the 1995 heat wave in Chicago. Ann Intern Med 1998; 129: 173–81.
14 Bynum GD, Pandolf KB, Schuette WH, Goldman RF, Lees DE, Whang-Peng J, *et al*. Induced hyperthermia in sedated humans and the concept of critical thermal maximum. Am J Physiol 1978; 235: R228–36.
15 Pettigrew RT, Galt JM, Ludgate CM, Horn DB, Smith AN. Circulatory and biochemical effects of whole body hyperthermia. Br J Surg 1974; 61: 727–30.
16 Chatterjee S, Premachandran S, Bagewadikar RS, Bhattacharya S, Chattopadhyay S, Poduval TB. Arginine metabolic pathways determine its therapeutic benefit in experimental heatstroke: role of Th1/Th2 cytokine balance. Nitric Oxide 2006; 15: 408–16.
17 Shen KH, Lin CH, Chang HK, Chen WC, Chen SH. Premarin can act via estrogen receptors to rescue mice from heatstroke-induced lethality. Shock 2008; 30: 668–74.
18 Birch PJ, Grossman CJ, Hayes AG. Kynurenic acid antagonises responses to NMDA via an action at the strychnine-insensitive glycine receptor. Eur J Pharmacol 1988; 154: 85–7.
19 Hilmas C, Pereira EF, Alkondon M, Rassoulpour A, Schwarcz R, Albuquerque EX. The brain metabolite kynurenic acid inhibits alpha7 nicotinic receptor activity and increases non-alpha7 nicotinic receptor expression: physiopathological implications. J Neurosci 2001; 21: 7463–73.

20 Wang J, Simonavicius N, Wu X, Swaminath G, Reagan J, Tian H, *et al*. Kynurenic acid as a ligand for orphan G protein-coupled receptor GPR35. J Biol Chem 2006; 281: 22021–8.
21 Hou ST, MacManus JP. Molecular mechanisms of cerebral ischemia-induced neuronal death. Int Rev Cytol 2002; 221: 93–148.
22 Coyle JT, Puttfarcken P. Oxidative stress, glutamate, and neurodegenerative disorders. Science 1993; 262: 689–95.
23 Prass K, Dirnagl U. Glutamate antagonists in therapy of stroke. Restor Neurol Neurosci 1998; 13: 3–10.
24 Pin JP, Duvoisin R. The metabotropic glutamate receptors: structure and functions. Neuropharmacology 1995; 34: 1–26.
25 Simon RP, Young RS, Stout S, Cheng J. Inhibition of excitatory neurotransmission with kynurenate reduces brain edema in neonatal anoxia. Neurosci Lett 1986; 71: 361–4.
26 Andine P, Lehmann A, Ellren K, Wennberg E, Kjellmer I, Nielsen T, *et al*. The excitatory amino acid antagonist kynurenic acid administered after hypoxic-ischemia in neonatal rats offers neuroprotection. Neurosci Lett 1988; 90: 208–12.
27 Germano IM, Pitts LH, Meldrum BS, Bartkowski HM, Simon RP. Kynurenate inhibition of cell excitation decreases stroke size and deficits. Ann Neurol 1987; 22: 730–4.
28 Sharma HS, Westman J, Cervos-Navarro J, Nyberg F. Role of neurochemicals in brain edema and cell changes following hyperthermic brain injury in the rat. Acta Neurochir Suppl 1997; 70: 269–74.
29 Chen SH, Chang FM, Chang HK, Chen WC, Huang KF, Lin MT. Human umbilical cord blood-derived $CD34^+$ cells cause attenuation of multiorgan dysfunction during experimental heatstroke. Shock 2007; 27: 663–71.
30 Choi DW. Glutamate neurotoxicity and diseases of the nervous system. Neuron 1988; 1: 623–4.
31 Dohmen C, Kumura E, Rosner G, Heiss WD, Graf R. Extracellular correlates of glutamate toxicity in short-term cerebral ischemia and reperfusion: a direct *in vivo* comparison between white and gray matter. Brain Res 2005; 1037: 43–51.
32 Swartz KJ, During MJ, Freese A, Beal MF. Cerebral synthesis and release of kynurenic acid: an endogenous antagonist of excitatory amino acid receptors. J Neurosci 1990; 10: 2965–73.
33 Fukui S, Schwarcz R, Rapoport SI, Takada Y, Smith QR. Blood-brain barrier transport of kynurenines: implications for brain synthesis and metabolism. J Neurochem 1991; 56: 2007–17.
34 Weaver CD, Gundersen V, Verdoorn TA. A high affinity glutamate/aspartate transport system in pancreatic islets of Langerhans modulates glucose-stimulated insulin secretion. J Biol Chem 1998; 273: 1647–53.
35 Gill SS, Mueller RW, McGuire PF, Pulido OM. Potential target sites in peripheral tissues for excitatory neurotransmission and excitotoxicity. Toxicol Pathol 2000; 28: 277–84.
36 Chou YT, Lai ST, Lee CC, Lin MT. Hypothermia attenuates circulatory shock and cerebral ischemia in experimental heatstroke. Shock 2003; 19: 388–93.
37 Wyble CW, Desai TR, Clark ET, Hynes KL, Gewertz BL. Physiologic concentrations of TNFalpha and IL-1beta released from reperfused human intestine upregulate E-selectin and ICAM-1. J Surg Res 1996; 63: 333–8.
38 Chen LW, Egan L, Li ZW, Greten FR, Kagnoff MF, Karin M. The two faces of IKK and NF-kappaB inhibition: prevention of systemic inflammation but increased local injury following intestinal ischemia-reperfusion. Nat Med 2003; 9: 575–81.
39 Kuzu MA, Koksoy C, Kuzu I, Gurhan I, Ergun H, Demirpence E. Role of integrins and intracellular adhesion molecule-1 in lung injury after intestinal ischemia-reperfusion. Am J Surg 2002; 183: 70–4.
40 Olanders K, Sun Z, Borjesson A, Dib M, Andersson E, Lasson A, *et al*. The effect of intestinal ischemia and reperfusion injury on ICAM-1 expression, endothelial barrier function, neutrophil tissue influx, and protease inhibitor levels in rats. Shock 2002; 18: 86–92.
41 Menger MD, Vollmar B. Adhesion molecules as determinants of disease: from molecular biology to surgical research. Br J Surg 1996; 83: 588–601.
42 Hogg N, Bates PA, Harvey J. Structure and function of intercellular adhesion molecule-1. Chem Immunol 1991; 50: 98–115.
43 Berg DJ, Kuhn R, Rajewsky K, Muller W, Menon S, Davidson N, *et al*. Interleukin-10 is a central regulator of the response to LPS in murine models of endotoxic shock and the Shwartzman reaction but not endotoxin tolerance. J Clin Invest 1995; 96: 2339–47.
44 Gerard C, Bruyns C, Marchant A, Abramowicz D, Vandenabeele P, Delvaux A, *et al*. Interleukin 10 reduces the release of tumor necrosis factor and prevents lethality in experimental endotoxemia. J Exp Med 1993; 177: 547–50.

Acta Pharmacologica Sinica (2011) 32: 175–181
 1671-4083/11 $32.00
www.nature.com/aps

Original Article

Alteration of synaptic plasticity in rat dorsal striatum induced by chronic ethanol intake and withdrawal via ERK pathway

Sheng-zhong CUI[1], Shen-jun WANG[1], Jing LI[2], Gui-qin XIE[1], Rong ZHOU[1], Ling CHEN[1], Xiao-ru YUAN[1, *]

[1]Department of Physiology, Nanjing Medical University, Nanjing 210029, China; [2]Department of Pathophysiology, Nanjing Medical University, Nanjing 210029, China

Aim: The dorsal striatum has been proposed to contribute to the formation of drug-seeking behaviors, leading to excessive and compulsive drug usage, such as addiction. The current study aimed to investigate the involvement of extracellular signal-regulated kinase (ERK) pathway in the modification of striatal synaptic plasticity.
Methods: Ethanol was administered to rats in drinking water at concentration of 6% (*v/v*) for 30 days. Rats were sacrificed on day 10, 20, or 30 during ethanol intake or on withdrawal day 1, 3, or 7 following 30-d ethanol intake. The striata were removed either for electrophysiological recording or for protein immuno-blot analysis. Extracellular recording technique was used to record population spikes (PS) induced by high-frequency stimulation (HFS) in the dorsolateral striatum (DLS).
Results: Corticostriatal long-term depression (LTD) was determined to be dependent upon ERK signaling. Chronic ethanol intake (CEI) attenuated ERK phosphorylation and LTD induction, whereas withdrawal for one day (W1D) potentiated ERK phosphorylation and LTD induction. These results showed that the impact of chronic ethanol intake and withdrawal on corticostriatal synaptic plasticity was associated with ethanol's effect on ERK phosphorylation. In particular, pharmacological inhibition of ERK hyper-phosphorylation by U0126 prevented LTD induction in the DLS and attenuated ethanol withdrawal syndrome as well.
Conclusion: In rat DLS, chronic ethanol intake and withdrawal altered LTD induction via ERK signaling pathway. Ethanol withdrawal syndrome is mediated, at least partly, by ERK hyper-phosphorylation in the DLS.

Keywords: long-term depression; ethanol; synaptic plasticity; dorsal striatum; extracellular signal-regulated kinase; U0126

Acta Pharmacologica Sinica (2011) 32: 175–181; doi: 10.1038/aps.2010.199

Introduction

Addiction is increasingly viewed as a pathological process of learning, involving cell signaling and synaptic mechanisms similar to those implicated in neural models of learning and memory[1–4]. Synaptic plasticity is required for neuroadaptations that result from a variety of environmental stimuli. Therefore, it is attractive to hypothesize that drug abuse causes long-term changes in behavior by altering synaptic function and plasticity in relevant brain circuits.

The involvement of the ventral striatum, or nucleus accumbens (NAc), in mediating drug reward and reinforcement is well established[2, 4–6]. Recently, it has also been proposed that the dorsal striatum (caudate nucleus and putamen) is likely to be involved in advanced stages of addiction when drug use progresses toward a compulsive, habitual pathology[2, 5, 6]. Previous work from our lab[7] has shown that synaptic plasticity in the rat dorsal striatum was altered by chronic ethanol exposure and withdrawal. However, the relevant underlying molecular mechanism remains unclear.

It has been reported that extracellular signal-regulated kinase (ERK1/2, also known as p44 and p42 MAPK) signaling plays an important role in the induction of long-term potentiation (LTP). For example, stimuli inducing LTP in area CA1 of the hippocampus potently activate ERK[8], whereas pharmacological inhibition of MEK, an upstream activator of ERK, inhibits LTP[8, 9]. The participation of ERK in synaptic plasticity has also been found in other brain regions[10, 11, 12] (*eg*, LTD in the cerebellum and LTP in the visual cortex).

Furthermore, several studies[13–15] have suggested that the ERK signaling pathway is one of the targets of ethanol. For example, acute application of ethanol has been shown to attenuate MAPK activation in cultured cortical neurons and in mouse cerebral cortex *in vivo*[13]. A reduction of MAPK activation by chronic intermittent ethanol treatment was

* To whom correspondence should be addressed.
E-mail xryuan@public1.ptt.js.cn
Received 2010-04-08 Accepted 2010-11-01

observed in the amygdala, the cerebellum, the striatum and the hippocampus[14].

Based on these results, we hypothesized that changes in ERK activation by ethanol may contribute to the modulation of corticostriatal plasticity following chronic ethanol intake (CEI) treatment. In the present study, we first investigated whether corticostriatal LTD, as indicated in other brain regions, was ERK dependent. We then compared the effects of CEI and withdrawal treatment on ERK activation and corticostriatal LTD induction. The results showed that the ERK signaling pathway was involved in both striatal LTD induction and the impairment of synaptic plasticity produced by CEI/withdrawal treatment.

Materials and methods

Animals and drug application

Male Sprague-Dawley rats (grade II) from the Experimental Animals Center of Jiangsu Province (Certification No 97001) weighing 150–170 g were housed in cages on a 12-h dark/light cycle (light on at 7:00 am) with *ad libitum* access to food and water. Upon arrival in the laboratory, the animals were allowed to acclimate to the housing facilities for 3 d before use. All procedures were performed in accordance with the guidelines for the care and use of animals provided by the Experimental Animal Center of Jiangsu Province.

Ethanol was administered in drinking water at a concentration of 6% (*v/v*) for 30 consecutive days. Rats were sacrificed on day 10, 20 or 30 during ethanol intake or on withdrawal day 1, 3 or 7 following 30 days of ethanol intake.

U0126, a selective inhibitor of MEK (ERK kinase), was dissolved in 1% dimethyl sulfoxide (DMSO) and delivered through intracerebroventricular (icv) injection (100 μg/rat) or bath application. DMSO was diluted with saline (sterilized 0.9% sodium chloride solution, pH 7.0). In contrast to icv injection, a final DMSO concentration of 0.1%, instead of 1%, was used in bath application.

For icv injection, rats were anesthetized with pentobarbital sodium (50 mg/kg, ip). Guide cannulas (2.5 mm in length, 23 gauge) were implanted bi-ventricularly (A-P -0.3 mm from bregma; M-L±1.2 mm from the midline) and anchored to the skull with stainless steel screws and dental cement. A wire stylet was inserted in the guide until microinjection was made. Freshly prepared reagents (U0126 or DMSO) were injected using a stepper-motorized micro-syringe (Stoelting, Wood Dale, IL, USA) at a rate of 1 μL/min (final volume=5 μL/side). The left half of the striata was used for phospho-ERK/ERK detection, whereas the right half of the striata was used for electrophysiological recording.

Brain slice preparation

Rats were anesthetized with halothane and killed by decapitation. The brains were then rapidly removed and cooled in ice-cold artificial cerebrospinal fluid (ACSF) containing (in mmol/L): 126 NaCl, 2.5 KCl, 1.2 NaH_2PO_4, 25 $NaHCO_3$, 11 *D*-glucose, 2.4 $CaCl_2$, and 1.2 $MgCl_2$ at pH 7.4. The brains were fixed to a silicone stage with cyanoacrylate. Coronal slices (400 μm thick) were cut with a manual vibratome (Campden Instruments, Loughborough, Leics, UK). The slices were immediately transferred to a holding chamber containing ACSF that was constantly oxygenated with 95% O_2 and 5% CO_2 and maintained at room temperature 22–25 °C for 1-h equilibration prior to recording. A hemi-slice containing cortex and striatum just anterior to the globus pallidus was then transferred to a recording chamber (TC-202A, Medical Systems Corp, NY), maintained at 32 °C and perfused with oxygenated ACSF (95% O_2, 5% CO_2) at a flow rate of 2 mL/min.

Field potential recording

Extracellular recording electrodes, pulled on a horizontal micropipette puller (Sutter P97; Sutter Instruments, Novato, CA, USA) and filled with 2 mol/L NaCl (electrode impedance 3-8 MΩ), were placed within the striatum, located 1–2 mm ventral from the white matter, and set at the depth where maximal evoked population spike (PS) amplitude was observed. Field potentials were evoked by a constant current stimulus (50–200 μA, 100 μs duration) applied to the white matter via a glass-coated tungsten bipolar stimulating electrode placed dorsally with respect to the recording electrode. Baseline responses were set to half-maximal amplitude. Stable responses were recorded for 20 min prior to high-frequency stimulation (HFS; four bursts consisting of 100 pulses at 100 Hz delivered every 20 s). Stimulus intensity was adjusted to a level evoking maximal response during HFS.

The majority of the slices were also subjected to maximal stimulation at the end of the experiment to ensure that no significant deterioration of the slices had occurred during the experiment, as determined by the presence of a maximal PS in response to such stimulation.

Data were filtered (high-pass, 0.1 Hz; low-pass 3 kHz), amplified and digitized using an Axoclamp 2B amplifier and Digidata 1200 interface (Axon Instruments, CA), and then stored in a computer by pClamp 6.0 software and analyzed using Clampfit software.

Western blot assays

Dorsolateral striata were micro-dissected on ice using established anatomical landmarks. They were then immediately frozen in liquid nitrogen and stored in a -80°C freezer until use. For experiments, all of the samples were homogenized in lysis buffer containing the following: 50 mmol/L Tris–HCl (pH 7.5), 150 mmol/L NaCl, 5 mmol/L EDTA, 10 mmol/L NaF, 1 mmol/L sodium orthovanadate, 1% TritonX-100, 0.5% sodium deoxycholate, 1 mmol/L phenylmethylsulfonyl fluoride and protease inhibitor cocktail (Complete; Roche, Mannheim, Germany). Protein extracts were quantified using BCA assay (Pierce, Rockford, IL, USA), normalized, size-fractionated by 10% SDS polyacrylamide gel electrophoresis (50 μg/lane) and transferred to nitrocellulose membranes. Then blots were blocked for 1 h with 5% bovine serum albumin or skim milk in 0.1% TBS-Tween at room temperature. Phosphorylated forms of ERK were determined by immunodetection with a specific antibody against Thr202 and Tyr204 phospho-

rylation sites (Cell Signaling Tech, MA) at a dilution of 1:1000 in the same solution used for blocking. After incubation overnight at 4 °C with the primary antibody, blots were repeatedly washed in 0.1% TBS-Tween and incubated with a 1: 2000 dilution of a HRP-conjugated secondary antibody in 0.1% TBS-Tween for 1 h. Following further washes and incubation with a chemiluminescent substrate (Pierce), the blots were exposed to Kodak Biomax MR film. Western blots probed for phosphorylated ERK were stripped in 62.5 mmol/L Tris-HCl (pH 6.8), 2% SDS, and 100 mmol/L 2-mercaptoethanol for 30 min at 50 °C. As a control, the blots were then blocked and reprobed to detect total ERK (non-phosphorylated + phosphorylated). Autoradiograms were scanned and quantified using Quantity-One software.

Data analysis

LTD was defined as a stable decrease in field potential amplitude (>15%) 40 min post-HFS. The percentage change in field potential amplitude was determined by normalizing the mean response measured 50–60 min post-HFS to the mean response measured over the 10-min period immediately prior to tetanic conditioning.

Statistical analyses were performed using ANOVA followed by Student-Newman-Keuls *post-hoc* test. To evaluate differences between two treatments, two-tailed Student's *t*-test comparison was performed. Values of $P<0.05$ were considered statistically significant. All values are expressed as means±SEM (unless otherwise stated).

Results

Induction of corticostriatal LTD was blocked by U0126

U0126 is a specific membrane-permeable inhibitor of MAPK kinase (MAPKK, also known as MEK), which phosphorylates and activates ERK1/2[16]. To assess whether ERK activation plays a role in striatal synaptic plasticity, as has been suggested for other brain regions, U0126 was bath applied to the recording slices. Four rats, weighing 250±8.2 g, were used in this experiment.

As shown in Figure 1A, Western blot analysis revealed that basal ERK phosphorylation in DLS was markedly reduced following 30-min bath application of 20 μmol/L U0126 (0.41±0.08, $n=4$, $P<0.05$ *vs* control), as we expected, whereas the basal ERK phosphorylation remained unchanged (0.93±0.06, $n=4$) following 30-min bath application of 0.1% DMSO compared to control.

The baseline PS amplitude (mean responses of 10 min immediately prior to HFS) was -0.8±0.15 mV ($n=8$ slices) in the control group, -0.77±0.18 mV ($n=8$ slices) in the DMSO group, and -0.75±0.14 mV ($n=7$ slices) in the U0126 group. There was no significant difference between baseline PS amplitude in the control group and DMSO/U0126 group, which indicates that bath application of either DMSO or U0126 had no direct effect on basal synaptic transmission in DLS.

In DMSO-treated slices, the mean PS amplitude, measured at 50–60 min post-HFS, decreased (relative to baseline) to 54.4%±5.2% ($n=8$ slices, Figure 1B), which was similar to that recorded in normal ACSF (49.8%±6.4%, $n=8$ slices, Figure 1B). This indicates that LTD can be reliably elicited in DMSO-treated slices, consistent with the above-mentioned results demonstrating that DMSO had no effect on ERK phosphorylation. In contrast, the mean PS amplitude post-HFS in U0126-treated slices was 96.3%±6.9% ($n=7$ slices, Figure 1B) of baseline, suggesting that 30-min bath application of 20 μmol/L U0126 abolished LTD induction.

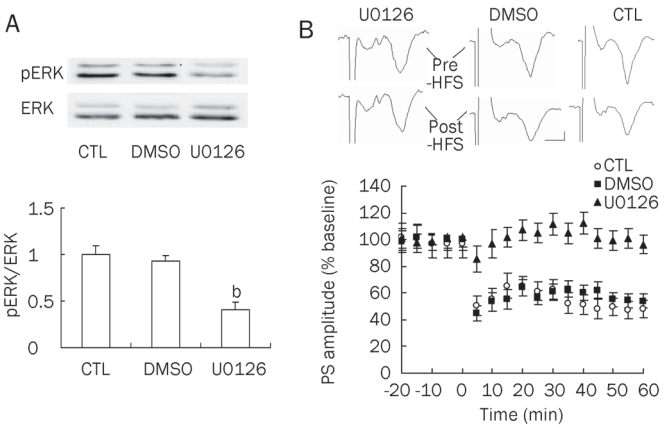

Figure 1. Effects of MEK inhibitor U0126 on striatal LTD induction and on ERK phosphorylation. (A) Thirty-minute bath application of 20 μmol/L U0126, but not 0.1% DMSO, inhibited ERK phosphorylation ($n=4$ in each group) in rat DLS. (B) Mean PS (population spike) amplitudes, expressed as a percentage of the mean baseline value, in 20 μmol/L U0126-treated slices ($n=7$), in 0.1% DMSO-treated slices ($n=8$), and in control (CTL) slices ($n=8$), respectively. U0126 or DMSO was present in the bath for 30 min before high-frequency stimulation (HFS). HFS was given at time 0 min. Upper panel: Sample traces of PS (5 min pre-HFS and 60 min post-HFS, respectively). Calibration: 2 ms, 0.2 mV. $^bP<0.05$ *vs* control.

ERK phosphorylation was altered during chronic ethanol intake and withdrawal

Rats were divided into seven groups ($n=5$ in each group): CTL (fed with tap water for 24 days), CEI10, CEI20, CEI30 (fed with 6% (*v/v*) ethanol for 10, 20, 30 d, respectively), WD1, WD3, and WD7 (withdrawal for 1, 3, and 7 d after 30 d of ethanol intake). The body weights (mean±SD in g) of rats in each group were as follows: CEI10 (205.6±10.9), CEI20 (245.2±11.3), CTL (262.2±10.2), CEI30 (297±10.5), WD1 (304.4±11.9), WD3 (318.2±14.8), and WD7 (336.6±16.1). Preliminary studies showed no significant differences in basal phospho- or total ERK protein levels within this weight range of rats.

Western blot results (Figure 2) showed that in DLS, chronic ethanol intake induced a decrease in ERK phosphorylation in the CEI10 (0.54±0.05, $P<0.05$), CEI20 (0.43±0.08, $P<0.05$) and CEI30 (0.76±0.07, $P<0.05$) groups, respectively, in comparison with the CTL group. In contrast, phospho-ERK levels increased in the WD1 group (1.32±0.08; $P<0.05$ *vs* CTL) and showed no statistically significant changes in either the WD3 group (0.96±0.10, $n=5$) or the WD7 group (0.88±0.12, $n=5$).

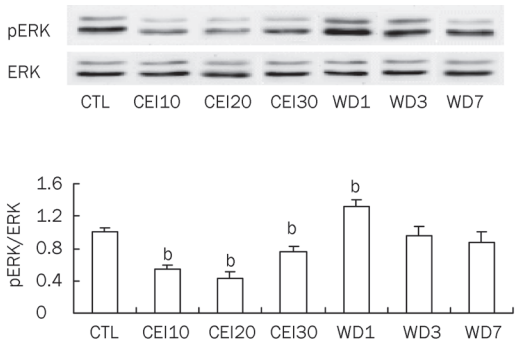

Figure 2. Chronic ethanol intake and withdrawal treatment changed phospho-ERK levels in rat DLS (n=5 in each group). The upper panel is a representative Western blot. CTL, control; CEI10, CEI20, and CEI30 represent chronic ethanol intake for 10, 20, and 30 days, respectively. WD1, WD3, and WD7 represent chronic ethanol withdrawal for 1 day, 3 days, and 7 days, respectively, after 30 days of ethanol intake. ^{b}P<0.05 *vs* control.

These results indicate that in the DLS, chronic ethanol intake reduces ERK phosphorylation, whereas ethanol withdrawal enhances ERK phosphorylation transiently. Next, we determined whether chronic ethanol intake– and withdrawal–induced activities of ERK phosphorylation correlated with striatal LTD induction.

Changes of striatal LTD induction caused by chronic ethanol intake and withdrawal were associated with alterations in ERK phosphorylation

CEI10 (lower phospho-ERK) and WD1 (higher phospho-ERK) groups were selected to determine whether changes in corticostriatal LTD induction would coincide with ERK phosphorylation following chronic ethanol intake or withdrawal.

U0126 or vehicle (1% DMSO) was delivered through icv injection for 3 consecutive days prior to decapitation to manipulate ERK activity to verify the relationship between corticostriatal synaptic plasticity and ERK phosphorylation. The pair-fed rats, as the control group, received sham surgery.

As shown in Figure 3, using a tetanus stimulation (four bursts consisting of 100 pulses at 100 Hz delivered every 20 s), LTD was readily induced in control brain slices (PS amplitudes post-HFS at 50.1%±5.1% of baseline, n=13. Figure 3B). In the CEI10+DMSO groups, the PS amplitudes post-HFS increased to 81.2%±4.4% of baseline (n=11, P<0.05 *vs* control), whereas phospho-ERK levels decreased to 0.58±0.11 (n=5, P<0.05 *vs* control; Figure 3A), which was consistent with the results shown in Figure 2. In the CEI10 + U0126 group, the PS amplitudes post-HFS increased to 101.7%±7.8% of baseline (n=10, P<0.01 *vs* control) along with a marked decrease in phospho-ERK levels (0.31±0.08, n=5, P< 0.01 *vs* control). These data demonstrated an increase in the PS amplitudes post-HFS (in comparison with CTL) that accompanied a decrease in phospho-ERK levels in the CEI10 group or the CEI10+U0126 group, indicating that the attenuation or blockade of LTD induction might be related to changes in ERK phosphorylation.

In the WD1+DMSO group, phospho-ERK levels increased to 1.53±0.1 of control (n=5, P<0.05 *vs* control; Figure 4A). However, no differences in the PS amplitudes post-HFS were found between the WD1+DMSO group and the CTL group (data not shown), as we would have expected.

This discrepancy could be accounted for the increased ERK phosphorylation as a result of HFS of corticostriatal fibers because corticostriatal fibers stimulate ERK signaling through the activation of glutamate receptors and an increase in intracellular calcium. In agreement with our hypothesis, when a weaker stimulation protocol (two bursts instead of four bursts) was utilized, a greater depression of the PS amplitudes post-HFS in WD1+DMSO groups (34.5%±4.8% of baseline *vs* 58.5%± 5.6% of baseline in CTL group, P<0.05, Figure 4B) was observed.

When U0126 was infused through icv injection in the WD1+U0126 group, the PS amplitudes post-HFS increased

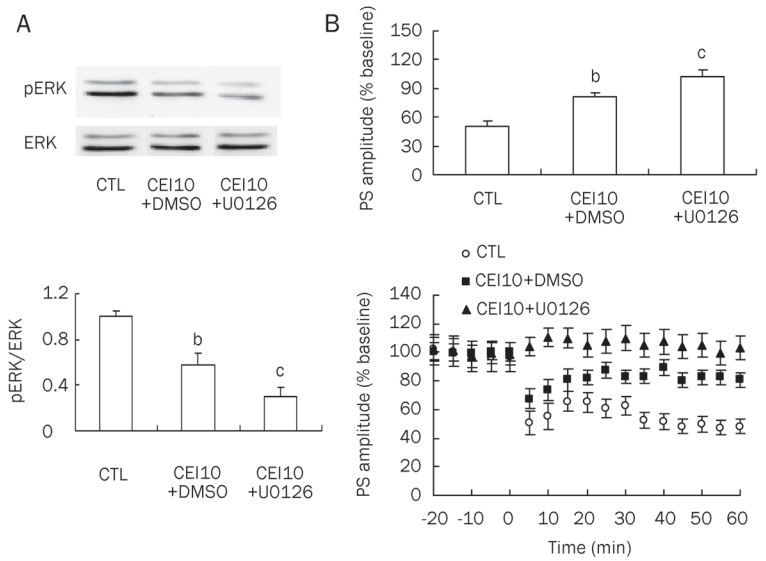

Figure 3. Ten days of chronic ethanol intake (CEI) decreased phospho-ERK levels and attenuated striatal LTD induction. MEK inhibitor U0126 enhanced the effects of CEI10 on both phospho-ERK levels and striatal LTD induction. (A) Phospho-ERK levels decreased in both CEI10 and CEI10+U0126 groups (n=5 in each group). (B) Induction of striatal LTD was attenuated in both CEI10 (n=11) and CEI10+U0126 groups (n=10; n=13 in CTL group). In the upper panel, the percentage change of PS amplitude is calculated by normalizing the mean response measured 50–60 min post-HFS to the mean response measured over the 10-min period immediately prior to HFS (baseline). In the lower panel, HFS was given at time 0 min. CTL, control; CEI10, 10 days of chronic ethanol intake. ^{b}P<0.05, ^{c}P< 0.01 *vs* control.

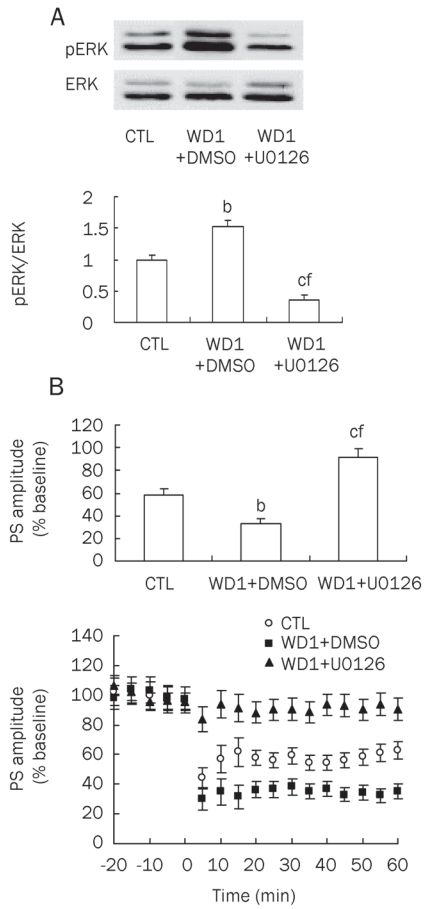

Figure 4. Effects of one-day withdrawal (WD1) and MEK inhibitor U0126 on both phospho-ERK levels and striatal LTD induction. (A) Phospho-ERK levels increased in WD1+DMSO group and decreased in WD1+U0126 group (n=5 in each group). (B) Striatal LTD induction was potentiated by WD1+DMSO treatment (n=10) and was blocked by WD1+U0126 treatment (n=11; n=14 in CTL group). In the lower panel, HFS was given at time 0 min. CTL, control; WD1, 1-day withdrawal after 30 days of ethanol intake. ^bP<0.05, ^cP<0.01 *vs* control; ^fP<0.01 *vs* WD1+DMSO.

to 91.7%±7.3% of baseline (n=11, P<0.01 *vs* control; P<0.01 *vs* WD1+DMSO, Figure 4A), whereas phospho-ERK levels decreased to 0.35±0.08 (n=5, P<0.01 *vs* control; P<0.01 *vs* WD1+DMSO, Figure 4B) of control, suggesting that LTD formation was inversely related to ERK activation.

Taken together, these results strongly indicated that chronic ethanol intake and withdrawal altered corticostriatal LTD induction via its effect on ERK phosphorylation in DLS.

Ethanol withdrawal syndrome was attenuated by the infusion of U0126

The ethanol withdrawal scores in both the WD1+DMSO group and the WD1+U0126 group were evaluated by an observer unaware of the drug treatment. The rating scale for the behavioral signs of ethanol withdrawal syndrome was used as described previously[7]. In congruence with the findings that icv infusion of U0126 can prevent both ERK hyperphosphorylation and LTD induction in WD1 rats (Figure 4), ethanol withdrawal signs were also alleviated by the infusion of U0126, which is illustrated in Figure 5.

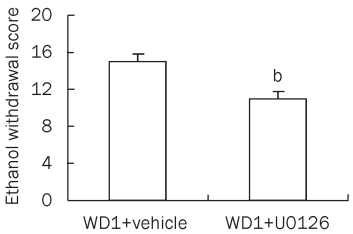

Figure 5. Ethanol withdrawal syndrome was attenuated by infusion of U0126 (n=5 in each group). U0126 or vehicle (1% DMSO) was delivered through icv injection for 3 consecutive days prior to evaluation. ^bP<0.05 *vs* WD1+vehicle.

Discussion

In the present study, we demonstrated that chronic ethanol intake decreased ERK phosphorylation, whereas ethanol withdrawal increased ERK phosphorylation transiently in rat DLS. Moreover, we showed that the alteration in corticostriatal synaptic plasticity induced by chronic ethanol intake and withdrawal occurred through the activation of ERK signaling pathway.

Both forms of long-lasting synaptic plasticity, LTP and LTD, can be induced by high-frequency synaptic stimulation of striatal neurons. *In vivo* studies demonstrated a preferential expression of LTP upon stimulation of cortical afferents[17, 18]. In contrast, in striatal slices, LTD is the predominant form of plasticity observed following high-frequency afferent stimulation[19–21]. LTP could only be induced *in vitro* using pharmacological manipulation, such as the blockade of dopamine receptors or the removal of extracellular magnesium[22]. Subsequent investigations delineated two intriguing factors that help to determine the direction of changes in synaptic efficacy at striatal synapses, namely the region of the striatum examined and the age of the animal[23, 24]. Accordingly, LTP is preferentially expressed in dorsomedial striatum in younger rats under normal physiological conditions. This is consistent with the fact that synapses within the striatum develop along a lateral-medial gradient, with the synapses in lateral striatum maturing earlier than those in medial striatum[25]. Nevertheless, it is not surprising that LTD was invariably recorded in our experiment, given the use of older rats (2–3 months) and the recording subregion of striatum (DLS).

Although it has been previously shown that ERK phosphorylation is required for both LTP[9, 10] and LTD[26, 11] in hippocampal CA1 as well as LTD in the cerebellum[8] and LTP in other cortical areas[12], we provide the first evidence that ERK activation is required for striatal LTD induction.

The ethanol-induced modulation of ERK activity *in vitro* has been controversial, with potentiation reported by some[27, 28] and depression by others[29–31]. However, *in vivo* exposure data are more consistent, revealing an ethanol-induced decrease in

ERK activation[13–15], except in the report from Bachtell *et al*[32]. Our data are in agreement with previous reports in which chronic ethanol exposure *in vivo* decreased ERK phosphorylation. It should be noted that in CEI30 groups, the suppression of phospho-ERK levels was, while still significant, attenuated, which may reflect the adaptation or tolerance to long-term alcohol consumption. We also demonstrated an enhancement of ERK phosphorylation briefly after withdrawal[14]. This may be related to increased neural activity following disinhibition or hyperexcitability caused by ethanol withdrawal.

The mechanisms underlying the effects of chronic ethanol exposure on ERK phosphorylation are still under investigation. However, studies showing the activation of MAP kinase by Ca^{2+} via NMDA receptors or voltage-dependent Ca^{2+} channels have been very well documented[33–35]. Since ethanol inhibits both voltage-gated Ca^{2+} channels and NMDA receptor-associated Ca^{2+} influx[36–38], it is possible that a decrease in the Ca^{2+} concentration in striatal neurons might decrease the phosphorylation of MAP kinase. Future studies will be required to identify the site and mechanism underlying the effects of ethanol on this pathway.

Anatomical studies have shown projections from the cortex to the medial striatum, including visual, auditory and limbic (ie, hippocampus, entorhinal and piriform cortices) afferents. In contrast, most cortical projections to the lateral striatum are of sensorimotor origin and, to a lesser degree, auditory and visual afferents[39]. Accordingly, recent studies suggest that the dorsomedial and dorsolateral striata have differential roles in different learning and memory paradigms. The dorsomedial striatum, in particular, has been shown to be critical for the learning of goal-directed actions. In contrast, the dorsolateral striatum appears to be involved in the formation of habits[40, 41]. By showing that chronic ethanol intake and withdrawal differentially altered synaptic plasticity in dorsolateral striatum through ERK signaling pathway, our findings suggest that chronic alcohol abuse could disrupt the habit-formation process, and this neural maladaptation may consequently lead to habitual drug-seeking behavior.

To summarize, our current studies have shown that induction of corticostriatal LTD in rat is differentially altered by chronic ethanol intake and withdrawal, which occurs through ERK signaling pathway. Understanding the biochemical mechanism underlying chronic ethanol treatment-induced changes in striatal synaptic plasticity may aid in the development of more effective therapeutic agents for alcohol abuse.

Acknowledgements

This project was supported by the National Natural Science Foundation of China (No 30572173) and the Natural Science Foundation of the Education Committee of Jiangsu Province, China (No 06KJB180071).

We thank Dr Shang SHEN at University of Nevada, Las Vegas, for critical reading of the manuscript.

Author contribution

Xiao-ru YUAN and Jing LI designed the research; Sheng-zhong CUI, Shen-jun WANG, Rong ZHOU, and Gui-qin XIE performed the research; Sheng-zhong CUI, Xiao-ru YUAN, and Ling CHEN analyzed the data and wrote the paper.

References

1 Nestler EJ. Molecular basis of long-term plasticity underlying addiction. Nat Rev Neurosci 2001; 2: 119–28.
2 Berke JD, Hyman SE. Addiction, dopamine, and the molecular mechanisms of memory. Neuron 2000; 25: 515–32.
3 Kelley AE. Memory and addiction: shared neural circuitry and molecular mechanisms. Neuron 2004; 44: 161–79.
4 Hyman SE, Malenka RC, Nestler EJ. Neural mechanisms of addiction: the role of reward–related learning and memory. Annu Rev Neurosci 2006; 29: 565–98.
5 Everitt BJ, Wolf ME. Psychomotor stimulant addiction: a neural systems perspective. J Neurosci 2002; 22: 3312–20.
6 Koob GF, Le Moal M. Drug addiction, dysregulation of reward, and allostasis. Neuropsychopharmacology 2001; 24: 97–129.
7 Xia JX, Li J, Zhou R, Zhang XH, Ge YB, Yuan XR. Alterations of rat corticostriatal synaptic plasticity after chronic ethanol exposure and withdrawal. Alcohol Clin Exp Res 2006; 30: 819–24.
8 English JD, Sweatt JD. A requirement for the mitogen-activated protein kinase cascade in hippocampal long term potentiation. J Biol Chem 1997; 272: 19103–6.
9 Kanterewicz BI, Urban NN, McMahon DB, Norman ED, Giffen LJ, Favata MF, *et al*. The extracellular signal-regulated kinase cascade is required for NMDA receptor-independent LTP in area CA1 but not area CA3 of the hippocampus. J Neurosci 2000; 20: 3057–66.
10 Kawasaki H, Fujii H, Gotoh Y, Morooka T, Shimohama S, Nishida E, *et al*. Requirement for mitogen-activated protein kinase in cerebellar long-term depression. J Biol Chem 1999; 274: 13498–502.
11 Gallagher SM, Daly CA, Bear MF, Huber KM. Extracellular signal-regulated protein kinase activation is required for metabotropic glutamate receptor-dependent long-term depression in hippocampal area CA1. J Neurosci 2004; 24: 4859–64.
12 Di Cristo G, Berardi N, Cancedda L, Pizzorusso T, Putignano E, Ratto GM, *et al*. Requirement of ERK activation for visual cortical plasticity. Science 2001; 292: 2337–40.
13 Kalluri HS, Ticku MK. Ethanol-mediated inhibition of mitogen-activated protein kinase phosphorylation in mouse brain. Eur J Pharmacol 2002; 439: 53–8.
14 Sanna PP, Simpson C, Lutjens R, Koob G. ERK regulation in chronic ethanol exposure and withdrawal. Brain Res 2002; 948: 186–91.
15 Roberto M, Nelson TE, Ur CL, Brunelli M, Sanna PP, Gruol DL. The transient depression of hippocampal CA1 LTP induced by chronic intermittent ethanol exposure is associated with an inhibition of the MAP kinase pathway. Eur J Neurosci 2003; 17: 1646–54.
16 Favata MF, Horiuchi KY, Manos EJ, Daulerio AJ, Stradley DA, Feeser WS, *et al*. Identification of a novel inhibitor of mitogen-activated protein kinase kinase. J Biol Chem 1998; 273: 18623–32.
17 Charpier S, Deniau JM. *In vivo* activity-dependent plasticity at corticostriatal connections: evidence for physiological long-term potentiation. Proc Natl Acad Sci USA 1997; 94: 7036–40.
18 Charpier S, Mahon S, Deniau JM. *In vivo* induction of striatal long-term potentiation by low-frequency stimulation of the cerebral cortex. Neurosci 1999; 91: 1209–22.
19 Calabresi P, Maj R, Pisani A, Mercuri NB, Bernardi G. Long-term synaptic depression in the striatum: physiological and pharmacological characterization. J Neurosci 1992; 12: 4224–33.
20 Lovinger DM, Tyler EC, Merritt A. Short- and long-term synaptic depres-

sion in rat neostriatum. J Neurophysiol 1993; 70: 1937–49.
21 Wickens JR, Begg AJ, Arbuthnott GW. Dopamine reverses the depression of rat corticostriatal synapses which normally follows high-frequency stimulation of cortex *in vitro*. Neuroscience 1996; 70: 1–5.
22 Calabresi P, Pisani A, Mercuri NB, Bernardi G. Long-term potentiation in the striatum is unmasked by removing the voltage-dependent magnesium block of NMDA receptor channels. Eur J Neurosci 1992; 4: 929–35.
23 Smith R, Musleh W, Akopian G, Buckwalter G, Walsh JP. Regional differences in the expression of corticostriatal synaptic plasticity. Neuroscience 2001; 106: 95–101.
24 Partridge JG, Tang KC, Lovinger DM. Regional and postnatal heterogeneity of activity-dependent long-term changes in synaptic efficacy in the dorsal striatum. J Neurophysiol 2000; 84: 1422–9.
25 Butler AK, Uryu K, Chesselet M. A role for *N*-methyl-*D*-aspartate receptors in the regulation of synaptogenesis and expression of the polysialylated form of the neural cell adhesion molecule in the developing striatum. Dev Neurosci 1998; 20: 253–62.
26 Thiels E, Kanterewicz BI, Norman ED, Trzaskos JM, Klann E. Long-term depression in the adult hippocampus *in vivo* involves activation of extracellular signal-regulated kinase and phosphorylation of Elk-1. J Neurosci 2002; 22: 2054–62.
27 Roivainen R, Hundle B, Messing RO. Ethanol enhances growth factor activation of mitogen-activated protein kinases by a protein kinase C-dependent mechanism. Proc Natl Acad Sci USA 1995; 92: 1891–5.
28 Smith TL, Navratilova E. The effect of ethanol exposure on mitogen-activated protein kinase activity and expression in cultured rat astrocytes. Neurosci Lett 2003; 341: 91–4.
29 Hallak H, Seiler AE, Green JS, Henderson A, Ross BN, Rubin R. Inhibition of insulin-like growth factor-I signaling by ethanol in neuronal cells. Alcohol Clin Exp Res 2001; 25: 1058–64.
30 Ma W, Li BS, Maric D, Zhao WQ, Lin HJ, Zhang L, *et al*. Ethanol blocks both basic fibroblast growth factor- and carbachol-mediated neuroepithelial cell expansion with differential effects on carbachol-activated signaling pathways. Neuroscience 2003; 118: 37–47.
31 Seiler AE, Ross BN, Green JS, Rubin R. Differential effects of ethanol on insulin-like growth factor-I receptor signaling. Alcohol Clin Exp Res 2000; 24: 140–8.
32 Bachtell RK, Tsivkovskaia NO, Ryabinin AE. Alcohol-induced c-Fos expression in the Edinger-Westphal nucleus: pharmacological and signal transduction mechanisms. J Pharmacol Exp Ther 2002; 302: 516–24.
33 Orban CP, Chapman FP, Brambilla R. Is Ras-MAPK signaling pathway necessary for long term memory formation? Trends Neurosci 1999; 22: 38–44.
34 Rosen BL, Ginty DD, Weber JM, Greenberg EM. Membrane depolarization and calcium influx stimulate MEK and MAP kinase via activation of Ras. Neuron 1994; 12: 1207–21.
35 Xia Z, Dudek H, Miranti KC, Greenberg ME. Calcium influx via the NMDA receptor induces immediate early gene transcription by a MAP kinase/ERK-dependent mechanism. J Neurosci 1996; 16: 5425–36.
36 Lovinger DM, White G, Weight FF. Ethanol inhibits NMDA activated ion current in hippocampal neurons. Science 1989; 243: 1721–4.
37 Lovinger DM, White G, Weight FF. NMDA receptor-mediated synaptic excitation selectively inhibited by ethanol in hippocampal slice from adult rat. J Neurosci 1990; 10: 1372–9.
38 Walter HJ, Messing RO. Regulation of neuronal voltage-gated calcium channels by ethanol. Neurochem Int 1999; 35: 95–101.
39 McGeorge AJ, Faull RLM. The organization of the projection from the cerebral cortex to the striatum in the rat. Neuroscience 1989; 29: 503–37.
40 Yin HH, Knowlton BJ. The role of the basal ganglia in habit formation. Nature Rev Neurosci 2006; 7: 464–76.
41 Yin HH, Knowlton BJ, Balleine BW. Lesions of dorsolateral striatum preserve outcome expectancy but disrupt habit formation in instrumental learning. Eur J Neurosci 2004; 19: 181–9.

Acta Pharmacologica Sinica (2011) 32: 182–187
 1671-4083/11 $32.00
www.nature.com/aps

Original Article

Novel neuroprotectant chiral 3-*n*-butylphthalide inhibits tandem-pore-domain potassium channel TREK-1

Xin-cai JI[1], Wan-hong ZHAO[1, 2], Dong-xu CAO[1], Qiao-qiao SHI[1], Xiao-liang WANG[1, *]

[1]*Department of Pharmacology, Institute of Materia Medica, Chinese Academy of Medical Sciences and Peking Union Medical College, Beijing 100050;* [2]*Faculty of Basic Medical Sciences, Hubei University of Medicine, Shiyan 442000, China*

Aim: To study the effects of 3-*n*-butylphthalide (NBP) on the TREK-1 channel expressed in Chinese hamster ovary (CHO) cells.
Methods: Whole-cell patch-clamp recording was used to record TREK-1 channel currents. The effects of varying doses of *l*-NBP on TREK-1 currents were also observed. Current-clamp recordings were performed to measure the resting membrane potential in TREK-1-transfected CHO (TREK-1/CHO) and wild-type CHO (Wt/CHO) cells.
Results: *l*-NBP (0.01–10 μmol/L) showed concentration-dependent inhibition on TREK-1 currents (IC_{50}=0.06±0.03 μmol/L), with a maximum current reduction of 70% at a concentration of 10 μmol/L. *l*-NBP showed a more potent inhibition on TREK-1 current than *d*-NBP or *dl*-NBP. This effect was partially reversed upon washout and was not voltage-dependent. *l*-NBP 10 μmol/L elevated the membrane potential in TREK-1/CHO cells from -55.3 mV to -42.9 mV. However, it had no effect on the membrane potential of Wt/CHO cells.
Conclusion: *l*-NBP potently inhibited TREK-1 current and elevated the membrane potential, which may contribute to its neuroprotective activity.

Keywords: Tandem-pore-domain potassium channel; TREK-1 channel; whole-cell patch-clamp recording; chiral 3-*n*-butylphthalide; membrane potential; neuroprotection

Acta Pharmacologica Sinica (2011) 32: 182–187; doi: 10.1038/aps.2010.210

Introduction

Two-pore-domain potassium (K2P) channels are a novel family of potassium channels with four transmembrane segments and two pore-forming domains located in tandem[1, 2]. These channels control neuronal excitability through their influence on resting membrane potential (RMP). Thus, they are classified as background potassium channels or leak potassium channels[3, 4]. To date, 17 human K2P channel subunits have been identified according to their amino acid sequence identity and regulatory mechanisms. They can be divided into six subfamilies: TWIK, THIK, TASK, TALK, TREK, and TRESK[5, 6].

TREK-1 is one of the most important members of the K2P channel family and is expressed throughout the central nervous system (CNS)[4, 7]. In addition to its unusual gating properties, such as background channel activity and sensitivity to membrane stretch, the TREK-1 channel can be modulated by many different intracellular and extracellular chemical agents. For example, TREK-1 is activated by increased temperature, membrane stretch and internal acidosis and is also sensitive to the presence of some polyunsaturated fatty acids [such as arachidonic acid (AA)] and gaseous general anesthetics (such as halothane and nitrous oxide)[8–11]. It has been recently reported that the TREK-1 channel is also modulated by neuroprotective agents such as riluzole and plays an important role in neuroprotection[12, 13]. In our previous studies, we showed that the expression of TREK-1 mRNA and protein significantly increased after acute and chronic cerebral ischemia, suggesting that the TREK-1 channel may be closely linked to pathological conditions such as cerebral ischemia[14, 15].

3-*n*-Butylphthalide (NBP) is a potent neuroprotectant that was approved by the State Food and Drug Administration (SFDA) of China at the end of 2002 as a new drug for the treatment of ischemic stroke[16]. Pre-clinical and clinical studies have demonstrated that racemic NBP (*dl*-NBP) is a promising drug for the treatment of ischemic stroke. This neuroprotectant influences several pathophysiological processes such as improving rat brain microcirculation, inhibiting platelet aggregation, preventing oxidative damage from ischemia and reducing

* To whom correspondence should be addressed.
E-mail wangxl@imm.ac.cn
Received 2010-07-01 Accepted 2010-11-23

neuronal apoptosis[17–21]. However, the molecular mechanisms underlying the actions of *dl*-NBP remain unclear. Recently, we have found that the optical isomer *l*-NBP is more potent in terms of neuronal protection against ischemic stroke than *dl*-NBP[16]. This study aimed to compare the effect of *dl*-NBP and its optical isomers on the TREK-1 channel and to further elucidate the mechanism of the protective effects of *l*-NBP against ischemia.

Materials and methods

Materials

l-NBP, *dl*-NBP, and *d*-NBP (purity >99%) (Figure 1A) were provided by the Department of Medical Synthetic Chemistry, Institute of Materia Medica. HEPES, EGTA, Na_2ATP, AA, penicillin G, and streptomycin sulfate were purchased from Sigma Chemical Co (St Louis, MO, USA); Dulbecco's modified Eagle's medium (DMEM), trypsin and G418 were purchased from GibcoBRL (Gaithersburg, MD, USA). Other reagents were provided by Beijing Chemical Company (Beijing, China).

Cell culture

A stable cell line of wild-type Chinese hamster ovary (Wt/CHO) cells expressing rat TREK-1 channels was maintained in culture medium (DMEM) supplemented with 10% (*v/v*) heat-inactivated fetal bovine serum, 100 μg/mL penicillin G and 100 μg/mL streptomycin sulfate in a humidified incubator with an atmosphere of 95% air and 5% CO_2 at 37 °C. G418 was added into the culture medium to select for transfected cells. When the cells were 80% confluent, they were split and plated onto 35-mm culture dishes. The cells were assayed 24 h later.

Electrophysiology and drug application

Membrane currents were recorded using a whole-cell voltage-clamp configuration. Recording glass pipettes had a resistance of 3–5 MΩ. The external solution contained the following (in mmol/L): NaCl, 150; KCl, 5.4; $MgCl_2$, 2; $CaCl_2$, 1.2; glucose, 15; and HEPES, 5 (titrated to pH 7.4 with NaOH). The patch-pipette solution contained the following (in mmol/L): KCl, 140; $MgCl_2$, 0.5; EGTA, 10; and HEPES, 10 (titrated to pH 7.2 with KOH). Currents were evoked in response to voltage ramps, and voltage steps were generated using an EPC-10 patch-clamp amplifier (HEKA Electronics, Lambrecht, Germany), filtered at 2.9 kHz, digitized at 10 kHz and stored on a computer. Data were analyzed using Pulse 8.6 software (HEKA Electronics, Lambrecht, Germany). Before seal formation, the voltage offset between the patch electrode and the bath solution was adjusted to produce zero current. After seal formation (≥1 GΩ) and membrane rupturing, the cells were allowed to stabilize for approximately 5 min. The holding potential during experiments was set at -80 mV. All electrophysiological measurements were carried out at room temperature (23–25 °C).

Data analysis and statistics

All data were analyzed using Pulsefit 8.6 (HEKA Electronics, Lambrecht, Germany) and MicroCal Origin software and are expressed as means±SEM. For dose-response experiments, current amplitudes at +60 mV in the presence and absence of NBP were measured by evoking the currents with a ramp pulse protocol from -80 mV to +60 mV over 400 ms. To obtain concentration-response curves, the percent inhibition of the current by NBP was quantified at various test concentrations according to the following equation: percent inhibition=100(1–$I_{drug}/I_{control}$). The current density of TREK-1 was calculated by dividing the current by the whole-cell capacitance (expressed in pA/pF). Significant differences between groups were assessed by unpaired Student's *t*-test and one-way analysis of variance (ANOVA). The criterion for significance was $P<0.05$ in all analyses. *n* values indicate the number of experiments performed.

Results

Electrophysiological properties of TREK-1 channels

Under the current-clamp configuration, the RMPs of Wt/CHO and TREK-1/CHO cells were -17.6±4.0 mV ($n=7$) and -55.3±2.4 mV ($n=25$), respectively (Figure 1B). A large, depolarizing voltage step from -80 mV to +80 mV evoked a dramatic, outward, non-inactivating current in TREK-1/CHO cells but not in Wt/CHO cells (Figure 1C). We also found that 10 μmol/L AA increased TREK-1 current by 60.0%±3.6% ($n=6$) (Figure 1Cc). These results are consistent with previous reports regarding the properties of TREK-1 channels[22].

Effect of NBP isomers on TREK-1 channel currents

To investigate whether *dl*-NBP isoforms modulate transfected TREK-1 channels, we exposed TREK-1/CHO cells to *dl*-NBP and its optical isomers after a 5-min control period and then washed out the drugs with the control solution. TREK-1 currents were evoked by a ramp protocol from a holding potential of -80 mV to +60 mV over 400 ms. A typical control current is shown in Figure 2A, and a comparison of the inhibitory effects of NBP isoforms at +60 mV is shown in Figure 2B ($P<0.05$). We found that 10 μmol/L of *l*-NBP, *dl*-NBP, and *d*-NBP inhibited the current by 70.0%±2.0% ($n=8$), 50.9%±4.8% ($n=9$) and 55.8%±3.4% ($n=9$), respectively. Current inhibition was not caused by rundown, which was less than 10% over a 20-min period. This result indicates that *l*-NBP is much more potent than *dl*- and *d*-NBP in the inhibition of TREK-1 currents. Therefore, we focused on *l*-NBP alone for the remainder of the study. The inhibitory effects of NBP isomers on TREK-1 currents were partially reversed upon washout.

l-NBP inhibited TREK-1 channel currents in a dose-dependent manner

We elicited TREK-1 currents with depolarizing voltage steps from a holding potential of -80 mV (Figure 3A). *l*-NBP-mediated inhibition of TREK-1 currents was partially reversed upon washout. This inhibition was concentration dependent over the range of 0.01 to 10 μmol/L. The maximum inhibition of TREK-1 current by *l*-NBP (70.0%±2.0%, $n=8$) was observed at a concentration of 10 μmol/L (Figure 3B). This dose-dependent response was well fitted to the Hill equation, with an IC_{50}

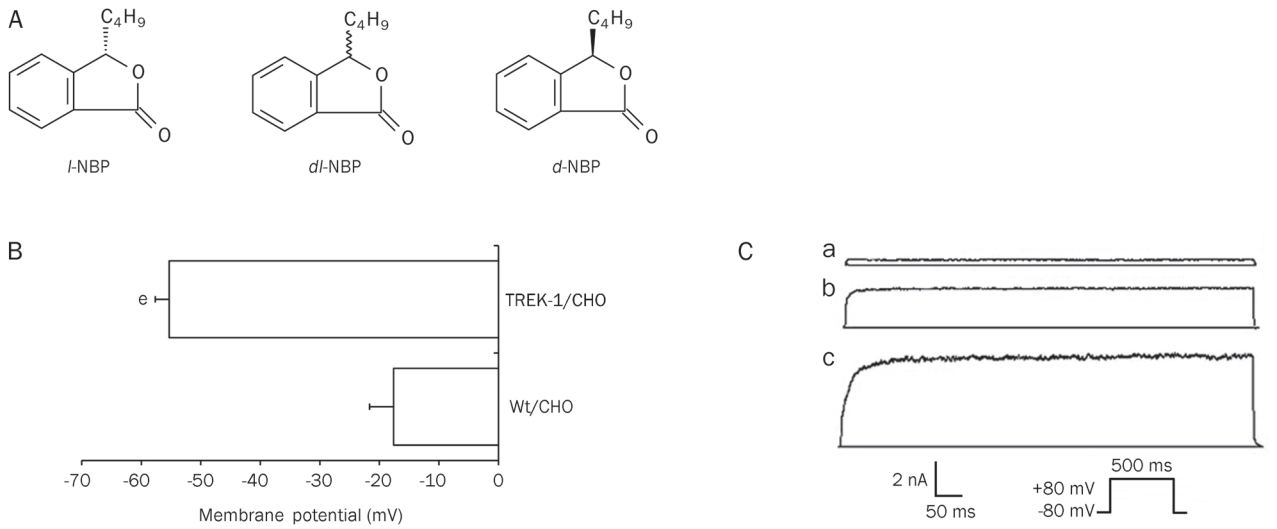

Figure 1. Chemical structures of NBP and basic properties of the TREK-1 channel. (A) Chemical structures of racemic *dl*-NBP and its optical isomers. (B) The transfection of CHO cells with TREK-1 channels hyperpolarized the membrane potential, from -17.6±4.0 mV (Wt/CHO, *n*=7) to -55.3±2.4 mV (TREK-1/CHO, *n*=25). Values are expressed as the mean±SEM; $^eP<0.05$ *vs* Wt/CHO cells. (C) Electrophysiological verification of the presence of TREK-1 channels in transfected CHO cells. a: Current elicited from Wt/CHO cells after being depolarized to +80 mV from a holding potential of -80 mV. b: Current elicited from TREK-1/CHO cells. c: Activation of TREK-1 currents by AA.

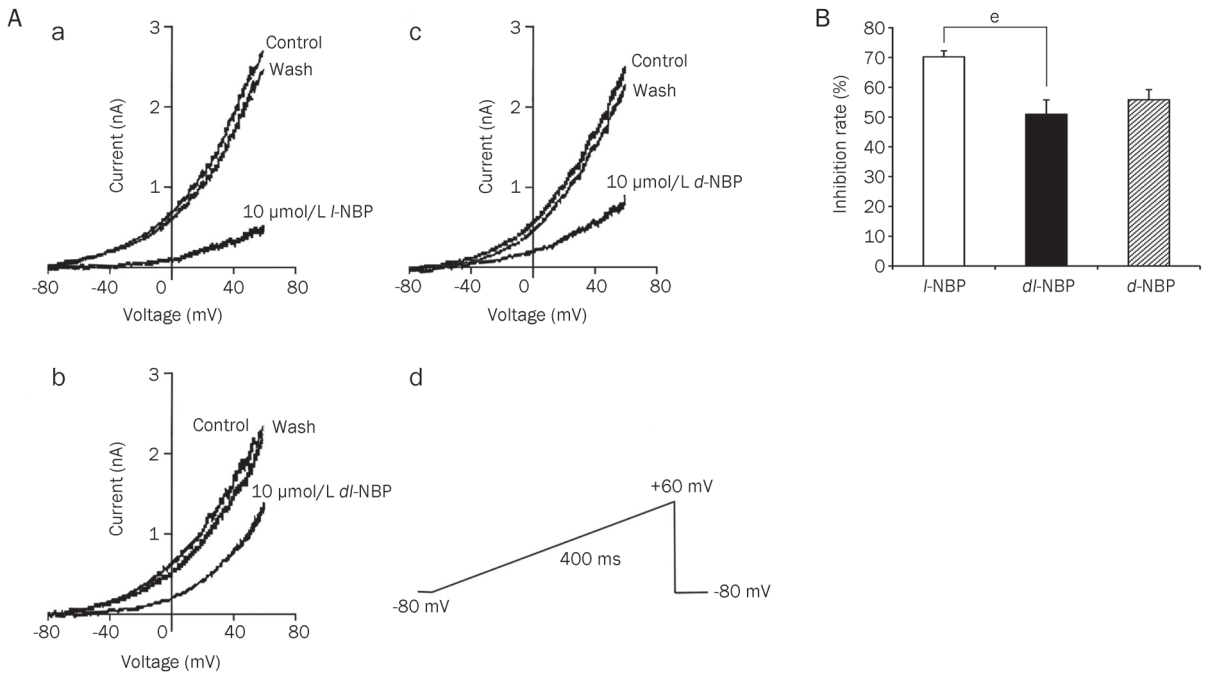

Figure 2. Effect of NBP isomers on TREK-1 channel currents. (A) Whole-cell ramp currents as a function of membrane potential before, during and after application of (a) 10 μmol/L *l*-NBP (*n*=8), (b) 10 μmol/L *dl*-NBP (*n*=9) and (c) 10 μmol/L *d*-NBP (*n*=9). (d) Whole-cell ramp current recording protocol. The currents were evoked from a holding potential of -80 mV by ramping the membrane potential from -80 mV to +60 mV over 400 ms. (B) Comparison of the inhibition rates of TREK-1 currents by NBP isoforms (*l*-NBP *n*=8, *dl*-NBP *n*=9 and *d*-NBP *n*=9) measured at +60 mV using TREK-1/CHO cells. The currents were evoked from a holding potential of -80 mV, and the membrane was ramped from -80 mV to +60 mV over 400 ms. Values are expressed as percentages of the control (means±SEM); $^eP<0.05$ *vs* *dl*-NBP group.

of 0.06±0.03 μmol/L and a Hill coefficient of 0.54±0.13. Figure 3C shows the current-voltage relationship (*I*–*V*) curve for the inhibition of TREK-1 channels by 0.3 μmol/L *l*-NBP. The inhibition was gradual and usually reached a peak 3–5 min after *l*-NBP exposure. Whole-cell current density was normalized to control currents, and the voltage dependence of the block-

ade by 10 μmol/L *l*-NBP was calculated (Figure 3D). The inhibition did not change substantially between -80 mV and +80 mV, indicating a lack of voltage dependence for the effect of *l*-NBP. This effect was partially reversed upon washout.

Effects of *l*-NBP on the membrane potential of TREK-1/CHO cells

Inhibition of TREK-1 channels has been reported to depolarize the cell membrane[7, 12]. Therefore, we compared the effects of *l*-NBP on the RMPs of Wt/CHO and TREK-1/CHO cells in current-clamp mode. The results show that 10 μmol/L *l*-NBP shifted the RMP from -55.3±2.4 mV to -42.9±2.1 mV (n=25, Figure 4, P<0.05) in TREK-1/CHO cells but not in Wt/CHO cells (n=7), confirming the role of this channel in the maintenance of the RMP.

Discussion

Two-pore-domain potassium channels form a novel class of K^+ channels identified in various types of neurons[23, 24]. They are open when membrane potentials are in the physiological range and are therefore likely to contribute to background or leak currents. They are also crucial in shaping neuronal excitability by regulating the RMP. The TREK-1 channel is an important member of the K2P family and is expressed throughout the CNS. The TREK-1 channel is voltage independent and is not inactivated[25].

TREK-1 has been previously reported to play an important role in neuroprotection against acid pathological conditions[4, 7, 12, 26]. In electrophysiological studies, some lipids substantially increase the probability of these K2P channels being open, thus hyperpolarizing the membrane potential and reducing neuronal excitability[12, 27–30]. This action on the part of lipids would be predicted to counteract the neuronal damage that arises from the increased membrane excitability that often accompanies CNS insults such as ischemia. A link between

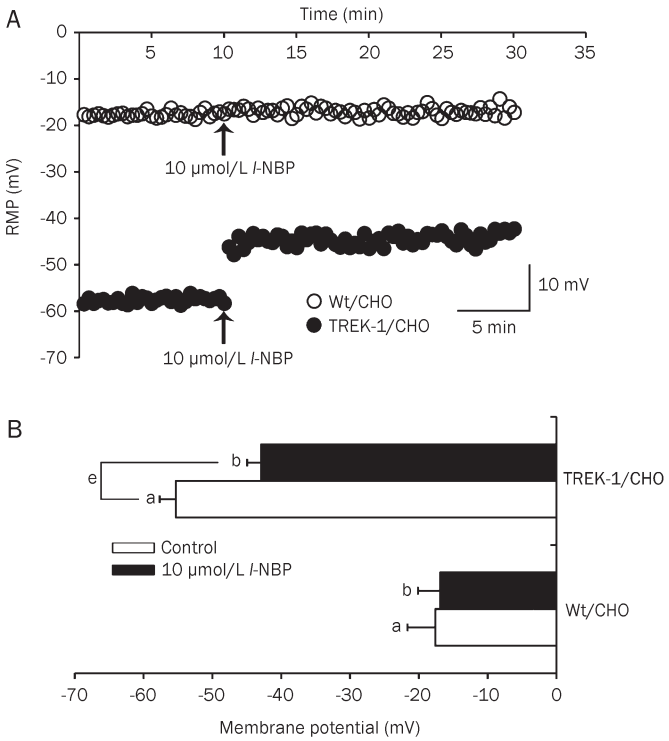

Figure 4. *l*-NBP depolarized the membrane potential of TREK-1/CHO cells but not Wt/CHO cells. (A) Effects of 10 μmol/L *l*-NBP on the RMPs of Wt/CHO cells and TREK-1/CHO cells. Under a current clamp, the RMPs of the two cell lines were measured similarly every 20 s for 30 min. The RMPs for control cells and cells treated with 10 μmol/L *l*-NBP were monitored at 10 and 20 min, respectively. (B) Summary the RMP changes in Wt/CHO and TREK-1/CHO cells before and after exposure to 10 μmol/L *l*-NBP. Bar a shows the control RMPs of Wt/CHO cells and TREK-1/CHO cells. The effects of 10 μmol/L *l*-NBP on the RMP of the two cell lines are shown in bar b. The results are presented in pA/pF as means±SEM (Wt/CHO, n=7; TREK-1/CHO, n=25); ^eP<0.05 *vs* control.

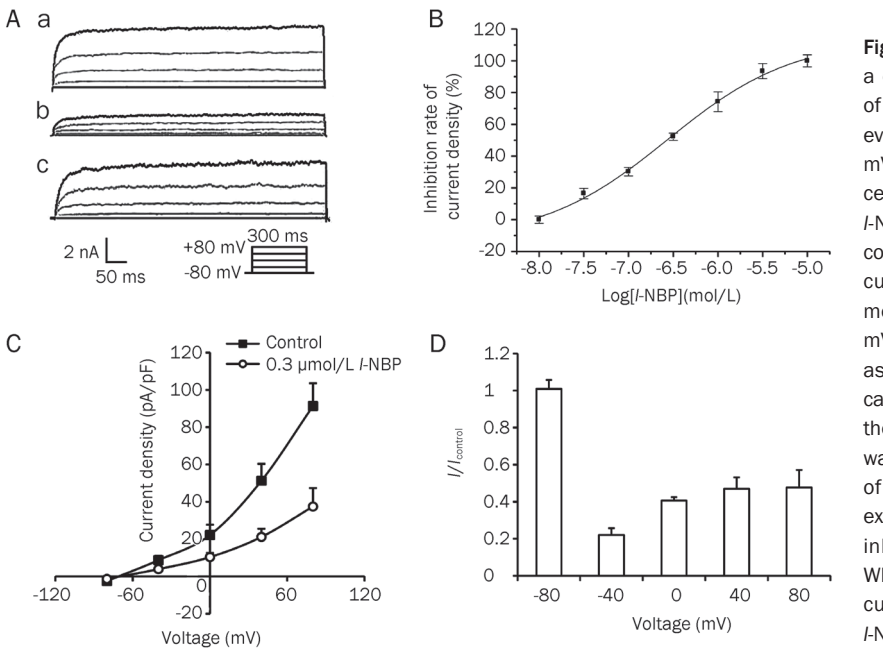

Figure 3. *l*-NBP inhibited TREK-1 channel currents in a concentration-dependent manner. (A) The inhibition of TREK-1 currents by *l*-NBP. Representative current evoked by 300-ms voltage pulses from -80 mV to +80 mV in 40 mV increments. (a) Currents in TREK-1/CHO cells. (b) Inhibition of TREK-1 currents by 10 μmol/L *l*-NBP. (c) The TREK-1 currents returned to near the control level after washout. (B) Concentration-response curve for the inhibition of TREK-1 channels by *l*-NBP measured at +80 mV from the holding potential -80 mV at the end of a 300-ms pulse. Data are expressed as means±SEM from at least six cells. The IC_{50} was calculated as 0.06±0.03 μmol/L. (C) The *I*–*V* curve for the inhibition of TREK-1 channels by 0.3 μmol/L *l*-NBP was measured at +80 mV from the holding potential of -80 mV at the end of a 300-ms pulse. Data are expressed as means±SEM. (D) Voltage-independent inhibition of TREK-1 currents by *l*-NBP (10 μmol/L). Whole-cell current densities were normalized to control currents ($I_{control}$). The normalized current density for *l*-NBP-treated cells did not change significantly.

TREK-1 and neuroprotection, although a highly attractive hypothesis, has not been unequivocally demonstrated, mainly due to the lack of selective K2P antagonists[13, 31].

In this study, we demonstrated that NBP, a neuroprotective agent, potently inhibited the TREK-1 channel expressed in CHO cells in a concentration-dependent manner. This study is the first description of the inhibition of TREK-1 by NBP, and this property may underlie its beneficial neuroprotective activity[31]. Moreover, the inhibition of TREK-1 currents by *l*-NBP was more significant than that by *d*- and *dl*-NBP. Therefore, the optical activity of NBP may have a close relationship with its biological activities.

Our data stand somewhat in contrast to the neuroprotection reported for TREK-1 facilitators, such as unsaturated fatty acids, riluzole and volatile anesthetics. Thus, although TREK-1 potentiation may be neuroprotective, our data also suggest that the inhibition of these channels may yield significant cell protection, similar to the effects of the neuroprotective agent sipatrigine on TREK-1 channels[31].

It is well known that K2P channels can modulate the RMP and that their activity may regulate cell excitability. K2P antagonism would produce depolarization and increased membrane excitability, which may induce or enhance neuronal damage. However, recent studies have shown that the regulation of K2P channels may be complex under pathological conditions[12, 32]. As reported by Meadows *et al*[31], TREK-1 antagonism produced greater changes in the excitability of inhibitory neurons than their excitatory counterparts. An increase in inhibitory tone could represent a neuroprotective mechanism. Furthermore, some immunohistochemical studies indicate that TREK-1 is predominantly expressed in GABAergic interneurons of the hippocampus, isocortex, thalamus and cerebellum[7, 28, 33, 34].

Decreasing glutamate release is a widely accepted neuroprotective strategy and is also a previously well-demonstrated activity of NBP[18, 31]. Thus, one potential mechanism of K2P inhibition-related neuroprotection would occur through an increase in glutamate uptake by astrocytes. It has been demonstrated that TREK-1 is expressed in astrocytes, and the activators of TREK-1, including arachidonic acid and chloroform, significantly attenuate glutamate uptake by astrocytes[35–37]. Therefore, *l*-NBP-mediated inhibition of TREK-1 channels may help to maintain or increase the function of glutamate uptake by astrocytes during brain ischemia. Furthermore, the TREK-1 channel is known to be an O_2-sensitive K^+ channel, and acute hypoxia can occlude its activation by AA and other activators[38, 39]. This finding suggests that TREK-1 may not be activated during systemic hypoxia (as occurs during cerebral ischemia). Therefore, it is difficult to explain the role of TREK-1 in neuroprotection. One possibility is that this property may depend on the expression pattern of TREK-1[31, 38, 40, 41]. Further investigation into the role of TREK-1 in neuronal damage/protection is needed.

In summary, this study demonstrated that NBP (and especially *l*-NBP), a novel neuroprotective agent, potently inhibits TREK-1 channels. The inhibition of TREK-1 channels results in the depolarization of the cell membrane. We suggest that the effects of NBP on TREK-1 channels are closely related to its neuroprotective role. TREK-1 channels may represent a target for NBP in treatment of cerebral ischemia and neurodegenerative diseases. However, the mechanism of protection of neurons via TREK-1 inhibition by NBP requires further study.

Acknowledgements

Our study was supported by the National Science Foundation of China (No 90913019) and a grant from the Ministry of Science and Technology of China (No 2009Zx09303-003).

We thank Dr Grilles Martin for expert technical and language assistance.

Author contribution

Xiao-liang WANG and Xin-cai JI designed the research; Xin-cai JI, Wan-hong ZHAO, Dong-xu CAO, and Qiao-qiao SHI performed the research; Xin-cai JI and Qiao-qiao SHI analyzed the data; Xin-cai JI and Xiao-liang WANG wrote the paper.

References

1 Fink M, Duprat F, Lesage F, Reyes R, Romey G, Heurteaux C, *et al*. Cloning, functional expression and brain localization of a novel unconventional outward rectifier K^+ channel. EMBO J 1996; 15: 6854–62.

2 Goldstein SA, Bockenhauer D, O'Kelly I, Zilberberg N. Potassium leak channels and the KCNK family of two-P-domain subunits. Nat Rev Neurosci 2001; 2: 175–84.

3 Patel AJ, Honore E. Properties and modulation of mammalian 2P domain K^+ channels. Trends Neurosci 2001; 24: 339–46.

4 Lesage F, Lazdunski M. Molecular and functional properties of two-pore-domain potassium channels. Am J Physiol Renal Physiol 2000; 279: F793–801.

5 Tsai SJ. Sipatrigine could have therapeutic potential for major depression and bipolar depression through antagonism of the two-pore-domain K^+ channel TREK-1. Med Hypotheses 2008; 70: 548–50.

6 Sano Y, Inamura K, Miyake A, Mochizuki S, Kitada C, Yokoi H, *et al*. A novel two-pore domain K^+ channel, TRESK, is localized in the spinal cord. J Biol Chem 2003; 278: 27406–12.

7 Heurteaux C, Guy N, Laigle C, Blondeau N, Duprat F, Mazzuca M, *et al*. TREK-1, a K^+ channel involved in neuroprotection and general anesthesia. EMBO J 2004; 23: 2684–95.

8 Honore E, Maingret F, Lazdunski M, Patel AJ. An intracellular proton sensor commands lipid- and mechano-gating of the K^+ channel TREK-1. EMBO J 2002; 21: 2968–76.

9 Maingret F, Honore E, Lazdunski M, Patel AJ. Molecular basis of the voltage-dependent gating of TREK-1, a mechano-sensitive K^+ channel. Biochem Biophys Res Commun 2002; 292: 339–46.

10 Maingret F, Lauritzen I, Patel AJ, Heurteaux C, Reyes R, Lesage F, *et al*. TREK-1 is a heat-activated background K^+ channel. EMBO J 2000; 19: 2483–91.

11 Patel AJ, Honore E, Lesage F, Fink M, Romey G, Lazdunski M. Inhalational anesthetics activate two-pore-domain background K^+ channels. Nat Neurosci 1999; 2: 422–6.

12 Honore E. The neuronal background K2P channels: focus on TREK1. Nat Rev Neurosci 2007; 8: 251–61.

13 Duprat F, Lesage F, Patel AJ, Fink M, Romey G, Lazdunski M. The neuroprotective agent riluzole activates the two P domain K^+ channels TREK-1 and TRAAK. Mol Pharmacol 2000; 57: 906–12.

14 Li ZB, Zhang HX, Li LL, Wang XL. Enhanced expressions of arachidonic acid-sensitive tandem-pore domain potassium channels in rat experimental acute cerebral ischemia. Biochem Biophys Res Commun 2005; 327: 1163–9.
15 Xu X, Pan Y, Wang X. Alterations in the expression of lipid and mechano-gated two-pore domain potassium channel genes in rat brain following chronic cerebral ischemia. Brain Res Mol Brain Res 2004; 120: 205–9.
16 Ma S, Xu S, Liu B, Li J, Feng N, Wang L, Wang X. Long-term treatment of *l*-3-*n*-butylphthalide attenuated neurodegenerative changes in aged rats. Naunyn Schmiedebergs Arch Pharmacol 2009; 379: 565–74.
17 Peng Y, Xing C, Lemere CA, Chen G, Wang L, Feng Y, *et al*. *l*-3-*n*-Butylphthalide ameliorates beta-amyloid-induced neuronal toxicity in cultured neuronal cells. Neurosci Lett 2008; 434: 224–9.
18 Peng Y, Zeng X, Feng Y, Wang X. Antiplatelet and antithrombotic activity of *L*-3-*n*-butylphthalide in rats. J Cardiovasc Pharmacol 2004; 43: 876–81.
19 Deng W, Feng Y. Effect of *dl*-3-*n*-butylphthalide on brain edema in rats subjected to focal cerebral ischemia. Chin Med Sci J 1997; 12: 102–6.
20 Dong GX, Feng YP. Effects of 3-*n*-butylphthalide on cortical calcineurin and calpain activities in focal cerebral ischemia rats. Yao Xue Xue Bao 2000; 35: 790–2.
21 Lin JF, Feng YP. Effect of *dl*-3-*n*-butylphthalide on delayed neuronal damage after focal cerebral ischemia and intrasynaptosomes calcium in rats. Yao Xue Xue Bao 1996; 31: 166–70.
22 Punke MA, Licher T, Pongs O, Friederich P. Inhibition of human TREK-1 channels by bupivacaine. Anesth Analg 2003; 96: 1665–73
23 Kim D. Physiology and pharmacology of two-pore domain potassium channels. Curr Pharm Des 2005; 11: 2717–36.
24 Gurney A, Manoury B. Two-pore potassium channels in the cardiovascular system. Eur Biophys J 2009; 38: 305–18.
25 Liu H, Enyeart JA, Enyeart JJ. Potent inhibition of native TREK-1 K^+ channels by selected dihydropyridine Ca^{2+} channel antagonists. J Pharmacol Exp Ther 2007; 323: 39–48.
26 Segal-Hayoun Y, Cohen A, Zilberberg N. Molecular mechanisms underlying membrane-potential-mediated regulation of neuronal K2P2.1 channels. Mol Cell Neurosci 2010; 43: 117–26.
27 Lauritzen I, Blondeau N, Heurteaux C, Widmann C, Romey G, Lazdunski M. Polyunsaturated fatty acids are potent neuroprotectors. EMBO J 2000; 19: 1784–93.
28 Talley EM, Solorzano G, Lei Q, Kim D, Bayliss DA. Cns distribution of members of the two-pore-domain (KCNK) potassium channel family. J Neurosci 2001; 21: 7491–505.
29 Maingret F, Patel AJ, Lesage F, Lazdunski M, Honore E. Lysophospholipids open the two-pore domain mechano-gated K^+ channels TREK-1 and TRAAK. J Biol Chem 2000; 275: 10128–33.
30 Heurteaux C, Laigle C, Blondeau N, Jarretou G, Lazdunski M. Alpha-linolenic acid and riluzole treatment confer cerebral protection and improve survival after focal brain ischemia. Neuroscience 2006; 137: 241–51.
31 Meadows HJ, Chapman CG, Duckworth DM, Kelsell RE, Murdock PR, Nasir S, *et al*. The neuroprotective agent sipatrigine (BW619C89) potently inhibits the human tandem pore-domain K^+ channels TREK-1 and TRAAK. Brain Res 2001; 892: 94–101.
32 Lawson K, McKay NG. Modulation of potassium channels as a therapeutic approach. Curr Pharm Des 2006; 12: 459–70.
33 Hervieu GJ, Cluderay JE, Gray CW, Green PJ, Ranson JL, Randall AD, *et al*. Distribution and expression of TREK-1, a two-pore-domain potassium channel, in the adult rat CNS. Neuroscience 2001; 103: 899–919.
34 Medhurst AD, Rennie G, Chapman CG, Meadows H, Duckworth MD, Kelsell RE, *et al*. Distribution analysis of human two pore domain potassium channels in tissues of the central nervous system and periphery. Brain Res Mol Brain Res 2001; 86: 101–14.
35 Zhou M, Xu G, Xie M, Zhang X, Schools GP, Ma L, *et al*. TWIK-1 and TREK-1 are potassium channels contributing significantly to astrocyte passive conductance in rat hippocampal slices. J Neurosci 2009; 29: 8551–64.
36 Seifert G, Huttmann K, Binder DK, Hartmann C, Wyczynski A, Neusch C, *et al*. Analysis of astroglial K^+ channel expression in the developing hippocampus reveals a predominant role of the Kir4.1 subunit. J Neurosci 2009; 29: 7474–88.
37 Volterra A, Trotti D, Racagni G. Glutamate uptake is inhibited by arachidonic acid and oxygen radicals via two distinct and additive mechanisms. Mol Pharmacol 1994; 46: 986–92.
38 Miller P, Kemp PJ, Lewis A, Chapman CG, Meadows HJ, Peers C. Acute hypoxia occludes hTREK-1 modulation: re-evaluation of the potential role of tandem P domain K^+ channels in central neuroprotection. J Physiol 2003; 548: 31–7.
39 Miller P, Peers C, Kemp PJ. Polymodal regulation of hTREK1 by pH, arachidonic acid, and hypoxia: physiological impact in acidosis and alkalosis. Am J Physiol Cell Physiol 2004; 286: C272–82.
40 Kemp PJ, Peers C, Lewis A, Miller P. Regulation of recombinant human brain tandem P domain K^+ channels by hypoxia: a role for O_2 in the control of neuronal excitability? J Cell Mol Med 2004; 8: 38–44.
41 Caley AJ, Gruss M, Franks NP. The effects of hypoxia on the modulation of human TREK-1 potassium channels. J Physiol 2005; 562: 205–12.

Acta Pharmacologica Sinica (2011) 32: 188–193
 1671-4083/11 $32.00
www.nature.com/aps

Original Article

High glucose stimulates TNFα and MCP-1 expression in rat microglia via ROS and NF-κB pathways

Yi QUAN[1, *], Chang-tao JIANG[1], Bing XUE[3], Shi-gong ZHU[1], Xian WANG[1, 2]

[1]Department of Physiology and Pathophysiology, School of Basic Medical Science; [2]Key Laboratory of Molecular Cardiovascular Science, Ministry of Education; [3]Neuroscience Research Institute and Department of Neurobiology, Key Laboratory for Neuroscience of the Ministry of Education, Peking University, Beijing 100191, China

Aim: To investigate whether high glucose stimulates the expression of inflammatory cytokines and the possible mechanisms involved.
Methods: ELISA and real-time PCR were used to determine the expression of the inflammatory factors, and a chemiluminescence assay was used to measure the production of reactive oxygen species (ROS).
Results: Compared to low glucose (10 mmol/L), treatment with high glucose (35 mmol/L) increased the secretion of tumor necrosis factor (TNF)α and monocyte chemotactic protein-1 (MCP-1), but not interleukin (IL)-1β and IL-6, in a time-dependent manner in primary cultured rat microglia. The mRNA expression of TNFα and MCP-1 also increased in response to high glucose. This upregulation was specific to high glucose because it was not observed in the osmotic control. High-glucose treatment stimulated the formation of ROS. Furthermore, treatment with the ROS scavenger NAC significantly reduced the high glucose-induced TNFα and MCP-1 secretion. In addition, the nuclear factor kappa B (NF-κB) inhibitors MG132 and PDTC completely blocked the high glucose-induced TNFα and MCP-1 secretion.
Conclusion: We found that high glucose induces TNFα and MCP-1 secretion as well as mRNA expression in rat microglia *in vitro*, and this effect is mediated by the ROS and NF-κB pathways.

Keywords: high glucose; microglia; tumor necrosis factor α; monocyte chemotactic protein-1; reactive oxygen species; NF-κB

Acta Pharmacologica Sinica (2011) 32: 188–193; doi: 10.1038/aps.2010.174

Introduction

Inflammation plays a key role in central nervous system diseases. As the immune cells in the brain, microglia play an important role in the pathogenesis of central nervous system. In 2000, using nonradioactive *in situ* hybridization, Gregersen reported that microglia were one of the major sources of TNF after the induction of stroke in mice[1]. Glutamate was released by the oxygen and glucose deprivation-stressed neuron-astrocyte cultures, and then activated microglia by mGluRIIs to produce and release tumor necrosis factor (TNF) α, which induced neurotoxicity in this stroke model[2]. These results show that cytokines, such as TNFα, released by microglia contribute to the development of neuronal damage during a stroke. Other studies have suggested that microglia might be involved in the pathogenesis of Parkinson's disease. In the mesencephalic neuron-glia cultures, extracellular aggregated human α-synuclein activated microglia, and the activation of microglia enhanced dopaminergic neurodegeneration[3]. A loss of α-synuclein expression altered the morphology and inflammatory response of microglia and impaired microglial phagocytic ability[4]. Increased TNFα production from amyloid β-stimulated microglia led to elevated iNOS in astrocytes and neuronal apoptosis, illustrating that an increase in microglia-derived TNFα in response to amyloid β may be a contributor to neuron loss in Alzheimer's disease[5]. Moreover, the suppression of microglial derived TNFα and interleukin (IL)-1β by copolymer-1 diminished neurodegeneration in HIV-1 encephalitis[6]. Thus, inflammation induced by activated microglia is one of the major contributors to the pathogenesis of brain related diseases.

Diabetes causes many complications, including retinopathy, nephropathy, and peripheral neuropathy. In addition, diabetes has a central nervous system complication, diabetic encephalopathy, which leads to direct neuronal damage[7, 8]. Apoptosis-induced neuronal loss and damage in type 1 diabetes is associated with cognitive impairment[9]. Although the mechanisms of neuronal apoptosis in diabetic encephalopathy have not been clearly studied, hyperglycemia is thought to be

* To whom correspondence should be addressed.
E-mail yquan226@gmail.com
Received 2010-06-01 Accepted 2010-09-04

one of the most important factors[10–12]. An increased level of glucose in the brain induced by hyperglycemia leads to neuronal apoptosis and impaired cognition[9, 12–15]. However, the effect of hyperglycemia on the activation of microglia and the role of inflammation in the pathogenesis of diabetic encephalopathy is still unclear. We previously reported that high glucose can activate microglia and significantly increase the secretion and mRNA expression of growth-regulated oncogene (GRO), a member of the IL-8 family, in rat microglia *in vitro*[16]. This finding suggests that in the central nervous system of patients with diabetes mellitus, high concentrations of glucose may induce microglial activation and the secretion of IL-8, thus contributing to the development of diabetic encephalopathy. In this study, we investigated the effect of high glucose on the inflammatory function of microglia. We found that compared with low glucose (10 mmol/L), high glucose (35 mmol/L) increased the secretion and mRNA expression of TNFα and monocyte chemoattract protein-1 (MCP-1) in rat microglia *in vitro*. Reactive oxygen species (ROS) and nuclear factor kappa B (NF-κB) pathways were involved in this process. However, there were no effects of high glucose on the secretion of IL-1β and IL-6.

Materials and methods

Reagents

The OX-42 antibody was purchased from Serotec (Oxford, UK). The MCP-1 antibody was purchased from Santa Cruz Biotechnology (Santa Cruz, CA, USA). The glial fibrillary acidic protein (GFAP) antibody was purchased from Zhongshan Goldenbridge Biotechnology (Beijing, China). Poly-*L*-lysine, *N*-acetyl-*L*-cysteine (NAC), MG132 and pyrrolidine dithiocarbamate (PDTC) were purchased from Sigma Chemical Co (St Louis, MO, USA). Culture medium RPMI-1640 was obtained from Hyclone (Logan, UT, USA). *D*-glucose was obtained from Beihua Fine Chemicals (Beijing, China). Mannitol was obtained from DCPC (Beijing, China). A TNFα ELISA kit was obtained from Jingmei Biotech Co (Beijing, China).

Rat microglia primary culture

The treatment of laboratory animals and experimental protocols adhered to the guidelines of the Health Science Center of Peking University and were approved by the Institutional Authority for Laboratory Animal Care. Rat microglial cells were isolated as previously described[16]. In brief, cortical tissue was carefully freed from the blood vessels and meninges, minced, mechanically agitated, and washed. Single cortical cells were cultured in RPMI-1640 containing 10% fetal bovine serum (Invitrogen, Karlsruhe, Germany), 2 mmol/L glutamine, 100 U/mL penicillin G sodium and 100 μg/mL streptomycin sulfate (medium was changed every 4 d). After 14 d, the microglia were separated from the underlying astrocytic monolayer by gentle agitation and spun down. The cell pellet was resuspended and plated on uncoated Costar culture dishes. Non-adherent cells were removed after 30–60 min by changing the medium, and the adherent microglia were incubated for 24 h in culture medium before use. The purity of the microglial cultures was assessed by fluorescence immunocytochemistry with antibodies against OX-42 (microglial marker) and GFAP (astrocyte marker). This procedure produced pure primary microglial cultures that were more than 95% microglia (data not shown).

Cytokine and chemokine secretion analysis

After being seeded for 24 h, the cells were stimulated with low glucose (LG; 10 mmol/L) or high glucose (HG; 35 mmol/L). The treatment was stopped at different times, and samples of the supernatants were collected and frozen at -40 °C. MCP-1 secreted into the medium was detected using ELISA, as previously described[16]. TNFα and IL-6 were measured with an enzyme-linked immunosorbent assay (ELISA) kit (Jingmei Biotech Co, Beijing, China). IL-1β was quantified with a commercial kit (R&D Systems, Minneapolis, MN, USA).

Real-time quantitative RT-PCR

Total RNA was isolated using RNAtrip from Applygene (Beijing, China) and converted into first-strand cDNA with AMV reverse transcriptase, 40 U/μL of RNase inhibitor and 500 ng/μL Oligo $(dT)_{15}$ primer (Promega, Madison, WI, USA). Real-time PCR was performed using 1–3 μL of the reverse transcription product, 0.5 μL HotStart Taq DNA Polymerase (TIANGEN, China), SYBR Green I (Molecular Probes, Eugene, OR, USA), 1 mmol/L dNTPs, and 0.2 μmol/L of each primer. Cycling conditions were 5 min at 95 °C, followed by 40 cycles of 30 s at 95 °C, 30 s at 58 °C, and 30 s at 72 °C, and a final incubation for 5 min at 72 °C. The primers for TNFα were 5′-TCC CAA CAA GGA GGA GAA GT-3′ and 5′-TGG TAT GAA GTG GCA AAT CG-3′. The primers for MCP-1 were 5′-GGC CTG TTG TTC ACA GTT GCT-3′ and 5′-TCT CAC TTG GTT CTG GTC CAG T-3′. The β-actin primers were 5′-GAG ACC TTC AAC ACC CCA GCC-3′ and 5′-TCG GGG CAT CGG AAC CGC TCA-3′. To assure the specificity of the primers, the amplicons underwent melting-curve analysis. Quantification of the PCR product was carried out using the relative quantification method. Results are expressed as arbitrary units and normalized against β-actin mRNA expression, as previously described[16].

Detection of reactive oxygen species

The production of ROS, especially H_2O_2, in rat microglia was detected with luminol plus horseradish peroxide-derived chemiluminescence in a light tight box using a luminescence analyzer (BPCL Ultra-weak, Beijing, China) at 37 °C[17, 18]. Photon counts were integrated over 1 s and digitized onto a computer monitor. Preparation of the reaction buffer was described previously[18]. Briefly, 10 mg/mL horseradish peroxide, 0.5 mmol/L luminol and HG or NG were dissolved in a total volume of 2 mL.

Statistical analyses

The results are expressed as means±SD. The differences between two groups were analyzed by Student's *t*-test. Multiple comparisons were made using a one-way ANOVA as

appropriate with Bonferroni *post-hoc* test. Statistical analysis was carried out using the Prism program from GraphPad Software.

Results

High glucose induces the inflammatory reaction of rat microglia

We used ELISA to examine the level of TNFα in the culture medium. Treatment with high glucose increased TNFα secretion from rat microglia in a time-dependent manner beginning at 6 h and continuing to 24 h. The final concentration was 2-fold higher than that observed in cells treated with low glucose (Figure 1A). Incubation with mannitol for 24 h had no effect on TNFα secretion (Figure 1B). These results demonstrate that the high glucose-induced TNFα secretion was not due to osmotic pressure.

The level of MCP-1 in the culture medium was also determined by ELISA. MCP-1 secretion from high glucose-treated rat microglia increased in a time-dependent manner, with a final 1.5-fold increase compared to treatment with low glucose (Figure 1C). Incubation with mannitol for 24 h had no effect on MCP-1 secretion (Figure 1D). However, treatment with high glucose for 24 h had no effect on either IL-1β or IL-6 (Figure 1E, 1F) secretion compared with low glucose.

High glucose elevates TNFα and MCP-1 mRNA expression

We also investigated whether high-glucose treatment could upregulate the mRNA expression of TNFα. Using real-time PCR, we found that high glucose treatment induced a 6-fold increase in TNFα mRNA expression after 1 h and a 3-fold increase after 3 h compared with low glucose (Figure 2A). However, there was no difference in TNFα mRNA expression between low glucose and high glucose treatment after 6 h. Similarly, the induction of TNFα mRNA by high glucose incubation was independent of hyperosmolality, since equimolar amounts of mannitol had no effect (Figure 2B).

Treatment with high glucose also induced MCP-1 mRNA expression in a time-dependent manner (Figure 2C). Rat microglia treated with high glucose for 3 h showed a 2-fold increase in MCP-1 mRNA expression compared to low glucose and an even higher increase after 6 h. Equimolar amounts of mannitol did not increase MCP-1 mRNA expression; thus, the high glucose-induced MCP-1 mRNA expression was also

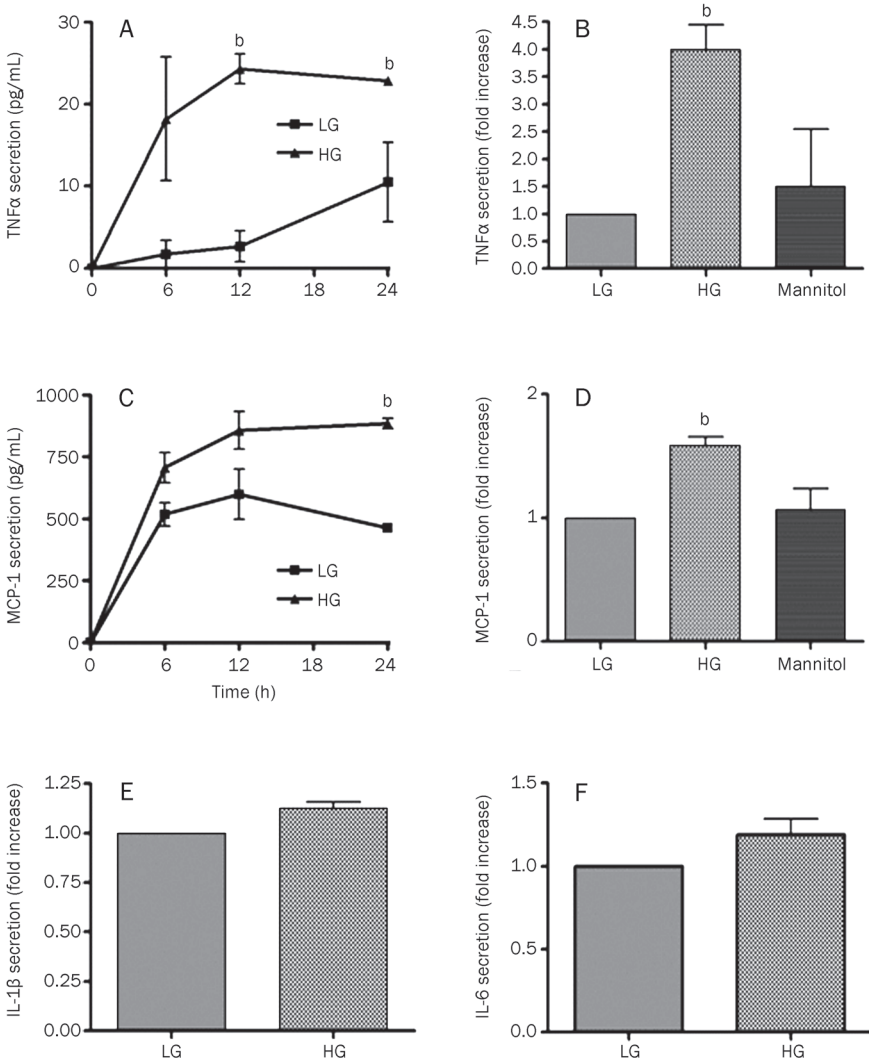

Figure 1. High glucose induces an inflammatory reaction in rat microglia. (A) Time course of TNFα secretion stimulated by high-glucose treatment. Rat microglia were cultured under low glucose (LG; 10 mmol/L) or high glucose (HG; 35 mmol/L), and the secretion of TNFα in the supernatant was measured with ELISA at the indicated time points. (B) The high-glucose treatment increased TNFα secretion independent of osmotic pressure. Rat microglia were cultured for 24 h in LG, HG, or mannitol (25 mmol/L+10 mmol/L glucose). (C) Time course of MCP-1 secretion stimulated by the high-glucose treatment. (D) The high-glucose treatment increased MCP-1 secretion independent of osmotic pressure. (E, F) High glucose had no effect on IL-1β and IL-6 secretion. The data represent the mean±SD of three independent experiments. $^{b}P<0.05$ *vs* LG.

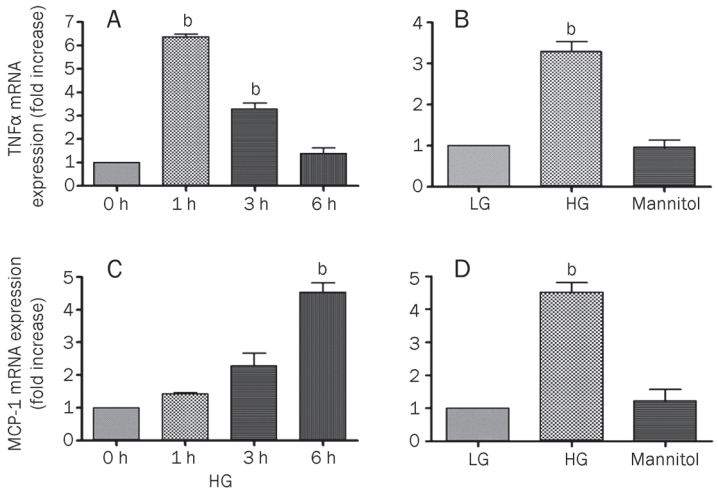

Figure 2. High-glucose treatment promotes the expression of TNFα and MCP-1 mRNA in rat microglia. (A) Real-time PCR analysis of the upregulation of TNFα mRNA by HG at different time points. $^{b}P<0.05$ *vs* 0 h. (B) Treatment with high glucose elevated TNFα mRNA independent of osmotic pressure. Rat microglia was treated with LG, HG or mannitol for 3 h. $^{b}P<0.05$ *vs* LG. (C) Real-time PCR analysis of the upregulation of MCP-1 mRNA by HG at different time points. $^{b}P<0.05$ *vs* 0 h. (D) Treatment with high glucose increased MCP-1 mRNA independent of osmotic pressure. Rat microglia was treated with LG, HG or mannitol for 6 h. The data represent the mean±SD of three individual experiments. $^{b}P<0.05$ *vs* LG.

independent of osmotic pressure (Figure 2D).

Reactive oxygen species are involved in high glucose-induced secretion of TNFα and MCP-1

The ROS pathway is one of the most important contributors to hyperglycemia-induced cell damage[19]. To examine whether high-glucose treatment induces ROS production in cultured rat microglia, we measured ROS levels using chemiluminescence. After incubation with low glucose and high glucose for 20 min, we observed ROS production. Compared with low glucose, high glucose stimulated the chemiluminescence photon production and the photon-signal peak for high glucose-treated cells occurred at 1500 s (Figure 3A). To detect the involvement of ROS in the TNFα and MCP-1 secretion induced by high glucose, we tested the effect of a non-specific ROS scavenger, NAC. Microglia were pretreated with 2 mmol/L NAC for 60 min and then exposed to high glucose treatment for 24 h. NAC significantly prevented the high glucose-induced secretion of TNFα and MCP-1 (Figure 3B, 3C), but NAC alone had no effect on TNFα and MCP-1 secretion.

NF-κB plays a key role in high glucose-induced TNFα and MCP-1 secretion from rat microglia

NF-κB is one of the most important transcription factors in the expression of inflammatory genes[20] and is associated with the gene expression of TNFα and MCP-1[20, 21]. High glucose incubation has been shown to significantly enhance NF-κB activation by increasing its DNA binding activity[16]. We investigated the role of NF-κB in high glucose-induced TNFα and IL-6 secretion at the transcriptional level. We pretreated rat microglia with the NF-κB inhibitors MG132 (10 μmol/L) or PDTC (5 μmol/L) for 60 min and then exposed them to low or high glucose for 24 h. Both MG132 and PDTC completely blocked the high glucose-induced TNFα and IL-6 secretion (Figure 4A and 4B), but neither had an effect on TNFα and IL-6 secretion alone.

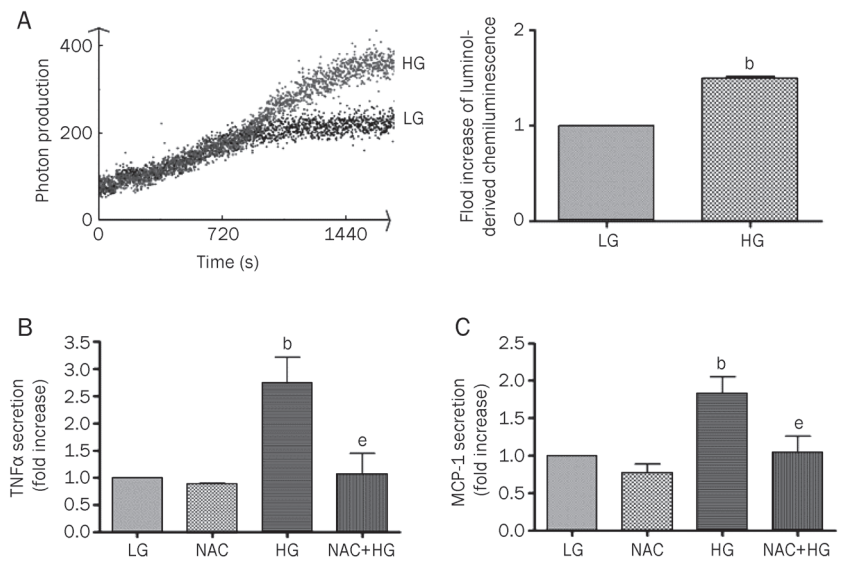

Figure 3. ROS play a key role in the high glucose-induced secretion of TNFα and MCP-1 in rat microglia. (A) Effect of LG and HG on cellular ROS level. Microglia was stimulated with LG and HG for 20 min followed by a luminol-derived chemiluminescent assay. Cellular ROS levels were quantified. (B) The role of ROS in high glucose-induced TNFα secretion. (C) The role of ROS in high glucose-induced MCP-1 secretion. After treatment with 2 mmol/L of the ROS scavenger NAC for 1 h, microglia was cultured in LG or HG for 24 h. The medium was collected and the levels of TNFα and MCP-1 were analyzed by ELISA. Data represent the mean±SD of three experiments. $^{b}P<0.05$ *vs* LG. $^{e}P<0.05$ *vs* HG.

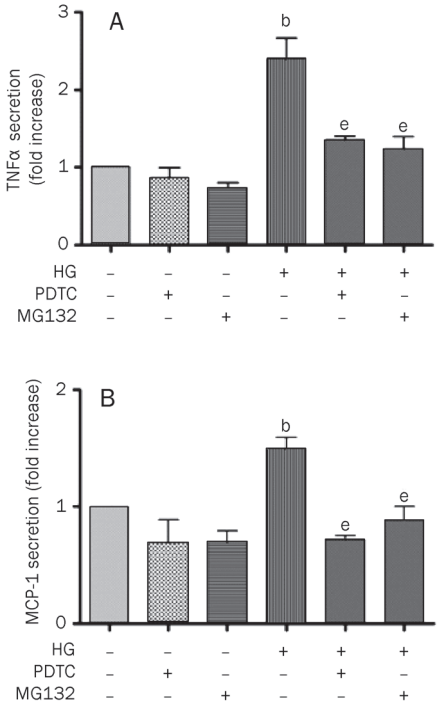

Figure 4. NF-κB is essential for high glucose-induced TNFα and MCP-1 secretion in rat microglia. After treatment with 10 μmol/L MG132 or 5 μmol/L PDTC for 1 h, microglia was cultured in LG or HG for 24 h. The medium was collected and the secretion of TNFα and MCP-1 was measured by ELISA. (A) Inhibition of the NF-κB pathway blocked high glucose-mediated TNFα secretion. (B) Inhibition of the NF-κB pathway blocked high glucose-mediated MCP-1 secretion. Data represent the mean±SD of three experiments. $^{b}P<0.05$ *vs* control. $^{e}P<0.05$ *vs* HG.

Discussion

We have shown that high glucose increases the secretion and mRNA expression of TNFα and MCP-1 in rat microglia. These effects are specific to high glucose rather than hyperosmolality. ROS and NF-κB pathways mediate the high glucose-induced secretion of TNFα and MCP-1. However, high glucose has no effect on the secretion of IL-1β and IL-6 compared to low glucose.

TNFα, a proinflammatory cytokine, is synthesized and released by microglia and can activate the caspase pathway, leading to neural apoptosis through the TNF receptor[22, 23]. It has been reported that fewer sympathetic and sensory neurons died during the phase of naturally occurring neuronal death in TNF-deficient embryos, and neurons from these embryos also survived in the culture better than wild-type neurons[24]. In addition to its role in apoptotic events, TNFα acts as a regulator of synaptic plasticity. Using TNFα knockout mice, Golan *et al* showed that TNFα may specifically suppress hippocampal function in adult mice through the suppression of NGF expression and dentate gyrus development[25]. MCP-1, one of the most important chemokines, plays a critical role in the migration of bone marrow derived and resident cells to sites of inflammation[26]. Huang *et al* found that MCP-1 null mice exhibited markedly reduced clinical and histological autoimmune encephalomyelitis (EAE) compared with wild-type animals. These results suggest that MCP-1 plays a crucial role in Th1 immune responses during EAE induction[27]. MCP-1 has been shown to inhibit HIV-tat and NMDA-induced apoptosis in mixed cultures of human neurons and astrocytes by reducing the extracellular levels of glutamate and regulating the intracellular trafficking of tat and NMDA receptor 1 expression in neurons. This finding suggests that MCP-1 may play a novel role as a protective agent against the toxic effects of glutamate and HIV-tat[28]. In the CNS of diabetic patients, high concentrations of glucose may induce microglial activation and the secretion of TNFα and MCP-1, thus contributing to the development of diabetic encephalopathy.

Oxidative injury induced by high glucose concentrations plays a central role in the pathogenesis of diabetic complications[29]. Recent observations suggest that hyperglycemia-triggered ROS contribute to the development of diabetic nephropathy[30, 31]. High glucose-induced ROS activated NF-κB and increased MCP-1 production, which may cause macrophage recruitment and activation, resulting in diabetic renal injury[32]. In addition, the formation of oxygen-derived radicals led to the activation of NF-κB, which increased the expression of vascular cell adhesion molecule 1 and MCP-1 in human aortic endothelial cells. Thus, ROS-mediated NF-κB activation may play a role in the onset of atherosclerosis in diabetic patients[33]. The involvement of ROS and NF-κB in high glucose-induced apoptosis has also been demonstrated in cultured human endothelial cells[34]. We found that treatment with a high concentration of glucose induced ROS formation and that the ROS scavenger NAC significantly reduced the high glucose-induced secretion of TNFα and MCP-1. Furthermore, the NF-κB inhibitors MG132 and PDTC completely prevented the high glucose-induced TNFα and MCP-1 secretion. Thus, ROS and NF-κB pathways mediate high glucose-induced secretion of TNFα and MCP-1 from rat microglia.

In conclusion, in our diabetic model, microglia are activated by high glucose treatment to produce ROS, which, in turn, activate the transcription factor NF-κB. Activation of NF-κB leads to the transcription of TNFα and MCP-1, resulting in an increased expression of TNFα and MCP-1. The release of inflammatory TNFα and MCP-1 by microglia may be involved in the pathogenesis of neuronal injury in diabetic encephalopathy. Overall, our study demonstrates that microglia might be a new target for the treatment of diabetic encephalopathy.

Acknowledgements

This study was supported by the Major National Basic Research Program of China (No 2006CB503802) and the Program for Changjiang Scholars and Innovative Research Team in Universities, as well as the National Natural Science Foundation of China (No 30330250) awarded to Xian WANG.

Author contribution

Most experiments were done by Yi QUAN and she also wrote the paper. Chang-tao JIANG, Bing XUE, and Shi-gong ZHU

did some of the experiments. Xian WANG and Yi QUAN designed the experiments together.

References

1 Gregersen R, Lambertsen K, Finsen B. Microglia and macrophages are the major source of tumor necrosis factor in permanent middle cerebral artery occlusion in mice. J Cereb Blood Flow Metab 2000; 20: 53–65.
2 Kaushal V, Schlichter LC. Mechanisms of microglia-mediated neurotoxicity in a new model of the stroke penumbra. J Neurosci 2008; 28: 2221–30.
3 Zhang W, Wang T, Pei Z, Miller DS, Wu X, Block ML, *et al*. Aggregated alpha-synuclein activates microglia: a process leading to disease progression in Parkinson's disease. Faseb J 2005; 19: 533–42.
4 Austin SA, Floden AM, Murphy EJ, Combs CK. Alpha-synuclein expression modulates microglial activation phenotype. J Neurosci 2006; 26: 10558–63.
5 Akama KT, Van Eldik LJ. Beta-amyloid stimulation of inducible nitric-oxide synthase in astrocytes is interleukin-1beta- and tumor necrosis factor-alpha (TNFalpha)-dependent, and involves a TNFalpha receptor-associated factor- and NFkappaB-inducing kinase-dependent signaling mechanism. J Biol Chem 2000; 275: 7918–24.
6 Gorantla S, Liu J, Sneller H, Dou H, Holguin A, Smith L, *et al*. Copolymer-1 induces adaptive immune anti-inflammatory glial and neuroprotective responses in a murine model of HIV-1 encephalitis. J Immunol 2007; 179: 4345–56.
7 Li ZG, Sima AA. C-peptide and central nervous system complications in diabetes. Exp Diabesity Res 2004; 5: 79–90.
8 Sima AA, Kamiya H, Li ZG. Insulin, C-peptide, hyperglycemia, and central nervous system complications in diabetes. Eur J Pharmacol 2004; 490: 187–97.
9 Li ZG, Zhang W, Grunberger G, Sima AA. Hippocampal neuronal apoptosis in type 1 diabetes. Brain Res 2002; 946: 221–31.
10 Ceriello A, Quatraro A, Giugliano D. Diabetes mellitus and hypertension: the possible role of hyperglycaemia through oxidative stress. Diabetologia 1993; 36: 265–6.
11 Sima AA. New insights into the metabolic and molecular basis for diabetic neuropathy. Cell Mol Life Sci 2003; 60: 2445–64.
12 Makimattila S, Malmberg-Ceder K, Hakkinen AM, Vuori K, Salonen O, Summanen P, *et al*. Brain metabolic alterations in patients with type 1 diabetes-hyperglycemia-induced injury. J Cereb Blood Flow Metab 2004; 24: 1393–9.
13 Knudsen GM, Jakobsen J, Barry DI, Compton AM, Tomlinson DR. Myo-inositol normalizes decreased sodium permeability of the blood-brain barrier in streptozotocin diabetes. Neuroscience 1989; 29: 773–7.
14 Sredy J, Sawicki DR, Notvest RR. Polyol pathway activity in nervous tissues of diabetic and galactose-fed rats: effect of dietary galactose withdrawal or tolrestat intervention therapy. J Diabet Complications 1991; 5: 42–7.
15 Li ZG, Zhang W, Sima AA. C-peptide enhances insulin-mediated cell growth and protection against high glucose-induced apoptosis in SH-SY5Y cells. Diabetes Metab Res Rev 2003; 19: 375–85.
16 Quan Y, Du J, Wang X. High glucose stimulates GRO secretion from rat microglia via ROS, PKC, and NF-kappaB pathways. J Neurosci Res 2007; 85: 3150–9.
17 Allen RC. Phagocytic leukocyte oxygenation activities and chemiluminescence: a kinetic approach to analysis. Methods Enzymol 1986; 133: 449–93.
18 Chang L, Xu J, Yu F, Zhao J, Tang X, Tang C. Taurine protected myocardial mitochondria injury induced by hyperhomocysteinemia in rats. Amino Acids 2004; 27: 37–48.
19 Rolo AP, Palmeira CM. Diabetes and mitochondrial function: role of hyperglycemia and oxidative stress. Toxicol Appl Pharmacol 2006; 212: 167–78.
20 Sun Z, Andersson R. NF-kappaB activation and inhibition: a review. Shock 2002; 18: 99–106.
21 Zeng X, Dai J, Remick DG, Wang X. Homocysteine mediated expression and secretion of monocyte chemoattractant protein-1 and interleukin-8 in human monocytes. Circ Res 2003; 93: 311–20.
22 Harry GJ, Lefebvre d'Hellencourt C, McPherson CA, Funk JA, Aoyama M, Wine RN. Tumor necrosis factor p55 and p75 receptors are involved in chemical-induced apoptosis of dentate granule neurons. J Neurochem 2008; 106: 281–98.
23 Bertazza L, Mocellin S. Tumor necrosis factor (TNF) biology and cell death. Front Biosci 2008; 13: 2736–43.
24 Barker V, Middleton G, Davey F, Davies AM. TNFalpha contributes to the death of NGF-dependent neurons during development. Nat Neurosci 2001; 4: 1194–8.
25 Golan H, Levav T, Mendelsohn A, Huleihel M. Involvement of tumor necrosis factor alpha in hippocampal development and function. Cereb Cortex 2004; 14: 97–105.
26 Baggiolini M. Chemokines and leukocyte traffic. Nature 1998; 392: 565–8.
27 Huang DR, Wang J, Kivisakk P, Rollins BJ, Ransohoff RM. Absence of monocyte chemoattractant protein 1 in mice leads to decreased local macrophage recruitment and antigen-specific T helper cell type 1 immune response in experimental autoimmune encephalomyelitis. J Exp Med 2001; 193: 713–26.
28 Eugenin EA, D'Aversa TG, Lopez L, Calderon TM, Berman JW. MCP-1 (CCL2) protects human neurons and astrocytes from NMDA or HIV-tat-induced apoptosis. J Neurochem 2003; 85: 1299–311.
29 Brownlee M. Biochemistry and molecular cell biology of diabetic complications. Nature 2001; 414: 813–20.
30 Ha H, Lee HB. Reactive oxygen species amplify glucose signalling in renal cells cultured under high glucose and in diabetic kidney. Nephrology (Carlton) 2005; 10: S7–10.
31 Ha H, Lee HB. Reactive oxygen species and matrix remodeling in diabetic kidney. J Am Soc Nephrol 2003; 14: S246–9.
32 Ha H, Yu MR, Choi YJ, Kitamura M, Lee HB. Role of high glucose-induced nuclear factor-kappaB activation in monocyte chemoattractant protein-1 expression by mesangial cells. J Am Soc Nephrol 2002; 13: 894–902.
33 Piga R, Naito Y, Kokura S, Handa O, Yoshikawa T. Short-term high glucose exposure induces monocyte-endothelial cells adhesion and transmigration by increasing VCAM-1 and MCP-1 expression in human aortic endothelial cells. Atherosclerosis 2007; 193: 328–34.
34 Sheu ML, Ho FM, Yang RS, Chao KF, Lin WW, Lin-Shiau SY, *et al*. High glucose induces human endothelial cell apoptosis through a phosphoinositide 3-kinase-regulated cyclooxygenase-2 pathway. Arterioscler Thromb Vasc Biol 2005; 25: 539–45.

Acta Pharmacologica Sinica (2011) 32: 194–200
 1671-4083/11 $32.00
www.nature.com/aps

Original Article

Role of vascular K_{ATP} channels in blood pressure variability after sinoaortic denervation in rats

Zhong-wei YANG[1, #], Dong-jie LI[1, #], Chong LIU[1], Ping HAN[1], Yi-li YANG[2], Ding-feng SU[1], Fu-ming SHEN[1, *]

[1]*Department of Pharmacology, School of Pharmacy, Second Military Medical University, Shanghai 200433, China;* [2]*Cancer and Developmental Biology Laboratory, National Cancer Institute, National Institutes of Health, Frederick, MD 21702, USA*

Aim: To investigate the role of ATP-sensitive potassium (K_{ATP}) channels on blood pressure variability (BPV) in sinoaortic denervated (SAD) rats.

Methods: SAD was performed on male Sprague-Dawley rats 4 weeks before the study. mRNA expression of Kir6.1, Kir6.2 and SUR2 in aorta and mesenteric artery was determined using real-time quantitative polymerase chain reaction, and confirmed at the protein level using Western blotting and laser confocal immunofluorescence assays. Concentration-response curves of isolated aortic and mesenteric arterial rings to adenosine and pinacidil were established. Effects of K_{ATP} channel openers and blocker on BPV were examined in conscious SAD rats.

Results: Aortic SUR2 expression was significantly greater, while Kir6.1 was lower, in SAD rats than in sham-operated controls. In contrast, in the mesenteric artery both SUR2 and Kir6.1 expression were markedly lower in SAD rats than controls. For both arteries, Kir6.2 expression was indistinguishable between sham-operated and SAD rats. These findings were confirmed at the protein level. Responses of the aorta to both adenosine and pinacidil were enhanced after SAD, while the mesenteric response to adenosine was attenuated. Pinacidil, diazoxide, nicorandil, and glibenclamide significantly decreased BPV.

Conclusion: These findings indicate that expression of vascular K_{ATP} channels is altered by chronic SAD. These alterations influence vascular reactivity, and may play a role in the increased BPV in chronic SAD rats.

Keywords: ATP-sensitive potassium channels; blood pressure variability; sinoaotic denervation

Acta Pharmacologica Sinica (2011) 32: 194–200; doi: 10.1038/aps.2010.195

Introduction

Sinoaortic denervation (SAD), referring to removal of the carotid sinus and aortic arch baroreceptors[1], results in baroreflex failure bringing about increase in blood pressure variability (BPV) with 24 h mean blood pressure level unchanged or only slightly increased[2, 3]. It has been demonstrated that BPV was correlated with target-organ damage independent of mean blood pressure levels in hypertensive subjectives[4]. More recently the importance of BPV in prediction of risk of vascular events and in accounting for benefits of antihypertensive drugs, especially in prevention of stroke, was emphasized[5–7]. Multiple studies have investigated the roles of resting vascular tone changes, arterial pressure levels, the sympathetic nervous system, and vasoactive substances in the increased BPV after SAD[3, 8–14]. However, the definite mechanism by which BPV dramatically increase after SAD surgery is still unclear.

ATP-sensitive potassium (K_{ATP}) channels are critical regulators of vascular tone, forming a focal point for signaling by many vasoactive transmitters, including adenosine, calcitonin gene-related peptide, noradrenaline, insulin, prostaglandin E_1, and arginine vasopressin[15–19]. It is therefore a molecular sensor, responding to local metabolic need and vasoactive transmitters, altering smooth muscle contractility and so blood flow to retain homeostasis[20–22]. If expression of vascular K_{ATP} channels was altered in different blood vessels after SAD surgery, response of K_{ATP} channels to vasoactive transmitters would be altered too, which might influence vascular tone and contribute to the increased BPV. Previous studies suggested that persistent high BPV following SAD led to pathological changes, the aorta was most sensitive to increased BPV[23], and BPV was mostly determined by resistance vessels[8, 9, 11]. In this study, we compared the channel expression in aorta and mesenteric artery of sham-operated and SAD rats to demonstrate our hypothesis that expression of vascular K_{ATP} channels was

# These authors contributed equally to this work.
* To whom correspondence should be addressed.
E-mail fumingshen@126.com
Received 2010-06-23 Accepted 2010-10-13

altered after SAD surgery. We also examined the effects of K_{ATP} channel openers or blocker to assess the role of K_{ATP} channels in BPV in chronic SAD rats.

Materials and methods

Animals and drugs

Rats were purchased from the Sino-British SIPPR/BK Lab (Shanghai, China), housed in controlled conditions (temperature: 21±2 °C and lighting: 8:00–20:00) and received a standard rat chow and tap water *ad libitum*. All surgical and experimental procedures were in accordance with institutional animal care guidelines.

Pinacidil, diazoxide, nicorandil, glibenclamide, phenylephrine and adenosine were purchased from Sigma Chemical Co (St Louis, MO, USA).

Sinoaortic denervation

Sinoaortic denervation (SAD) was performed according to the previously described method[1, 12]. Briefly, rats were anaesthetized with a combination of ketamine (50 mg/kg, ip) and diazepam (5 mg/kg, ip) and medicated with atropine sulfate (0.5 mg/kg, ip) and procaine benzylpenicillin (60 000 U, im). After a midline neck incision and bilateral isolation of the neck muscles, aortic arch baroreceptor denervation was carried out bilaterally by cutting the superior laryngeal nerves near the vagi, removing the superior cervical ganglia, including a small section of the sympathetic trunk, and sectioning the aortic depressor nerves. The carotid sinus baroreceptors were denervated bilaterally by stripping the carotid bifurcation and its branches, followed by the application of 10% phenol (in 95% ethanol) to the external, internal and common carotid arteries and the occipital artery. The sham operation included the midline neck incision and bilateral isolation of the neck muscles. Animals were allowed to recover spontaneously after surgery. The completeness of SAD was assessed by intravenous injection of phenylephrine (2–5 μg/kg) via the left femoral vein. If a 50 mmHg pressor response to phenylephrine was associated with a bradycardia less than 20 beats/min, the SAD was considered complete. Sham-operated animals exhibited a bradycardia of 60–100 beats/min in response to phenylephrine.

Tissue preparation

Four weeks after SAD or sham-operation, rats were anaesthetized with sodium pentobarbitone (50 mg/kg, ip) and killed by exsanguination. Care was taken to ensure that comparable arteries were examined from sham-operated and SAD rats. The thoracic aorta was carefully dissected from surrounding fat and connective tissue. The mesenteric artery was removed from each rat, and the superior mesenteric artery was located and cleaned of connective tissue until the sixth branch leading to the gut wall was exposed.

Real-time quantitive polymerase chain reaction

Total RNA was extracted from aorta (7 aortas from 7 rats, n=7 for both sham-operated and SAD groups) and mesenteric artery (including the superior mesenteric artery itself until the sixth branch: 21 rats were used per group but 3 arteries were pooled as one sample so that n=7 for both groups) using the TRIzol method (Invitrogen, Carlsbad, CA, USA). With the use of 2 μg total RNA, first strand of cDNA was synthesized by the M-MLV enzyme in a 25 μL reaction mixture (Promega, Madison, WI, USA). With the use of aliquots (2 μL) of reverse transcriptase products, real-time quantitative PCR was performed in a final volume of 20 μL using the gene-specific primers listed in Table 1. Amplification was processed as: 95 °C, 10 s, 1 cycle; 95 °C, 5 s and 60 °C, 20 s for 40 cycles; then melt curve. Gene transcripts were quantified with SYBR Premix Ex Taq Kit (Takara, Otsu, Japan). Data were calculated by the $2^{-\Delta\Delta CT}$ method, and presented as fold change of transcripts for Kir6.1, Kir6.2, and SUR gene in aortas and mesenteric arteries of SAD rats compared with sham-operated group (defined as 1.0-fold). Rat β-actin was used as an internal control. The relative expression of the target gene was normalized to the β-actin level.

Table 1. Nucleotide sequences of primers used for real-time PCR and expected size of the real-time PCR product.

mRNA	Expected Size	Primer sequence (5′→3′)	Accession
Kir6.1	182 bp	Forward-TCTGCCGTCTGTGTGACCAAT Reverse-ATGCAGCCCAACATGACCG	NM 017099
Kir6.2	118 bp	Forward-TCGCCCATGTTAATAGTCCCTAC Reverse-CGATCACGACGGTTGACATTTA	NM 031358
SUR2	129 bp	Forward-GCCCTCACGATAACCAATTACCT Reverse-CATGGTGCCTTCATAGTTCTCAGA	NM 013040
β-actin	113 bp	Forward-AGACCTCATTGCCAACACAGTGC Reverse-GAGCCACCAATCACACACAGAGT	NM 031144

A primer pair specific for β-actin served as efficiency control for RNA isolation.

Western blotting

Protein level of Kir6.1, Kir6.2, and SUR2 of both aorta (6 rats were used per group but 2 aortas were pooled as one sample so that n=3 for both groups) and mesenteric artery (including the superior mesenteric artery itself until the sixth branch: 15 rats were used per group but 5 arteries were pooled as one sample so that n=3 for both group) from sham-operated and SAD rats were determined. Tissues were washed with ice-cold phosphate-buffered saline (PBS), and then homogenized with ice-cold lysis buffer (20 mmol/L Tris-HCl, pH 7.4, 2.5 mmol/L EDTA, 1% Triton X-100, 10% glycerol, and 1 mmol/L PMSF, 1 mmol/L DTT, 10 mg/mL leupeptin), and the supernatant was obtained by centrifugation at 11 000×g for 15 min at 4 °C. Samples were separated on 8% SDS-PAGE gels, transferred to a polyvinylidene difluoride (PVDF) membrane, and blocked by 3 h incubation at 25 °C in TBST (Tris-buffered saline with 0.1% Tween 20, pH 7.4) plus 10% skimmed milk powder. The PVDF membrane was incubated overnight at 4 °C with pri-

mary antibodies for Kir6.1 (1:200; Alomone Labs Ltd, Jerusalem, Israel), Kir6.2 (1:200; Alomone Labs Ltd) or SUR2 (1:200; Santa Cruz, CA, USA). PVDF membranes were washed for 10 min 3 times with TBST and incubated with secondary antibodies conjugated with horseradish peroxidase. The bound antibody was visualized on Kodak Biomax film (Eastman Kodak, Rochester, NY, USA) using a Pierce Supersignal substrate chemiluminescence detection kit. Results from these analyses were quantified through densitometry.

Confocal imaging

Frozen sections (4–8 μm) of both aortas and superior mesenteric arteries were blocked in 3% normal goat serum/0.3% Triton X-100/0.1% Bovine serum albumin (BSA) in PBS (room temperature for 1 h), followed by incubation with either rabbit anti-kir6.1 (1:100), rabbit anti-Kir6.2 (1:100), or goat anti-SUR2 (1:200) at 4 °C overnight. Subsequently, the sections were incubated with the affinity-purified second antibody, goat anti-rabbit or rabbit anti-goat fluorescein isothiocyanate (FITC) antibody (1:200; Sigma Chemical Co, St Louis, MO, USA). Sections were then rinsed, dried, and coverslipped with Dako fluorescence mounting medium. Laser scanning confocal microscopy was performed with the use of a Leica TCS SP2 system (Leica, Wetzlar, Germany). The objective was ×20. FITC was excited at 488 nm and emission was detected at 500–600 nm. The imagines were analyzed with Leica Confocal software.

Vascular reactivity

To determine if vascular reactivity to adenosine (an endogenous vasoactive substance, relaxing vascular smooth muscle cells by opening K_{ATP} channels[20]) and pinacidil (a nonselective opener of K_{ATP} channels) was altered in chronic SAD rats. 5 mm long thoracic aortic rings (17–21 aortic rings obtained from 11 rats for both the sham and SAD groups) or superior mesenteric arterial rings (12 superior mesenteric arterial rings from 9 rats for both the sham and SAD groups) were prepared for assessment of vascular reactivity (IOX software, EMKA Technology, Inc., Paris, France). Resting tension was 2.5 g or 0.8 g respectively, and contraction was induced by phenylephrine (3×10^{-7} mol/L). The relaxant effects of adenosine (10^{-7} to 3×10^{-4} mol/L) and pinacidil (10^{-8} to 3×10^{-5} mol/L for aorta, 10^{-8} to 3×10^{-6} mol/L for superior mesenteric artery) were assessed.

Blood pressure measurement

To assess the role of K_{ATP} channels in BPV in chronic SAD rats, the effects of K_{ATP} channel openers or blocker on BPV were examined 4 weeks after the surgery. Four groups (n=8–10 for each group) were designed: 1) pinacidil, 2 mg/kg; 2) diazoxide, 20 mg/kg; 3) nicorandil, 10 mg/kg; 4) glibenclamide, 20 mg/kg. Blood pressure was recorded by a computerized system (MPA 2000M, Alcott Biotech Co LTD, Shanghai, China) using a previously described method[12]. Two 60-min sampling periods were programmed. Before the beginning of first period, isotonic saline was administered intravenously in a volume of 3 mL/kg over a 5-min period. After a 15-min equilibration period, arterial pressure was then recorded for 60-min. Before the beginning of the second period, one of the drug treatments listed above was given as a 5-min infusion, and after a 15-min equilibration period data were recorded for 60-min. The final 30-min of each 60-min period was used for analysis. Systolic and diastolic BP and heart period were averaged beat-to-beat during the 30-min test period. BPV was defined as the standard deviation of beat-to-beat systolic or diastolic BP over the 30-min analysis period.

Statistical analyses

Data are presented as mean±SEM. Differences in both mRNA and protein between sham-operated and SAD group were analyzed using Student's un-paired t-test. Differences in vascular reactivity between sham-operated and SAD group were analyzed by repeated measures analysis of variance. Changes of BPV, BP and heart period before and after drug infusion were analyzed by paired t-tests. Two-tailed $P<0.05$ was considered statistically significant.

Results

Presence of Kir6.1, Kir6.2, and SUR2

SUR2 mRNA expression was significantly greater in the aorta of SAD rats (1.67±0.370) compared with controls (1.00±0.084; n=7, $P<0.05$). In contrast, aortic Kir6.1 mRNA expression was lower in SAD rats than controls (0.67±0.052 *vs* 1.00±0.095, n=7, $P<0.05$). In the mesenteric artery both SUR2 (0.45±0.084 *vs* 1.00±0.141, n=7, $P<0.05$) and Kir6.1 expression (0.76±0.047 *vs* 1.00±0.049, n=7, $P<0.05$) were lower in SAD rats than in controls. No significant differences were observed in Kir6.2 expression between sham-operated and SAD rats for both kinds of arteries. Results of protein analysis by Western blotting were in agreement with the mRNA expression (Figure 1). Confocal imaging using fluorescence-labeled antibodies to Kir6.1, Kir6.2 and SUR2 localized these proteins in both kinds of arteries, as predicted by the western blot results (Figure 2). These results demonstrate that in chronic SAD rats K_{ATP} channels are altered when compared with the controls, that is, expression of both Kir6.1 and SUR2 are significantly reduced in mesenteric artery; decrease in Kir6.1 expression accompanied with increase in SUR2 expression is found in aorta.

Vasodilatation induced by adenosine and pinacidil

In phenylephrine-contracted, endothelium-intact aortic rings, both adenosine and pinacidil induced concentration-dependent relaxation. Compared to the sham-operated group, the relaxation response of the aorta to both adenosine and pinacidil was significantly enhanced in SAD rats (Figure 3A and 3B); the relaxation response of the mesenteric artery to adenosine was obviously attenuated (Figure 3C). However, pinacidil did not induce relaxation differences between the sham operated and SAD group. These data suggest that vasodilatation by opening K_{ATP} channels may depend on the level SUR2 expression.

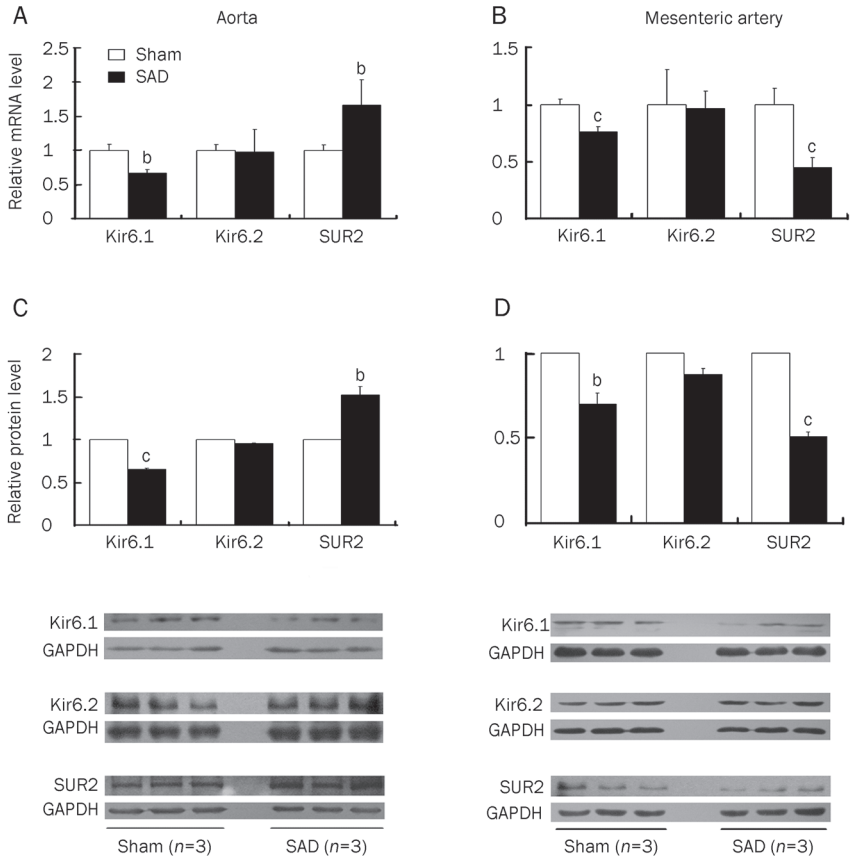

Figure 1. Expression of Kir6.1, Kir6.2 and SUR2 in both aorta and mesenteric artery in sinoaortic denervated and sham-operated rats. A and B, fold changes of mRNA level (Kir6.1, Kir6.2, and SUR2) in aorta and mesenteric artery (n=7). C and D, fold changes of protein level (Kir6.1, Kir6.2, and SUR2) in aorta and mesenteric artery (n=3). The representative images are from three independent experiments. Data are expressed as mean±SEM. $^bP<0.05$, $^cP<0.01$ *vs* sham-operated rats by unpaired Student's *t*-test.

Blood pressure induced by K_{ATP} channel openers and blocker

Table 2 summarizes the effects of pinacidil, diazoxide, nicorandil, and glibenclamide on systolic and diastolic BP and heart period in SAD rats. The K_{ATP} channel openers, pinacidil, diazoxide and nicorandil, significantly decreased systolic and diastolic BP, and slightly but significantly shortened heart period. The K_{ATP} channel blocker, glibenclamide, significantly increased BP but did not obviously alter heart period.

Table 2. Effects of K_{ATP} channel openers and blocker on SBP, DBP, and HP in sinoaortic denervated (SAD) rats. Values are expressed as mean±SEM. $^bP<0.05$, $^cP<0.01$ *vs* isotonic saline by paired *t*-test.

Groups	*n*	SBP (mmHg)	DBP (mmHg)	HP (ms)
Isotonic saline	10	151±4.3	105±3.5	139±4.6
Pinacidil	10	94±2.8^c	58±3.1^c	127±4.1^c
Isotonic saline	8	137±5.3	98±2.3	149±4.4
Diazoxide	8	90±2.8^c	57±2.5^c	135±2.9^b
Isotonic saline	8	146±3.2	104±3.6	145±5.3
Nicorandil	8	89±5.7^c	60±3.9^c	128±3.6^c
Isotonic saline	10	149±4.1	101±3.1	145±3.6
Glibenclamide	10	160±3.8^c	112±3.4^b	146±2.3

SBP, DBP, and HP are the average values of these parameters obtained beat by beat during the 30-min test period. *n*, number of rats; SBP, systolic BP; DBP, diastolic BP; HP, heart period.

Blood pressure variability induced by K_{ATP} channel openers and blocker

The effects of the different K_{ATP} channel openers and blocker on BPV in SAD rats are shown in Figure 4. Pinacidil and diazoxide reduced SBPV by 40%±4.9% or 34%±6.1%, and DBPV by 40%±5.4% or 38%±6.8% (Figure 4A and 4B). Nicorandil had a similar effect, reducing SBPV by 45%±5.3% and DBPV by 45%±4.7% (Figure 4C). The K_{ATP} channel blocker glibenclamide also significantly decreased SBPV by 35%±7.0% and DBPV by 38%±8.3% (Figure 4D), despite the fact that this agent increased resting BP whereas pinacidil, diazoxide and nicorandil reduced it (Table 2). These results that either opening or blocking K_{ATP} channels reduced BPV suggest that K_{ATP} channels play a role in the increased BPV in chronic SAD rats.

Discussion

The current study provides two new findings. Firstly, we demonstrate that expression of vascular K_{ATP} channels is altered by chronic SAD. The SUR2 subunit was upregulated in the aorta but downregulated in the mesenteric artery. Consistent with this finding, vasodilator responses to K_{ATP} channel opener pinacidil were enhanced in the aorta of SAD rats but blunted in the mesenteric artery. Thus, chronic SAD results in changes in the expression and function of K_{ATP} channels that differ according to vascular territory. Our second major finding was that either opening or blocking K_{ATP} channels

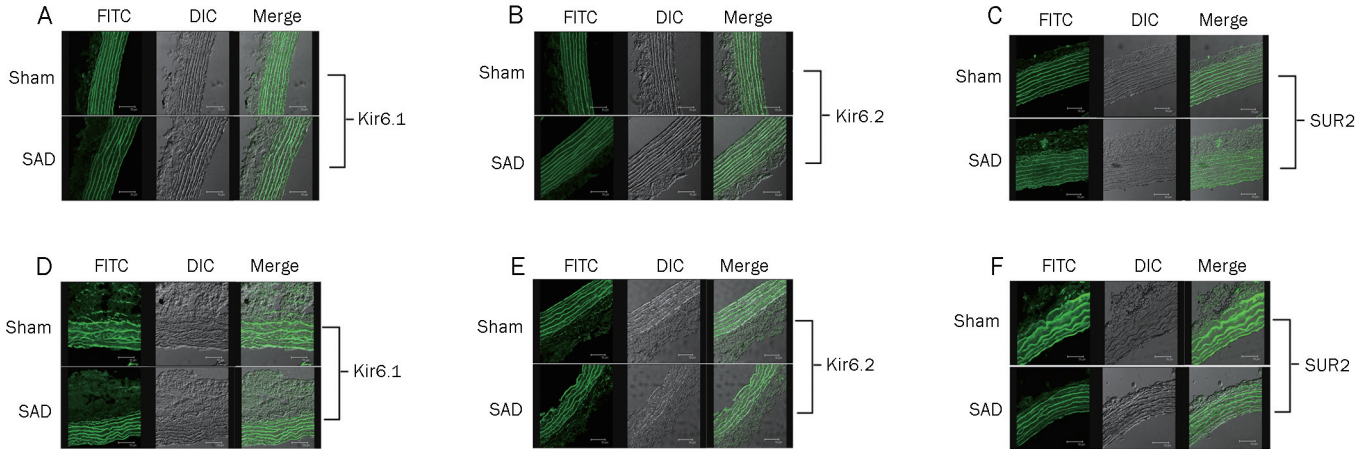

Figure 2. Representative images of Kir6.1, Kir6.2, and SUR2 expression in aorta (A–C) and mesenteric artery (D–F) from sinoaortic denervated (SAD) and sham-operated rats using laser scanning confocal microscopy. Aortic SUR2 expression was greater, while Kir6.1 was lower, in SAD rats than in sham-operated controls (A and C). In the mesenteric artery both SUR2 and Kir6.1 expression were markedly lower in SAD rats than controls (D and F). For both arteries, Kir6.2 expression was indistinguishable in sham-operated compared with SAD rats (B and E). Similar images were observed in vessels from at least 3 rats for each group. FITC,fluorescein isothiocyanate; DIC, differential interference contrast. The objective was ×20, scale bar: 50 μm.

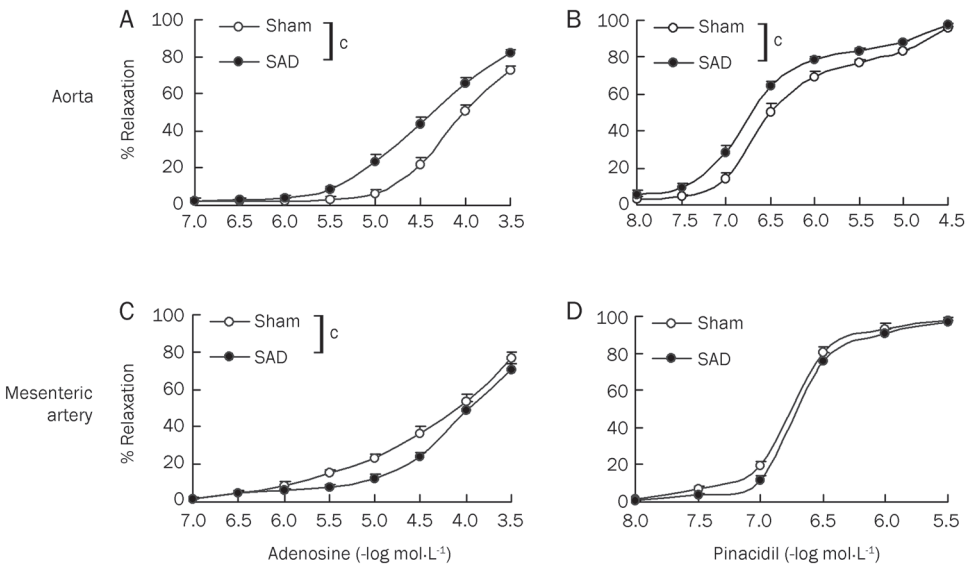

Figure 3. Vasodilatation induced by adenosine and pinacidil in phenylephrine-precontracted intact rat aorta (A, B) and mesenteric artery (C, D). Relaxant responses are expressed as the percentage reduction in tension produced by phenylephrine. Each point represents mean±SEM. (thoracic aorta, 17–21 aortic rings obtained from 9–12 rats; superior mesenteric artery, 12 superior mesenteric arterial rings from 9–12 rats). Sham, sham operation. $^{c}P<0.01$ *vs* sham-operated rats by repeated measures analysis of variance.

decreased BPV in SAD rats. We interpret these findings to indicate that K_{ATP} channels with a functional state play a role in enhanced BPV in chronic SAD rats.

K_{ATP} channels are hetero-octamers consisting of 4 sulfonylurea receptors (SUR) interacting with 4 channel subunits (Kir channels)[21]. The major isoform of the K_{ATP} channel in vascular muscle cells is composed of Kir6.1 and SUR2B subunits[24, 25]. In the vasculature, K_{ATP} channels provide a background potassium conductance critical for regulation of arterial tone in response to local metabolic need and vasoactive factors[15, 26], and operate as molecular sensors of cellular metabolism[21]. Genetic disruption of the abcc9 (SUR2) gene leads to coronary artery vasospasm and raises resting BP[27]. The function and/or expression of the K_{ATP} channels appears to be altered under a range of circumstances such as diabetes mellitus[28, 29], myocardial ischemia[30], and hypertension[31, 32]. We hypothesized that expression of K_{ATP} channels is altered in chronic SAD rats. In the present study, the impact of chronic SAD on the expression of vascular K_{ATP} channels was examined. We determined the expression of SUR2, Kir6.1, and Kir6.2 of both the aorta and mesenteric artery. In SAD rats, aortic expression of SUR2 was significantly greater than that in control rats while Kir6.1 expression was lower. In the case of mesenteric artery both SUR2 and Kir6.1 expression were markedly lower in SAD rats than controls. No significant differences in Kir6.2 expression were observed between SAD and sham-operated rats for both kinds of arteries. These results show that expression of vascular K_{ATP} channels is altered after SAD surgery. The factors

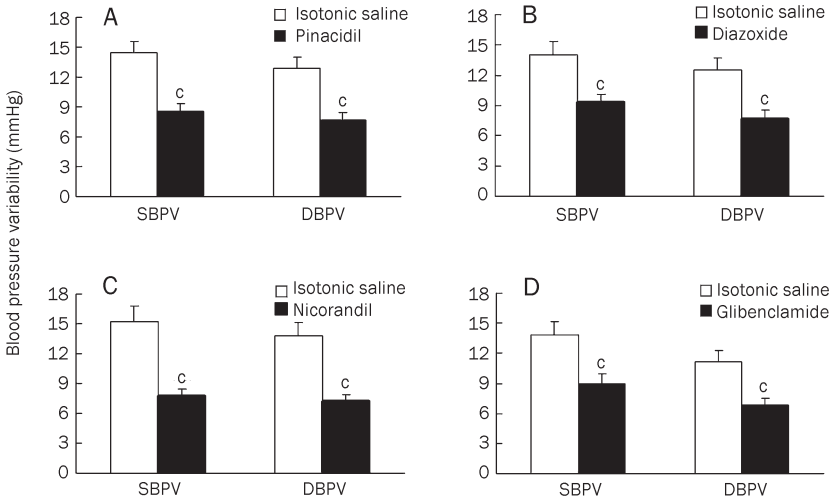

Figure 4. Effects of K_{ATP} channel openers and blocker on blood pressure variability (BPV) in sinoaortic denervated (SAD) rats. Pinacidil (n=10), diazoxide (n=8), nicorandil (n=8), and glibenclamide (n=10) significantly decreased BPV. SBPV, systolic BPV; DBPV, diastolic BPV. Data are expressed as mean±SEM. $^cP<0.01$ *vs* isotonic saline by paired *t*-test.

leading to these alterations in chronic SAD remain to be determined, but could include enhanced sympathetic drive[8, 33], haemodynamic variability[9], and adaptive changes in the function of local vasoactive substances[11, 20] after loss of baroreflex control of peripheral resistance.

K^+ channel-opener drugs activate K_{ATP} channels by interacting with the SUR subunit[21]. Adenosine, a metabolite of ATP, acts on adenosine A_{2A} receptors in vascular smooth muscle cell to cause dilatation by opening K_{ATP} channels[20]. In our work, both pinacidil and adenosine were used to assess vascular reactivity in sham-operated and SAD rats. We found that responses of the aorta to both adenosine and pinacidil were enhanced 4 weeks after SAD, while the mesenteric responses to adenosine were attenuated. Thus, changes in SUR2 expression appear to translate into changes in vascular function, this seems consistent with the idea suggested by Farzaneh *et al*[34]: in Kir6.1/SUR2, it is the SUR that underlies the metabolic sensitivity. It is tempting to speculate that such changes in SUR2 expression in the vessels may also be present in the microvasculature, and so lead to changes in the control of peripheral resistance and perhaps BPV.

Blood pressure variability has important physiological and clinical implications[4–7, 35, 36]. The most simple and commonly held explanation for the rise in BPV after SAD is the loss of the regulatory feedback function of the baroreceptor reflex. However, much remains to be understood concerning the dramatic increase in BPV after SAD[1–3]. Alper *et al*[8] suggested that instability of BP was related to fluctuation in sympathetic vasomotor tone. Julien *et al*[33] suggested that the sympathetic nervous system might directly generate part of the lability of BP in SAD rats. It has also been suggested that endogenous vasoconstrictors, by affecting the level of vascular tone, increased BPV[11]. Thus, basal vascular tone may be critical for the generation of BPV associated with SAD. These observations suggest that regulation of BPV in SAD rats is rather complex.

K_{ATP} channels, working as molecular sensors of cellular metabolism[21], regulate vascular tone in response to endogenous substances, such as adenosine, noradrenaline and vasopressin[15-19]. We hypothesized that K_{ATP} channels contribute to the BPV after SAD. To test this hypothesis we examined the impact, on BPV in the SAD rat, of eliminating the ability of vasoactive substances signaling through K_{ATP} channels. To interfere with K_{ATP} channel signaling we administered K_{ATP} channel openers or blocker. We found that pinacidil (a nonselective opener of K_{ATP} channels) and diazoxide (being able to open most of the K_{ATP} channels except the cardiac sarcolemmal K_{ATP} channels), and nicorandil (the vascular relevant opener) all significantly decreased BPV in SAD rats. To further investigate our hypothesis, the K_{ATP} channel blocker glibenclamide (a nonselective blocker of K_{ATP} channels) was used. BPV was significantly decreased even though this agent had the opposite effect on basal BP (increased) to the openers (reduced). Thus, either opening or blocking K_{ATP} channels decreases BPV in SAD rats, support our idea that K_{ATP} channels play a role in the increased BPV in chronic SAD rats.

In summary, this study showed that both expression and function of vascular K_{ATP} channels was altered by chronic SAD, and either opening or blocking K_{ATP} channels decreased BPV in SAD rats. These data support the concept that vascular K_{ATP} channels play a role in the increased BPV in chronic SAD rats.

Acknowledgements

This work was supported in part by the grants from National Natural Science Foundation of China (81070118), Shanghai Municipal Education Commission (10ZZ52), and the National Basic Research Program of China (2009CB521900).

Author contribution

Fu-ming SHEN, Ding-feng SU, and Yi-li YANG designed the research; Zhong-wei YANG, Dong-jie LI, Chong LIU, and Ping HAN performed the research and analyzed the data; Zhong-wei YANG, and Dong-jie LI wrote the paper.

References

1 Krieger EM. Neurogenic hypertension in the rat. Circ Res 1964; 15: 511–21.
2 Norman RA Jr, Coleman TG, Dent AC. Continuous monitoring of arterial pressure indicates sinoaortic denervated rats are not hypertensive. Hypertension 1981; 3: 119–25.
3 Pires SL, Julien C, Chapuis B, Sassard J, Barres C. Spontaneous renal blood flow autoregulation curves in conscious sinoaortic baroreceptor-denervated rats. Am J Physiol Renal Physiol 2002; 282: F51–8.
4 Tatasciore A, Renda G, Zimarino M, Soccio M, Bilo G, Parati G, *et al.* Awake systolic blood pressure variability correlates with target-organ damage in hypertensive subjects. Hypertension 2007; 50: 325–32.
5 Rothwell PM. Limitations of the usual blood-pressure hypothesis and importance of variability, instability, and episodic hypertension. Lancet 2010; 375: 938–48.
6 Rothwell PM, Howard SC, Dolan E, O'Brien E, Dobson JE, Dahlof B, *et al.* Effects of beta blockers and calcium-channel blockers on within-individual variability in blood pressure and risk of stroke. Lancet Neurol 2010; 9: 469–80.
7 Webb AJ, Fischer U, Mehta Z, Rothwell PM. Effects of antihypertensive-drug class on interindividual variation in blood pressure and risk of stroke: a systematic review and meta-analysis. Lancet 2010; 375: 906–15.
8 Alper RH, Jacob HJ, Brody MJ. Regulation of arterial pressure lability in rats with chronic sinoaortic deafferentation. Am J Physiol 1987; 253: H466–74.
9 Trapani AJ, Barron KW, Brody MJ. Analysis of hemodynamic variability after sinoaortic denervation in the conscious rat. Am J Physiol 1986; 251: R1163–9.
10 Jacob HJ, Alper RH, Brody MJ. Lability of arterial pressure after baroreceptor denervation is not pressure dependent. Hypertension 1989; 14: 501–10.
11 Jacob HJ, Alper RH, Grosskreutz CL, Lewis SJ, Brody MJ. Vascular tone influences arterial pressure lability after sinoaortic deafferentation. Am J Physiol 1991; 260: R359–67.
12 Shen FM, Su DF. The effect of adenosine on blood pressure variability in sinoaortic denervated rats is mediated by adenosine A2a-receptor. J Cardiovasc Pharmacol 2000; 36: 681–6.
13 Pires SL, Barres C, Sassard J, Julien C. Renal blood flow dynamics and arterial pressure lability in the conscious rat. Hypertension 2001; 38: 147–52.
14 Stauss HM, Petitto CE, Rotella DL, Wong BJ, Sheriff DD. Very low frequency blood pressure variability is modulated by myogenic vascular function and is reduced in stroke-prone rats. J Hypertens 2008; 26: 1127–37.
15 Quayle JM, Nelson MT, Standen NB. ATP-sensitive and inwardly rectifying potassium channels in smooth muscle. Physiol Rev 1997; 77: 1165–232.
16 Tan JH, Al Abed A, Brock JA. Inhibition of K_{ATP} channels in the rat tail artery by neurally released noradrenaline acting on postjunctional alpha2-adrenoceptors. J Physiol 2007; 581: 757–65.
17 Yasui S, Mawatari K, Kawano T, Morizumi R, Hamamoto A, Furukawa H, *et al*. Insulin activates ATP-sensitive potassium channels via phosphatidylinositol 3-kinase in cultured vascular smooth muscle cells. J Vasc Res 2008; 45: 233–43.
18 Eguchi S, Kawano T, Yinhua, Tanaka K, Yasui S, Mawatari K, *et al.* Effects of prostaglandin E1 on vascular ATP-sensitive potassium channels. J Cardiovasc Pharmacol 2007; 50: 686–91.
19 Shi W, Cui N, Shi Y, Zhang X, Yang Y, Jiang C. Arginine vasopressin inhibits Kir6.1/SUR2B channel and constricts the mesenteric artery via V1a receptor and protein kinase C. Am J Physiol Regul Integr Comp Physiol 2007; 293: R191–9.
20 Bryan PT, Marshall JM. Cellular mechanisms by which adenosine induces vasodilatation in rat skeletal muscle: significance for systemic hypoxia. J Physiol 1999; 514: 163–75.
21 Nichols CG. K_{ATP} channels as molecular sensors of cellular metabolism. Nature 2006; 440: 470–6.
22 Colantuono G, Tiravanti EA, Di Venosa N, Cazzato A, Rastaldo R, Cagiano R, *et al*. Hyperoxia confers myocardial protection in mechanically ventilated rats through the generation of free radicals and opening of mitochondrial ATP-sensitive potassium channels. Clin Exp Pharmacol Physiol 2008; 35: 64–71.
23 Miao CY, Su DF. The importance of blood pressure variability in rat aortic and left ventricular hypertrophy produced by sinoaortic denervation. J Hypertens 2002; 20: 1865–72.
24 Li L, Wu J, Jiang C. Differential expression of Kir6.1 and SUR2B mRNAs in the vasculature of various tissues in rats. J Membr Biol 2003; 196: 61–9.
25 Shi Y, Cui N, Shi W, Jiang C. A short motif in Kir6.1 consisting of four phosphorylation repeats underlies the vascular K_{ATP} channel inhibition by protein kinase C. J Biol Chem 2008; 283: 2488–94.
26 Suzuki M, Li RA, Miki T, Uemura H, Sakamoto N, Ohmoto-Sekine Y, *et al.* Functional roles of cardiac and vascular ATP-sensitive potassium channels clarified by Kir6.2-knockout mice. Circ Res 2001; 88: 570–7.
27 Chutkow WA, Pu J, Wheeler MT, Wada T, Makielski JC, Burant CF, *et al.* Episodic coronary artery vasospasm and hypertension develop in the absence of Sur2 K_{ATP} channels. J Clin Invest 2002; 110: 203–8.
28 Miura H, Wachtel RE, Loberiza FR Jr, Saito T, Miura M, Nicolosi AC, *et al.* Diabetes mellitus impairs vasodilation to hypoxia in human coronary arterioles: reduced activity of ATP-sensitive potassium channels. Circ Res 2003; 92: 151–8.
29 Fan LH, Tian HY, Ma AQ, Hu Z, Huo JH, Cao YX. Altered ATP-sensitive potassium channels may underscore obesity-triggered increase in blood pressure. Acta Pharmacol Sin 2008; 29: 1167–74.
30 Akao M, Otani H, Horie M, Takano M, Kuniyasu A, Nakayama H, *et al.* Myocardial ischemia induces differential regulation of K_{ATP} channel gene expression in rat hearts. J Clin Invest 1997; 100: 3053–9.
31 Ghosh M, Hanna ST, Wang R, McNeill JR. Altered vascular reactivity and K_{ATP} channel currents in vascular smooth muscle cells from deoxycorticosterone acetate (DOCA)-salt hypertensive rats. J Cardiovasc Pharmacol 2004; 44: 525–31.
32 Shimokawa J, Yokoshiki H, Tsutsui H. Impaired activation of ATP-sensitive K^+ channels in endocardial myocytes from left ventricular hypertrophy. Am J Physiol Heart Circ Physiol 2007; 293: H3643–9.
33 Julien C, Zhang ZQ, Barres C. Role of vasoconstrictor tone in arterial pressure lability after chronic sympathectomy and sinoaortic denervation in rats. J Auton Nerv Syst 1993; 42: 1–10.
34 Farzaneh T, Tinker A. Differences in the mechanism of metabolic regulation of ATP-sensitive K^+ channels containing Kir6.1 and Kir6.2 subunits. Cardiovasc Res 2008; 79: 621–31.
35 Wu MY, Ma XJ, Yang C, Tao X, Liu AJ, Su DF, *et al.* Effects of allisartan, a new AT_1 receptor blocker, on blood pressure and end-organ damage in hypertensive animals. Acta Pharmacol Sin 2009; 30: 307–13.
36 Wang JL, Wang L, Wu ZT, Yuan WJ, Su DF, Ni X, *et al.* Low dose of moxonidine within the rostral ventrolateral medulla improves the baroreflex sensitivity control of sympathetic activity in hypertensive rat. Acta Pharmacol Sin 2009; 30: 1594–600.

Acta Pharmacologica Sinica (2011) 32: 201–208
 1671-4083/11 $32.00
www.nature.com/aps

Original Article

Adeno associated viral vector-delivered and hypoxia response element-regulated CD151 expression in ischemic rat heart

Quan WEI, Xiao-lin HUANG*, Jing-yang LIN#, Yu-jie FEI, Zheng-xiang LIU*, Xin A ZHANG§

Department of Rehabilitation Medicine of Tongji Hospital, Tongji Medical College, Huazhong University of Science and Technology, Wuhan 430030, China

Aim: The aim of this study was to improve the delivery efficacy and target specificity of the pro-angiogenic gene CD151 to the ischemic heart.
Methods: To achieve the inducible expression of adeno-associated viral (AAV)-delivered CD151 gene in only the ischemic myocardium, we generated an AAV construct in which CD151 expression can be controlled by the hypoxia response element (HRE) sequence from the human Enolase gene. The function of this vector was examined in rat H9C2 cardiac myoblasts and in ischemic rat myocardium. The expression of CD151 in the areas of ischemic myocardium was confirmed at the mRNA level by real-time PCR and on the protein level by Western blot, whereas the CD151 expression in the microvessels within the areas of ischemic myocardium was detected by immunohistochemistry.
Results: HRE significantly enhances the expression of CD151 under hypoxic conditions or in the ischemic myocardium, and forced CD151 expression increases the number of microvessels in the ischemic myocardium.
Conclusion: The AAV-mediated, HRE regulated delivery of the CD151 gene shows higher expression in the ischemic myocardium and more efficiently targets CD151 to the hypoxic regions after myocardial infarction.

Keywords: cardiac ischemia; CD151; angiogenesis; gene therapy; gene expression; hypoxia response element

Acta Pharmacologica Sinica (2011) 32: 201–208; doi: 10.1038/aps.2010.205; published online 17 Jan 2011

Introduction

The transfer of angiogenic genes to the ischemic myocardium likely provides a useful approach for the treatment of coronary artery disease[1]. The CD151 protein is a member of the tetraspanin superfamily and contains four hydrophobic transmembrane domains, two extracellular loops, and two short cytoplasmic tails[2, 3]. Tetraspanins associate both with each other and with other integral membrane proteins, including integrins and members of the immunoglobulin superfamily[4, 5]. CD151 is expressed in various cell types, including epidermal basal cells, smooth cells, skeletal cells, cardiac muscle cells, endothelial cells, epithelial cells, platelets, and Schwann cells; it is also characteristically localized in intracellular vesicles and cell adhesion structures[4, 6]. Our previous studies have shown that the direct injection of an AAV vector carrying the CD151 gene to the ischemic rat myocardium induces neovasculature formation, and the CD151 gene delivery increases the number of microvessels in an ischemic rat hind limb model[7, 8]. Further studies with a swine myocardial infarction model indicated that CD151 gene delivery induces both angiogenesis and arteriogenesis by increasing the capillary and arteriole density[9, 10]. These observations strongly suggest that CD151 can be used for gene therapy with myocardial ischemia by promoting angiogenesis.

With the continued progress of gene therapy, there have been more concerns regarding the safety of gene therapy and the routes of gene delivery. The current routes of gene delivery to the heart include direct myocardial, trans-catheter myocardial, coronary artery, and intravenous injections. Intravenous injection is a non-invasive, safe gene-import method; however, it is not possible to introduce high concentrations of exogenous genes into the ischemic myocardium to induce sufficient angiogenesis using this method. If high doses of exogenous genes are administered, there would be an increase

#Now in *Department of Cardiology of Zhejiang Provincial People's Hospital, Hangzhou 310014, China*.
§ Now in *Vascular Biology and Cancer Centers, University of Tennessee Health Science Center, Memphis, Tennessee, USA*.
* To whom correspondence should be addressed.
E-mail liuzhengxiang@hotmail.com (Zheng-xiang LIU);
xiaolinh2006@yahoo.com.cn (Xiao-lin HUANG)
Received 2010-09-02 Accepted 2010-11-02

in the exposure of the gene to the normoxic myocardium as well as other organs and also an increase in the potential side effects in non-ischemic sites such as hemangioma formation and retinopathy[11, 12]. Although such complications were not observed in our previous animal studies on CD151, it is crucial to minimize these complications for the upcoming clinical applications of CD151. Thus, for intravenous administration, it is of immediate concern to find a method that will increase CD151 expression specifically in the ischemia myocardium but not in the normoxic myocardium and other organs.

For the treatment of ischemic heart disease, an ideal control for CD151 gene expression seems to be the response to hypoxia; that is, there is high expression of the CD151 gene in the ischemic areas and low expression in the non-ischemia areas. Hypoxia-inducible factor-1 (HIF-1) is induced or upregulated under conditions of hypoxia and regulates gene expression by binding to a cis-acting hypoxia-responsive element (HRE)[13, 14]. The HRE has been found in human enolase (ENO)[15], erythropoietin (Epo)[16], and several other genes. The core consensus sequence is (A/G)CGT(G/C)C. HRE sequences of ENO and Epo have been used to regulate the expression of genes such as vascular endothelial growth factor (VEGF)[14] and suicide[17] or apoptosis[18] genes.

In this study, we use the AAV-HRE-CD151 vector, which carries one copy of the HRE from ENO, to determine the applicability and feasibility of the hypoxia-induced, HRE-driven expression of CD151 in the ischemic myocardium. Our study demonstrated that the ENO HRE can induce CD151 expression under hypoxic conditions in both cultured cardiomyocytes *in vitro* and ischemic rat myocardium *in vivo*.

Materials and methods

Vector construction and production

The AAV constructs carrying human CD151 or green fluorescent protein (GFP) cDNA were generated as described previously[7, 19]. Based on the previous study by Philips *et al*[20], a 68-bp HRE sequence from the human *Enolase* 1 gene was inserted into the pAAV-CD151 construct between the *Mlu*I and *BamH*I restriction sites upstream of the cytomegalovirus promotor to generate the pAAV-HRE-CD151 construct.

Cell culture and transfection

Rat cardiac myoblasts (H9C2) were obtained from American Type Culture Collection, cultured in Dulbecco's modified Eagle's medium supplemented with 10% fetal bovine serum (FBS) and maintained in 5% CO_2/95% air at 37 °C. Hypoxia conditions were achieved in the tightly sealed hypoxia chambers by repeated evacuation and filling of 5% O_2/1% CO_2/94% N_2 at 37 °C.

To examine the hypoxia-induced expression of CD151, H9C2 cells were cultured in 6-well plates to 70%–90% confluence and then transfected with pAAV-HRE-CD151, pAAV-CD151, or pAAV-GFP using the FuGENE HD transfection reagent (Roche, MA, Germany). Non-transfected H9C2 cells were included as a control. At 48 h after the transfection, the infected cells were split into two parts: one part was cultured under normoxic conditions (95% air, 5% CO_2) and the other part was cultured under hypoxic conditions (94% N_2, 5% O_2, and 1% CO_2) in serum-free medium for 16 h. The individual experiments were repeated (n=6).

Ischemic heart model and injection of the plasmids

Adult male Sprague-Dawley Rats (Animal Use and Care Center, Tongji Medical College, Wuhan, China) with weights of 200–250 g underwent a coronary artery ligation surgery. Under the anesthesia of pentobarbital (60 mg/kg, intraperitoneally), acute myocardial infarction (AMI) was induced by ligation of the left anterior descending coronary artery. Briefly, after intubation of the trachea, an incision was made in the skin overlying the 4th intercostal space, with the overlying muscles separated and kept aside. The animals were placed under positive-pressure ventilation (frequency 65–70/min, tidal volume 3 mL), and the thoracic cavity was opened by cutting the intercostal muscles. The heart was carefully pushed to the left, and a 6–0 silk suture was looped under the left descending coronary artery near the origin of the pulmonary artery. Proper occlusion of the coronary artery resulted in an extensive transmural infarction comprising a major part of the left ventricle (LV) free wall, with small variations in size. Coronary occlusion was confirmed by the raised segment (ST) stages on the electrocardiogram and ventricular arrhythmias within the first 20–30 min after the occlusion. Twenty-four survived rats were randomly divided into four groups one day after the surgery. The rats in the control group (n=6) received a single dose of 1 mL saline solution by the sublingual vein, whereas the rats in the treatment groups (n=6 per group) were injected through the same route with a single dose of 1 mL saline solution containing 200 μg of pAAV-GFP, pAAV-CD151, or pAAV-HRE-CD151 plasmids[21, 22]. The animal protocols used were in compliance with the Guide for the Care and Use of Laboratory Animals and were approved by the Chinese Academy of Sciences.

Western blot analysis

Cardiac myoblasts were scraped off the plates and lysed in RIPA buffer (50 mmol/L Tris-HCl (pH 8.0), 150 mmol/L NaCl, 1% Nonidet-P40, 0.5% deoxycholic acid and 0.1% SDS) and centrifuged at 14 000×g at 4°C for 30 min. Tissues from the infarcted heart areas were dissected. The tissues were homogenized in 500 μL of 25 mmol/L Tris-HCl (pH 7.4) containing 1% Triton X-100, 0.1% SDS, 2 mmol/L EDTA, and 1% protease inhibitor and centrifuged at 14 000×g at 4°C for 30 min. The protein concentration was measured by the Bradford method with bovine serum albumin as the standard. The cell and tissue lysates (50 μg protein) were separated in SDS-PAGE, electrically transferred to polyvinyl difluoride membranes, and probed with antibodies against CD151 (Abcam, CA, UK) and β-actin (Sigma-Aldrich, MO, USA), followed by incubation with the horseradish peroxidase-conjugated 2nd antibody and chemiluminescence detection. The intensities of the protein bands were quantified by densitometry.

Real-time quantitative PCR

Tissue samples from the infarcted heart areas were homogenized in TRIZOL solution (Invitrogen, CA, USA) and RNA was extracted from the tissue following the manufacturer's instruction. CD151 mRNA in the heart tissue was detected by real-time quantitative PCR. One microgram of total RNA was reverse-transcribed in a 20-μL reaction mixture containing 4 μL 5×PrimeScript Buffer, 1 μL Primescript RT Enzyme *Mix* I, 1 μL Oligo dT Primer (50 μmol/L), 1 μL Random 6 mers (100 μmol/L), and 9 μL RNAse-free H_2O (TaKaRa, Dalian, China). The mixture was incubated at 37 °C for 15 min and 85 °C for 5 s. Then, real-time PCR was performed in an Mx3000P system (Stratagene, CA, USA) using the SYBR® Premix Ex Taq™ (TaKaRa, Dalian, China) and 2 μL of cDNA was amplified in a 25-μL reaction mixture containing 12.5 μL of the SYBR Premix Ex Taq, 0.5 μL of the forward primer (10 μmol/L), 0.5 μL of the reverse primers (10 μmol/L), 0.5 μL of the ROX Reference Dye, and 9 μL of dH_2O. Amplifications were as follows: 95 °C for 30 s, followed by 40 cycles of 95 °C for 5 s, 58 °C for 20 s, and 72 °C for 15 s. The forward and reverse primers for CD151 are 5′-TGGGTGAGTTCAACGAGAAG-3′ and 5′-AGCCAGAAGCAGCAATTGTA-3′, respectively, and those for β-actin are 5′-CCCATCTATGAGGGTTACGC-3′ and 5′-TTTAATGTCACGCACGATTTC-3′, respectively. The reverse-transcribed cDNA samples were amplified, and cycle threshold (Ct) values were determined. The mRNA levels of CD151 were normalized to the mRNA levels of the housekeeping gene β-actin. The comparative Ct method ($2^{-\Delta\Delta Ct}$)[23] was used to analyze the differences in the level of CD151 mRNA between each group.

Immunohistochemistry analysis and data acquisition

Heart tissue specimens were taken from the infarcted regions in the left ventricle 4 weeks after the plasmid administration, fixed in 10% formalin, embedded in paraffin, and cut into 4-μm thick sections. Some sections were stained with hematoxylin and eosin (H–E), and others were used for immunohistochemical staining with vWF (Santa Cruz, CA, USA) and SMα-actin (Sigma-Aldrich, MO, USA) antibodies for capillaries and arterioles, respectively. The densities of capillaries and arterioles were assessed according to the method previously described[10]. Five regions that are rich in blood vessels were selected, and the vessels of each region that are within 400×microscopic field (for capillary) or 100×microscopic field (for arteriole) were counted by two blinded investigators without knowledge of the group identity. The numbers of capillaries (vWF positive) and arterioles (SM α-actin positive) in each field were counted under ocular micrometers (Olympus, Tokyo, Japan), and a total of five high-powered fields (HPF) per region per heart were quantified.

Statistical analysis

The statistical comparisons of the data were performed with a one-way analysis of variance (ANOVA), followed by the Newman-Keuls test for unpaired data. The results were expressed as the mean±standard error of the mean (SEM). A probability value of less than 5% was considered statistically significant.

Results

Construction of pAAV-HRE-CD151 plasmid

To induce CD151 expression in a hypoxia-dependent manner, we generated a recombinant pAAV-HRE-CD151 vector by placing the 68-bp HRE sequence from the human ENO gene between the *Mlu* I and *BamH* I restriction sites upstream of the cytomegalovirus promotor in the pAAV-CD151 plasmid. The correct insertion and intactness of the HRE sequence was confirmed by the nucleotide sequencing of the pAAV-HRE-CD151 vector (Figure 1).

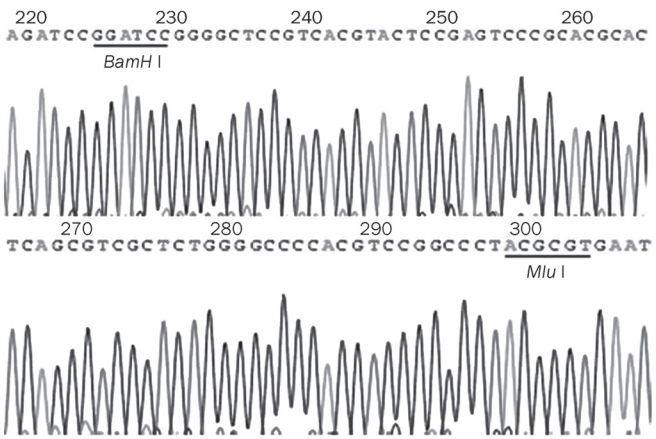

Figure 1. Identification of pAAV-HRE-CD151 by nucleotide sequencing. The sequence between the *BamH* I and *Mlu* I restriction sites is the HRE reverse complementary sequence (68 bp).

HRE-induced *in vitro* CD151 expression in cardiac myoblasts

To determine if the HRE enhancer can conditionally induce AAV-mediated CD151 gene expression under hypoxic conditions, we expressed the plasmids of pAAV-HRE-CD151, pAAV-CD151, and pAAV-GFP in H9C2 cardiac myoblasts. Under the hypoxic conditions, CD151 protein expression was significantly increased in the pAAV-HRE-CD151 group compared to the pAAV-CD151, pAAV-GFP, and non-transfected cardiac myoblast groups ($P<0.01$). Under the normoxic conditions, CD151 protein expression was increased significantly in the pAAV-HRE-CD151 group compared to the pAAV-GFP and non-transfected cardiac myoblast groups ($P<0.01$); however, there was no significant difference in CD151 expression between the pAAV-HRE-CD151 and pAAV-CD151 groups. These results indicated that the HRE of ENO enhanced the AAV vector-mediated CD151 expression in cultured cardiac myoblasts under the hypoxic condition (Figure 2). In all experiments, an equal number of cells were lysed from each group to level the total protein loading, and actin expression was used to normalize the CD151 expression in each group.

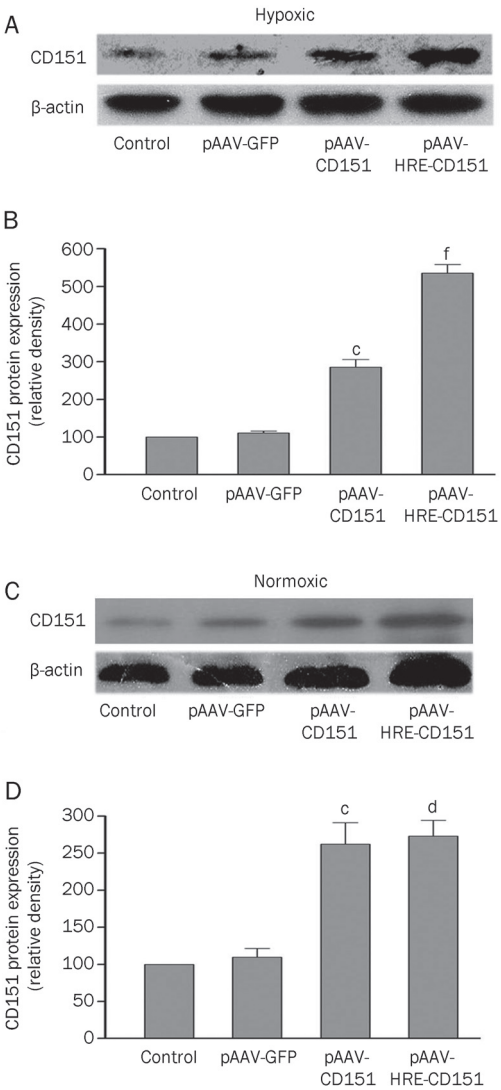

Figure 2. Hypoxic induction of CD151 expression in H9C2 cells after CD151-expressing vector transfection. (A) Western blot analysis of CD151 expression in hypoxic conditions. β-actin was used as an internal control. (B) Quantitative analysis of CD151 protein expression. The mean density of CD151 in the control group was defined as 100%. Data are presented as means±SEM (n=4–6 per group). ^{c}P<0.01 *vs* control and pAAV-GFP groups. ^{f}P<0.01 *vs* the pAAV-CD151 group. (C) Western blot analysis of CD151 expression in normoxic conditions. β-actin was used as an internal control. (D) Quantitative analysis of CD151 protein expression. The mean density of CD151 in the control group was defined as 100%. Data are presented as means±SEM (n=4–6 per group). ^{c}P<0.01 *vs* control and pAAV-GFP groups, ^{d}P>0.05 *vs* the pAAV-CD151 group.

Induction of CD151 expression by HRE in the ischemic myocardium

The ENO HRE-driven *in vivo* expression of CD151 was assessed by intravenously injecting pAAV-GFP, pAAV-CD151, and pAAV-HRE-CD151 vectors into the ischemic rat heart. CD151 expression was analyzed at the mRNA level using real time PCR. The CD151 level in the ischemic hearts of the pAAV-HRE-CD151 group was markedly higher than that in the saline control and pAAV-GFP groups (P<0.01) (Figure 3). In the same model, the CD151 level in the pAAV-HRE-CD151 group was higher than that in the pAAV-CD151 group (P<0.01). Consistent with the results *in vitro*, ENO HRE significantly enhances CD151 expression in the ischemic myocardium *in vivo*.

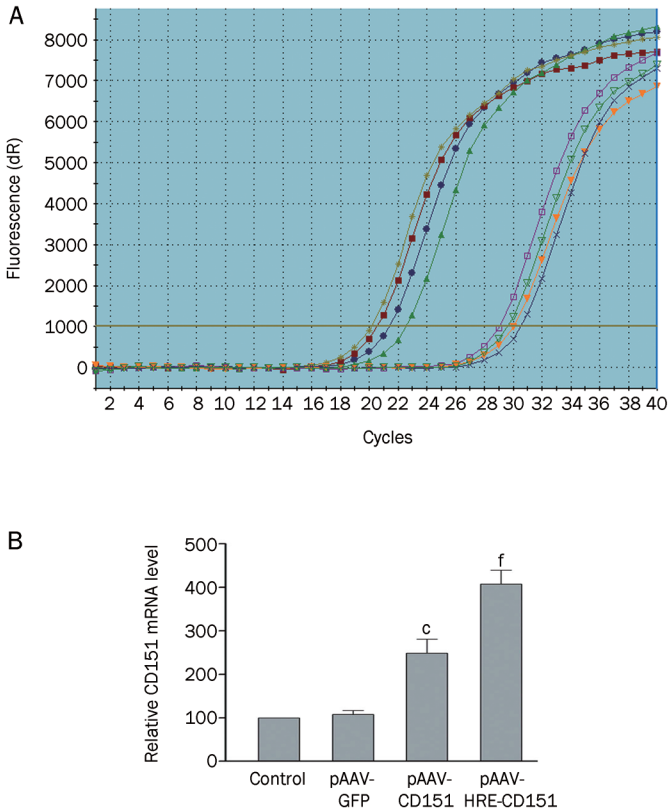

Figure 3. Induction of CD151 expression by HRE in the ischemic myocardium after CD151 gene delivery. Four weeks after coronary artery ligation, samples were collected from the same heart regions. (A) Real-time PCR amplification plots of CD151 and β-actin. (B) The mRNA levels for CD151 and β-actin after gene delivery. β-Actin was used as an internal control. In each group, the CD151 mRNA level was normalized to the β-actin mRNA level. The data are presented as the ratio of the treated group to the saline control group, which was defined as 100%. The results are presented as means±SEM (n=4–5 per group); ^{c}P<0.01 between the pAAV-CD151 group and the saline control and pAAV-GFP groups. ^{f}P<0.01 between the pAAV-HRE-CD151 group and the saline control, pAAV-GFP, or pAAV-CD151 groups.

Western blot analysis demonstrated that the levels of human CD151 proteins extracted from ischemic myocardium were increased significantly in the pAAV-CD151 and pAAV-HRE-CD151 groups compared with the saline control and pAAV-GFP groups (P<0.01, Figure 4). In contrast, the expression of CD151 proteins in the pAAV-HRE-CD151 group was higher than that in the pAAV-CD151 group (P<0.01). There was no significant difference in the level of CD151 proteins between the saline control and pAAV-GFP groups (P>0.05). These

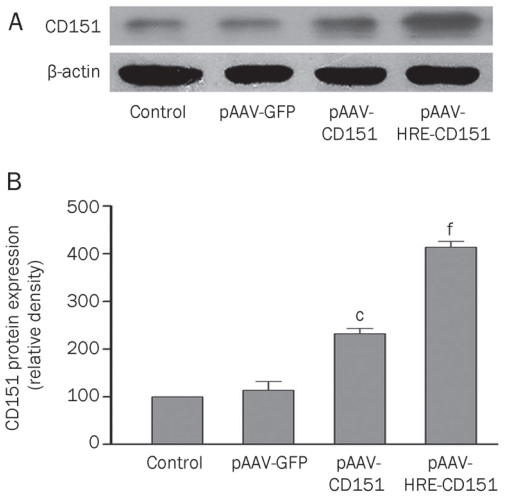

Figure 4. Enhancement of CD151 expression by HRE in the ischemic myocardium after CD151 gene delivery. Four weeks after coronary artery ligation, tissue samples were collected from the same heart regions. (A) Western blot analysis for CD151 and β-actin. β-Actin serves as an internal protein loading control. (B) Quantification of CD151. The density of the CD151 band in the saline control group was arbitrarily defined as 100 units, and the densities in other groups are the relative levels to 100 units. Data are presented as means±SEM (n=6−8). ^{c}P<0.01 between the pAAV-CD151 group and the saline control and pAAV-GFP groups. ^{f}P<0.01 between the pAAV-HRE-CD151 group and the saline control, pAAV-GFP, or pAAV-CD151 groups.

results indicate that AAV-mediated CD151 gene delivery promotes CD151 protein expression in myocardial tissue and that ENO HRE can induce higher CD151 expression in the ischemic myocardium *in vivo*.

Analysis of arteriole and capillary density

The formation of capillaries and arterioles was evaluated by vWF and SM α-actin staining, respectively, at 4 weeks after the plasmid injections. Higher microvessel densities were found in the pAAV-HRE-CD151 and pAAV-CD151 groups and less neovascularization was found in the saline control and pAAV-GFP groups (Figure 5). There were no significant differences in the numbers of microvessels (P>0.05) between the saline control and pAAV-GFP groups. In contrast, the capillary and arteriole densities in the pAAV-HRE-CD151 group were markedly higher than that in the pAAV-CD151 group (P<0.01). These findings indicate that the ENO HRE-induced higher CD151 expression is correlated with more neovascularization in the ischemic myocardium. This further supports our earlier observation that CD151 gene delivery increases the formation of capillaries and arterioles.

Discussion

Despite the success of bypass surgery and angioplasty, many patients have a limited opportunity to accomplish revascularization in the ischemia myocardium because of diffused coronary artherosclerosis, occluded bypass grafts, or excessive risk of surgery. Hence, ischemic heart disease remains the leading cause of morbidity and mortality in the world. Therapeutic angiogenesis, using angiogenic growth factors or cytokines to stimulate collateral blood vessel formation, has been tested as an alternative treatment[14, 24, 25]. The pro-angiogenesis factors that have been investigated include CD151, VEGFs[1, 7], FGFs[25], and angiopoietins[26]. As a member of the tetraspanin family, CD151 plays a role in regulating endothelial cell (EC) motility and angiogenesis *in vitro*[4, 27]. A recent study demonstrates that the mouse lung ECs (MLECs) from CD151-null mice display marked reduction in the angiogenesis-related endothelial events including migration, spreading, invasion, Matrigel contraction, tube and cable formation, and spheroid sprouting[28]. Conversely, overexpression of CD151 in human umbilical vein ECs enhances cell proliferation, migration, and capillary tube formation on Matrigel[29]. We have reported that CD151 gene delivery increases the number of microvessels in a rat myocardial ischemia model and an ischemic rat hindlimb model[7, 8]. Further studies have underlined that CD151 gene delivery promotes angiogenesis in a pig myocardial ischemia model and demonstrated that CD151-induced neovascularization effectively enhances the myocardial perfusion and markedly ameliorates the regional myocardial dysfunction based on ^{13}N-NH_3 PET imaging and echocardiography[9, 10]. All these observations strongly suggest that CD151 can be useful for gene therapy to target myocardial ischemia by promoting angiogenesis.

The adeno-associated virus (AAV) vector belongs to the nonpathogenic member of the parvovirus family. It has several advantages over other viral vectors such as low immunogenicity, a long-term expression of transgene, and an ability to infect both dividing and nondividing cells[30]. Our previous studies have also found that AAV is an efficient vector for the *in vivo* transfer and sustained expression of the CD151 gene in the myocardium. AAV-mediated CD151 gene transfer provides heart with effective and long-lasting protection from acute myocardial infarction-induced injuries.

A potential problem associated with exogenous gene therapy is that different dosages and durations of the exogenous gene stimulation may yield different results. A relatively low level of the angiogenic factor in the myocardium is insufficient to induce angiogenesis, because transient exposure to the exogenous genes in humans was insufficient to trigger and maintain a therapeutically meaningful angiogenic response in clinical trials, especially when patients also had an extensive atherosclerotic disease[31]. The administration or expression of angiogenic factors for the short term and/or at low levels either could not stimulate myocardial angiogenesis in initial clinical trials and induced only a short-lived angiogenic response[32] or led to nonfunctional, hypo-perfused capillaries that regress when the levels of angiogenic factors drop[32]. For the treatment of ischemic heart disease, angiogenic therapy is aimed at stimulating functional and sustainable new blood vessels. However, an excessively high-level expression of the angiogenic factor *in vivo* may result in side effects in non-ischemic sites such as excessive angiogenesis, which will lead

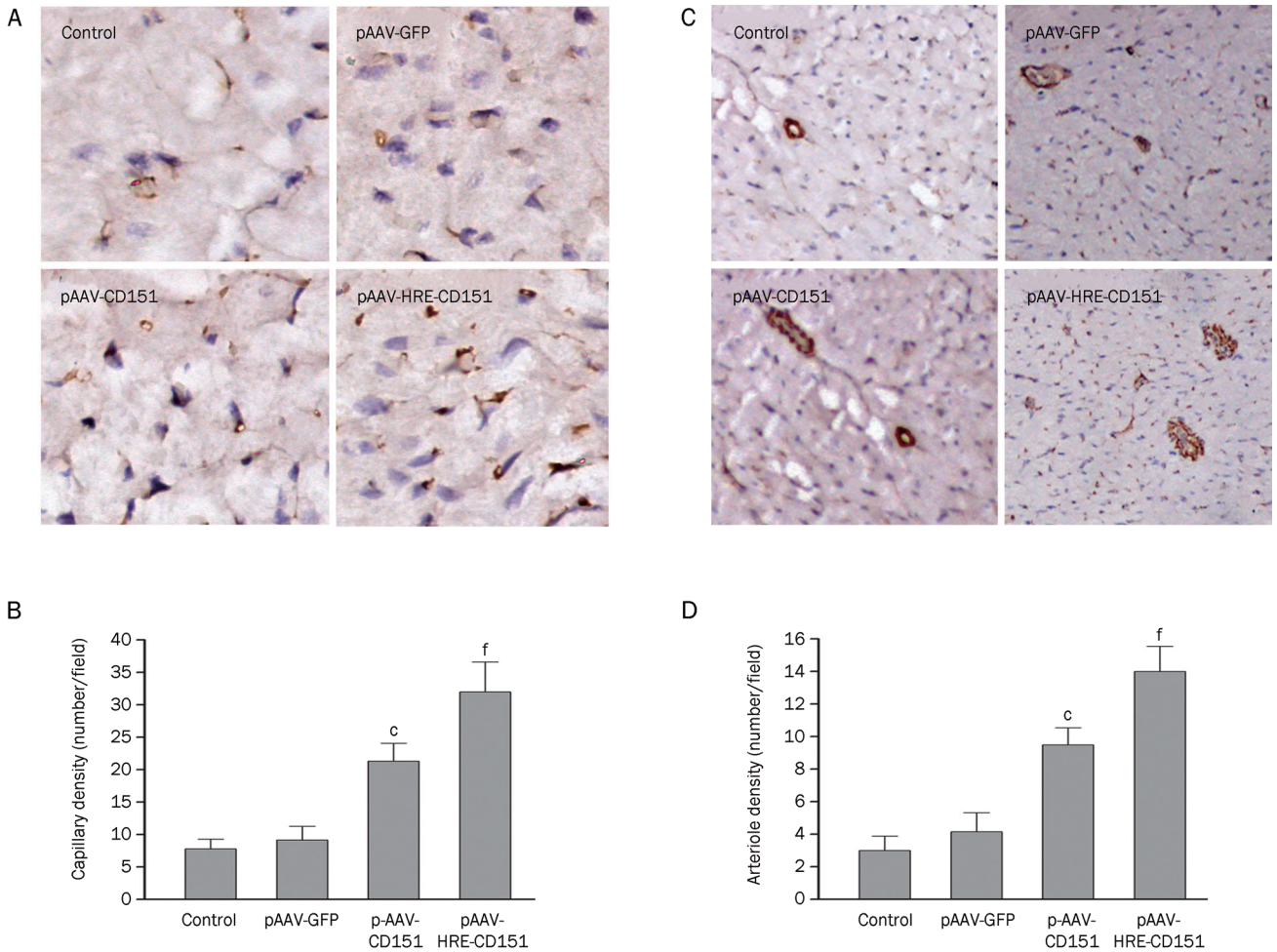

Figure 5. Overexpression of CD151 increases the densities of capillaries and arterioles. (A) Immunohistochemical staining of capillaries with antibody to von Willebrand factor (vWF). The ECs are stained in brown. (B) Quantification of the density of myocardial capillaries. (C) Immunohistochemical staining of arterioles with antibody to SM α-actin. The smooth muscle cells are indicated in brown. (D) Quantification of the density of myocardial arterioles. Data are projected as means±SEM (n=4−6 per group). ^{c}P<0.01 between the pAAV-CD151 group and the saline control and pAAV-GFP groups. ^{f}P<0.01 between the pAAV-HRE-CD151 group and the saline control, pAAV-GFP, or pAAV-CD151 groups.

to adverse consequences in the retina, synovium, and other areas[12, 33]. Thus, long-lasting and reasonably high levels of exogenous gene stimulation are needed for clinical success. More importantly, it is crucial to increase the exogenous gene expression only in the ischemic myocardium without significantly affecting the global level of this gene in the body.

One ideal mechanism to regulate the exogenous gene expression in the ischemic heart is to allow the expression of this gene in response to hypoxia. Earlier studies demonstrated that an increased level of HIF-1α in the ischemic myocardium was found as early as 2 days after the coronary artery occlusion and lasted until 2 weeks later[14]. Therefore, the HIF-1α/HRE is an ideal regulatory system to be used for controlling exogenous gene expression in the ischemic myocardium. To maintain a higher level of CD151 expression in the ischemic regions and meanwhile reduce the side-effects, we chose to inject a lower level of the CD151 gene and make use of HRE to induce higher CD151 gene expression in the hypoxic area. Consequently, the angiogenesis induced by uncontrolled and persistently expressed exogenous gene can be avoided by HRE-controlled CD151 expression. We chose to use ENO HRE in our study because Phillips *et al* showed that HRE from ENO yielded the best induction of gene expression under hypoxic conditions[20]. CD151 expression under the control of a HRE enhancer and CMV promoter exhibited marked upregulation under hypoxic conditions. This upregulation is likely mediated by HIF-1α in cardiomyocytes because H9C2 cells express HIF-1α in hypoxia[14]. In accordance with higher CD151 expression, the formation of capillaries and arterioles in the ischemic myocardium was also elevated under the HRE enhancer. These findings together suggest that hypoxia enhances CD151 expression in the ischemic myocardium in an HRE-dependent manner and that higher CD151 gene expression in turn results in increased neovascularization.

In conclusion, we have demonstrated that ENO HRE enhances the AAV vector-mediated CD151 gene expression in

cultured cardiomyocytes *in vitro* and ischemic rat myocardium *in vivo*. These results further demonstrate that the HIF-1/HRE axis is a useful system for controlling CD151 expression in the treatment of ischemic heart disease and potentiates the efficacy of CD151-based gene therapy.

Acknowledgements

This work was supported by a grant from the National Natural Science of China (No 30670856).

Author contribution

Xiao-lin HUANG and Zheng-xiang LIU designed the study and handled funding; Quan WEI, Jing-yang LIN, and Yu-jie FEI performed the research, analyzed the data and drafted the manuscript; Xin A ZHANG contributed the reagents and analytical tools and reviewed and revised the manuscript.

References

1 Su H, Lu R, Kan YW. Adeno-associated viral vector-mediated vascular endothelial growth factor gene transfer induces neovascular formation in ischemic heart. Proc Natl Acad Sci USA 2000; 97: 13801–6.
2 Fitter S, Tetaz TJ, Berndt MC, Ashman LK. Molecular cloning of cDNA encoding a novel platelet-endothelial cell tetra-span antigen, PETA-3. Blood 1995; 86: 1348–55.
3 Hasegawa H, Utsunomiya Y, Kishimoto K, Yanagisawa K, Fujita S. SFA-1, a novel cellular gene induced by human T-cell leukemia virus type 1, is a member of the transmembrane 4 superfamily. J Virol 1996; 70: 3258–63.
4 Sincock PM, Fitter S, Parton RG, Berndt MC, Gamble JR, Ashman LK. PETA-3/CD151, a member of the transmembrane 4 superfamily, is localised to the plasma membrane and endocytic system of endothelial cells, associates with multiple integrins and modulates cell function. J Cell Sci 1999; 112: 833–44.
5 Zhang XA, Bontrager AL, Hemler ME. Transmembrane-4 superfamily proteins associate with activated protein kinase C (PKC) and link PKC to specific beta(1) integrins. J Biol Chem 2001; 276: 25005–13.
6 Sincock PM, Mayrhofer G, Ashman LK. Localization of the transmembrane 4 superfamily (TM4SF) member PETA-3 (CD151) in normal human tissues: comparison with CD9, CD63, and alpha5beta1 integrin. J Histochem Cytochem 1997; 45: 515–25.
7 Lan RF, Liu ZX, Liu XC, Song YE, Wang DW. CD151 promotes neovascularization and improves blood perfusion in a rat hind-limb ischemia model. J Endovasc Ther 2005; 12: 469–78.
8 Zheng Z, Liu Z. CD151 gene delivery activates PI3K/Akt pathway and promotes neovascularization after myocardial infarction in rats. Mol Med 2006; 12: 214–20.
9 Zuo HJ, Liu ZX, Liu XC, Yang J, Liu T, Wen S, *et al*. Assessment of myocardial blood perfusion improved by CD151 in a pig myocardial infarction model. Acta Pharmacol Sin 2009; 30: 70–7.
10 Zuo H, Liu Z, Liu X, Yang J, Liu T, Wen S, *et al*. CD151 gene delivery after myocardial infarction promotes functional neovascularization and activates FAK signaling. Mol Med 2009; 15: 307–15.
11 Schwarz ER, Speakman MT, Patterson M, Hale SS, Isner JM, Kedes LH, *et al*. Evaluation of the effects of intramyocardial injection of DNA expressing vascular endothelial growth factor (VEGF) in a myocardial infarction model in the rat — angiogenesis and angioma formation. J Am Coll Cardiol 2000; 35: 1323–30.
12 Lee RJ, Springer ML, Blanco-Bose WE, Shaw R, Ursell PC, Blau HM. VEGF gene delivery to myocardium: deleterious effects of unregulated expression. Circulation 2000; 102: 898–901.
13 Su H, Kan YW. Adeno-associated viral vector-delivered hypoxia-inducible gene expression in ischemic hearts. Methods Mol Biol 2007; 366: 331–42.
14 Su H, Arakawa-Hoyt J, Kan YW. Adeno-associated viral vector-mediated hypoxia response element-regulated gene expression in mouse ischemic heart model. Proc Natl Acad Sci USA 2002; 99: 9480–5.
15 Semenza GL, Jiang BH, Leung SW, Passantino R, Concordet JP, Maire P, *et al*. Hypoxia response elements in the aldolase A, enolase 1, and lactate dehydrogenase A gene promoters contain essential binding sites for hypoxia-inducible factor 1. J Biol Chem 1996; 271: 32529–37.
16 Gupta M, Mungai PT, Goldwasser E. A new transacting factor that modulates hypoxia-induced expression of the erythropoietin gene. Blood 2000; 96: 491–7.
17 Koshikawa N, Takenaga K, Tagawa M, Sakiyama S. Therapeutic efficacy of the suicide gene driven by the promoter of vascular endothelial growth factor gene against hypoxic tumor cells. Cancer Res 2000; 60: 2936–41.
18 Ruan H, Su H, Hu L, Lamborn KR, Kan YW, Deen DF. A hypoxia-regulated adeno-associated virus vector for cancer-specific gene therapy. Neoplasia 2001; 3: 255–63.
19 Lan R, Liu Z, Song Y, Zhang X. Effects of rAAV-CD151 and rAAV-antiCD151 on the migration of human tongue squamous carcinoma cell line Tca8113. J Huazhong Univ Sci Tech Med Sci 2004; 24: 556–9.
20 Phillips MI, Tang Y, Schmidt-Ott K, Qian K, Kagiyama S. Vigilant vector: heart-specific promoter in an adeno-associated virus vector for cardioprotection. Hypertension 2002; 39: 651–5.
21 Xia JL, Dai C, Michalopoulos GK, Liu Y. Hepatocyte growth factor attenuates liver fibrosis induced by bile duct ligation. Am J Pathol 2006; 168: 1500–12.
22 Deng X, Szabo S, Khomenko T, Jadus MR, Yoshida M. Gene therapy with adenoviral plasmids or naked DNA of vascular endothelial growth factor and platelet-derived growth factor accelerates healing of duodenal ulcer in rats. J Pharmacol Exp Ther 2004; 311: 982–8.
23 Schmittgen TD, Livak KJ. Analyzing real-time PCR data by the comparative C(T) method. Nat Protoc 2008; 3: 1101–8.
24 Yla-Herttuala S, Martin JF. Cardiovascular gene therapy. Lancet 2000; 355: 213–22.
25 Simons M, Annex BH, Laham RJ, Kleiman N, Henry T, Dauerman H, *et al*. Pharmacological treatment of coronary artery disease with recombinant fibroblast growth factor-2: double-blind, randomized, controlled clinical trial. Circulation 2002; 105: 788–93.
26 Sung HK, Kim YW, Choi SJ, Kim JY, Jeune KH, Won KC, *et al*. COMP-angiopoietin-1 enhances skeletal muscle blood flow and insulin sensitivity in mice. Am J Physiol Endocrinol Metab 2009; 297: E402–409.
27 Zhang XA, Kazarov AR, Yang X, Bontrager AL, Stipp CS, Hemler ME. Function of the tetraspanin CD151-alpha6beta1 integrin complex during cellular morphogenesis. Mol Biol Cell 2002; 13: 1–11.
28 Takeda Y, Kazarov AR, Butterfield CE, Hopkins BD, Benjamin LE, Kaipainen A, *et al*. Deletion of tetraspanin Cd151 results in decreased pathologic angiogenesis *in vivo* and *in vitro*. Blood 2007; 109: 1524–32.
29 Zheng ZZ, Liu ZX. Activation of the phosphatidylinositol 3-kinase/protein kinase Akt pathway mediates CD151-induced endothelial cell proliferation and cell migration. Int J Biochem Cell Biol 2007; 39: 340–8.
30 Shen F, Su H, Fan Y, Chen Y, Zhu Y, Liu W, *et al*. Adeno-associated

viral-vector-mediated hypoxia-inducible vascular endothelial growth factor gene expression attenuates ischemic brain injury after focal cerebral ischemia in mice. Stroke 2006; 37: 2601–6.

31 Ferrara N, Alitalo K. Clinical applications of angiogenic growth factors and their inhibitors. Nat Med 1999; 5: 1359–64.

32 Pettersson A, Nagy JA, Brown LF, Sundberg C, Morgan E, Jungles S, *et al*. Heterogeneity of the angiogenic response induced in different normal adult tissues by vascular permeability factor/vascular endothelial growth factor. Lab Invest 2000; 80: 99–115.

33 Shen F, Fan Y, Su H, Zhu Y, Chen Y, Liu W, *et al*. Adeno-associated viral vector-mediated hypoxia-regulated VEGF gene transfer promotes angiogenesis following focal cerebral ischemia in mice. Gene Ther 2008; 15: 30–9.

Acta Pharmacologica Sinica (2011) 32: 209–216
 1671-4083/11 $32.00
www.nature.com/aps

Original Article

N-benzyl-5-phenyl-1*H*-pyrazole-3-carboxamide promotes vascular endothelial cell angiogenesis and migration in the absence of serum and FGF-2

Hai-yan ZHANG[1, 2], Le SU[1, 2], Bin HUANG[1, 2], Jing ZHAO[1, 2], Bao-xiang ZHAO[3, *], Shang-li ZHANG[1, 2], Jun-ying MIAO[1, 2, *]

[1]Shandong Provincial Key Laboratory of Animal Cells and Developmental Biology, School of Life Science, Shandong University, Ji-nan 250100, China; [2]The Key Laboratory of Cardiovascular Remodeling and Function Research, Chinese Ministry of Education and Chinese Ministry of Health, Shandong University, Qilu Hospital, Ji-nan 250012, China; [3]Institute of Organic Chemistry, School of Chemistry and Chemical Engineering, Shandong University, Ji-nan 250100, China

Aim: To investigate the effect of *N*-benzyl-5-phenyl-1*H*-pyrazole-3-carboxamide (BPC) on angiogenesis in human umbilical vein endothelial cells (HUVECs).
Methods: Capillary-like tube formation on matrigel and cell migration analyses were performed in the absence of serum and fibroblast growth factor (FGF-2). Reactive oxygen species (ROS) were measured using a fluorescent probe, 2', 7'- dichlorodihydrofluorescein (DCHF). The nitric oxide (NO) production of HUVECs was examined using a NO detection kit. Morphological observation under a phase contrast microscope, a viability assay using 3-[4, 5-dimethylthiazol-2-yl]-2, 5-diphenyl-tetrazolium (MTT) and a lactate dehydrogenase (LDH) activity analysis by a detection kit were performed to evaluate the toxicity of BPC on HUVECs in the presence of serum and FGF-2. The level of hypoxia-inducible factor 1α (HIF-1α) and the release of vascular endothelial growth factor (VEGF) were measured by Western blot and ELISA, respectively.
Results: In the absence of serum and FGF-2, cells treated with BPC (5–20 μmol/L) rapidly aligned with one another and formed tube-like structures within 12 h. In the presence of serum and FGF-2, cells treated with BPC for 24, 48 and 72 h had no changes in morphology, viability or LDH release compared with the control group. Cell migration in the BPC-treated group was significantly increased compared with the control group. During this process, NO production and ROS level were elevated dramatically, and the levels of HIF-1α and VEGF were increased dependent on the generation of ROS.
Conclusion: BPC most effectively promoted angiogenesis and migration in HUVECs in the absence of FGF-2 and serum.

Keywords: pyrazole derivatives; angiogenesis; reactive oxygen species; nitric oxide; human umbilical vein endothelial cells; hypoxia-inducible factor 1α; vascular endothelial growth factor

Acta Pharmacologica Sinica (2011) 32: 209–216; doi: 10.1038/aps.2010.201

Introduction

More and more people are suffering from chronic ischemic diseases. Ischemia, defined as the insufficiency or even loss of blood flow to an organ, occurs as a result of various pathologies associated with vascular obstruction or disruption. These can include myocardial infarction, stroke and pulmonary embolism[1]. Newly formed blood vessels provide a route for supplying metabolic requirements such as nutrients, growth factors and oxygen to the site of hypoxic or ischemic tissues and organs affected by defective blood circulation and functionally improve ischemia-associated tissue damage and injury[2].

The pyrazole unit is a core structure in a number of natural products. Pyrazole derivatives are known to exhibit a wide range of biological properties. It has been widely reported that pyrazole derivatives could inhibit cell proliferation and promote cell apoptosis. In our laboratory, several pyrazole derivatives have been synthesized. We found that 1-arylmethyl-3-aryl-1*H*-pyrazole-5-carbohydrazide hydrazone derivatives could suppress A549 lung cancer cell growth[3], 1-(2'-hydroxy-3'-aroxypropyl)-3-aryl-1*H*-pyrazole-5-carbohydrazide derivatives induced A549 cell autophagy[4] and ethyl 3-(*o*-chlorophenyl)-5-methyl-1-phenyl-1*H*-pyrazole-4-carboxylate inhibited human umbilical vein endothelial cell (HUVEC) apoptosis[5]. Nevertheless, no reports about the effects of

* To whom correspondence should be addressed.
E-mail miaojy@sdu.edu.cn (Jun-ying MIAO);
bxzhao@sdu.edu.cn (Bao-xiang ZHAO)
Received 2010-05-25 Accepted 2010-11-01

multi-substituted pyrazole derivatives on the angiogenesis of vascular endothelial cells have yet been documented.

In our previous papers, we synthesized a series of pyrazole derivatives and obtained their crystal structures[6–9]. After screening, we identified *N*-benzyl-5-phenyl-1*H*-pyrazole-3-carboxamide (BPC) as a proangiogenic agent (Figure 1). Reactive oxygen species (ROS) and nitric oxide (NO) played important roles in angiogenesis. It was reported that ROS regulated angiogenesis and tumor growth through hypoxia-inducible factor 1α (HIF-1α) and vascular endothelial growth factor (VEGF)[10]. However, little is known about the ROS-HIF-1α-VEGF pathway in angiogenesis under ischemic conditions. Our current results show that BPC could effectively induce angiogenesis by increasing ROS and NO when deprived of FGF-2 and serum and that ROS regulates angiogenesis through HIF-1α and VEGF. The data reveal that BPC (5 μmol/L) exhibits protective proangiogenic properties. This suggests that BPC may represent a promising strategy for treating ischemic diseases.

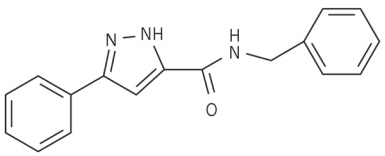

Figure 1. The structure of *N*-benzyl-5-phenyl-1*H*-pyrazole-3-carboxamide (BPC).

Materials and methods

Materials

HUVECs were obtained in our laboratory using the method of Jaffe *et al*[11]. Fetal bovine serum (FBS) was purchased from Hyclone Lab (USA). M199 medium was purchased from Gibco (USA). Matrigel was purchased from BD Biosciences (USA). The NO detection kit and LDH kit were purchased from Nanjing Jiancheng Bioengineering Institute (China). A fluorescent probe, 2′,7′-dichlorodihydrofluorescein (DCHF) was obtained from Sigma-Aldridch (USA). Chemicals including dimethyl sulfoxide (DMSO), 3-[4,5-dimethylthiazol-2-yl]-2,5-diphenyl-tetrazolium (MTT), *N*-acetyl-*L*-cysteine (antioxidant and free radical scavenger, NAC) and protease inhibitor cocktail were obtained from Sigma-Aldrich (St Louis, MO). All other chemicals were purchased from original sources and were of superior grade and purity.

Cell culture

HUVECs were cultured in M199 medium supplemented with 20% fetal bovine serum and FGF-2 (70 ng/mL) in a humidified incubator at 37 °C with 5% CO_2. The medium was refreshed on every second day. The experiments were performed on cells with a population doubling level (PDL) of 5–10.

Exposure of HUVECs to BPC

When the cultures of HUVECs reached sub-confluency, the medium was replaced with basal M199 medium (without serum and FGF-2) after one wash with the same medium. The cells were then treated in two ways: (a) cells deprived of serum and FGF-2 were cultured in basal M199 medium with DMSO [<0.1% (*v*/*v*)] (control group) and (b) cells cultured in basal M199 medium (without serum and FGF-2) were treated with 5, 10, 20, or 40 μmol/L BPC (test group). BPC was dissolved in DMSO and applied to cells such that the final concentration of DMSO in the culture medium was below 0.1% (*v*/*v*). DMSO at a concentration of 0.1% (*v*/*v*) does not affect cell viability. The morphological changes of cells were observed under a phase contrast microscope (Nikon, Japan) at 24, 48, and 72 h. To further investigate the roles of ROS in this process, we treated the cells with NAC (10 mmol/L) to depress the levels of ROS[12].

Cell viability assay

HUVECs were plated in 96-well cell culture plates. When the cultured cells became sub-confluent, they were washed once with basal M199 medium. Then the cells were treated with 5, 10, or 20 μmol/L of BPC in the presence of serum and FGF-2. At 24, 48, and 72 h, cell viability was determined by MTT assay, as described previously[13]. The viability was calculated as: percent=(*OD* of treated group/*OD* of control group)×100.

Lactate dehydrogenase (LDH) assay

An LDH assay was performed on the cells treated with BPC for 48 h using an LDH kit according to the manufacturer's protocol. LDH catalyzes the reduction of pyruvate to *L*-lactate with a concomitant oxidation of $NADH_2$ to NAD. Because the oxidation of $NADH_2$ is directly proportional to the reduction of pyruvate in equimolar amounts, LDH activity can be calculated from the rate of decrease in absorbance at 440 nm[14]. Light absorption was measured with a Cintra 5 UV-vis spectrometer (GBC, Australia), and LDH activity was calculated as follows:

$$\text{LDH (U/L)}=(\Delta A_{\text{sample/min}}-\Delta A_{\text{blank/min}})\times F$$

$F=1000\times V_{\text{total}}/(V_{\text{sample}}\times\text{extinction coefficient})$; where ΔA= change in absorbance, min=minute, V=volume in mL and extinction coefficient=mmol absorptivity of NADH at 440 nm (which was 6.3).

Capillary-like tube formation assay

The formation of vascular-like structures in HUVECs was assessed by growth-factor-reduced Matrigel as previously described[15]. HUVECs were seeded on 24-well plates coated with Matrigel at 4×10^4–5×10^4 cells/well in basal M199 medium and incubated at 37 °C for 1 h. Cells were treated with or without 5, 10, or 20 μmol/L BPC in the absence of FGF-2 and serum, then incubated at 37 °C for 12 h. Tube formation was observed with an inverted-phase contrast microscope (Nikon, Tokyo, Japan) at 2, 4, and 8 h. The degree of tube formation was quantified by measuring the length of tubes in random fields from each well using the National Institutes of Health (NIH) Image Program.

Cell migration assay

The cell migration assay was performed as described previously[16, 17]. Cells were seeded on 24-well plates. When cells reached a post-confluent state, wounds of a 1 mm width were created by scraping the cell monolayer with a sterile pipette tip. Cells were treated with 5, 10, or 20 μmol/L BPC in the absence of FGF-2 and serum, then incubated at 37 °C for 24 h. Migration was documented by photos taken immediately after scraping. Cell migration was quantified by measuring the distance between the wound edges at 0, 12, and 24 h using the NIH Image Program.

NO production assay

HUVECs were treated as described above for 3, 6, and 12 h. Then 100 μL of culture solution was used for the NO assay. NO production was detected with a NO detection kit following the manufacturer's protocol. The optical density was measured at a wavelength of 550 nm. NO production was expressed as μmol/L.

Intracellular ROS assay

HUVECs were treated as described above for 3, 6, and 12 h. Intracellular ROS levels were measured using a fluorescent probe, 2′,7′-dichlorodihydrofluorescein (DCHF) (Sigma), which could be rapidly oxidized into the highly fluorescent 2′,7′-dichlorofluorescein (DCF) in the presence of intracellular ROS[18]. Fluorescence was monitored with a laser scanning confocal microscope (Leica, Germany) using an excitation wavelength of 488 nm. The amount of ROS was quantified as the relative fluorescence intensity of DCF per cell in the scan area.

VEGF release assay

HUVECs were treated as described above for 3, 6, and 12 h. The culture supernatants were collected and the level of VEGF in the culture media was quantified using a commercially available ELISA kit (R&D, USA) according to the manufacturer's instructions. The optical density was measured at a wavelength of 450 nm.

Western blot analysis

Cells with various treatments were lysed in lysis buffer containing 25 mmol/L Tris-HCl (pH 6.8), 2% SDS, 6% glycerol, 1% 2-mercaptoethanol, 2 mmol/L PMSF, 0.2% bromophenol blue and a protease inhibitor cocktail for 10 min at room temperature and boiled for another 10 min. Protein concentration was determined by Coomassie brilliant blue protein assay. Equal amounts of total protein (40 mg) were separated with 15% SDS-PAGE and were electroblotted onto polyvinylidene difluoride membranes. The membrane was blocked with 5% (*w*/*v*) nonfat dry milk in PBS–Tween 20 (0.05% PBST) for 1 h and incubated with anti-HIF-1α and anti-GAPDH antibodies (1/1000) at 4–8 °C overnight. After washing in TBST and TBS, the membrane was incubated with appropriate horseradish peroxidase-conjugated secondary antibodies (1/5000) for 1 h at room temperature. The immunoreactive bands were chromogenously developed with 3,30-diaminobenzidine. GAPDH was used as a loading control. The relative quantity of proteins was analyzed by use of Quantity One software (Bio-Rad, Hercules, CA). HIF-1α levels were measured relative to the loading control (GAPDH). The densitometric analysis of HIF-1α levels, from experiments performed at least in triplicate, was shown relative to GAPDH levels.

Statistical analyses

Data were expressed as the means±SEM. (n>3) and analyzed by t-test. Differences at P<0.05 and P<0.01 were considered statistically significant and dramatically significant, respectively.

Results

Effects of BPC on endothelial cell morphology in the absence and presence of serum and FGF-2

When deprived of serum and FGF-2, HUVECs gradually detach from the dish and undergo apoptosis. This is an *in vitro* model commonly used to mimic the *in vivo* ischemic condition[19]. In this study, we screened proangiogenic agents using this model of the ischemic condition. When deprived of serum and FGF-2 for 48 h, cells treated with BPC were elongated and formed capillary-like structures in morphology compared with control cells (Figure 2A).

To investigate the toxicity of BPC on HUVECs under normal conditions, we examined the morphology, viability and LDH activity of HUVECs treated with BPC in the presence of serum and FGF-2. The results showed no morphological changes among these groups at each time point (Figure 2B). In addition the MTT assay showed that under normal conditions, cell viability was not affected (Figure 2C). As shown in Figure 2D, the release of LDH from HUVECs was not increased by BPC. The data showed that BPC was not toxic to cells under normal conditions.

BPC induces endothelial cell differentiation into capillary-like tube structures *in vitro*

To demonstrate the proangiogenic function of BPC on HUVECs, we performed a capillary-like tube formation assay on Matrigel. Capillary-like tubes developed in HUVECs treated with BPC (5, 10, or 20 μmol/L) on Matrigel-coated 24-well plates with basal M199 medium at 2, 4, and 8 h. At the early stage, HUVECs could not differentiate towards capillary-like tube structures without BPC. In the presence of BPC, the cells rapidly aligned with one another and formed tube-like structures within 12 h (Figure 3). BPC (5 μmol/L) significantly promoted the capillary-like tube formation compared with control at 8 h (P<0.01) (Figure 3B).

BPC promotes migration of endothelial cells *in vitro*

Migration of endothelial cells plays an importnat role in angiogenesis[20]. To examine the effect of BPC on cell migration, we performed the cell monolayer wound healing assay. As shown in Figure 4, cells without BPC treatment showed little migratory capacity at the 12 and 24 h time points. Cell

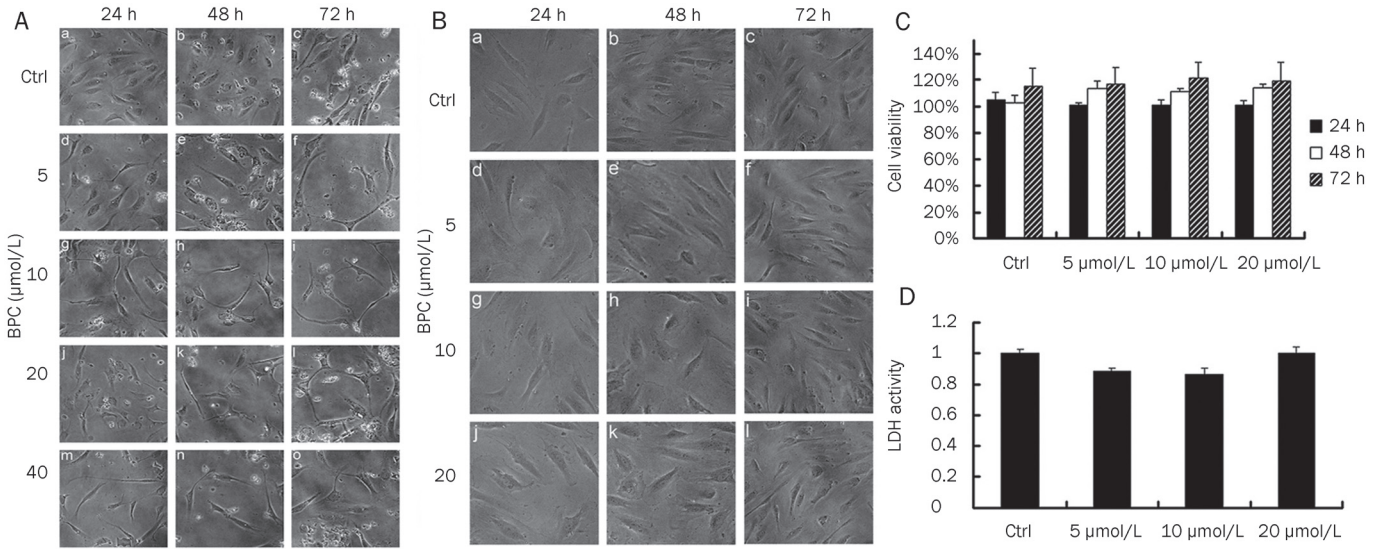

Figure 2. Effects of BPC on endothelial cells in the absence and presence of serum and FGF-2. (A) Cell morphological micrographs were obtained under a phase contrast microscope at 24, 48 and 72 h (×200). In the control group (Ctrl), cells were cultured in basal M199 medium (without serum and FGF-2) with DMSO [<0.1% (*v/v*)]. In the experimental groups, cells were treated with 5 (d–f), 10 (g–i), 20 (j–l), or 40 (m–o) μmol/L BPC. (B) Cell morphological micrographs obtained under a phase contrast microscope at 24, 48 and 72 h (×200). In the control group (Ctrl), cells were cultured in M199 medium with DMSO [<0.1% (*v/v*)]. In the experimental groups, cells were treated with 5 (d–f), 10 (g–i), or 20 (j–l) μmol/L BPC. (C) Cell viability was determined using MTT assay at 24, 48 and 72 h in the presence of serum and FGF-2 (n=3). (D) LDH assay was performed on cells treated as described in the text for 48 h in the presence of serum and FGF-2 (n=3).

migration in the BPC treated group was significantly increased compared with control (P<0.05, P<0.01). BPC at 5 μmol/L promoted cell migration most effectively (Figure 4B).

BPC enhances ROS levels and intracellular NO generation

ROS plays an important role in modulating angiogenesis. We detected the levels of intracellular ROS in the cells treated as described above at 3, 6, and 12 h. As shown in Figure 5A, the level of ROS in cells treated with BPC increased in a dose-dependent manner at 6 and 12 h (P<0.05, P<0.01). After incubation with NAC, the cells did not differentiate towards a capillary-like tube structure compared with those not treated with NAC 10 mmol/L (Figure 5C), but ROS levels were effectively depressed (data not shown).

It is well known that NO participates in multiple events in HUVECs, including differentiation and migration. NO production was examined after treatment with BPC for 3, 6, and 12 h. The results showed that NO production of HUVECs treated with BPC was altered significantly at 3 and 6 h (P<0.05, P<0.01) (Figure 5D). To further analyze the relationship between ROS and NO, we examined NO production after incubation with NAC 10 mmol/L. The results showed that NO generation was not affected (Figure 5E).

BPC enhanced the HIF-1α level and VEGF release depending on the generation of ROS

VEGF plays a major role in the induction of angiogenesis and is transcriptionally regulated by HIF-1 in response to hypoxia[21]. In previous studies, endogenous ROS levels could regulate HIF-1α expression[22]. In this study, HIF-1α was increased after BPC treatment. However, HIF-1α expression was inhibited when NAC was used to eliminate ROS (Figure 6A, 6B). The results indicate that HIF-1α expression depends on the generation of cellular ROS.

After treatment with BPC, we examined VEGF levels using ELISA. As shown in Figure 6C, the release of VEGF was enhanced by BPC. To test whether ROS affected VEGF release, we used NAC to eliminate ROS. The results show that the release of VEGF was inhibited when ROS levels were depressed (Figure 6D).

Discussion

Angiogenesis generally refers to the growth of microvessels that sprouts the size of capillary blood vessels[23]. It plays a critical role in both physiological processes, such as wound healing, embryological development and the menstrual cycle, and the pathogenesis of various diseases, such as cancer, diabetic retinopathy and rheumatoid arthritis[24, 25]. In the last century, emerging evidence suggested that angiogenesis may be an ideal strategy to treat ischemic diseases. The promotion of angiogenesis facilitates various physiological processes and the treatment of diseases including inflammatory diseases, cardiac ischemia, peripheral vascular diseases and myocardial infarction. In our study, pyrazole derivatives were synthesized and screened. We identified BPC as a proangiogenic agent in the absence of serum and FGF-2. Our data showed that BPC at 5 μmol/L could effectively induce endothelial cell angiogenesis in the absence of FGF-2 and serum. The identification of BPC may contribute to further work in the development of a potential drug for treating ischemic diseases.

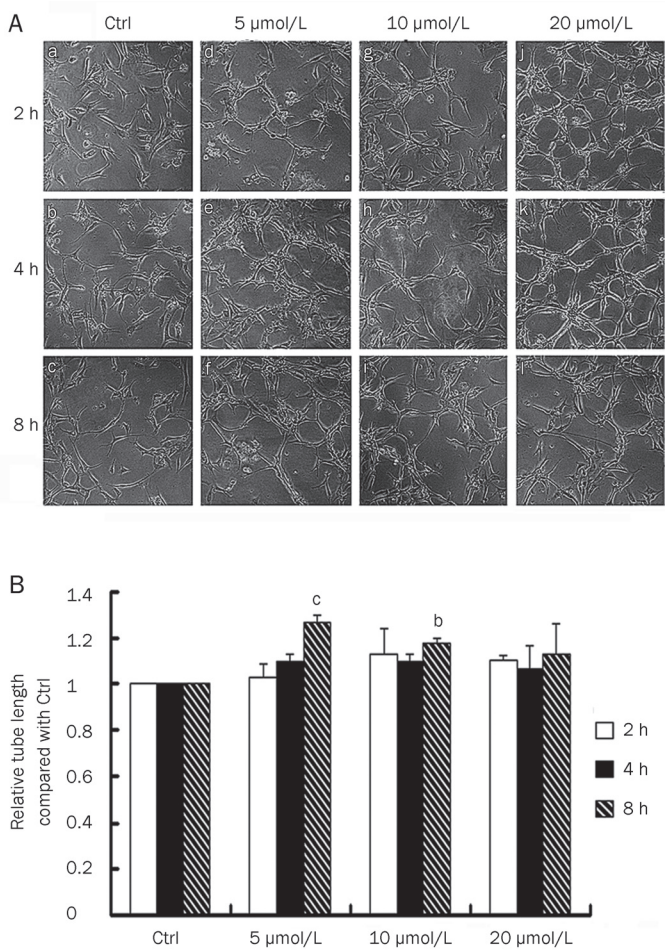

Figure 3. BPC induced endothelial cell differentiation into capillary-like structures *in vitro*. (A) BPC promoted vascular structure formation in an *in vitro* Matrigel assay without FGF-2 and serum (×200). HUVECs were seeded without BPC (a–c) and with BPC (d–l) for 2, 4, and 8 h. (B) Quantitative assessment of the extent of tube formation ($^bP<0.05$, $^cP<0.01$ *vs* Ctrl, $n=5$).

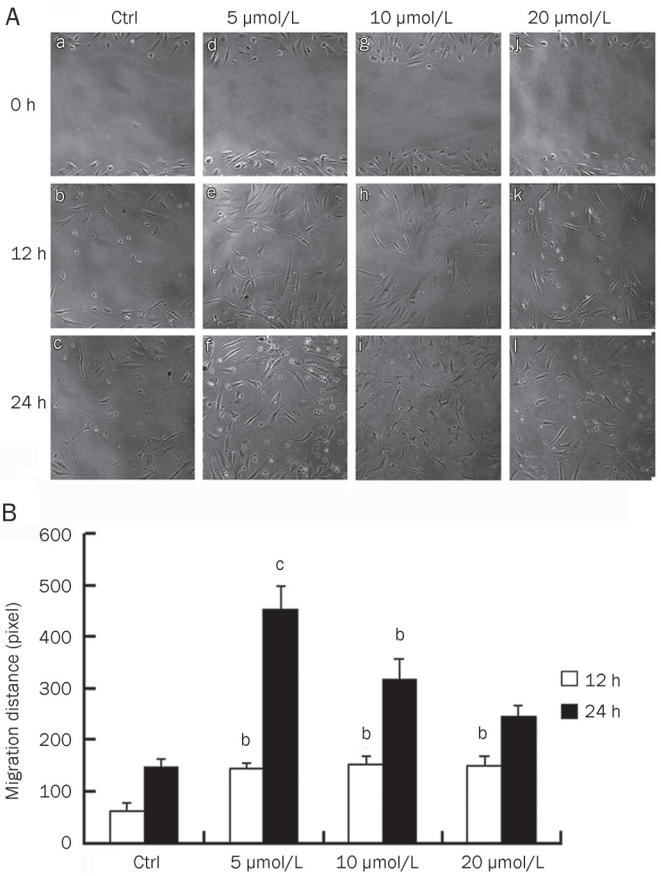

Figure 4. BPC promotes migration of endothelial cells *in vitro*. BPC induced HUVEC migration in the absence of FGF-2 and serum (200×). (A) Representative photomicrographs of migration. Cells migrated in FGF-2 and serum-free medium at 0, 12, and 24 h in the absence (a–c) and presence of BPC (d–l). (B) Quantitative assessment of migration distance ($^bP<0.05$, $^cP<0.01$ *vs* Ctrl, $n=4$).

ROS generated by endothelial cells include superoxide and hydroxyl, nitric oxide (NO) and non-radical species such as hydrogen peroxide (H_2O_2)[24]. Accumulating evidence suggests that high levels of ROS could act as signaling molecules to mediate various growth-related responses, including angiogenesis. It has been reported that VEGF (vascular endothelial growth factor) and angiopoietin-1 (Ang1), two angiogenic growth factors, induce EC migration through an increase in ROS[13, 26]. Recently, Zhao *et al* reported that ROS promote the formation of new vessels in the infracted heart and contribute to cardiac repair[25]. In our study, BPC promoted HUVEC angiogenesis, while ROS were significantly increased. VEGF is considered to be the most important growth factor involved in angiogenesis, which is mainly regulated by HIF-1 in response to hypoxia. HIF-1 is a heterodimeric basic helix-loop-helix transcription factor composed of HIF-1α and HIF-1β subunits[22]. It has been reported that endogenous ROS levels could regulate HIF-1α and VEGF expression to induce angiogenesis in ovarian cancer cells[10]. However, the role of the ROS-HIF-1α-VEGF pathway in angiogenesis under ischemic conditions remains to be defined. Our results showed that the levels of HIF-1α and VEGF were modulated by ROS during this process. It suggests that BPC promotes angiogenesis through the ROS-HIF-1α-VEGF pathway.

Nitric oxide (NO) is a short-lived free radical that acts as a small biological molecule and exists extensively in the body. NO, a highly diffusible intercellular signaling molecule with a wide range of biological effects, is generated by nitric oxide synthase (NOS), which catalyzes the conversion of *L*-arginine to *L*-citrulline[27]. Since it was discovered 20 years ago, NO has been found to play an important role in angiogenesis and in the nervous and immune systems. The release of NO is of great importance for regulating endothelial cell function during vasodilatation, vascular remodeling and angiogenesis[28]. It has been reported that NO is required in VEGF-induced angiogenesis in HUVECs[29]. Our results showed that BPC increased the release of NO in this process. NO may act as an important modulator in BPC-induced angiogenesis.

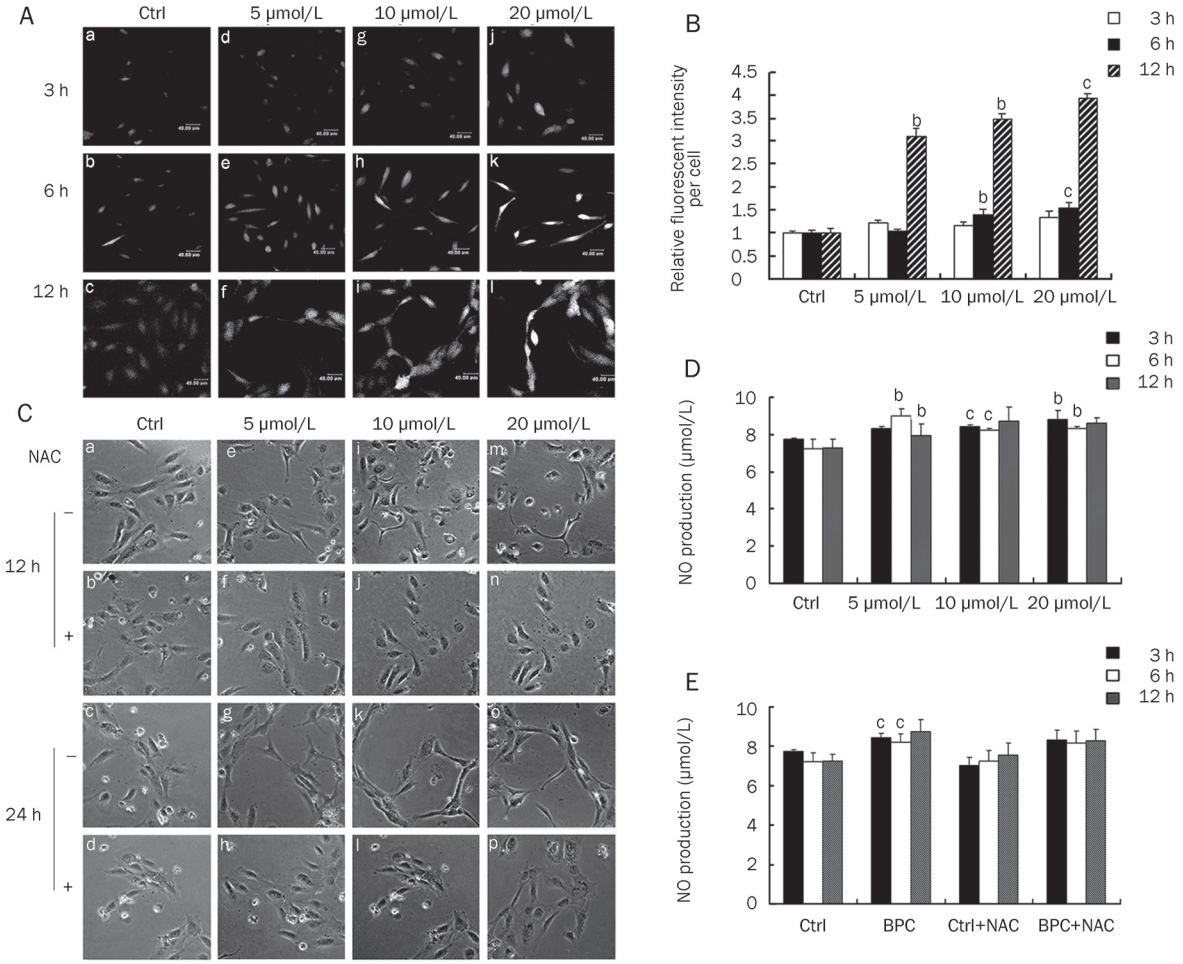

Figure 5. BPC induces angiogenesis through increase in ROS and NO. (A) An intracellular ROS assay was performed on the cells treated with BPC 5–20 μmol/L for 3, 6, and 12 h (×200). Relative DCF fluorescence reflected the intensity of ROS in Ctrl and BPC groups. (B) Quantitative assessment of ROS levels using relative fluorescence intensity of DCF per cell in the scan. $^{b}P<0.05$, $^{c}P<0.01$ *vs* Ctrl. (C) NAC inhibited angiogenesis induced by BPC (×200). (D)The change of NO production in cells treated with BPC 5–20 μmol/L for 3, 6, and 12 h. $^{b}P<0.05$, $^{c}P<0.01$ vs Ctrl, $n = 3$. (E) NO increase was not affected by NAC 10 mmol/L. Ctrl cells were cultured in M199 medium with DMSO. BPC cells were treated with 10 μmol/L BPC ($^{c}P<0.01$ *vs* ctrl, $n=3$).

Pyrazole compounds can act as inhibitors and cytotoxic agents. It has been reported that 4′-(6,7-disubstituted-2,4-dihydro-indeno [1,2-c]pyrazol-3-yl)-biphenyl-4-ol can act as a potent Chk1 inhibitor and that the pyrazole-based compound could inhibit the activity of heat shock protein 90[30, 31]. In our present study, we found that BPC was not toxic to endothelial cells under normal conditions. Furthermore, BPC could effectively induce endothelial cell angiogenesis in the absence of serum and FGF-2. These data reveal that BPC, with its remarkable biological properties and no toxic properties, exhibits exceptional characteristics among the multitudinous pyrazole compounds. This suggests that BPC could be practically used in clinical trials.

In summary, the results of this study showed that BPC could induce HUVEC angiogenesis and promote migration in the absence of FGF-2 and serum *in vitro*. The results also revealed that 5 μmol/L BPC significantly promoted angiogenesis and migration. Angiogenesis induced by BPC was mediated by the ROS-HIF-1α-VEGF and NO signal pathways. Moreover, in the presence of FGF-2 and serum, BPC did not affect cell morphology and viability and did not increase LDH activity. The data indicated that BPC at 5 μmol/L exhibited significant proangiogenic properties and that it might represent a potential agent for the development of therapeutic drugs to treat ischemic diseases.

Acknowledgements

This work was financially supported by the National 973 Research Project (No 2011CB503906), the National Natural Science Foundation of China (No 90813022 and 20972088) and the Science and Technology Developmental Project of Shandong Province (No 2008GG10002034 and Z2008D04).

Author contribution

Jun-ying MIAO and Bao-xiang ZHAO designed the research; Hai-yan ZHANG, Le SU, Bin HUANG, Jing ZHAO, and

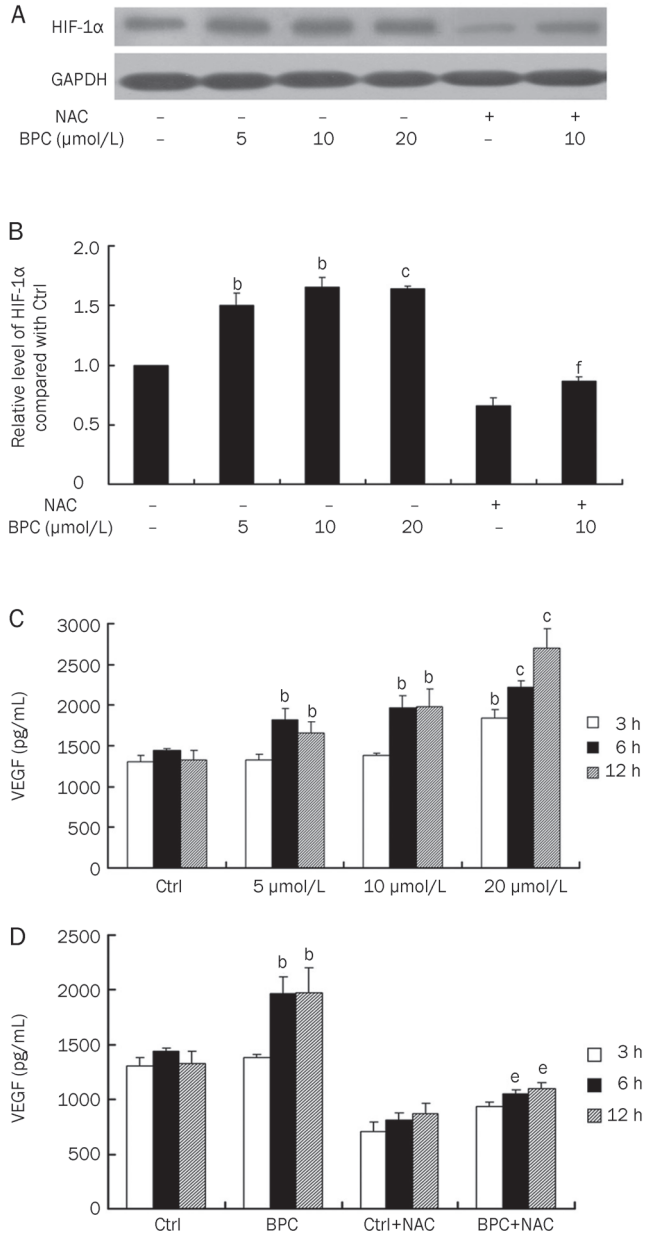

Figure 6. BPC enhanced HIF-1α levels and VEGF release dependent on the generation of ROS. (A) BPC-enhanced HIF-1α expression was inhibited by NAC 10 mmol/L at 6 h. (B) Bar graph plots of relative HIF-1α levels ($^bP<0.05$, $^cP<0.01$ *vs* Ctrl. $^fP<0.01$ *vs* 10 μmol/L BPC; $n=3$). (C) BPC enhanced VEGF release. In the control group (Ctrl), cells were cultured in M199 medium with DMSO [<0.1% (*v*/*v*)]. In the experimental groups, cells were treated with BPC at 5, 10, or 20 μmol/L. ($^bP<0.05$, $^cP<0.01$ *vs* Ctrl. $n=3$). (D) BPC-enhanced VEGF release was inhibited by NAC 10 mmol/L. Ctrl cells were cultured in M199 medium with DMSO [<0.1% (*v*/*v*)]. BPC cells were treated with 10 μmol/L BPC ($^bP<0.05$ *vs* Ctrl. $^eP<0.05$ *vs* 10 μmol/L BPC; $n=3$).

Shang-li ZHANG performed the research; Shang-li ZHANG analyzed the data; Hai-yan ZHANG wrote the paper.

References

1 Chatterjee S, Chapman KE, Fisher AB. Lung ischemia: a model for endothelial mechanotransduction. Cell Biochem Biophys 2008; 52: 125–38.
2 Chunga BH, Leec JJ, Kimb JD, Jeoungd D, Leed H, Choe J, *et al*. Angiogenic activity of sesamin through the activation of multiple signal pathways. Biochem Biophys Res Commun 2009; 391: 254–60.
3 Xia Y, Fan CD, Zhao BX, Zhao J, Shin DS, Miao JY. Synthesis and structure-activity relationships of novel 1-arylmethyl-3-aryl-1*H*-pyrazole-5-carbohydrazide hydrazone derivatives as potential agents against A549 lung cancer cells. Eur J Med Chem 2008; 43: 2347–53.
4 Fan CD, Zhao BX, Wei F, Zhang GH, Dong WL, Miao JY. Synthesis and discovery of autophagy inducers for A549 and H460 lung cancer cells, novel 1-(2′-hydroxy-3′-aroxypropyl)-3-aryl-1*H*-pyrazole-5-carbohydrazide derivatives. Bioorg Med Chem Lett 2008; 18: 3860–4.
5 Zhao BX, Zhang L, Zhu XS, Wan MS, Zhao J, Zhang Y, *et al*. Synthesis and discovery of a novel pyrazole derivative as an inhibitor of apoptosis through modulating integrin beta4, ROS, and p53 levels in vascular endothelial cells. Bioorg Med Chem 2008; 16: 5171–80.
6 Ge YQ, Xia Y, Wei F, Dong WL, Zhao BX. *N*-Benzyl-5-phenyl-1*H*-pyrazole-3-carboxamide. Acta Cryst 2007; E63: o1186–o1187.
7 Ge YQ, Dong WL, Xia Y, Wei F, Zhao BX. Ethyl 3-(2-hydroxy-5-methylphenyl)-1*H*-pyrazole-5-carboxylate. Acta Cryst 2007; E63: o1313–o1314.
8 Dong WL, Ge YQ, Xia Y, Zhao BX. Ethyl 5-(ethoxycarbonyl)-3-phenyl-1*H*-pyrazole-1-acetate. Acta Cryst 2007; E63: o4701.
9 Dong WL, Ge YQ, Zhao BX. Ethyl 5-(ethoxycarbonyl)-3-(4-methoxyphenyl)-1*H*-pyrazole-1-acetate. Acta Cryst 2008; E64: o64.
10 Xia C, Meng Q, Liu LZ, Rojanasakul Y, Wang XR, Jiang BH. Reactive oxygen species regulate angiogenesis and tumor growth through vascular endothelial growth factor. Cancer Res 2007; 67: 10823–30.
11 Jaffe EA, Nachman RL, Becker CG, Minick CR. Culture of human endothelial cells derived from umbilical veins. Identification by morphologic and immunologic criteria. J Clin Invest 1973; 52: 2745–56.
12 Chen YH, Xu X, Sheng MJ, Zhang XY, Gu Q, Zheng Z. PRMT-1 and DDAHs-induced ADMA upregulation is involved in ROS- and RAS-mediated diabetic retinopathy. Exp Eye Res 2009; 89: 1028–34.
13 Price P, McMillan TJ. Use of the tetrazolium assay in measuring the response of human tumor cells to ionizing radiation. Cancer Res 1990; 50: 1392–6.
14 Meng N, Wu L, Gao J, Zhao J, Su L, Su H, *et al*. Lipopolysaccharide induces autophagy through BIRC2 in human umbilical vein endothelial cells. J Cell Physiol 2010; 225, 174–9.
15 Kureishi Y, Luo Z, Shiojima I, Bialik A, Fulton D, Lefer DJ, *et al*. The HMG-CoA reductase inhibitor simvastatin activates the protein kinase Akt and promotes angiogenesis in normocholesterolemic animals. Nat Med 2000; 6: 1004–10.
16 Burk RR. A factor from a transformed cell line that affects cell migration. Proc Natl Acad Sci USA 1973; 70: 369–72.
17 Vasvari GP, Dyckhoff G, Kashfi F, Lemke B, Lohr J, Helmke BM, *et al*. Combination of thalidomide and cisplatin in an head and neck squamous cell carcinomas model results in an enhanced antiangiogenic activity *in vitro* and *in vivo*. Int J Cancer 2007; 121: 1697–704.
18 Su L, Zhao B, Lv X, Wang N, Zhao J, Zhang S, *et al*. Safrole oxide induces neuronal apoptosis through inhibition of integrin beta4/SOD activity and elevation of ROS/NADPH oxidase activity. Life Sci 2007; 80: 999–1006.
19 Araki S, Shimada Y, Kaji K, Hayashi H. Apoptosis of vascular endothelial cells by fibroblast growth factor deprivation. Biochem Biophys Res Commun 1990; 168: 1194–200.
20 Matsunaga N, Shimazawa M, Otsubo K, Hara H. Phosphatidylinositol

inhibits vascular endothelial growth factor-A–induced migration of human umbilical vein endothelial cells. J Pharmacol Sci 2008; 106: 128–35.

21 Gao N, Ding M, Zheng JZ, Zhang Z, Leonard SS, Liu KJ, *et al*. Vanadate-induced expression of hypoxia-inducible factor 1α and vascular endothelial growth factor through phosphatidylinositol 3-kinase/Akt pathway and reactive oxygen species. J Biol Chem 2002; 277: 31963–71.

22 Liu LZ, Hu XW, Xia C, He J, Zhou Q, Shi X, *et al*. Reactive oxygen species regulate epidermal growth factor-induced vascular endothelial growth factor and hypoxia-inducible factor-1α expression through activation of AKT and P70S6K1 in human ovarian cancer cells. Free Radic Biol Med 2006; 41: 1521–33.

23 Folkman J. Angiogenesis: an organizing principle for drug discovery? Nat Rev Drug Discov 2007; 6: 273–86.

24 Ushio-Fukai M, Alexander RW. Reactive oxygen species as mediators of angiogenesis signaling: role of NAD(P)H oxidase. Mol Cell Biochem 2004; 264, 85–97.

25 Zhao W, Zhao T, Chen Y, Ahokas RA, Sun Y. Reactive oxygen species promote angiogenesis in the infarcted rat heart. Int J Exp Pathol 2009; 90: 621–9.

26 Harfouche R, Malak NA, Brandes RP, Karsan A, Irani K, Hussain SN. Roles of reactive oxygen species in angiopoietin-1/tie-2 receptor signaling. FASEB J 2005; 19: 1728–30.

27 Kung HN, Chien CL, Chau GY, Don MJ, Lu KS, Chau YP. Involvement of NO/cGMP signaling in the apoptotic and anti-angiogenic effects of beta-lapachone on endothelial cells *in vitro*. J. Cell Physiol 2007; 2: 522–32.

28 Borgmann S, Radtke I, Erichsen T, Blochl A, Heumann R, Schuhmann W. Electrochemical high-content screening of nitric oxide release from endothelial cells. Chembiochem 2006; 4: 662–8.

29 Cudmore M, Ahmad S, Al-Ani B, Hewett P, Ahmed S, Ahmed A. VEGF-E activates endothelial nitric oxide synthase to induce angiogenesis via cGMP and PKG-independent pathways. Biochem Biophys Res Commun 2006; 345: 1275–82.

30 Sharp SY, Boxall K, Rowlands M, Prodromou C, Roe SM, Maloney A, *et al*. *In vitro* biological characterization of a novel, synthetic diaryl pyrazole resorcinol class of heat shock protein 90 inhibitors. Cancer Res 2007; 67: 2206–16.

31 Tao ZF, Li G, Tong Y, Chen Z, Merta P, Kovar P, *et al*. Synthesis and biological evaluation of 4′-(6,7-disubstituted-2,4-dihydro-indeno [1,2-c]pyrazol-3-yl)-biphenyl-4-ol as potent Chk1 inhibitors. Bioorg Med Chem Lett 2007; 17: 4308–15.

Acta Pharmacologica Sinica (2011) 32: 217–222
 1671-4083/11 $32.00
www.nature.com/aps

Original Article

Fluoxetine inhibited extracellular matrix of pulmonary artery and inflammation of lungs in monocrotaline-treated rats

Xue-qin LI[1, 3], Han-ming WANG[1], Chun-guang YANG[1], Xin-hua ZHANG[1], Dan-dan HAN[1], Huai-liang WANG[1, 2, *]

[1]Department of Clinical Pharmacology, College of Pharmacy and [2]National Key Subject, Division of Respiratory Diseases, China Medical University, Shenyang 110001, China; [3]Department of Pharmacy, Zhongshan City People's Hospital, Zhongshan 528403, China

Aim: To investigate the effects of the selective serotonin reuptake inhibitor (SSRI) fluoxetine on extracellular matrix (ECM) remodeling of the pulmonary artery and inflammation of the lungs in pulmonary arterial hypertension (PAH) induced by monocrotaline in rats.
Methods: MCT-induced chronic PAH was established in Wistar rats. After treatment with fluoxetine for 3 weeks, pulmonary hemodynamic measurement and morphological investigation of lung tissues were undertaken. The main components of the ECM, elastin and collagen, were detected using Van Gieson stain and Orcein stain, respectively, or using Victoria-ponceau's double stain. The ECM proteolytic enzymes matrix metalloproteinase (MMP)-2 and MMP-9, and the tissue inhibitors of metalloproteinase (TIMP)-1 and TIMP-2, were detected by Western blot. Inflammation of lung tissue was assayed using lung morphology and inflammatory cytokine expression.
Results: Fluoxetine (2 and 10 mg/kg) significantly inhibited MCT-induced PAH, attenuated pulmonary arterial muscularization and ECM remodeling, and decreased MMP/TIMP expression. Fluoxetine also suppressed inflammatory responses in lung tissue and inhibited the expression of the inflammatory cytokines interleukin-1β (IL-1β), tumor necrosis factor-α (TNF-α), monocyte chemotactic protein (MCP-1) and intercellular adhesion molecule-1 (ICAM-1).
Conclusion: Fluoxetine inhibited MCT-induced ECM remodeling of the pulmonary artery and inflammation of lung tissue. These effects were related to its inhibition on MMPs/TIMPs and cytokine productions.

Keywords: extracellular matrix; inflammation; pulmonary arterial hypertension; selective serotonin reuptake inhibitor

Acta Pharmacologica Sinica (2011) 32: 217–222; doi: 10.1038/aps.2010.187; published online 10 Jan 2011

Introduction

Pulmonary arterial hypertension (PAH) is characterized by a sustained and progressive increase in pulmonary arterial pressure (PAP) with pathological changes involving vasoconstriction, vascular remodeling and inflammation, which may lead to right-heart failure and ultimately death. Whereas the pathogenesis of PAH is complicated, it is believed that the main processes lead to progressive pulmonary arterial remodeling, including hypertrophy and hyperplasia of pulmonary arterial smooth muscle cells (PASMCs), muscularization of normally nonmuscular peripheral arteries, and deposition of the extracellular matrix (ECM)[1–3].

The ECM, as a biologically active and dynamic composition of vasculature, plays important roles in maintaining the histological structure of the vessel wall and regulating PASMCs contractility and proliferation[4]. Collagen and elastin are the major structural components of the ECM, which interlace in a complex network and are well adapted to accomplish mechanical tasks[5, 6]. The ECM is regulated by specific and unique proteolytic enzymes, the matrix metalloproteinases (MMPs). Among the MMPs, MMP-2, and MMP-9 degrade collagen more efficiently than the others, and they are involved in the vascular smooth muscle cell activation and neointimal formation that characterize arterial tissue remodeling after injury[7, 8]. MMPs are modulated by the tissue inhibitors of metalloproteinase (TIMP)-1 and TIMP-2. The imbalance of MMPs/TIMPs induces matrix abnormality and remodeling, which has been found in idiopathic PAH patients[9]. Thus, the integrity and balance of ECM is essential for normal lung function and response to injury[10], and identifying MMP/TIMP changes will help us better understand the pathobiology of PAH.

Serotonin, as a type of vasoconstrictor and mitogen for smooth muscle cells, is an important endogenous vasoactive substance involved in PAH. The internalization of

* To whom correspondence should be addressed.
E-mail hlwang@mail.cmu.edu.cn
Received 2010-05-30 Accepted 2010-09-29

serotonin into PASMCs by high-affinity serotonin transporters (SERT) promoted smooth muscle cell hyperplasia and hypertrophy[11, 12]. It was reported that the plasma concentration in serotonin was significantly increased in PAH patients[13]. We have previously reported that serotonin induced PASMCs mitogenesis in vitro, and serotonin selective reuptake inhibitor (SSRI) fluoxetine inhibited serotonin-induced PASMCs proliferation via blocking SERT[14]. We have also found that SSRI fluoxetine and sertraline protected against pulmonary vascular remodeling by inhibiting pulmonary vascular muscularization in monocrotaline (MCT)-induced pulmonary hypertensive rats[15, 16]. However, whether SSRI has a protective effect against ECM remodeling in the pulmonary artery remains unknown.

Inflammatory mechanisms play an important role in the development of PAH. It has been demonstrated that lymphocytes and macrophages were present in the vicinity of remodeled pulmonary vessels and that cytokines such as interleukin (IL)-1, IL-6, IL-8, tumor necrosis factor-α (TNF-α), monocyte chemotactic protein-1 (MCP-1) and intercellular adhesion molecule-1 (ICAM-1) were increased in PAH patients[17–20]. We have also reported previously that chronic lung inflammation existed in MCT-induced PAH rats[21]. However, several studies have shown that fluoxetine had an anti-inflammatory effect by decreasing cytokine production from peripheral blood in patients suffering from major depressive disorder[22] and by attenuating carrageenan-induced inflammation response in rats[23]. Yet, whether fluoxetine inhibits an inflammatory response in PAH is not clear.

Therefore, the present study is to investigate the effects of fluoxetine on the extracellular matrix of the pulmonary artery and on the inflammation of lung tissue in MCT-induced PAH rats.

Materials and methods

Animal models

Male Wistar rats (167±18 g) from Animal Resource Center, China Medical University (Certification No: Liaoning 034) were divided into four groups, *ie*, control, MCT, MCT plus fluoxetine 2 $mg{\cdot}kg^{-1}{\cdot}d^{-1}$ (MCT+F2) and MCT plus fluoxetine 10 $mg{\cdot}kg^{-1}{\cdot}d^{-1}$ (MCT+F10). Rats in the MCT, MCT+F2, and MCT+F10 groups were treated with a single intraperitoneal injection of 60 mg/kg MCT (Sigma, St Louis, USA), and rats in the control group were treated with an equivalent amount of vehicle. Rats in the MCT+F2 and MCT+F10 groups also received fluoxetine (Eli Lilly, Indianapolis, USA) at doses of 2 $mg{\cdot}kg^{-1}{\cdot}d^{-1}$ and 10 $mg{\cdot}kg^{-1}{\cdot}d^{-1}$ by gavage, respectively. Meanwhile, rats in the control and MCT groups received vehicle only. Rats were fed with solid food and water *ad lib* in an alternating 12 h light/dark cycle under controlled temperature (18–22 °C) and humidity (50%–65%) for 3 weeks.

Hemodynamic measurement

After 3 weeks, rats were anaesthetized with 3% sodium pentobarbital (40 mg/kg). A polyethylene catheter (PE-50) was inserted into the right carotid artery to measure systemic arterial pressure (SAP). A PV-1 catheter was inserted into the pulmonary artery through the right jugular vein via the right atrium and ventricle for measurement of pulmonary arterial pressure (PAP). Hemodynamic variables were measured with a pressure transducer and recorded on a polygraph system (RM6000, Kohden, Tokyo, Japan).

Lung morphology

The lower lobe of right lungs and pulmonary arteries were fixed with formalin solution. After paraffin embedding, 5 μm sections were stained with hematoxylin and eosin for investigation of inflammation and the thickness of the pulmonary arterial wall by light microscopy. The external and internal diameters of 7–10 intra-acinar pulmonary arteries per rat were measured in 5 rats of each group. The ratio of the medial thickness of the pulmonary artery was calculated by the equation shown as follows[24]:

$$\text{The thickness of pulmonary arterial wall} = \frac{\text{External diameter} - \text{internal diameter}}{\text{External diameter}} \times 100\%$$

Collagen and elastin staining

Serial paraffin sections were stained with Van Gieson stain, Orcein stain, or Victoria-ponceau's double stain to localize collagen and elastin in lungs and pulmonary arteries.

Western blot

The left lungs were immediately removed to liquid nitrogen for measurement of protein expression. Lung samples were homogenized in lysis buffer. Total protein from each sample was separated by sodium dodecyl sulfate polyacrylamide gel electrophoresis and transferred to nitrocellulose membrane. The membranes were blocked by TBS-0.05% Tween-20 (TBS-T) with 5% nonfat dry milk for 60 min and were then incubated with mouse anti-rat MMP-2 (1:600, Santa Cruz, California, USA) and TIMP-2 (1:400, Santa Cruz, California, USA); goat anti-rat MMP-9 (1:600, Santa Cruz, California, USA), TIMP-1 (1:400, Santa Cruz, California, USA) and TNF-α (1:1000, Santa Cruz, California, USA); rabbit anti-rat IL-1β (1:400, USCN, Missouri, USA), ICAM-1 (1:800, Santa Cruz, California, USA), MCP-1 (1:400, Boster, Wuhan, China) and β-actin (1:2000, Santa Cruz, California, USA) antibodies in TBS-T with 5% BSA overnight at 4 °C, respectively. After a corresponding secondary antibody treatment, the membranes were exposed to a mixture of enhanced chemiluminescence reagent (Applygen Technologies Inc., Beijing, China), and the resulting chemiluminescent reaction was detected by Fuji X-ray film. Then the film was scanned, and the intensity of immunoblot bands was quantified by densitometry using imaging software.

Statistical methods

All data are expressed as the mean±SD. Statistical comparisons were made by one-way analysis of variance, and statistical differences between two groups were established using the least significant difference test.

Results

Effect of fluoxetine on hemodynamics and the thickness of the pulmonary arterial wall

The mean PAP was elevated in the MCT group compared with the control group (P<0.01). Mean PAPs in the MCT+F2 and MCT+F10 groups were both decreased significantly (P<0.05, *vs* MCT). However, the SAPs in the four groups were not significantly different. The muscularization of lung tissue from the right lower lobe was investigated under light microscope. The thickness of pulmonary arterial walls in the MCT group was increased (P<0.01 *vs* control). Also, fluoxetine decreased the thickness ratio in the MCT+F2 and MCT+F10 groups compared with the MCT group in a dose-related manner (P<0.01, Table 1).

Evaluation of elastin and collagen

Figure 1A shows collagen staining of lung tissue, and demonstrates that collagen in the MCT group was significantly increased and was diffused all around the lungs and pulmonary arterioles; fluoxetine markedly decreased collagen deposition and ameliorated structural destruction of lungs in a dose-related manner. Figure 1B shows elastin staining of the main pulmonary arteries and demonstrates that the elastic fibers in the MCT group were significantly increased and disrupted; fluoxetine at doses of 10 mg/kg decreased elastic fiber hyperplasia and kept the integrity of the arterial structure. Similar results were also found in Figure 1C and 1D indicating that fluoxetine markedly decreased remodeling and destruction of elastin and collagen induced by MCT treatment.

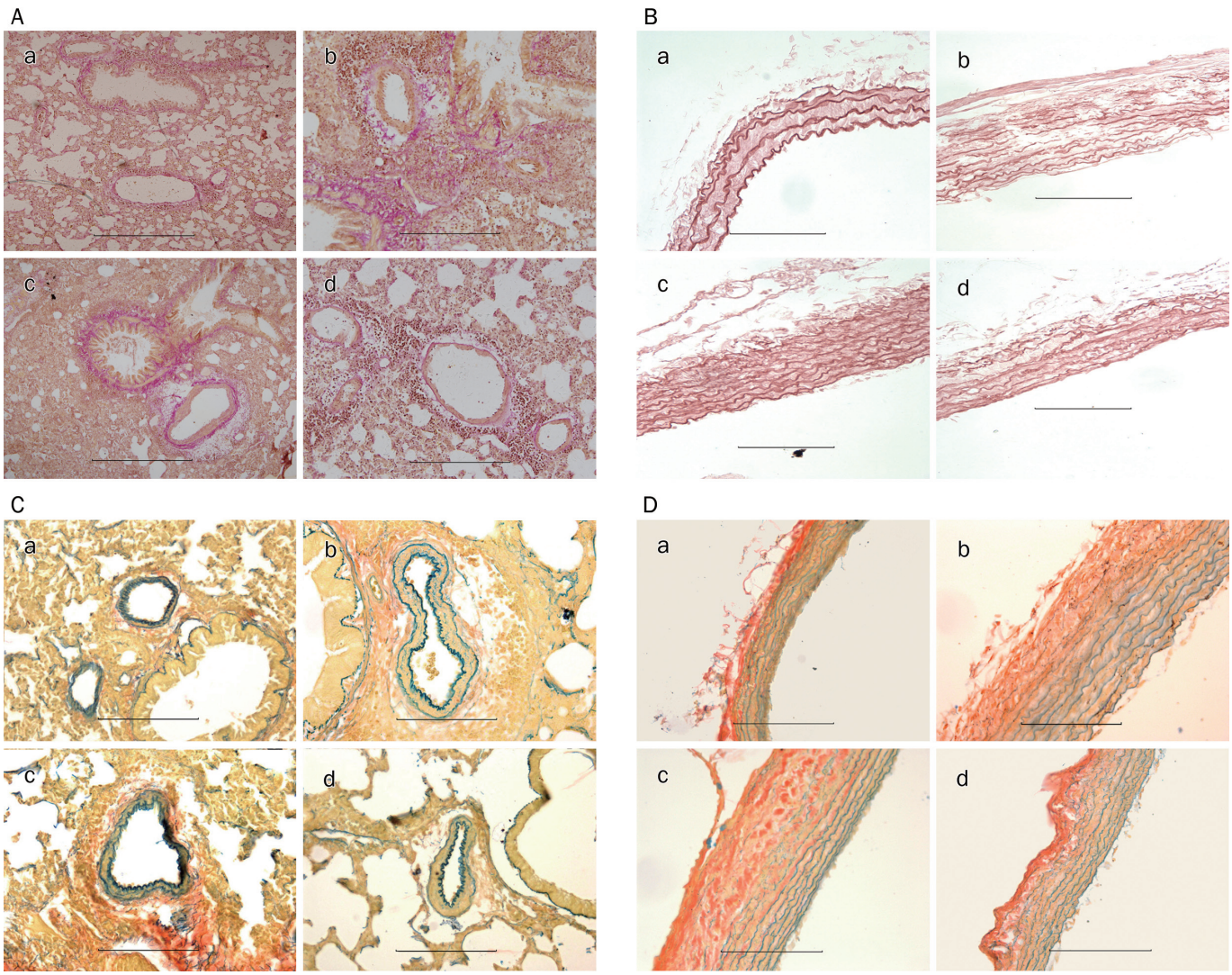

Figure 1. Comparison of elastin and collagen deposition in different groups. (A) collagen deposition (staining red) in lungs. a, b, c, and d represent control, MCT, MCT+F2, and MCT+F10 group, respectively (bars, 100 μm). (B) elastin in main pulmonary arteries. a, b, c, and d represent control, MCT, MCT+F2, and MCT+F10 group, respectively (bars, 100 μm). (C) Double staining in elastin and collagen in lungs. a, b, c and d represent elastin(staining bluish green) and collagen (staining red) in control, MCT, MCT+F2, and MCT+F10 group, respectively (bars, 100 μm). (D) Double staining in elastin and collagen in main pulmonary arteries. a, b, c, and d represent elastin (staining bluish green) and collagen (staining red) in control, MCT, MCT+F2, and MCT+F10 group (bars, 100 μm).

Table 1. Comparison of hemodynamic measurement and the thickness of pulmonary arteries in different groups. Data were expressed as mean±SD. $^{c}P<0.01$ *vs* control. $^{e}P<0.05$, $^{f}P<0.01$ *vs* MCT group.

	Control (*n*=15)	MCT (*n*=10)	MCT+F2 (*n*=9)	MCT+F10 (*n*=9)
Body weight (g)	260±21	236±29	226±36	241±20
SAP (mmHg)	120.2±10.7	108.3±16.3	110.3±9.3	110.3±13.4
PAP (mmHg)	17.4±1.7	29.8±7.5^{c}	26.9±5.7^{e}	24.5±3.3^{e}
Ratio of medial thickness of pulmonary artery (%)	36.1±10.3	53.5±8.8^{c}	44.7±9.7^{f}	38.5±10.1^{f}

Evaluation of lung inflammation

As shown in Figure 2, marked perivascular and peribronchiolar inflammatory cell infiltration and angiogenesis of lung tissues were found in the MCT group. Fluoxetine predominantly attenuated MCT-induced inflammation and angiogenesis of lung tissues.

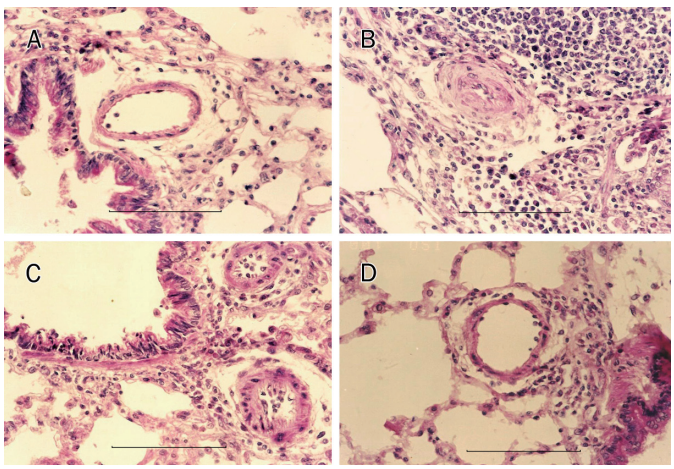

Figure 2. Comparison of lung inflammatory changes illustrated by representative photomicrographs. A, B, C, and D represent control, MCT, MCT+F2, and MCT+F10 group, respectively (bars, 100 μm).

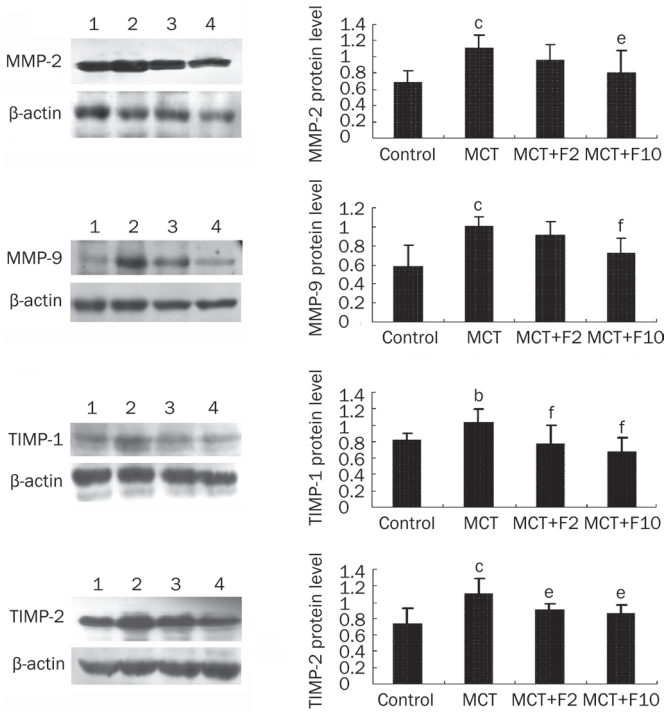

Figure 3. Comparison of MMP-2, MMP-9, TIMP-1, and TIMP-2 protein expression in lungs from different groups 1, 2, 3, and 4 represent control, MCT, MCT+F2, and MCT+F10 group, respectively. Data expressed as mean±SD (*n*=4). $^{b}P<0.05$, $^{c}P<0.01$ compared with control. $^{e}P<0.05$, $^{f}P<0.01$ compared with MCT.

MMP-2, MMP-9, TIMP-1, and TIMP-2 protein expressions

As shown in Figure 3, the levels of MMP-2, MMP-9, TIMP-1, and TIMP-2 in the MCT group were significantly increased compared with control. Fluoxetine inhibited MCT-induced increase of MMPs and TIMPs in a dose-dependent manner.

Inflammatory cytokine IL-1β, TNF-α, MCP-1, and ICAM-1 expressions

Compared with the control group, the levels of IL-1β, TNF-α, MCP-1, and ICAM-1 in the MCT group were significantly increased from 0.74±0.19, 0.58±0.24, 0.64±0.11, and 0.91±0.11 to 1.16±0.22, 1.00±0.22, 0.92±0.12, and 1.04±0.08, respectively. Fluoxetine inhibited MCT-induced increase of these cytokines in a dose dependent manner (Figure 4).

Discussion

The present study shows that MCT-induced PAH is accompanied by an ECM remodeling of pulmonary arteries and an inflammatory response of lung tissue, in which there are marked fragmentation and reconstruction of elastin and collagen, increased expression of MMP-2, 9 and TIMP-1, 2, and increased expression of inflammatory cytokines. ECM remodeling, as an important change in pulmonary arterial reconstruction, results from a complex interplay between synthesis and proteolysis of ECM constituents. Early clinical studies have shown that fragmentation of the internal elastic lamina and an increase of active MMPs exist in the pulmonary arteries of PAH patients[9]. In animal PAH models, the progression of hypoxia-induced PAH is associated with a time-dependent increase in MMP activity that is mainly related to an increase of MMP-2[8]. Higher expressions of MMP-2, 9, TIMP-1 mRNA, and enzymatic activity of MMP-2, 9 in lungs were also found

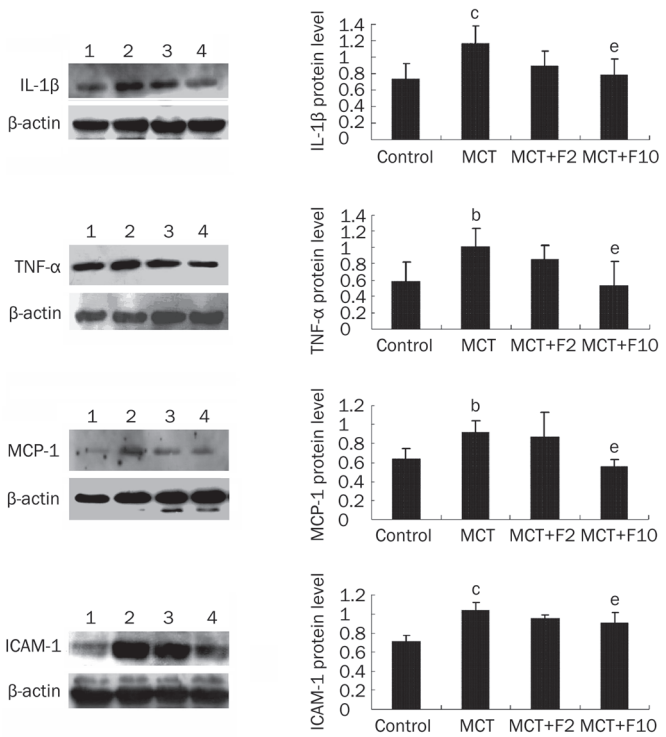

Figure 4. IL-1β, TNF-α, MCP-1, and ICAM-1 protein expression in lung tissues from different groups by Western blot. 1, 2, 3, and 4 represent control, MCT, MCT+F2, and MCT+F10 group, respectively. Data expressed as mean±SD (n=4). $^{b}P<0.05$, $^{c}P<0.01$ compared with control. $^{e}P<0.05$, $^{f}P<0.01$ compared with MCT.

in MCT-induced PAH rats[25]. It is thought that injection of MCT causes endothelial cell injury in pulmonary arteries and inflammatory response in lungs[21] and induces MMPs to be secreted from injured endothelial cells and inflammatory cells (such as mast cells, monocytes, macrophages)[26, 27]. The activation of MMPs initiates ECM degradation, and TIMPs expression is augmented for keeping a dynamic balance between ECM construction and destruction. The above mentioned evidence indicates that the present findings, in which MCT induced increases of MMP-2, 9/TIMP-1, 2 in lungs, are in accordance with the results from previous studies.

In the present study, fluoxetine markedly inhibits MCT-induced pulmonary arterial hypertension and attenuated pulmonary artery muscularization, as we have reported previously[15]. Furthermore, we also found that fluoxetine reduced the elastin and collagen deposition and destruction in pulmonary arteries induced by MCT, in which MMP-2, 9/TIMP-1, 2 expressions are obviously suppressed. It is known that serotonin is involved in the pathophysiology of lung fibrosis via increasing proliferation and collagen synthesis by fibroblasts[28] and that it has reciprocal effects on collagens and collagenase (a type of MMP)[29]. Shum JK *et al* reported that serotonin induces MMP production via phospholipase C, protein kinase C, and extracellular signal-regulated kinase (ERK) 1/2 pathway in smooth muscle cells[30]. Our previous study showed that the serotonin-induced mitogenesis of PASMCs is mediated by SERT, in which the signal transduction for serotonin is dependent on the ERK1/2 pathway[14]. Benekareddy *et al* also reported that fluoxetine regulates MMP-2/MMP-9 and TIMP1-4 in the adult rat hippocampus[31]. Taken this information and the present results together, we believe that fluoxetine-induced regulation of MMP-2, 9/TIMP-1, 2 is closely related to the inhibition of ECM remodeling, in which the serotonin intracellular signal pathway might be involved. In the fluoxetine group, we found that both MMP and TIMP expressions were inhibited. It is known that regulation of MMP expression also affects TIMP expression, and therefore a delicate balance exists between MMP activation and inhibition by TIMPs[32]. It is thought that a reduction of TIMP expression is related to the inhibition of MMPs expression and ECM remodeling by fluoxetine.

We have also shown how fluoxetine remarkably inhibits MCT-induced pulmonary inflammation and how this inhibition is accompanied by the decreased expression of inflammatory cytokines. Some studies report that serotonin is closely linked to inflammatory responses, including the induction of mast cell adhesion and migration, activation of alveolar macrophages, and development and maintenance of arterial remodeling through the release of cytokines[33–35]. It is found that fluoxetine has anti-inflammatory properties and that there is a positive correlation between SERT and cytokine mRNA expression in patients with depression, who are affected by chronic treatment with fluoxetine[22]. Also, the present study found that fluoxetine suppressed inflammatory responses in MCT-induced PAH rats, in which inhibition of inflammatory cytokines is involved. Thus, it is thought that the serotonergic system is likely to be involved in the modulation of peripheral inflammation, and SSRIs may play an important role in working against the inflammatory response in PAH. It is known that MMPs act broadly in physiological and pathological inflammatory processes via regulating inflammatory cytokines activity[7]. MMPs are regulated by many cytokines, notably TNF-α and IL-1β, that induce MMP activity markedly and increase their mRNA levels via action through the promoter region of MMP genes[36]. Kubera *et al* also reported that the anti-inflammatory effects of fluoxetine developed through suppression of the interferon-gamma/interlenkin-10 production ratio in the central nervous system[37]. Therefore, there is a complex interaction between MMPs and inflammatory response which might be involved in the mechanism of fluoxetine protection against PAH.

In conclusion, fluoxetine inhibited MCT-induced ECM remodeling of pulmonary artery and inflammation of lungs, effects which were related to its inhibition on MMPs/TIMPs and cytokine productions.

Acknowledgements

Projects supported by National Natural Science Foundation of China (No 30973533 and No 30572194).

Author contribution

Xue-qin LI and Huai-liang WANG designed the research and

wrote the paper. Xue-qin LI, Han-ming WANG, Chun-guang YANG, and Dan-dan HAN performed the research. Xin-hua ZHANG offered technical assistance.

References

1 Morrell NW, Adnot S, Archer SL, Dupuis J, Jones PL, MacLean MR, *et al*. Cellular and molecular basis of pulmonary arterial hypertension. J Am Coll Cardiol 2009; 54: S20–31.
2 Tuder RM. Pathology of pulmonary arterial hypertension. Semin Respir Crit Care Med 2009; 30: 376–85.
3 Raiesdana A, Loscalzo J. Pulmonary arterial hypertension. Ann Med 2006; 38: 95–110.
4 Eble JA, Niland S. The extracellular matrix of blood vessels. Curr Pharm Des 2009; 15: 1385–400.
5 Lammers SR, Kao PH, Qi HJ, Hunter K, Lanning C, Albietz J, *et al*. Changes in the structure-function relationship of elastin and its impact on the proximal pulmonary arterial mechanics of hypertensive calves. Am J Physiol Heart Circ Physiol 2008; 295: H1451–9.
6 Frisdal E, Gest V, Vieillard-Baron A, Levame M, Lepetit H, Eddahibi S, *et al*. Gelatinase expression in pulmonary arteries during experimental pulmonary hypertension. Eur Respir J 2001; 18: 838–45.
7 Ambalavanan N, Nicola T, Li P, Bulger A, Murphy-Ullrich J, Oparil S, *et al*. Role of matrix metalloproteinase-2 in newborn mouse lungs under hypoxic conditions. Pediatr Res 2008; 63: 26–32.
8 Novotná J, Herget J. Possible role of matrix metalloproteinases in reconstruction of peripheral pulmonary arteries induced by hypoxia. Physiol Res 2002; 51: 323–34.
9 Lepetit H, Eddahibi S, Fadel E, Frisdal E, Munaut C, Noel A, *et al*. Smooth muscle cell matrix metalloproteinases in idiopathic pulmonary arterial hypertension. Eur Respir J 2005; 25: 834–42.
10 Aytekin M, Comhair SA, de la Motte C, Bandyopadhyay SK, Farver CF, Hascall VC, *et al*. High levels of hyaluronan in idiopathic pulmonary arterial hypertension. Am J Physiol Lung Cell Mol Physiol 2008; 295: L789–99.
11 MacLean MR, Dempsie Y. Serotonin and pulmonary hypertension — from bench to bedside? Curr Opin Pharmacol 2009; 9: 281–6.
12 MacLean MR, Dempsie Y. The serotonin hypothesis of pulmonary hypertension revisited. Adv Exp Med Biol 2010; 661: 309–22.
13 Kéreveur A, Callebert J, Humbert M, Hervé P, Simonneau G, Launay JM, *et al*. High plasma serotonin levels in primary pulmonary hypertension: effect of long-term epoprostenol (prostacyclin) therapy. Arterioscler Thromb Vasc Biol 2000; 20: 2233–9.
14 Song D, Wang HL, Wang S, Zhang XH. 5-Hydroxytryptamine-induced proliferation of pulmonary artery smooth muscle cells are extracellular signal-regulated kinase pathway dependent. Acta Pharmacol Sin 2005; 26: 563–7.
15 Li XQ, Hong Y, Wang Y, Zhang XH, Wang HL. Sertraline protects against monocrotaline-induced pulmonary hypertension in rats. Clin Exp Pharmacol Physiol 2006; 33: 1047–51.
16 Zhai FG, Zhang XH, Wang HL. Fluoxetine protects against monocrotaline-induced pulmonary arterial hypertension: potential roles of induction of apoptosis and upregulation of Kv1.5 channels in rats. Clin Exp Pharmacol Physiol 2009; 36: 850–6.
17 Dorfmüller P, Perros F, Balabanian K, Humber M. Inflammation in pulmonary arterial hypertension. Eur Respir J 2003; 22: 358–63.
18 Mathew R. Inflammation and pulmonary hypertension. Cardiol Rev 2010; 18: 67–72.
19 Chaouat A, Savale L, Chouaid C, Tu L, Sztrymf B, Canuet M, *et al*. Role for interleukin-6 in COPD-related pulmonary hypertension. Chest 2009; 136: 678–87.
20 Hassoun PM, Mouthon L, Barberà JA, Eddahibi S, Flores SC, Grimminger F, *et al*. Inflammation, growth factors, and pulmonary vascular remodeling. J Am Coll Cardiol 2009; 54: S10–9.
21 Wang HL. The serotonin receptor and transporter are potential therapeutic targets for pulmonary hypertension. Curr Opin Investig Drugs 2004; 5: 963–6.
22 Tsao CW, Lin YS, Chen CC, Bai CH, Wu SR. Cytokines and serotonin transporter in patients with major depression. Prog Neruopsychopharmacol Biol Psychiatry 2006; 30: 899–905.
23 Abdel-Salam OM, Baiuomy AR, Arbid MS. Studies on the anti-inflammatory effect of fluoxetine in rat. Pharmacol Res 2004; 49: 119–31.
24 Guignabert C, Raffestin B, Benferhat R, Raoul W, Zadigue P, Rideau D, *et al*. Serotonin transporter inhibition prevents and reversers monocrotaline-induced pulmonary hypertension in rats. Circulation 2005; 111: 2812–9.
25 Wang XM, Zhou TF, Liu B, Wei L, Shi K, Zhao SS, *et al*. Changes of MMP-2,9 and TIMP-1 expressions in rats with pulmonary arterial hypertension after captopril and losartan interventions. Sichuan Da Xue Xue Bao Yi Xue Ban 2009; 40: 255–9.
26 Tozzi CA, Thakker-Varia S, Yu SY, Bannett RF, Peng BW, Poiani GJ, *et al*. Mast cell collagenase correlateds with regression of pulmonary vascular remodeling in the rat. Am J Respir Cell Mol Biol 1998; 18: 497–510.
27 Emonard H, Grimoud JA. Matrix metalloproteinases. Cell Mol Biol 1990; 36: 131–53.
28 Fabre A, Marchal-Sommé J, Marchand-Adam S, Quesnel C, Borie R, Dehoux M, *et al*. Modulation of bleomycin-induced lung fibrosis by serotonin receptor antagonists in mice. Eur Respir J 2008; 32: 426–36.
29 Passaretti TV, Wilcox BD, Jeffrey JJ. Serotonin regulation of gene expression in uterine extracellular matrix: reciprocal effects on collagens and collagenase. Mol Cell Endocrinol 1996; 120: 125–32.
30 Shum JK, Melendez JA, Jeffrey JJ. Serotonin-induced MMP-13 production is mediated via phospholipase C, protein kinase C, and ERK1/2 in rat uterine smooth muscle cells. J Biol Chem 2002; 277: 42830–40.
31 Benekareddy M, Mehrotra P, Kulkarni VA, Ramakrishnan P, Dias BG, Vaidya VA. Antidepressant treatments regulate matrix metalloproteinases-2 and -9 (MMP-2/MMP-9) and tissue inhibitors of the metalloproteinases (TIMPS 1-4) in the adult rat hippocampus. Synapse 2008; 62: 590–600.
32 Keller KE, Aga M, Bradley JM, Kelley MJ, Acott TS. Extracellular matrix turnover and outflow resistance. Exp Eye Res 2009; 88: 676–82.
33 Kushnir-Sukhov NM, Gilfillan AM, Coleman JW, Brown JM, Bruening S, Toth M, *et al*. 5-hydroxytryptamine induces mast cell adhesion and migration. J Immunol 2006; 177: 6422–32.
34 Mikulski Z, Zaslona Z, Cakarova L, Hartmann P, Wilhelm J, Tecott LH, *et al*. Serotonin activates murine alveolar macrophages through 5-HT2C receptors. Am J Physiol Lung Cell Mol Physiol 2010; 299: L272–80.
35 Lima C, Souza VM, Soares AL, Macedo MS, Tavares-de-Lima W, Vargaftig BB. Interference of methysergide, a specific 5-hydroxytryptamine receptor antagonist, with airway chronic allergic inflammation and remodeling in a murine model of asthma. Clin Exp Allergy 2007; 37: 723–34.
36 Manicone AM, McGuire JK. Matrix metalloproteinases as modulators of inflammation. Cell Dev Biol 2008; 19: 34–41.
37 Kubera M, Lin AH, Kenis G, Bosmans E, van Bockstaele D, Maes M. Anti-inflammatory effects of antidepressants through suppression of the interferon-gamma/interleukin-10 production ratio. J Clin Psychopharmacol 2001; 21: 199–206.

Acta Pharmacologica Sinica (2011) 32: 223–229

www.nature.com/aps

Original Article

Isoproterenol-induced FKBP12.6/12 downregulation is modulated by ET_A and ET_B receptors and reversed by argirhein, a derivative of rhein

Guo-lin ZHANG[1], De-zai DAI[1, *], Tao XI[1, *], Xiao-dong CONG[2], Yun ZHANG[2], Yin DAI[1]

[1]*China Pharmaceutical University, Nanjing 210009, China;* [2]*Zhejiang Chinese Medical University, Hangzhou 311401, China*

Aim: To investigate which endothelin receptors mediated isoproterenol (ISO)-induced downregulation of FKBP12.6/12 in cardiomyocytes and study whether argirhein, a novel compound containing rhein and *L*-arginine that has anti-inflammatory activity, could reverse the downregulation of FKBP12.6/12 induced by ISO.

Methods: Neonatal rat cardiomyocytes were incubated with ISO to downregulate FKBP12.6/12. Then the cells were treated with a selective ET_A blocker (PD156707) and a ET_B blocker (IRL1038), a dual ET_A/ET_B antagonist (CPU0213), and argirhein, respectively. FKBP12.6/12 expression was assayed by RT-PCR, Western blot, and immunocytochemistry.

Results: The expression of FKBP12.6 mRNA was reduced by 37.7% (P<0.01) and 28.9% (P<0.05) relative to the control by ISO 1 and 0.1 μmol/L, respectively, but no response to ISO 0.01 μmol/L was observed *in vitro*. FKBP12.6/12 protein expression was reduced by 47.2% (P<0.01) and 37.8% (P<0.05) by ISO 1 and 0.1 μmol/L, respectively. This decrease was reversed significantly by PD156707, or IRL1038, and CPU0213. CPU0213 was more potent than either PD156707 or IRL-1038. Argirhein 10 μmol/L blunted the down-regulation of FKBP12.6/12 by ISO, as demonstrated by the rising mRNA and protein levels and by the fluorescent density of the ISO-incubated cardiomyocytes.

Conclusion: In cardiomyocytes, the ISO induced downregulation of FKBP12.6/12 is modulated by both ET_A and ET_B. A new compound, argirein, reversed the down-regulation of FKBP12.6/12 expression in myocardial cells stimulated with ISO.

Keywords: isoproterenol; FKBP12.6/12; ET_A receptor; ET_B receptor; argirhein; rhein

Acta Pharmacologica Sinica (2011) 32: 223–229; doi: 10.1038/aps.2010.177

Introduction

Severe arrhythmias and congestive heart failure have become major problems affecting humans, and the annual incidence of sudden cardiac death (SCD) in the general population is estimated to be 1 in 1000[1]. Mutations in the potassium channels KCNQ2 and KCNH2, and in the sodium channel SCN5A serve as markers only for polymorphism, and severe arrhythmias may occur in the presence of triggering factors[2]. Trigger factors, including stress caused by β-adrenergic stimulation and some medications, affect K^+ currents during repolarization, resulting in tachyarrhythmias in patients with mutated genes. Tricyclic antidepressants may trigger the appearance of Brugada syndrome (Brugada ECG and life-threatening ventricular arrhythmias) in patients with the SCN5A polymorphism (His558Arg)[3]. Mutation of the ryanodine receptor type 2 (RyR2) alone does not appear to cause tachyarrhythmias; however, patients with RyR2 mutations may present with CPVT (catecholaminergic polymorphism ventricular tachyarrhythmias) while engaging in physical exercise, which is always associated with β-adrenoceptor stimulation[4]. Life threatening arrhythmias are likely to occur in patients with cardiac disease such as heart failure, in which multiple steps are needed to trigger events, including profound activation of β-adrenoceptor[5, 6], and many causal factors are implicated in the pathogenesis of failing hearts in which an excess of reactive oxygen species (ROS) and inflammatory factors exist, resulting from the downstream events of β-adrenergic stimulation. Some inflammatory factors that have been revealed in the pathogenesis of congestive heart failure may participate in mechanisms underlying life threatening arrhythmias in failing hearts[7].

FKBP12.6 (calstabin 2) is a key subunit that binds to RyR2 at the sarcoplasmic reticulum (SR) and is involved in calcium handling activity in the myocardium. FKBP12.6 also plays a role in the molecular mechanisms underlying severe arrhythmias and cardiac insufficiency[8]. CPVT may be the conse-

* To whom correspondence should be addressed.
E-mail dezaidai@vip.sina.com; xi_tao18@sina.com; azai308@163.com
Received 2010-06-20 Accepted 2010-09-12

quence of dissociated/downregulated FKBP12.6/12 related to profound β-adrenoceptor activation that keeps RyR2 channels closed loosely, allowing calcium leaks during diastole. RyR2 is phosphorylated by protein kinase A (PKA)[9]. FKBP12.6/12 dissociation from the binding site at RyR2 is likely due to a decrease in affinity, but this hypothesis is still controversial[10]. Elevated free calcium levels during diastole contribute to an increased risk for both cardiac tachyarrhythmias and exacerbated cardiac failure. Downregulation of FKBP12.6/12 in cardiomyocytes can be reproduced by isoproterenol (ISO) and can be induced by either endothelin-1 (ET) or H_2O_2[11]. The resulting calcium leaks can be predicted by the downregulation of FKBP12.6/12[12]; therefore, downregulated FKBP12.6/12 may be taken as a surrogate for calcium leaks, indicating an increased risk for severe arrhythmias and the deterioration of cardiac performance[13].

ET-1 is a cytokine that actively participates in inflammatory reactions and ROS genesis through activating NADPH oxidase[14]. An activation of the ET system is always associated with NADPH oxidase, forming the ET-NADPH oxidase pathway that is implicated in many cardiovascular diseases[15]. The biological activities of ET-1 are the result of the stimulation of ET receptors A (ET_A) and B (ET_B). In our previous study, ET-1 was shown to cause the downregulation/dissociation of FKBP12.6/12 in cardiomyocytes[11]; however, it is unclear whether ET_A and ET_B play separate roles in this process.

Argirhein, a new synthetic compound, contains rhein linked to *L*-arginine with a hydrogen bond in its moiety (Figure 1). Rhein relieves liver fibrosis and injury through anti-inflammatory activity[16, 17]. When argirhein is used as a medication, rhein can be released from argirhein and then display its anti-inflammatory activity, which may protect cardiomyocytes from ISO-induced insults; therefore, the activity of argirhein could be relevant in attenuating the downregulation of FKBP12.6/12 at the SR. We hypothesized that the downregulation of FKBP12.6/12 by ISO causes a disturbance in calcium homeostasis, which worsens arrhythmogenesis and cardiac performance. This downregulation could be mediated by ET_A and ET_B individually. Given the anti-inflammatory activity of rhein, argirhein may have an activity similar to that of ET blockers, which play a role in protecting the myocardium by alleviating ISO-induced downregulation of FKBP12.6/12.

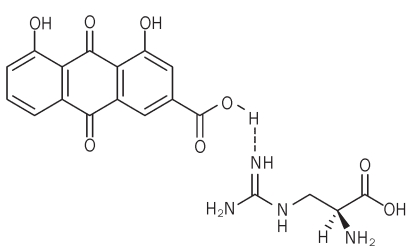

Figure 1. Chemical structure of argirhein.

Materials and methods

Animals

Animal handling procedures were conducted in accordance with the Laboratory Animal Regulations of the Bureau of Science and Technology, Jiangsu Province, China.

Reagents

Isoproterenol was purchased from Shanghai Hefeng Medicine Company (Shanghai, China). PD156707, a selective endothelin receptor A antagonist, and IRL-1038, a selective endothelin B receptor antagonist, were purchased from Sigma and Genscript Corporation, USA, respectively. M-MLV (Promega, USA) and Taq DNA Polymerase (Tiangne) were purchased from Nanjing Tianwei Corp, China. Polyclonal goat anti-FKBP12.6/12 IgG was obtained from Santa Cruz Biotechnology Inc, USA. Polyclonal rabbit anti-actin-IgG and FITC-conjugated rabbit anti-goat IgG were purchased from Boster, Wuhan, China. HRP-conjugated rabbit anti-goat IgG was from Dako, USA. Argirhein (AR) was sourced from Zhejiang Chinese Medical University.

Cell culture

Neonatal Sprague-Dawley rats were obtained from the Experimental Animal Center of Nanjing. Neonatal ventricular myocytes were obtained and cultured as described previously[9]. Briefly, myocytes were obtained and cultured in 20% FBS-DMEM culture medium with BrdU to suppress the growth of fibroblasts. The culture was changed to serum-free DMEM medium after three days, at which time the myocytes reached confluence. Except for the control groups, myocytes were incubated with ISO (0.01, 0.1, or 1 μmol/L) for 18 h to determine the appropriate ISO concentration. Cells were incubated with PD156707, IRL-1038, CPU0213 and argirhein (AR) at the 3 doses to prevent the adverse effects of ISO on FKBP12.6/12 in cardiomyocytes.

Semi-quantitative RT-PCR

After an 18-h incubation, RNA was extracted with Trizol solution, and cDNA was synthesized as described previously[12]. RT-PCR was performed in a volume of 25 μL, and the products were detected in 2% agarose. The target gene was quantified using β-actin as an internal control. The sequences of the forward and reverse primers for FKBP12.6 (length 427 bp) and β-actin (580 bp) are listed below: 5′-AAGGAAGGACGGAAGTG-3′ and 5′-GAATAGAAGACAACCGACG-3′; and 5′-GCCTCAAGATCATCAGCAAT-3′ and 5′-AGGTCCACCACTGACACCTT-3′, respectively. The densities of the bands were analyzed using a gel imaging analysis system (GeneGenius, Syngene, England), and the relative density of each DNA band was obtained by dividing by the density of β-actin.

Western blotting

Protein was extracted from the incubated myocytes as described previously[18]. Briefly, after determination of the pro-

tein concentration, the supernatant was stored at -20 °C before use. Aliquots of samples were heated to 98 °C in a loading buffer and fractionated using 10% SDS-PAGE. The separated proteins were transferred to a nitrocellulose membrane that was blocked with nonfat milk (5% *w/v*). The blocked nitrocellulose membranes were incubated at 4 °C overnight with the specific primary antibody. After 3 washes, the blots were incubated with horseradish peroxidase (HRP)-conjugated goat secondary antibody IgG for 1 h at room temperature. Antigen was detected with a DAB kit, visualized by imaging acquisition and quantified by densitometry. The relative abundance was obtained by normalizing the density of the FKBP12.6/12 protein against that of β-actin.

Immunocytochemical analysis

Cardiomyocytes were fixed with cold acetone for 10 min after incubation with ISO for 18 h. After the cells were dried at room temperature, the cell membrane permeability was increased by incubation with 1% Triton X-100 for 1 h. Then, cardiomyocytes were sealed with 2% bovine serum albumin for 1 h and incubated overnight with polyclonal goat anti-FKBP12.6/12-IgG. After being washed 3 times with PBS, the cardiomyocytes were incubated with FITC-conjugated rabbit anti-goat IgG for 1 h. Finally, cardiomyocytes were imaged by fluorescence microscopy and the gray density was assayed and compared[19].

Statistical analysis

All data are presented as the mean±SD and were analyzed with SPSS version 11.5 (USA). For statistical evaluation, a one-way analysis of variance was used, following Dunnett's test. The Student Newman Keuls test was performed when the variances were equal, and the Games-Howell test was used when the variances were not equal. A probability value of $P<0.05$ was considered statistically significant.

Results

Downregulation of FKBP12.6/12

The downregulation of FKBP12.6/12 in cardiomyocytes responded to ISO at 3 doses *in vitro*. The expression of FKBP12.6 mRNA was reduced by 37.7% ($P<0.01$) and 28.9% ($P<0.05$) relative to the control at ISO concentrations of 1 μmol/L and 0.1 μmol/L, respectively, but no response to ISO 0.01 μmol/L was observed. A reduction in FKBP12.6/12 protein expression of the same magnitude was found by Western blotting; the reductions were 47.2% ($P<0.01$) and 37.8% ($P<0.05$) for 1 μmol/L and 0.1 μmol/L, respectively (Figure 2A, 2B). Based on these results, an ISO concentration of 1 μmol/L was adopted for further experiments.

Responses to ET antagonists

The expression levels of FKBP12.6/12 mRNA and protein were downregulated in the presence of ISO, and then selective blockade of either ET_A or ET_B was analyzed. The ET_A antagonist PD156707 suppressed the changes in protein abundance significantly at concentrations of 0.1 and 1 μmol/L relative to

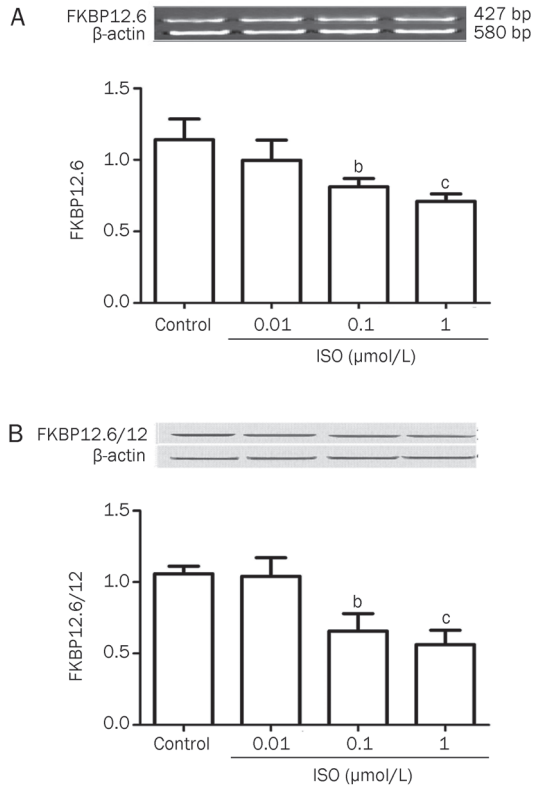

Figure 2. The mRNA (A) and protein (B) expression of FKBP12.6/12 in neonatal rat cardiomyocytes were downregulated after incubation with isoproterenol (ISO) for 18 h. $n=6$. Mean±SD, $^bP<0.05$, $^cP<0.01$ *vs* control. The relative expression of mRNA and protein was normalized by β-actin.

ISO alone (Figure 3A, 3B). It was found that the ET_B antagonist IRL-1038 at a concentration of 1 μmol/L only induced a reduction in the downregulation of FKBP12.6/12 toward the normal level (Figure 3D). At 0.1 μmol/L, PD156707 was able to upregulate the abundance of FKBP12.6/12 remarkably; however, IRL1038 had no significant effect. Thus, ET_A was more potent than ET_B in modulating changes in FKBP12.6/12 induced by ISO. mRNA and protein expression for FKBP12.6/12 were not changed in the absence of ISO after an 18-h incubation with either PD156707 or IRL-1038 alone (Figure 3E, 3F).

CPU0213, a dual ET_A and ET_B receptor antagonist, was added at concentrations ranging from 0.01 to 1 μmol/L to test its effects on the changes in FKBP12.6/12 expression induced by ISO. CPU0213 was able to significantly reverse the downregulation of the levels of mRNA and protein of FKBP12.6/12 at all three ISO concentrations. At a concentration as low as 0.01 μmol/L, CPU0213 was able to elevate the depressed FKBP12.6/12 levels significantly, while no response was observed to either PD156707 or IRL-1038. It appears that a combined blockade of the two subtypes of ET receptors is more potent than a single selective blockade (Figure 4).

Argirhein upregulates FKBP12.6/12

Compared with the ISO group, the argirhein group showed a significant reversal of the ISO-induced downregulation of

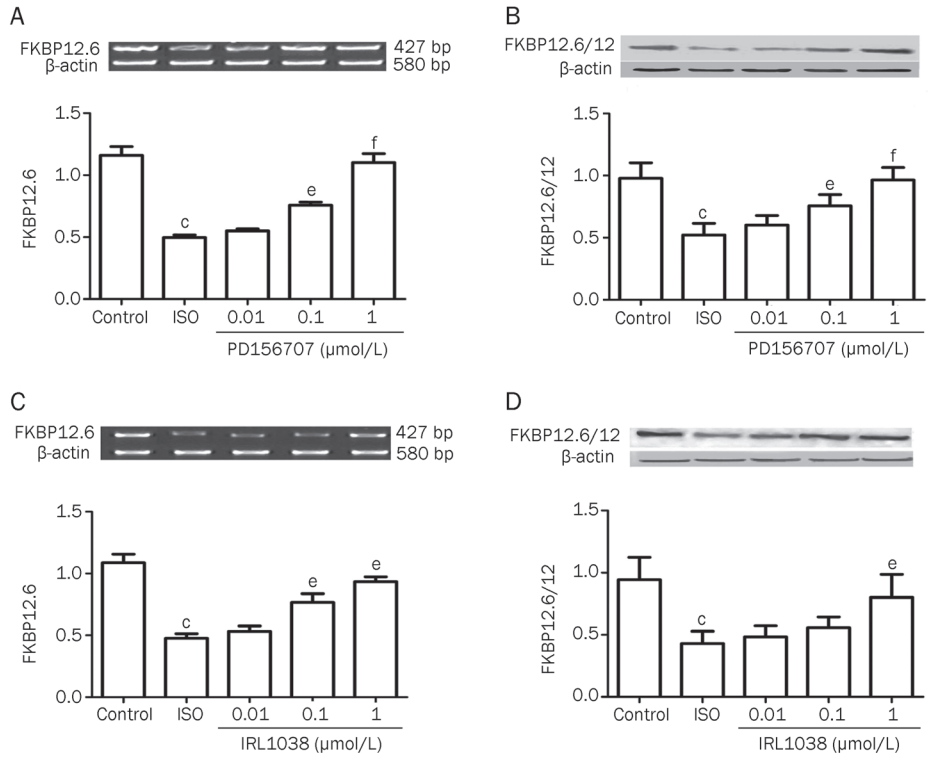

Figure 3. Selective ET_A antagonist PD156707 (A, B) and ET_B antagonist IRL1038 (C, D) reversed the ISO-induced downregulated mRNA and protein expression of FKBP12.6/12 normalized by β-actin in neonatal rat cardiomyocytes, but the expression of FKBP12.6/12 was not affected when incubation with drugs PD156707 and IRL1038 in the absence of ISO (E,F). n=6. Mean±SD. $^cP<0.01$ *vs* control. $^eP<0.05$, $^fP<0.01$ *vs* ISO.

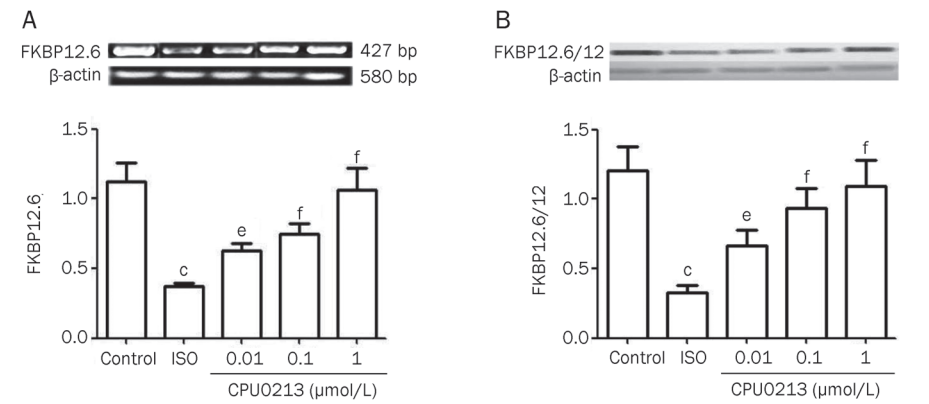

Figure 4. Dual ET antagonist CPU0213 reversed the ISO-induced downregulation of mRNA (A) and protein (B) expression of FKBP12.6/12 normalized by β-actin in neonatal rat cardiomyocytes. n=6. Mean±SD. $^cP<0.01$ *vs* control. $^eP<0.05$, $^fP<0.01$ *vs* ISO.

FKBP12.6/12 when argirhein was used at 10 μmol/L (Figure 5A, 5B). The activity of argirhein was similar to those of the ET antagonists and was less effective than either CPU0213 or PD156707. Cardiomyocytes incubated with argirhein alone has not altered expression of FKBP12.6/12 mRNA and protein (Figure 5C). This result indicates that argirhein counteracts the adverse effects of ISO on FKBP12.6/12 in cardiomyocytes.

Immunocytochemistry of FKBP12.6/12

In an immunocytochemistry assay, the fluorescence inten-

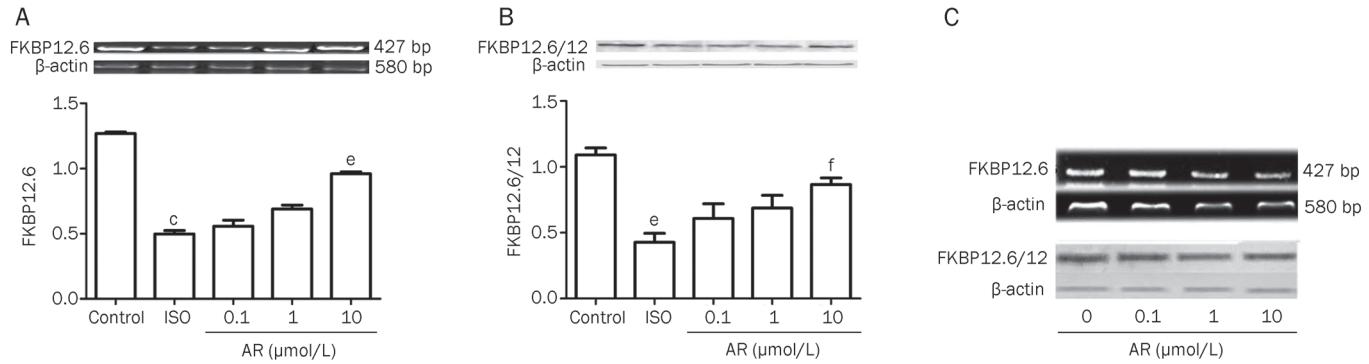

Figure 5. Downregulated expression of FKBP12.6/12 mRNA (A) and protein (B) normalized by β-actin were reversed by argirhein, but the expression of FKBP12.6/12 were not affected when incubation with argirhein in the absence of ISO (C). *n*=6. Mean±SD. ^{c}P<0.01 *vs* control. ^{e}P<0.05 *vs* ISO.

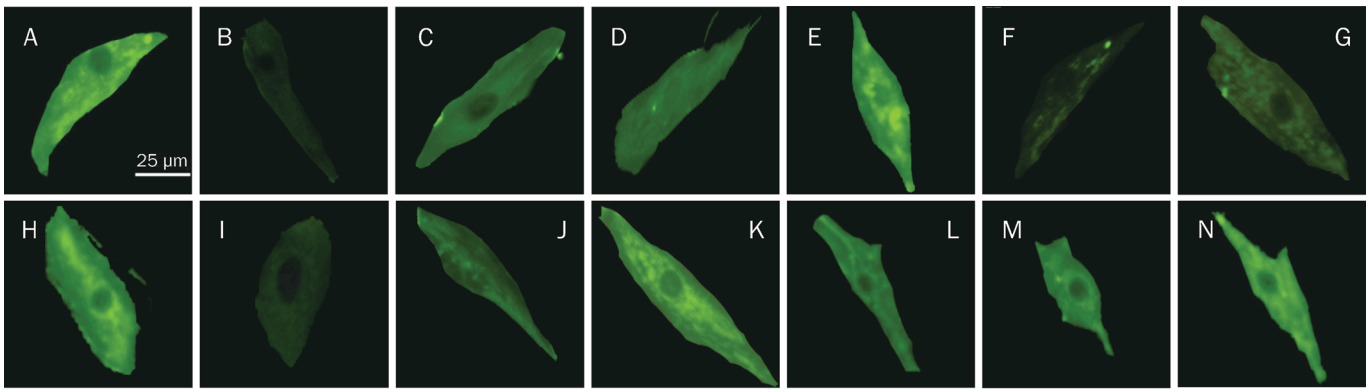

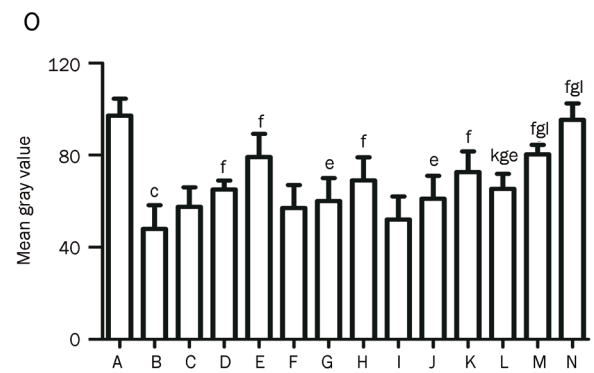

Figure 6. Downregulation of fluorescence intensity of FKBP12.6/12 in neonatal rat cardiomyocytes was induced by isoproterenol and was blunted by selective ET_A antagonist PD156707, ET_B antagonist IRL1038, dual ET antagonist CPU0213 and argirhein. (A) Control; (B) ISO (1 μmol/L); (C) ISO+PD156707 (0.01 μmol/L); (D) ISO+PD156707 (0.1 μmol/L); (E) ISO+PD156707 (1 μmol/L); (F) ISO+IRL1038 (0.01 μmol/L); (G) ISO+IRL1038 (0.1 μmol/L); (H) ISO+IRL1038 (1 μmol/L); (I) ISO+AR (0.1 μmol/L); (J) ISO+AR (1 μmol/L); (K) ISO+AR (10 μmol/L); (L) ISO+CPU0213 (0.01 μmol/L); (M) ISO+CPU0213 (0.1 μmol/L); (N) ISO+CPU0213 (1 μmol/L); (O) The gray density of immunocytochemistry of FKBP12.6. *n*=6. Mean±SD. ^{c}P<0.01 *vs* control. ^{e}P <0.05, ^{f}P <0.01 *vs* ISO. ^{g}P<0.05 *vs* PD156707. ^{k}P<0.05, ^{l}P<0.01 *vs* IRL1038.

sity of FKBP12.6/12 in single incubated cardiomyocytes was bright in untreated cells but appeared to be faint after exposure to ISO for 18 h (Figure 6A, 6B, 6O), clearly indicating the downregulation/dissociation of FKBP12.6/12 by ISO in cardiomyocytes. Both ET_A and ET_B antagonists (PD156707 and IRL1038, respectively) enhanced the fluorescence intensity of cardiomyocytes in a dose-dependent manner (Figure 6C–6H, 6O). The effect of IRL1038 was impressive but less potent. Additionally, the novel compound argirhein was shown to increase the fluorescence intensity of FKBP12.6/12 at concentrations of 10^{-6} and 10^{-5} mol/L (Figure 6J, 6K, 6O). The dual endothelin receptor antagonist CPU0213 was potent in escalating the fluorescence in single cardiomyocytes and the mean gray value was higher than that of either PD156707 or IRL1038 (Figure 6L–6N, 6O). These results indicate that ISO-induced FKBP12.6/12 downregulation is modulated dramatically by either ET_A or ET_B and that argirhein significantly reversed the changes in FKBP12.6/12 expression induced by ISO, but argirhein was less effective than PD156707 and CPU0213.

Discussion

Profound stimulation of β-receptors is commonly found in hearts that manifest worsening of arrhythmogenesis and declines in heart performance[20, 21]. It is believed that ISO worsens cardiac function and increases the risk of severe ventricular tachyarrhythmias. These activities are thought to

be related to an impairment of the calcium handling protein FKBP12.6/12 at the SR. Calcium leaks during diastole result from the downregulation of FKBP12.6/12, which loses the ability to control the calcium releasing channels (RyR2). This leads to slow down repolarization followed by prolonged APD (action potential duration), and causes EAD (early after depolarization), which predisposes the heart to tachyarrhythmias[12]. A significant reversal of the deterioration of cardiac function and arrhythmogenic trends of affected hearts can be achieved through rescuing the depressed the FKBP12.6/12 level by blocking the activity of the ET receptors using CPU0213, a dual endothelin receptor antagonist[12, 19, 22]. In addition to ET antagonists, there are some compounds that specifically normalize abnormal RyR2 (and FKBP12.6/12) resulting from calcium and potassium channel blocking agents such as JTV519[23] and CPU86017, which was developed at our laboratory[24, 25].

The downregulation of FKBP12.6/12 induced by ISO is not a single event and is associated with an increase in other inflammatory factors, including ET, ROS, leptin, and an activated NADPH oxidase, in mediating the adverse effects of strong β-adrenoceptor stimulation in the heart[18, 19, 25]. In this regard, the role of ISO in activating β-receptors to downregulate FKBP12.6 is mediated by ET receptors and related pathways. In the present study we show that a selective antagonist of ET_A and ET_B rescue the downregulation of FKBP12.6/12 individually, in which ET_B exerted an effect comparable to that of ET_A. This phenomenon suggests that ET_B is actively implicated in the hyperadrenergic state and triggers events that worsen cardiac performance and ventricular tachyarrhythmias. In cardiac fibroblasts incubated with ISO, ET_B plays a minor role in the upregulation of Cx43, MMP-2, MMP-9, and NADPH oxidase relative to ET_A[18]. We found that CPU0213 is more effective than PD156707 and IRL-1038 in modulating FKBP12.6/12, which is consistent with the findings in a previous study[18]. Our findings are supported by evidence that ET_A and ET_B are located on the sympathetic nerve ending in the myocardium and control release of norepinephrine individually[26].

Rhein, an active component of Rheum officinale Baill, has anti-inflammatory activity and helps to relieve hepatic fibrosis[16]. With the activity against inflammatory factors in the kidney, rhein has been shown to be effective in treating diabetic nephropathy either as a single therapy[27, 28] or in combination with benazepril[29]. The solubility of rhein is low, and chemical modification is encouraged to improve its chemical properties. Di-acetyl-rhein (diacerein, diacerhein) was produced by adding two acetyl groups to the moiety and was launched for treating osteoarthritis in Europe[30]. Rhein functions as the active metabolite of diacerein in treating osteoarthritis by suppressing osteoarthritic chondrocytes and osteoclastic differentiation/survival[30]. Diacerein suppresses proinflammatory cytokine expression in nonobese diabetic (NOD) mice[31]. The extracellular matrix activity is modulated by rhein, mediated by inhibiting the ERK and JNK-AP-1 pathways[32].

Argirhein is a new compound containing two active molecules, rhein and *L*-arginine. The compound easily dissociates to form the two compounds in the body. As a consequence, the pharmacological effects of argirhein are relevant to the anti-inflammatory activity of rhein. On the other hand, an improvement in endothelial cells could be achieved by releasing *L*-arginine, which is beneficial to the recovery of dysfunctions of the vascular endothelium. A normal vascular endothelium is essential for cardiac function[7]. Activated ET_A and ET_B which participate in inflammatory reactions have been shown to be inhibited by argirhein.

An increase in ROS, ET and other cytokines is implicated in the events following the application of ISO[33], and in patients with ventricular tachyarrhythmias, inflammatory factors are critically involved in the pathogenesis, which is triggered by β-receptor activation, of conditions such as hyperthyroidism in which the incidence of cardiac arrhythmias is common, in association with exaggerated stimulation of β-adrenoceptors[34, 35]. As compared to those happened in acquired heart diseases genetic mutation cover only a small portion of severe arrhythmias, such as arrhythmogenic cardiomyopathy[36] and arrhythmias in patients with Brugada syndrome[37], indicating that inflammatory factors are likely the major causal factors implicated in the affected myocardium responsible for arrhythmogenesis.

In conclusion, the downregulation of FKBP12.6/12, a calcium-modulating protein at the sarcoplasmic reticulum, is a key event involved in the worsening of heart dysfunction and in the arrhythmogenesis caused by stress related to β-receptor stimulation. We demonstrated that both ET_A and ET_B played individual roles in mediating the downregulation of FKBP12.6/12 caused by ISO application. ET_B is definitely an active participant in this regard. We also showed for the first time that argirhein, a new compound containing rhein and *L*-arginine, shared the activity attenuating the ISO-induced downregulation of FKBP12.6/12 with ET blockers. Argirhein is potential drug for use in relieving stress related exacerbation of cardiac failure and arrhythmias by rescuing downregulation of FKBP12.6/12.

Acknowledgements

This work was supported by the National Natural Science Foundation of China (No 81070145) and the National Key New Drug Innovation Program, Ministry of Science and Technology of China, No 2009ZX09308.

Author contribution

Guo-lin ZHANG conducted the project, processed the data and prepared the manuscript. De-zai DAI and Tao XI designed the project, discussed the mechanisms underlying the results and revised the manuscript. Xiao-dong CONG and Yun ZHANG investigated the new compound argirhein and discussed the data. Yin DAI supervised the experiment and reviewed the collected data.

References

1 Sen-Chowdhry S, McKenna WJ. Sudden cardiac death in the young: A

strategy for prevention by targeted evaluation. Cardiology 2006; 105: 196–206.
2 Gollob MH. Genetic profiling as a marker for risk of sudden cardiac death. Curr Opin Cardiol 2006; 21: 42–6.
3 Chow BJ, Gollob M, Birnie D. Brugada syndrome precipitated by a tricyclic antidepressant. Heart 2005; 91: 651.
4 Wehrens XH, Lehnart SE, Huang F, Vest JA, Reiken SR, Mohler PJ, *et al*. FKBP12.6 deficiency and defective calcium release channel (ryanodine receptor) function linked to exercise-induced sudden cardiac death. Cell 2003; 113: 829–40.
5 Tomaselli GF, Zipes DP. What causes sudden death in heart failure? Circ Res 2004; 95: 754–63.
6 Rubart M, Zipes DP. Mechanisms of sudden cardiac death. J Clin Invest 2005; 115: 2305–15.
7 Blum A: Heart failure--new insights. Isr Med Assoc J 2009; 11: 105–11.
8 Yano M, Yamamoto T, Ikeda Y, Matsuzaki M. Mechanisms of disease: ryanodine receptor defects in heart failure and fatal arrhythmia. Nat Clin Pract Cardiovasc Med 2006; 3: 43–52.
9 Blayney LM, Jones JL, Griffiths J, Lai FA. A mechanism of ryanodine receptor modulation by FKBP12/12.6, protein kinase A, and K201. Cardiovasc Res 2010; 85: 68–78.
10 Jiang D, Jones PP, Davis DR, Gow R, Green MS, Birnie DH, *et al*. Characterization of a novel mutation in the cardiac ryanodine receptor that results in catecholaminergic polymorphic ventricular tachycardia. Channels (Austin) 2010; 4; 302-10.
11 Li N, Jia N, Dai DZ, Hu C, Dai Y. Role of endothelin in the effects of isoprenaline on potassium currents and calsequestrin 2 expression in the heart. Clin Exp Pharmacol Physiol 2010; 37: 557–63.
12 Zhang Y, Huang ZJ, Dai DZ, Feng Y, Na T, Tang XY, *et al*. Downregulated FKBP12.6 expression and upregulated endothelin signaling contribute to elevated diastolic calcium and arrhythmogenesis in rat cardiomyopathy produced by l-thyroxin. Int J Cardiol 2008; 130: 463–71.
13 Györke S, Carnes C. Dysregulated sarcoplasmic reticulum calcium release: potential pharmacological target in cardiac disease. Pharmacol Ther 2008; 119: 340–54.
14 Loomis ED, Sullivan JC, Osmond DA, Pollock DM, Pollock JS. Endothelin mediates superoxide production and vasoconstriction through activation of NADPH oxidase and uncoupled nitric-oxide synthase in the rat aorta. J Pharmacol Exp Ther 2005; 315: 1058–64.
15 Dong F, Zhang X, Ren J. Leptin regulates cardiomyocyte contractile function through endothelin-1 receptor-NADPH oxidase pathway. Hypertension 2006; 47: 222–9.
16 Guo MZ, Li XS, Xu HR, Mei ZC, Shen W, Ye XF. Rhein inhibits liver fibrosis induced by carbon tetrachloride in rats. Acta Pharmacol Sin 2002; 23: 739–44.
17 Malaguti C, Vilella CA, Vieira KP, Souza GH, Hyslop S, Zollner Rde L. Diacerhein downregulate proinflammatory cytokines expression and decrease the autoimmune diabetes frequency in nonobese diabetic (NOD) mice. Int Immunopharmacol 2008; 8: 782–91.
18 Peng HJ, Dai DZ, Ji H, Dai Y. The separate roles of endothelin receptors participate in remodeling of matrix metalloproteinase and connexin 43 of cardiac fibroblasts in maladaptive response to isoproterenol. Eur J Pharmacol 2010; 634: 101–6.
19 Feng Y, Tang XY, Dai DZ, Dai Y. Reversal of isoproterenol-induced downregulation of phospholamban and FKBP12.6 by CPU0213-mediated antagonism of endothelin receptors. Acta Pharmacol Sin 2007; 28: 1746–54.
20 Chelu MG, Wehrens XH. Sarcoplasmic reticulum calcium leak and cardiac arrhythmias. Biochem Soc Trans 2007; 35: 952–6.
21 Huang F, Shan J, Reiken S, Wehrens XH, Marks AR. Analysis of calstabin2 (FKBP12.6)-ryanodine receptor interactions: rescue of heart failure by calstabin2 in mice. Proc Natl Acad Sci USA 2006; 103: 3456–61.
22 Cheng YS, Dai DZ, Dai Y. Stress-induced cardiac insufficiency relating to abnormal leptin and FKBP12.6 is ameliorated by CPU0213, an endothelin receptor antagonist, which is not affected by the CYP3A suppressing effect of erythromycin. J Pharm Pharmacol 2009; 61: 569–76.
23 Tateishi H, Yano M, Mochizuki M, Suetomi T, Ono M, Xu X, *et al*. Defective domain-domain interactions within the ryanodine receptor as a critical cause of diastolic Ca^{2+} leak in failing hearts. Cardiovasc Res 2009; 81: 536–45.
24 Qi MY, Feng Y, Dai DZ, Li N, Cheng YS, Dai Y. CPU86017, a berberine derivative, attenuates cardiac failure through normalizing calcium leakage and downregulated phospholamban and exerting antioxidant activity. Acta Pharmacol Sin 2010; 31: 165–74.
25 Na T, Dai DZ, Tang XY, Dai Y. Upregulation of leptin pathway correlates with abnormal expression of SERCA2a, phospholamban and the endothelin pathway in heart failure and reversal by CPU86017. Naunyn Schmiedebergs Arch Pharmacol 2007; 375: 39–49.
26 Isaka M, Kudo A, Imamura M, Kawakami H, Yasuda K. Endothelin receptors, localized in sympathetic nerve terminals of the heart, modulate norepinephrine release and reperfusion arrhythmias. Basic Res Cardiol 2007; 102: 154–62.
27 Zheng JM, Zhu JM, Li LS, Liu ZH. Rhein reverses the diabetic phenotype of mesangial cells over-expressing the glucose transporter (GLUT1) by inhibiting the hexosamine pathway. Br J Pharmacol 2008; 153: 1456–64.
28 Gao Q, Qin WS, Jia ZH, Zheng JM, Zeng CH, Li LS, *et al*. Rhein improves renal lesion and ameliorates dyslipidemia in *db/db* mice with diabetic nephropathy. Planta Med 2010; 76: 27–33.
29 Jia ZH, Liu ZH, Zheng JM, Zeng CH, Li LS. Combined therapy of rhein and benazepril on the treatment of diabetic nephropathy in *db/db* mice. Exp Clin Endocrinol Diabetes 2007; 115: 571–6.
30 Legendre F, Heuze A, Boukerrouche K, Leclercq S, Boumediene K, Galera P, *et al*. Rhein, the metabolite of diacerhein, reduces the proliferation of osteoarthritic chondrocytes and synoviocytes without inducing apoptosis. Scand J Rheumatol 2009; 38: 104–11.
31 Boileau C, Tat SK, Pelletier JP, Cheng S, Martel-Pelletier J. Diacerein inhibits the synthesis of resorptive enzymes and reduces osteoclastic differentiation/survival in osteoarthritic subchondral bone: a possible mechanism for a protective effect against subchondral bone remodelling. Arthritis Res Ther 2008; 10: R71.
32 Malaguti C, Vilella CA, Vieira KP, Souza GH, Hyslop S, Zollner Rde L. Diacerhein downregulate proinflammatory cytokines expression and decrease the autoimmune diabetes frequency in nonobese diabetic (NOD) mice. Int Immunopharmacol 2008; 8: 782–91.
33 Legendre F, Bogdanowicz P, Martin G, Domagala F, Leclercq S, Pujol JP, *et al*. Rhein, a diacerhein-derived metabolite, modulates the expression of matrix degrading enzymes and the cell proliferation of articular chondrocytes by inhibiting ERK and JNK-AP-1 dependent pathways. Clin Exp Rheumatol 2007; 25: 546–55.
34 Li N, Jia N, Dai DZ, Dai Y. Endothelin receptor antagonist CPU0213 and vitamin E reverse downregulation of FKBP12.6 and SERCA2a: a role of hyperphosphorylation of PKCepsilon. Eur J Pharmacol 2008; 591: 211–8.
35 Xia HJ, Dai DZ, Dai Y. Up-regulated inflammatory factors endothelin, NFkappaB, TNFalpha and iNOS involved in exaggerated cardiac arrhythmias in l-thyroxine-induced cardiomyopathy are suppressed by darusentan in rats. Life Sci 2006; 79: 1812–9.
36 Du RH, Yi HW, Dai DZ, Tang WH, Dai Y. Inflammatory factors that contribute to upregulation of ERG and cardiac arrhythmias are suppressed by CPU86017, a class III antiarrhythmic agent. J Pharm Pharmacol 2008; 60: 1089–95.
37 Altamirano E, Drut R. Arrhythmogenic cardiomyopathy in a patient with Noonan syndrome. Fetal Pediatr Pathol 2010; 29: 158–64.
38 Zumhagen S, Spieker T, Rolinck J, Baba HA, Breithardt G, Böcker W, *et al*. Absence of pathognomonic or inflammatory patterns in cardiac biopsies from patients with Brugada syndrome. Circ Arrhythm Electrophysiol 2009; 2: 16–23.

Acta Pharmacologica Sinica (2011) 32: 230–238
 1671-4083/11 $32.00
www.nature.com/aps

Original Article

17β-Estradiol inhibition of PPARγ-induced adipogenesis and adipocyte-specific gene expression

Sunhyo JEONG, Michung YOON*

Department of Life Sciences, Mokwon University, Daejeon 302-729, Korea

Aim: To investigate the molecular interaction of peroxisome proliferator-activated receptor γ (PPARγ) with 17β-estradiol (E) in the regulation of adipogenesis.
Methods: Female ovariectomized (OVX) mice and differentiated 3T3-L1 adipocytes were treated with combinations of the PPARγ agonist troglitazone or E, and the variables and determinants of adipogenesis were measured using *in vivo* and *in vitro* approaches.
Results: Troglitazone (250 mg·kg^{-1}·d^{-1} for 13 weeks) decreased the size of adipocytes without the change in white adipose tissue (WAT) mass and increased the expression of adipocyte-specific genes, such as PPARγ, adipocyte fatty acid binding protein, and lipoprotein lipase, compared with OVX control mice. E (0.05 mg/pellet, sc implanted) significantly reduced WAT mass, adipocyte size, and adipose marker gene expression. When mice were concomitantly treated with troglitazone and E, E blunted the effects of troglitazone on WAT mass, adipocyte size, and adipose PPARγ target gene expression. Consistent with the *in vivo* data, E (10 μmol/L) treatment inhibited lipid accumulation and the expression of adipocyte-specific genes caused by troglitazone (10 μmol/L) in 3T3-L1 cells. E (10 μmol/L) also decreased troglitazone-induced PPARγ reporter activity through both estrogen receptor (ER) α and ERβ. Mechanistic studies indicated that E (0.1 μmol/L) decreased the DNA binding of PPARγ induced by troglitazone (1 μmol/L) and inhibited the recruitment of the PPARγ coactivator CREB-binding protein.
Conclusion: These results suggest that *in vivo* and *in vitro* treatment of E interferes with the actions of PPARγ on adipogenesis by down-regulating adipogenesis-related genes, which are mediated through the inhibition of PPARγ coactivator recruitment. In addition, it is likely that the activities of PPARγ activators may be enhanced in estrogen-deficient states.

Keywords: PPARγ; adipogenesis; 17β-estradiol; troglitazone; coactivator recruitment; ovariectomized mice; 3T3-L1 cells

Acta Pharmacologica Sinica (2011) 32: 230–238; doi: 10.1038/aps.2010.198

Introduction

Peroxisome proliferator-activated receptor γ (PPARγ) is a ligand-activated transcription factor that plays a central role in adipocyte gene expression and differentiation. It is expressed at high levels, specifically in white (WAT) and brown adipose tissue (BAT), and its expression is turned on before transcriptional activation of most adipose-specific genes[1]. The importance of PPARγ in adipocyte differentiation has been extensively studied *in vitro* using a variety of cell types, including fibroblasts, adipocytes, and stem cell lines[2–4]. Thiazolidinediones (TZDs) are PPARγ agonists that promote adipogenesis, enhance lipid accumulation, and induce the expression of PPARγ-responsive genes during adipogenesis in these cell types[4, 5]. In adipose tissue, most PPARγ target genes are directly implicated in lipogenic pathways, including lipoprotein lipase (LPL), adipocyte fatty acid binding protein (aP2), acyl-CoA synthase, and fatty acid transport protein. The role of PPARγ in adipocyte development *in vivo* is also shown in several mouse models[6]. Embryonic stem cells lacking PPARγ cannot contribute to fat formation, and the PPARγ mutant mouse is deficient for WAT and BAT[3, 7–9]. In adult mice, PPARγ ablation in WAT and BAT results in adipocyte death within a few days, demonstrating that PPARγ is also required for the *in vivo* survival of mature adipocytes[10]. In addition to adipocyte development, TZDs induce the apoptosis of large adipocytes, resulting in adipose tissue remodeling[11, 12].

Adipose tissue is also a target for sex steroids because sex steroid receptors are expressed in rat and human adipose tissues[13, 14]. In particular, 17β-estradiol (E) has been recognized as a major factor in regulating adipose tissue metabolism in females. Ovariectomy in rodents leads to weight gain, primarily in the form of adipose tissue, which is reversed by physiologic E replacement[15, 16]. Loss of circulating E is associated with an increase in adiposity during menopause, whereas postmenopausal women who receive E replacement therapy do not display the characteristic abdominal weight gain pattern usually associated with menopause[17]. E also plays an important role in regulating adipocyte differentiation and development. E represses adipogenic differentiation and maturation via an estrogen receptor (ER)-dependent mecha-

* To whom correspondence should be addressed.
E-mail yoon60@mokwon.ac.kr
Received 2010-09-09 Accepted 2010-11-02

nism in human and mouse bone marrow stromal cells[18, 19]. The phytoestrogen genistein, which has high affinity for ERs, inhibits adipocyte differentiation, lipid accumulation, and the expression of adipocyte-specific genes in primary human adipocytes[20]. E was also reported to stimulate the proliferation of human preadipocytes, which can remain undifferentiated cells, into adipocytes[21].

Both PPARγ and ERs are members of the nuclear hormone receptor superfamily of ligand-activated transcription factors, and they share similar cofactors[22–24]. Transcriptional stimulation and suppression, in response to ligand binding to PPARγ or ERs, are mediated by interactions with coactivator proteins, such as steroid receptor coactivator-1 (SRC-1) and CREB-binding protein (CBP), and corepressor proteins, such as nuclear receptor CoR (a silencing mediator of retinoic acid) and thyroid hormone receptor. It has previously been shown that competition between nuclear receptors for coactivator binding results in a negative cross-talk between nuclear receptors[25, 26].

Several studies have suggested that a mutual signaling cross-talk exists between ERs and PPARγ. ERs are capable of inhibiting ligand-induced PPARγ activation in two different breast cancer cell lines[27]. Noticeably, it was reported that E regulates PPARγ activity on adipogenesis in KS483 cells, which concurrently differentiate into osteoblasts and adipocytes[28]. Our previous results showed that PPARγ did not induce adipogenesis in female mice with functioning ovaries, indicating that PPARγ activity on adipogenesis might be influenced by estrogens[29]. In addition, there is evidence that lack of E may potentiate the actions of TZDs on adipogenesis[28, 30]. Thus, we hypothesized that PPARγ-induced adipogenesis might be suppressed by E in females.

The aim of this study was to determine the molecular mechanism by which E inhibits the actions of troglitazone, a TZD PPARγ agonist, on adipogenesis in female mice. Using *in vivo* and *in vitro* approaches, we show that E suppresses the actions of troglitazone-activated PPARγ on adipogenesis and suppresses adipose-specific gene expression through inhibition of PPARγ coactivator recruitment.

Materials and methods

Animal treatments

For all experiments, 8-week-old female mice (C57BL/6J) were housed and bred at the Korea Research Institute of Bioscience and Biotechnology under pathogen-free conditions with a standard 12-h light/dark cycle. Prior to the administration of special diets, mice were fed standard rodent chow and water *ad libitum*. Female mice were ovariectomized (OVX) and then randomly divided into four groups (n=8 per group), which showed uniformity in response to each treatment in the pilot study. The first group was fed a regular chow diet (CJ, Incheon, Korea) for 13 weeks. The second group was given the same chow diet supplemented with troglitazone (Sankyo, Tokyo, Japan). Troglitazone (250 $mg \cdot kg^{-1} \cdot d^{-1}$) was given as food admixture at the concentration of 0.2%. The third group was fed a chow diet and subcutaneously implanted with E (0.05 mg per pellet; Innovative Research of America, Sarasota, FL, USA). The final group was given the troglitazone-supplemented diet and was also implanted with E.

In all experiments, body weights were measured daily using a top-loading balance, and the person measuring the body weight was blind to each treatment group. Animals were sacrificed by cervical dislocation, and tissues were harvested, weighed, snap-frozen in liquid nitrogen, and stored at -80 °C until use. All animal experiments were approved by the Institutional Animal Care and Use Committee of Mokwon University and followed National Research Council Guidelines.

Histological analysis

For hematoxylin and eosin (HE) staining, WAT was fixed in 10% phosphate-buffered formalin for 1 d and processed in a routine manner for paraffin sectioning. Tissue sections (4 μm) were cut and stained with HE for microscopic examination. To quantify adipocyte size, the HE-stained sections were analyzed using the Image-Pro Plus analysis system (Media Cybernetics, Bethesda, MD, USA).

Induction of preadipocyte differentiation

Mouse 3T3-L1 cells (ATCC) were proliferated in 6-well plates in DMEM containing 10% bovine calf serum (Invitrogen, Carlsbad, CA, USA). After cells were kept confluent for 2 d, they were incubated in an MDI induction medium (d 0) containing 0.5 mmol/L 1-methyl-3-isobutyl-xanthin, 1 μmol/L dexamethasone, and 1 μg/mL insulin in DMEM with 10% fetal bovine serum (FBS) (Invitrogen). The cultures were continued for 2 d to induce adipocyte differentiation. Thereafter, cells were cultured in DMEM with 10% FBS for the rest of the differentiation process. All other treatments were administered on d 0 to d 2 only, and the medium was changed every other day. Cells were stained at d 6 with Oil-red O and photographed.

Analysis of target gene expression

Total cellular RNA was prepared from parametrial WAT and 3T3-L1 cells using Trizol reagent (Invitrogen). For Northern blot analysis, RNA was analyzed by electrophoresis on 0.22 mol/L formaldehyde-containing 1.2% agarose gels. The separated RNA was transferred to Nytran membranes (Schneicher & Schuell, Dassel, Germany) by downward capillary transfer in the presence of 20× SSC buffer (3 mol/L NaCl and 0.3 mol/L sodium citrate, pH 7.0), then UV cross-linked and baked for 2 h at 80 °C. Probe hybridization and washing were performed using standard techniques. Blots were exposed to PhosphorImager screen cassettes and were visualized using a Molecular Dynamics Storm 860 PhosphorImager system (Sunnyvale, CA, USA). The probes used in this study were ^{32}P-labeled by the random-primer method using a Ready-to-Go DNA Labeling kit (Amersham-Pharmacia Biotech, Piscataway, NJ, USA). Densitometric analysis of the mRNA signals was performed using ImageQuant image analysis software (Molecular Dynamics).

For RT-PCR analysis, after 2 μg of total RNA was reverse-transcribed using Moloney murine leukemia virus reverse transcriptase (MMLV-RT; Promega, Madison, WI, USA) and an antisense primer, cDNA was generated, the RNA was

denatured for 5 min at 72 °C and then immediately placed on ice for 5 min. Denatured RNA was mixed with MMLV-RT, MMLV-RT buffer, and a dNTP mixture and incubated for 1 h at 42 °C. Synthesized cDNA fragments were amplified by PCR in an MJ Research Thermocycler (Waltham, MA, USA). The PCR primers used for gene expression analysis are shown in Table 1. The cDNA was mixed with PCR primers, Taq DNA polymerase (Solgent, Daejeon, Korea), and a dNTP mixture. The reaction consisted of 24–34 cycles of denaturation for 1 min at 94 °C, annealing for 1 min at 52–58 °C, and elongation for 1 min at 72 °C. The PCR products were analyzed by electrophoresis on a 1% agarose gel. Relative expression levels were presented as a ratio of target gene cDNA to β-actin cDNA. PCR products were quantified from agarose gels using the GeneGenius (Syngene, Cambridge, UK).

Table 1. Sequences of oligonucleotide primers and PCR conditions.

Genes	Size (bp)	Primer sequences	Annealing (°C)	Cycle
PPARγ	340	Forward: 5′-attctggcccaccaacttcgg-3′ Reverse: 5′-tggaagcctgatgctttatcccca-3′	58	28
aP2	417	Forward: 5′-caaaatgtgtgatgcctttgtg-3′ Reverse: 5′-ctcttcctttggctcatgcc-3′	58	24
LPL	770	Forward: 5′-atggagagcaaagccctgc-3′ Reverse: 5′-agtcctctctctgcaatcca-3′	52	34
β-acitn	350	Forward: 5′-tggaatcctgtggcatccatgaaa-3′ Reverse: 5′-taaaacgcagctcagtaacagtcc-3′	58	28

Transfection assays

The expression vectors for pSG5-mPPARγ and $PPRE_3$-tk-luc reporter genes were generously provided by Dr Frank GONZALEZ (National Cancer Institute, NIH, Bethesda, MD, USA). Expression vectors for pcDNA-ERα and pcDNA-ERβ were generously provided by Dr Matt BUROW (Tulane University Medical Center, New Orleans, LA, USA). Expression vectors for VP16-mPPARγ and GAL-CBP were generously provided by Steve KLIEWER (University of Texas Southwestern Medical Center, Dallas, TX, USA), and expression vectors for VP16-hERα and VP16-hERβ were generously provided by Dr Donald MCDONNELL (Duke University Medical Center, Durham, NC, USA). The GAL4-UAS luciferase reporter plasmid (pFR-Luc) was obtained from Stratagene (La Jolla, CA, USA). The murine preadipocyte cell line 3T3-L1 cells and monkey kidney cell line CV-1 cells were routinely cultured in DMEM containing 10% FBS, penicillin G (100 U/mL), streptomycin sulfate (100 μg/mL), amphotericin B (0.25 μg/mL), and 2-mercaptoethanol (50 μmol/L). Cells were seeded in 6-well tissue culture plates (2×10^4 cells/well) for 24 h prior to transfection. For all transfections, 200 ng/well of each of the appropriate plasmids were used. Transfections were performed using lipofectamine (Invitrogen) according to the manufacturer's instructions. After 6 h, the culture medium was changed and the test compounds, troglitazone and E (Sigma), were added. After incubation for 24 h in the presence of these chemicals, the cells were washed twice with phosphate-buffered saline and assayed for luciferase and β-galactosidase activities using commercial kits according to the manufacturer's instructions (Promega).

Electrophoretic mobility shift assay

The binding of PPARγ to a PPAR-specific oligonucleotide probe was accomplished by adding 8 μg of crude nuclear extract from WAT to each gel shift reaction mixture. An oligonucleotide consensus DR-1 element was synthesized with the following sequence: 5′–GAACTAGGTCAAAGGTCATCCCCT–3′ along with an oligonucleotide of a complementary sequence (Geno Tech, Daejeon, Korea). The oligonucleotides were mixed (50 ng/μL final concentration) and denatured by heating them to 95 °C for 10 min in 0.1 mol/L Tris-HCl and 50 mmol/L $MgCl_2$ (pH 7.9). They were then allowed to anneal by slowly cooling to room temperature. The annealed oligonucleotides were end-labeled with [γ-^{32}P]ATP using T4 polynucleotide kinase according to the supplier's instructions (Promega). In a total volume of 20 μL of binding buffer [25 mmol/L Tris-HCl (pH 7.5), 40 mmol/L KCl, 0.5 mmol/L $MgCl_2$, 0.1 mmol/L EDTA, 1 mmol/L dithiothreitol, and 10% glycerol], the following components were combined: 1 μg of poly(dI-dC), 2 μL of nuclear extract, and the indicated concentrations of troglitazone or E dissolved in DMSO. For a supershift experiment, 2 μg of goat anti-human PPARγ antibody (Santa Cruz Biotechnology, Santa Cruz, CA, USA) was added to the reaction mixture prior to the oligonucleotide probe. After a 20-min incubation at room temperature, 20 000 cpm of the labeled oligonucleotide was added, and the incubation was continued for a further 20 min. The samples were analyzed on a 5% non-denaturing polyacrylamide gel, containing 2.5% glycerol, in 0.4×TBE (1×=89 mmol/L Tri-HCl, 89 mmol/L boric acid, and 2 mmol/L EDTA). After drying, the gels were exposed to PhosphorImager screen cassettes and were visualized using a Molecular Dynamics Storm 860 PhosphorImager system.

Statistical analysis

Unless otherwise noted, all values are expressed as mean± standard deviation (SD). All data were analyzed by the unpaired, Student's *t*-test for significant differences between the mean values of each group using SigmaPlot 2001 (SPSS, Chicago, IL, USA).

Results

Body weight, WAT mass, and adipocyte size

Troglitazone did not cause significant changes in body and WAT weights; whereas E significantly decreased both compared with controls (Figure 1). A combination of troglitazone and E significantly reduced body and WAT weights compared with troglitazone alone, although not to the same extent as E alone.

Histological analysis showed that, compared with control, troglitazone and E decreased the size of adipocytes in parametrial WAT by 52.3% and 46.6%, respectively (Figure 2). The adipocyte size was further reduced by concomitant treatment

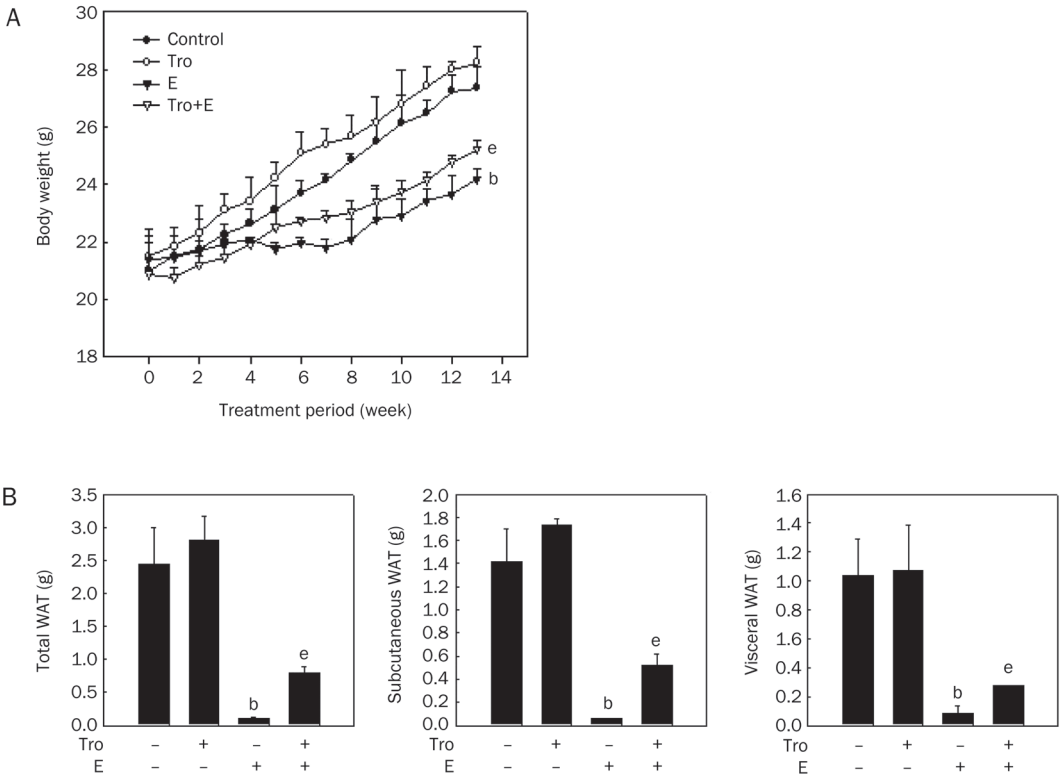

Figure 1. Body weight and WAT mass. Body weight (A) and WAT mass (B) were determined after 13 weeks of treatment with troglitazone (Tro; 250 mg·kg^{-1}·d^{-1}), 17β-estradiol (E; 0.05 mg/pellet), or Tro plus E in female OVX mice (n=8/group). All values are expressed as mean±SD. $^{b}P<0.05$ *vs* control group. $^{e}P<0.05$ *vs* Tro group.

with troglitazone and E.

Expression of PPARγ target genes in WAT

To determine whether the effects of E on troglitazone-regulated adipocyte size and WAT mass are associated with changes in PPARγ and PPARγ target gene expression in WAT, we measured mRNA levels of PPARγ and the PPARγ target genes aP2 and LPL. As expected, troglitazone substantially upregulated PPARγ, aP2, and LPL mRNA levels by 69.2%, 114.5%, and 81.9%, respectively, compared with controls, whereas E downregulated PPARγ, aP2, and LPL mRNA levels by 34.2%, 50%, and 60.4%, respectively (Figure 3). Co-administration of troglitazone and E decreased the troglitazone-induced PPARγ, aP2, and LPL mRNA expression by 38.8%, 63.6%, and 81.4%, respectively, compared with troglitazone alone. These results suggest that E may decrease adipose mRNA levels of troglitazone-induced PPARγ target genes, thereby preventing *in vivo* actions of PPARγ on body weight, WAT weight, and adipocyte size.

3T3-L1 differentiation and adipocyte-specific gene expression

Accumulation of triglyceride droplets in 3T3-L1 cells was evident on the sixth day following 2 d of MDI (Figure 4B) or troglitazone (Figure 4D) treatment, as shown by positive staining with Oil red O. Treatment of cells with E, however, inhibited triglyceride accumulation. The percentage of differentiated cells in the MDI and E-treated cells was approximately 73% (Figure 4C), and it was 81% in troglitazone and E-treated cells (Figure 4E).

To quantify changes in differentiation degree by troglitazone and E, we analyzed PPARγ and PPARγ-dependent gene expression. Troglitazone substantially upregulated PPARγ (Figure 4F) and aP2 (Figure 4G) mRNA levels by 68.8% and 70.8%, respectively, compared with controls. Whereas co-administration of troglitazone and E significantly decreased troglitazone-induced PPARγ and aP2 mRNA levels by 22.5% and 13.5%, respectively. Thus, E was inhibitory to MDI- or troglitazone-induced differentiation, in part through reductions in PPARγ target gene expression.

PPARγ reporter gene expression

To examine the mechanism by which E inhibited the troglitazone-induced PPARγ and PPARγ target gene expression, 3T3-L1 preadipocytes were transiently transfected with PPARγ, ERα, and ERβ expression constructs and a luciferase reporter gene construct ($PPRE_3$-tk-luc) containing three copies of the PPRE from the rat acyl-CoA oxidase gene. Overexpression of PPARγ alone significantly increased the expression of the luciferase reporter gene compared with controls (Figure 5, lane 2 *vs* lane 1), potentially due to endogenous ligands. Troglitazone significantly elevated the luciferase reporter activity induced by PPARγ transfection (Figure 5, lane 7 *vs* lane 2). Overexpression of ERα or ERβ substantially inhibited the induction of the luciferase activity caused by PPARγ (Figure 5, lanes 3 and 5) as well as PPARγ plus troglitazone (Figure 5, lanes 8 and 10). Moreover, treatment with E led to a further inhibition of constitutive- (Figure 5, lanes 4 and 6) and ligand-dependent PPARγ reporter activities by ERα or ERβ (Figure 5, lanes 9 and 11). These results suggest that E inhibits PPARγ-dependent transactivation through ERα and ERβ.

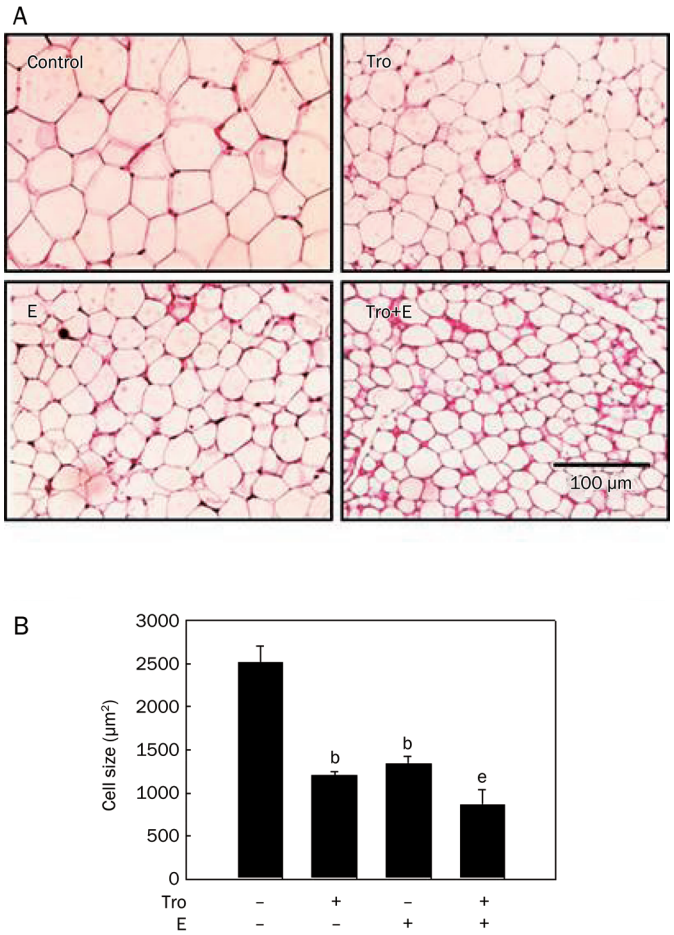

Figure 2. Histological analysis of parametrial WAT stained with hematoxylin and eosin (original magnification ×200). Adult female mice (n=8/group) received a chow diet with troglitazone (Tro; 250 mg·kg^{-1}·d^{-1}), 17β-estradiol (E; 0.05 mg/pellet), or Tro plus E for 13 weeks. (A) Representative hematoxylin and eosin (HE)-stained sections (4 μm thick) of female parametrial adipose tissue. (B) HE-stained sections were analyzed with an image analysis system, and the size of the adipocytes was quantified. All values are expressed as mean±SD. ^{b}P<0.05 *vs* control group. ^{e}P<0.05 *vs* Tro group.

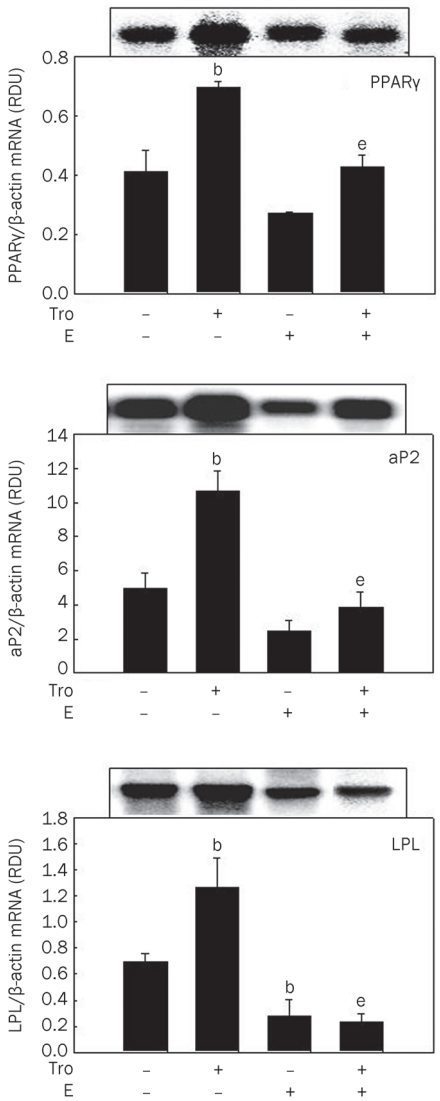

Figure 3. The mRNA expression levels of PPARγ and PPARγ target genes in WAT of female OVX mice. Female OVX mice (n=8/group) received a chow diet with troglitazone (Tro; 250 mg·kg^{-1}·d^{-1}), 17β-estradiol (E; 0.05 mg/pellet), or Tro plus E for 13 weeks. Total RNA was extracted from the parametrial adipose tissue and PPARγ, PPARγ target genes, and β-actin mRNA levels were measured as described in the Materials and methods section. All values are expressed as mean±SD of RDU (relative density units) using β-actin as a reference. Insets show representative autoradiograms of Northern blots used for quantification. ^{b}P<0.05 *vs* control group. ^{e}P<0.05 *vs* Tro group.

PPARγ binding to DNA

An electrophoretic mobility shift assay (EMSA) was performed to determine whether E interfered with the binding of PPARγ/RXRα to a consensus DR-1 sequence (AGGTCAAAGGTCA). Treatment of a nuclear extract containing the PPARγ/RXRα complex with 1 μmol/L troglitazone increased DNA binding of PPARγ/RXRα compared with vehicle (Figure 6A, lane 3 and Figure 6B, lane 3), whereas 1 μmol/L E decreased DNA binding to the complex (Figure 6A, lane 8 and Figure 6B, lane 4). However, E decreased the troglitazone-induced DNA binding of PPARγ/RXRα, as shown by the combination of troglitazone and E (Figure 6B, lane 5 *vs* lane 3), suggesting that E prevents PPARγ from binding to DNA. To verify the identity of the PPARγ/RXRα complex, we conducted a supershift assay using an anti-PPARγ antibody. The PPARγ/RXRα complex disappeared when an anti-PPARγ antibody was added (Figure 6B, lanes 6–8).

Cofactor recruitment

To determine whether changes in cofactor recruitment are involved in the E-mediated inhibition of PPARγ binding to DNA and PPARγ activity, the coactivator CBP was examined using a mammalian two-hybrid assay. The key components of this assay include the followings: 1) reporter constructs for full-length murine PPARγ fused to the transactivation domain of VP16 and 2) the nuclear receptor-interaction domains of

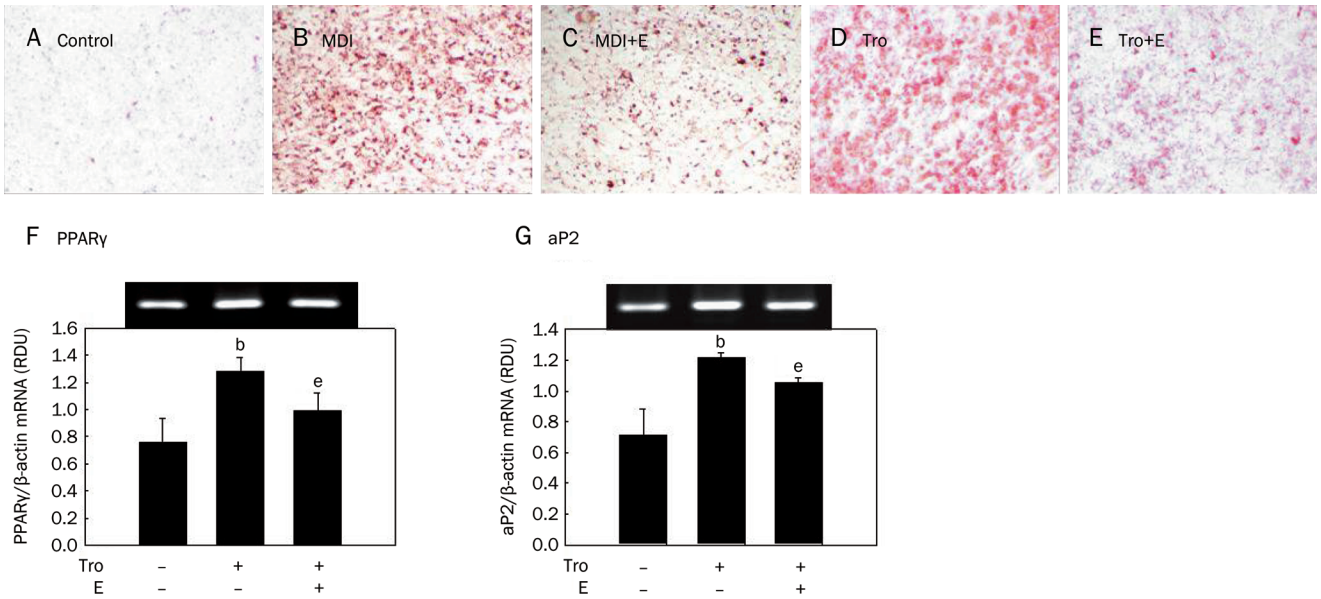

Figure 4. Adipocyte differentiation and adipose-specific gene expression in 3T3-L1 cells. 3T3-L1 preadipocytes were differentiated into mature adipocytes as described in the Materials and methods section. 3T3-L1 cells were treated with an MDI mix (MDI), 10 μmol/L troglitazone (Tro), 10 μmol/L 17β-estradiol (E), or 10 μmol/L Tro plus 10 μmol/L E. (A–E) At d 6 post-induction, cells were fixed and stained for neutral lipids with Oil red O. Magnification is ×10. (F and G) Total cellular RNA was extracted from differentiated cells on d 6, and mRNA levels of PPARγ, aP2, and β-actin were measured using RT-PCR. Insets show representative RT-PCR bands used for quantifictation. [b]*P*<0.05 *vs* control group. [e]*P*<0.05 *vs* Tro group.

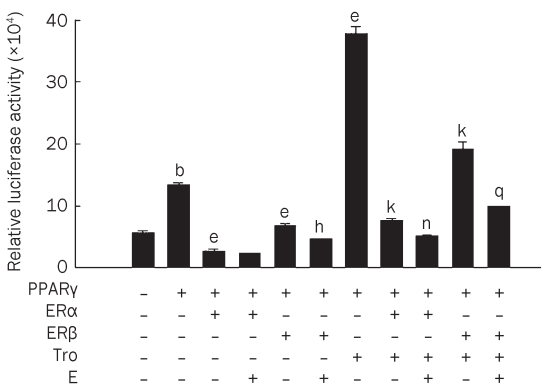

Figure 5. PPARγ reporter gene expression in 3T3-L1 cells. 3T3-L1 preadipocytes were transiently transfected with pSG5-mPPARγ, reporter plasmid PPRE-TK-Luc, and pcDNA-ERα or pcDNA-ERβ. Cells were treated with 10 μmol/L troglitazone (Tro) and/or 10 μmol/L 17β-estradiol (E). After incubation for 24 h, cells were harvested, lysed, and subsequently assayed for luciferase and β-galactosidase activities. All values are expressed as the mean±SD of relative luciferase units/β-galactosidase activity. Experiments were performed at least three times. [b]*P*<0.05 *vs* control group. [e]*P*<0.05 *vs* PPARγ group. [h]*P*<0.05 *vs* PPARγ/ERβ group. [k]*P*<0.05 *vs* PPARγ/Tro group. [n]*P*<0.05 *vs* PPARγ/Tro/ERα group. [q]*P*<0.05 *vs* PPARγ/Tro/ERβ group.

CBP fused to the DNA binding domain of GAL4. In CV-1 cells transfected with PPARγ and CBP, troglitazone caused efficient CBP recruitment, as evidenced by an increase in luciferase reporter gene activity (Figure 7, lane 2 *vs* lane 1). However, transfection with ERα or ERβ reduced the troglitazone-induced CBP association (Figure 7, lanes 3 and 5), and E markedly decreased the magnitude of the reporter gene inhibition by ERβ (Figure 7, lane 6) but not by ERα (lane 4).

Discussion

The present study demonstrates that *in vivo* and *in vitro* treatments with E negatively regulate the troglitazone-activated PPARγ actions on adipogenesis and adipocyte-specific gene expression. We further show that these events are mediated, at least in part, through the E inhibition of PPARγ coactivator recruitment.

Mice treated with troglitazone for 13 weeks exhibited a significant decrease in adipocyte size without changes in body weight gain and WAT weight compared with chow diet-fed controls. These data support previous results showing that troglitazone increased the number of small adipocytes without affecting body weight gain and WAT mass in obese Zucker rats[31]. However, a combination of troglitazone and E upset the effect of troglitazone. Body weight gain and WAT mass were decreased and adipocyte size was further decreased compared with troglitazone alone. According to the results from Kadowaki *et al* and Yamauchi *et al*, supraphysiological activation of PPARγ by PPARγ agonists stimulated the adipocyte differentiation and apoptosis of large adipocytes, thereby preventing adipocyte hypertrophy and increasing the small adipocytes, whereas reductions in PPARγ activity decreased adipocyte size and WAT mass via activation of fatty acid oxidation and energy dissipation[12, 32]. It is thought that both supraphysiological activation of PPARγ by PPARγ agonists and inhibition of PPARγ activity by E can lead to the reduced size of adipocytes through different mechanisms of action.

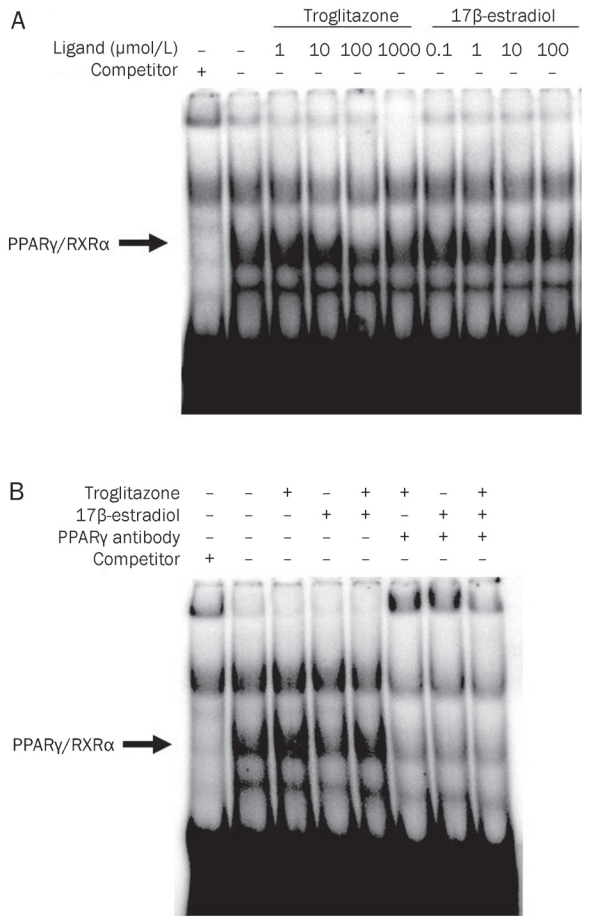

Figure 6. Binding of PPARγ to PPRE. EMSAs were performed using nuclear extracts from the WAT of female C57BL/6J mice. (A) While the PPARγ activator troglitazone increased PPARγ binding to the consensus DR-1 sequence containing PPRE, 17β-estradiol decreased the binding of PPARγ. (B) 17β-estradiol (0.1 μmol/L) inhibited the troglitazone (1 μmol/L)-induced PPARγ binding to PPRE. An anti-PPARγ antibody was included to show the identity of the PPARγ/RXRα complexes.

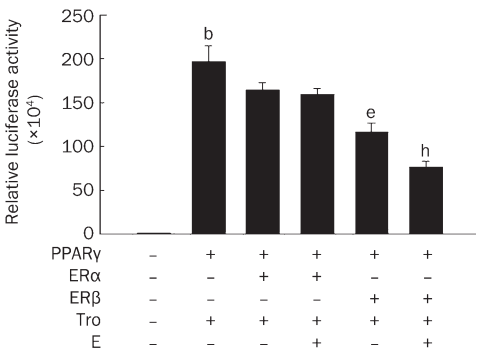

Figure 7. PPARγ coactivator recruitment. A mammalian two-hybrid assay was used to detect the ligand-dependent interaction of PPARγ with CBP. CV-1 cells were transiently transfected with expression plasmids for VP16-mPPARγ, GAL-CBP, reporter plasmid pFR-Luc, and VP16-hERα or VP16-hERβ. All values are expressed as the mean±SD for three experiments. $^{b}P<0.05$ *vs* control group. $^{e}P<0.05$ *vs* PPARγ/Tro group. $^{h}P<0.05$ *vs* PPARγ/Tro/ERβ group.

Thus, these results suggest that reduced PPARγ activity by E decreases the size of adipocytes and WAT mass.

The development of fat cells from preadipocytes, or adipogenesis, includes the followings: morphological changes, cessation of cell growth, expression of many lipogenic enzymes, and extensive lipid accumulation[33]. As expected, troglitazone increased the accumulation of triglyceride droplets in 3T3-L1 cells compared with vehicle-treated controls. However, E treatment prevented this troglitazone-induced lipid accumulation, indicating that E has an inhibitory effect on troglitazone-induced adipogenesis. Similarly, adipogenic differentiation and maturation are reported to be reduced by E and genistein via an ER-dependent mechanism[18–20]. PPARγ transcriptional activity and its effects on adipogenic differentiation were enhanced in the absence of E, whereas E inhibited PPARγ-mediated adipocyte differentiation[18, 28]. These results are paralleled by enhanced adipogenesis in E-deprived rats treated with the PPARγ agonist rosiglitazone[30]. Moreover, our previous study showed that troglitazone treatment did not significantly increase the smaller size of adipocytes in parametrial adipose tissue in female mice with functioning ovaries, although it did increase the number of small adipocytes in male animals[29]. Thus, PPARγ does not seem to be involved in the regulation of adipogenesis in female mice with functioning ovaries, suggesting that the effects of troglitazone on adipogenesis may be disrupted by a sex-related factor, namely E, in female mice.

Adipogenesis is initiated by the production of the key transcription factor PPARγ, which is responsible for inducing the expression of adipocyte-specific genes. Consistent with the effects of E on troglitazone-induced adipogenesis, E decreased the expression of PPARγ and the PPARγ target genes aP2 and LPL, which are directly implicated in lipogenic pathways, in both WAT of OVX mice and in 3T3-L1 adipocytes. Previous studies reported that E and genistein may have anti-lipogenic and anti-adipogenic effects by downregulating the expression of adipocyte-specific genes, such as PPARγ, CCAAT/enhancer binding protein α, aP2, and LPL, in OVX mice, primary human adipocytes, and mouse and human bone marrow stromal cells[18–20, 28]. Similarly, troglitazone did not affect PPARγ mRNA expression or adipocyte-specific gene expression in E-producing female mice. Thus, these results suggest that E can prevent the ability of troglitazone to regulate adipogenesis and lipogenesis through inhibiting PPARγ and PPARγ target gene expression.

There is evidence to show that a bidirectional signaling cross-talk exists between PPARγ and ERs[34–38]. Keller *et al* demonstrated that the PPARγ/RXRα complex inhibited transcription by ERs through a competition for estrogen response element binding in the vitellogenin A2 promoter[34]. Wang *et al* demonstrated that both ERα and ERβ were capable of inhibiting PPARγ transactivation in PPARγ-expressing MDA-MB-231 and MCF-7 breast cancer cells[27]. Expression of ERα or ERβ lowered both basal and stimulated PPARγ-mediated reporter activities, and deletion of the ER DNA-binding domain rendered ERs unable to inhibit either basal or stimulated PPAR transactivation[27]. These data suggest that both ERs are capa-

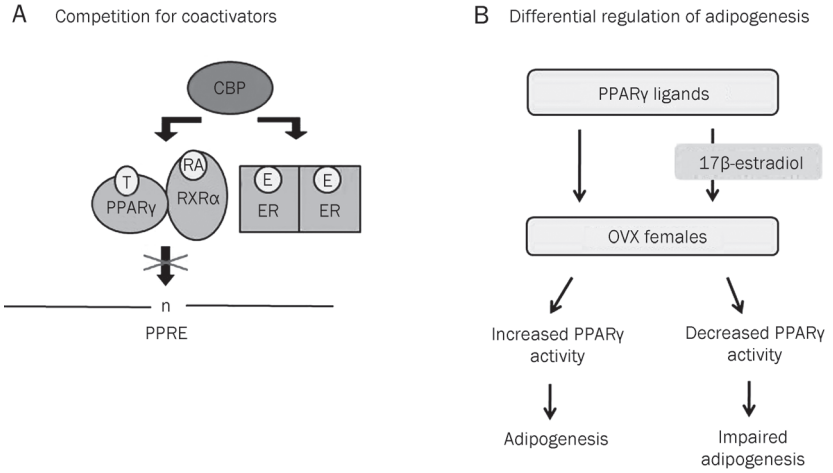

Figure 8. A proposed mechanism for the inhibition of PPARγ-induced adipogenesis by 17β-estradiol. (A) Competition between PPARγ and estrogen receptors (ERs) for coactivator binding, which results in decreased PPRE binding of PPARγ. (B) Inhibition of PPARγ actions on adipogenesis by 17β-estradiol (E). E impairs the ability of PPARγ ligands to induce adipogenesis in female ovariectomized (OVX) mice. T, troglitazone; RA, 9-*cis*-retinoic acid.

ble of repressing PPAR transactivation in these cells. Similar to these results, our results show that E inhibits the levels of troglitazone-induced PPARγ reporter gene activation through both ERα and ERβ in 3T3-L1 preadipocytes. Overexpression of ERα or ERβ decreased basal and troglitazone-induced luciferase reporter activities. Moreover, treatment with E led to a further inhibition of both. Thus, these data indicate that E inhibits PPARγ-dependent transactivation through ERs. Recently, Foryst-Ludwig *et al* also reported that ERβ inhibited ligand-mediated PPARγ transcriptional activity in 3T3-L1 preadipocytes transfected with PPARγ[26]. In contrast to our results, these authors found that pioglitazone-stimulated PPARγ activity was not blocked by ERα. This difference may be due to differences in the PPARγ agonists used in the transfection assays. While pioglitazone stimulation substantially increased luciferase activity by 15-fold in their system, troglitazone increased such activity by only three-fold in our system. Accordingly, ERα may be able to inhibit the troglitazone-induced luciferase activity, but not suppress the pronounced activation of PPARγ by pioglitazone.

The molecular mechanism by which E-activated ERs inhibit PPARγ transactivation was examined by EMSA and a mammalian two-hybrid assay. EMSA revealed that E inhibited DNA binding of PPARγ. Treatment of a nuclear extract with troglitazone increased PPARγ-binding activity, but E interfered with the troglitazone-induced DNA binding of PPARγ. Similarly, other research has shown that E and E-like compounds inhibited the DNA-binding activity of PPARγ and that nuclear extracts isolated from adipose tissues of ERβ-KO mice showed increased binding of endogenous PPARγ in comparison with wild-type mice[26]. PPARγ-binding activity was also markedly decreased in the phytoestrogen genistein-treated cells compared with untreated control[39]. The mammalian two-hybrid assay showed that E significantly decreased the troglitazone-induced CBP association in the presence of ERα or ERβ and that this effect was more prominent by ERβ. It has previously been shown that competition of nuclear receptors for coactivator binding results in a negative cross-talk between nuclear receptors[25]. Overexpression of nuclear coactivators, such as SRC-1 and transcriptional intermediary factor 2, prevented the ERβ-mediated inhibition of PPARγ activity[26]. Considering that both PPARγ and the ERs belong to the nuclear hormone receptor superfamily and share similar coactivators[22–24, 40], our data suggest that the suppressive effects of the ERs may be a result of CBP interaction with ERs, thereby preventing the binding of PPARγ to CBP.

In conclusion, *in vivo* and *in vitro* studies demonstrate that E inhibits PPARγ-mediated adipogenesis and adipocyte-specific gene expression. Our data also suggest that the coactivator CBP is involved in this inhibition (Figure 8A). In addition, the use of PPARγ activators may be effective in E-deficient states, such as in men and postmenopausal women (Figure 8B).

Acknowledgements

This work was supported by Mid-career Researcher Program (No 2009-0083990) and Female Scientist Program (No 2010-0017313) through an NRF grant funded by the MEST, Korea.

Author contributions

Michung YOON designed the research, analyzed the data, and wrote the paper. Sunhyo JEONG performed the research, analyzed the data, and wrote the paper.

Abbreviations

aP2, adipocyte fatty acid binding protein; BAT, brown adipose tissue; CBP, CREB-binding protein; E, 17β-estradiol; ER, estrogen receptor; HE, hematoxylin and eosin; LPL, lipoprotein lipase; MMLV-RT, Moloney murine leukemia virus reverse transcriptase; OVX, ovariectomized; PPARγ, peroxisome proliferator-activated receptor γ; PPRE, PPAR response element; TZDs, thiazolidinediones; WAT, white adipose tissue.

References

1 Kliewer SA, Forman BM, Blumberg B, Ong ES, Borgmeyer U, Mangelsdorf DJ, *et al*. Differential expression and activation of a family of murine peroxisome proliferator-activated receptors. Proc Natl Acad Sci USA 1994; 91: 7355–9.

2 Tontonoz P, Hu E, Spiegelman BM. Stimulation of adipogenesis in fibroblasts by PPAR gamma 2, a lipid-activated transcription factor. Cell 1994; 79: 1147–56.

3 Rosen ED, Sarraf P, Troy AE, Bradwin G, Moore K, Milstone DS, *et al*. PPAR gamma is required for the differentiation of adipose tissue *in*

vivo and *in vitro*. Mol Cell 1999; 4: 611–7.
4 Sottile V, Seuwen K. Bone morphogenetic protein-2 stimulates adipogenic differentiation of mesenchymal precursor cells in synergy with BRL 49653 (rosiglitazone). FEBS Lett 2000; 475: 203–4.
5 Gimble JM, Robinson CE, Wu X, Kelly KA, Rodriguez BR, Kliewer SA, *et al*. Peroxisome proliferator-activated receptor-gamma activation by thiazolidinediones induces adipogenesis in bone marrow stromal cells. Mol Pharmacol 1996; 50: 1087–94.
6 Lefterova MI, Lazar MA. New developments in adipogenesis. Trends Endocrinol Metab 2009; 20: 107–14.
7 He W, Barak Y, Hevener A, Olson P, Liao D, Le J, *et al*. Adipose-specific peroxisome proliferator-activated receptor gamma knockout causes insulin resistance in fat and liver but not in muscle. Proc Natl Acad Sci USA 2003; 100: 15712–7.
8 Jones JR, Barrick C, Kim KA, Lindner J, Blondeau B, Fujimoto Y, *et al*. Deletion of PPARgamma in adipose tissues of mice protects against high fat diet-induced obesity and insulin resistance. Proc Natl Acad Sci USA 2005; 102: 6207–12.
9 Zhang J, Fu M, Cui T, Xiong C, Xu K, Zhong W, *et al*. Selective disruption of PPARgamma 2 impairs the development of adipose tissue and insulin sensitivity. Proc Natl Acad Sci USA 2004; 101: 10703–8.
10 Imai T, Takakuwa R, Marchand S, Dentz E, Bornert JM, Messaddeq N, *et al*. Peroxisome proliferator-activated receptor gamma is required in mature white and brown adipocytes for their survival in the mouse. Proc Natl Acad Sci USA 2004; 101: 4543–7.
11 Auwerx J. PPARgamma, the ultimate thrifty gene. Diabetologia 1999; 42: 1033–49.
12 Kadowaki T, Hara K, Yamauchi T, Terauchi Y, Tobe K, Nagai R. Molecular mechanism of insulin resistance and obesity. Exp Biol Med (Maywood) 2003; 228: 1111–7.
13 Pedersen SB, Børglum JD, Eriksen EF, Richelsen B. Nuclear estradiol binding in rat adipocytes. Regional variations and regulatory influences of hormones. Biochim Biophys Acta 1991; 1093: 80–6.
14 Dieudonne MN, Pecquery R, Leneveu MC, Giudicelli Y. Opposite effects of androgens and estrogens on adipogenesis in rat preadipocytes: evidence for sex and site-related specificities and possible involvement of insulin-like growth factor 1 receptor and peroxisome proliferator-activated receptor gamma2. Endocrinology 2000; 141: 649–56.
15 Jeong S, Han M, Lee H, Kim M, Kim J, Nicol CJ, *et al*. Effects of fenofibrate on high fat diet-induced body weight gain and adiposity in female C57BL/6J mice. Metabolism 2004; 53: 1284–9.
16 Jeong S, Yoon M. Inhibition of the actions of peroxisome proliferator-activated receptor alpha on obesity by estrogen. Obesity (Silver Spring) 2007; 15: 1430–40.
17 Carani C, Qin K, Simoni M, Faustini-Fustini M, Serpente S, Boyd J, *et al*. Effect of testosterone and estradiol in a man with aromatase deficiency. N Engl J Med 1997; 337: 91–5.
18 Okazaki R, Inoue D, Shibata M, Saika M, Kido S, Ooka H, *et al*. Estrogen promotes early osteoblast differentiation and inhibits adipocyte differentiation in mouse bone marrow stromal cell lines that express estrogen receptor (ER) alpha or beta. Endocrinology 2002; 143: 2349–56.
19 Heim M, Frank O, Kampmann G, Sochocky N, Pennimpede T, Fuchs P, *et al*. The phytoestrogen genistein enhances osteogenesis and represses adipogenic differentiation of human primary bone marrow stromal cells. Endocrinology 2004; 145: 848–59.
20 Park HJ, Della-Fera MA, Hausman DB, Rayalam S, Ambati S, Baile CA. Genistein inhibits differentiation of primary human adipocytes. J Nutr Biochem 2009; 20: 140–8.
21 Roncari DA, Van RL. Promotion of human adipocyte precursor replication by 17beta-estradiol in culture. J Clin Invest 1978; 62: 503–8.
22 Gronemeyer H, Gustafsson JA, Laudet V. Principles for modulation of the nuclear receptor superfamily. Nat Rev Drug Discov 2004; 3: 950–64.
23. Glass CK. Going nuclear in metabolic and cardiovascular disease. J Clin Invest 2006; 116: 556–60.
24. Guan HP, Ishizuka T, Chui PC, Lehrke M, Lazar MA. Corepressors selectively control the transcriptional activity of PPARgamma in adipocytes. Genes Dev 2005; 19: 453–61.
25 Lopez GN, Webb P, Shinsako JH, Baxter JD, Greene GL, Kushner PJ. Titration by estrogen receptor activation function-2 of targets that are downstream from coactivators. Mol Endocrinol 1999; 13: 897–909.
26 Foryst-Ludwig A, Clemenz M, Hohmann S, Hartge M, Sprang C, Frost N, *et al*. Metabolic actions of estrogen receptor beta (ERbeta) are mediated by a negative cross-talk with PPARgamma. PLoS Genet 2008; 4: e1000108.
27 Wang X, Kilgore MW. Signal cross-talk between estrogen receptor alpha and beta and the peroxisome proliferator-activated receptor gamma1 in MDA-MB-231 and MCF-7 breast cancer cells. Mol Cell Endocrinol 2002; 194: 123–33.
28 Dang ZC, van Bezooijien RL, Karperien M, Papapoulos SE, Lowik CW. Exposure of KS483 cells to estrogen enhances osteogensis and inhibits adipogenesis. J Bone Miner Res 2002; 17: 394–405.
29 Yoon M, Jeong S. Peroxisome proliferator-activated receptor γ is not associated with adipogenesis in female mice. J Biomed Lab Sci 2008; 14: 139–46.
30 Sottile V, Seuwen K, Kneissel M. Enhanced marrow adipogenesis and bone resorption in estrogen-deprived rats treated with the PPARgamma agonist BRL49653 (rosiglitazone). Calcif Tissue Int 2004; 75: 329–37.
31 Okuno A, Tamemoto H, Tobe K, Ueki K, Mori Y, Iwamoto K, *et al*. Troglitazone increases the number of small adipocytes without the change of white adipose tissue mass in obese Zucker rats. J Clin Invest 1998; 101: 1354–61.
32 Yamauchi T, Kamon J, Waki H, Murakami K, Motojima K, Komeda K, *et al*. The mechanisms by which both heterozygous peroxisome proliferator-activated receptor gamma (PPARgamma) deficiency and PPARgamma agonist improve insulin resistance. J Biol Chem 2001; 276: 41245–54.
33 Rosen ED, Spiegelman BM. Molecular regulation of adipogenesis. Annu Rev Cell Dev Biol 2000; 16: 145–71.
34 Keller H, Givel F, Perroud M, Wahli W. Signaling cross-talk between peroxisome proliferator-activated receptor/retinoid X receptor and estrogen receptor through estrogen response elements. Mol Endocrinol 1995; 9: 794–804.
35 Nunez SB, Medin JA, Keller H, Wang K, Ozato K, Wahli W, *et al*. Retinoid X receptor beta and peroxisome proliferator-activated receptor activate an estrogen response element. Recent Prog Horm Res 1995; 50: 409–16.
36 Zhu Y, Kan L, Qi C, Kanwar YS, Yeldandi AV, Rao MS, *et al*. Isolation and characterization of peroxisome proliferator-activated receptor (PPAR) interacting protein (PRIP) as a coactivator for PPAR. J Biol Chem 2000; 275: 13510–6.
37 Nunez SB, Medin JA, Braissant O, Kemp L, Wahli W, Ozato K, *et al*. Retinoid X receptor and peroxisome proliferator-activated receptor activate an estrogen responsive gene independent of the estrogen receptor. Mol Cell Endocrinol 1997; 127: 27–40.
38 Tcherepanova I, Puigserver P, Norris JD, Spiegelman BM, McDonnell DP. Modulation of estrogen receptor-alpha transcriptional activity by the coactivator PGC-1. J Biol Chem 2000; 275: 16302–8.
39 Liao QC, Li YL, Qin YF, Quarles LD, Xu KK, Li R, *et al*. Inhibition of adipocyte differentiation by phytoestrogen genistein through a potential downregulation of extracellular signal-regulated kinases 1/2 activity. J Cell Biochem 2008; 104: 1853–64.
40 Kumar R, Thompson EB. The structure of the nuclear hormone receptors. Steroids 1999; 64: 310–9.

Acta Pharmacologica Sinica (2011) 32: 239–244
 1671-4083/11 $32.00
www.nature.com/aps

Original Article

The effect of the fibrinolytic enzyme FII_a from *Agkistrodon acutus* venom on acute pulmonary thromboembolism

Xi LIN[1], Xiu-xia LIANG[2], Jian-jun TANG[3], Jia-shu CHEN[2, *], Peng-xin QIU[2], Guang-mei YAN[2]

[1]Department of Pharmacology, Medical College, Ji-nan University, Guangzhou 510632, China; [2]Department of Pharmacology, Zhongshan Medical College, Sun Yat-sen University, Guangzhou 510080, China; [3]Department of Physiology, Medical College, Ji-nan University, Guangzhou 510632, China

Aim: To evaluate the effects of the fibrinolytic enzyme FII_a from *Agkistrodon acutus* venom on acute pulmonary thromboembolism (APT) in animal models.

Methods: Both rabbit and dog APT models were used. For the rabbit APT model, the thrombi weight before and after administration was measured. Central venous pressure (CVP) and mean arterial pressure (MAP) were measured before and 15, 30, 60, and 120 min after the injection of the blood clot. Partial thromboplastin time (APTT), prothrombin time (PT), platelet count, and fibrinogen concentration were measured using auto analyzers. Plasminogen activity was measured based on chromogenic substrates. In the dog APT model, pulmonary blood flow was recorded using pulmonary angiography.

Results: Intravenous administration of FIIa (0.1–5.0 mg/kg) improved the APT-induced hemodynamic derangements and reduced thrombi weight. The angiography evidence also showed that the pulmonary emboli had almost disappeared after FII_a infusion. FII_a (0.1, 0.5, or 1.0 mg/kg) did not impair the coagulation pathways, although very high doses of FII_a (5.0 mg/kg) could stimulate the production of plasminogen and result in impairment of the pathways.

Conclusion: FII_a could effectively protect against APT via degradation of thrombi with less activation of plasminogen, and may provide a novel fibrinolytic enzyme for targeting the main pathological processes of the disease.

Keywords: snake venom; fibrinolytic enzyme; pulmonary thromboembolism; angiography; plasminogen; central venous pressure; mean arterial pressure; urokinase; plasminogen

Acta Pharmacologica Sinica (2011) 32: 239–244; doi: 10.1038/aps.2010.193

Introduction

Acute pulmonary thromboembolism (APT) is defined as an embolic occlusion of a pulmonary artery, which results in a sudden increase in pulmonary resistance, right ventricular afterload, and O_2 consumption with a reduction in right coronary artery perfusion[1]. Despite advances in diagnosis and therapy, the mortality associated with APT remains high[2, 3]. Various approaches are available for the treatment of APT, including anticoagulant drugs and thrombolytic agents. Anticoagulant therapy, such as heparin, is thought to enhance the effect on thrombolysis by preventing formation of new thrombi[4, 5]. However, anticoagulants have minimal effects on previously existing thrombi. Enhanced fibrinolysis prevents disturbances in the circulation to organs by dissolving thrombi. It may be reasonable to assume that fibrinolytic therapy is effective against APT[6–10]. Current thrombolytic agents, such as tissue plasminogen activator (t-PA) and urokinase, which act as plasminogen activators, are effective at dissolving intravascular thrombi. These agents act indirectly on the thrombi by converting plasminogen, both circulating and fibrin-bound, into plasmin, which is the primary enzyme responsible for the removal of emboli. These conditions may "overflow" the systemic circulation and lead to systemic fibrinolysis and degradation of other clotting proteins[11], which may increase the bleeding tendency or may result in local activation of coagulation.

FII_a is a novel fibrinolytic enzyme that is purified from Anhui *Agkistrodon acutus* venom and is a type of snake venom metalloproteinase. Based on its crystal structure, binding to ZnP^{2+} is known to be essential for it hydrolytic activity[12, 13]. We have demonstrated that FII_a has the ability to directly degrade fibrin *in vitro* and effectively dissolve thrombi *in vivo*

* To whom correspondence should be addressed.
E-mail jiashu_sysu@hotmail.com
Received 2010-07-07 Accepted 2010-10-12

without activating plasminogen or influencing the activities of t-PA and plasminogen activator inhibitor-1 (PAI-1)[14, 15]. These findings show that FII_a has a different mechanism of action from t-PA and urokinase. Additionally, upon examination of the tissue sections from kidney, liver, heart, and lung[16], the thrombolytic activities of FII_a did not lead to hemorrhage. Although many of the fibrinolytic properties of FII_a are known, there are few studies investigating its fibrinolytic effects on APT. In the present study, we mimicked clinical APT models and found that FII_a could ameliorate the hemodynamic derangements by degrading fibrin clots.

Materials and methods

Preparation of the enzyme FII_a

FII_a, the fibrinolytic enzyme that was isolated from *Agkistrodon acutus* venom, was prepared according to the method previously described by Liang *et al*[14].

Reagents

Urokinase was purchased from Sigma (St Louis, USA). The reagent pack for the plasminogen activity assay was obtained from Sun Biotechnology Company (Shanghai, China). All other reagents were of analytical grade and obtained from commercial sources.

Animals

All animal experiments were conducted in accordance with the National Guide for the Care and Use of Laboratory Animals and were approved by Sun Yat-sen University Animal Care and Use Committee (Guangzhou, China). Adult male New Zealand white rabbits (weight 2–3 kg, grade II) were supplied by the Experimental Animal Center of Zhongshan Medical College, Sun Yat-san University (China). Adult male Beagle dogs (weight 15–20 kg, grade II) were supplied by the Experimental Animal Center of Guangdong Province, China.

Experimental model and hemodynamic measurements in rabbits

The APT experimental model in the rabbit was performed according to the method described by Todd[17]. An autologous thrombus was produced in a 10-mL tube (ID=0.2 cm) by incubation at 37 °C for 2 h with constant agitation using a clinical rotor (160 r/min). Thrombus fragments (2 cm) were cut and weighed according to an established protocol. The extracted blood clots were injected into the lungs through the right ventricular catheter, which then embolized the pulmonary arteries. Mean artery pressure (MAP) and central venous pressure (CVP) were measured before and 15, 30, 60, and 120 min after the injection of the blood clot.

Treatment was started simultaneously with the injection of the blood clots through the left marginal ear vein. Seven different groups were established, each containing 10 animals as follows: treatment groups were injected with 0.1 mg/kg, 0.5 mg/kg, 1.0 mg/kg or 5.0 mg/kg FII_a in 20 mL of saline solution over a period of 2 h (at a rate of 10 mL/h); the embo-control group was infused with saline solution (at a rate of 10 mL/h) instead of FII_a; the urokinase-control group was infused with 100 000 IU/kg over a period of 2 h (10 mL/h); and the remaining rabbits, which were neither injected with blood clots nor FII_a, were regarded as the sham-operated group and were infused with saline solution through the left marginal ear vein.

Two hours after the start of the experiments, the animals were sacrificed with an intravenous injection of 60 mg/kg pentobarbital sodium. The blood clots were carefully removed from the lungs and weighed.

Pulmonary angiography in dogs

This animal model was performed according to the methods described in Dias-Junior *et al*[18]. Under sterile dissection, a polyethylene catheter was placed into the right pulmonary artery through the right femoral vein. An autologous thrombus was produced in a 20-mL tube (ID=0.2 cm) by incubation at 37 °C for 2 h with constant agitation using a clinical rotor (160 r/min). Then, APT was induced by infusing the prepared clot into the lung through the polythene catheter. A pigtail catheter was repositioned in the pulmonary trunk. The extent of pulmonary embolism and the reperfusion rate were documented by the method of intra-arterial digital subtraction angiography (DFP-2000A, Toshiba) at 0, 30, and 60 min following the infusion of FII_a.

FII_a infusions were performed 2 h after the injection of the blood clots. Two different groups were established, each containing 6 animals as follows: (1) the dogs in the FII_a group were embolized animals that received FII_a infusions (1 mg/kg) over 1 h (at a rate of 10 mL/h); and (2) the dogs in the embo-control group were embolized animals that were infused with saline solution instead of FII_a.

Sample collection and handling

Blood samples from rabbits were obtained immediately before and 2 h after blood clot injection through a catheter that was inserted into a femoral artery. Blood samples were collected in 3.8% sodium citrate (1:10 *v/v* citrate/blood) and centrifuged at 2000×*g* for 15 min at 4 °C. All samples were then stored at -70 °C until assayed.

Laboratory methods

An auto analyzer (Sysmex CA1500, Japan) was used to determine the partial thromboplastin time (APTT), prothrombin time (PT), and fibrinogen concentration. An automatic blood cell analyzer (Sysmex SE-9500, Japan) was used to determine platelet counts. Plasminogen activity was measured according to the reagent pack instructions based on chromogenic substrates.

Data analysis

Data at 2 h were converted to percentages, with a value of 100% corresponding to basal data, and were expressed as mean±SEM. One-way ANOVA, followed by Tukey's B test was used for multiple comparisons. A non-parametric test (Kruskal–Wallis H test) was used to determine the changes in the hemodynamic and biochemical parameters as well as to

compare the embo-control, FII_a and urokinase-control groups. Differences with P values of less than 0.05 were considered to be statistically significant.

Results

Effect of FII_a on coagulation in APT in rabbits

To elucidate the effect of FII_a on APT, we systematically investigated its coagulation effects using a rabbit model. Table 1 summarizes the APTT, PT, platelet counts, fibrinogen concentration and plasminogen activity in normal rabbits, embo-control rabbits, FII_a -treated rabbits and urokinase-treated rabbits. APTT, PT, and plasminogen values in the urokinase-control group were all significantly higher than those in the sham-operated group (P<0.05). However, the values for plasma levels of both fibrinogen concentration and platelet count were significantly lower than those of the normal rabbits (P<0.05). No changes were detected in the hemodynamic parameters that were measured 2 h post-FII_a infusion (0.1, 0.5, or 1.0 mg/kg) compared with the sham-operated group. Although a significant decrease in fibrinogen and platelet count was observed, APTT, PT, and plasminogen activity increased in the animals that were treated with the highest dose of FII_a (P<0.05, compared with sham-operated group). No blood loss was observed at the site of infusion in any treatment group.

Effect of FII_a on APT-induced hemodynamic derangements in rabbits

Baseline hemodynamic parameters were similar in all experimental groups and showed no significant changes in the sham-operated animals throughout the study period (Figure 1). APT caused a sustained reduction in MAP and an increase in CVP in embolized animals, compared with the sham-operated group (P<0.05, Figure 1).

The animals treated with urokinase showed a decrease in CVP throughout the study period. An increase in MAP was observed 30 min following infusion of urokinase (P<0.05, compared with sham-operated group).

Two-hour measurements taken at all doses of infused FII_a showed the following: a decrease in CVP throughout the study period (P<0.05, compared with the embo-control group, Figure 1); an increase in MAP for 60 min following the infusion of FII_a in the 0.1 mg/kg and 0.5 mg/kg dose groups; and an increase in MAP for 30 min following the infusion of FII_a in the 1.0 mg/kg and 5.0 mg/kg dose groups (P<0.05, compared with the embo-control group, Figure 1).

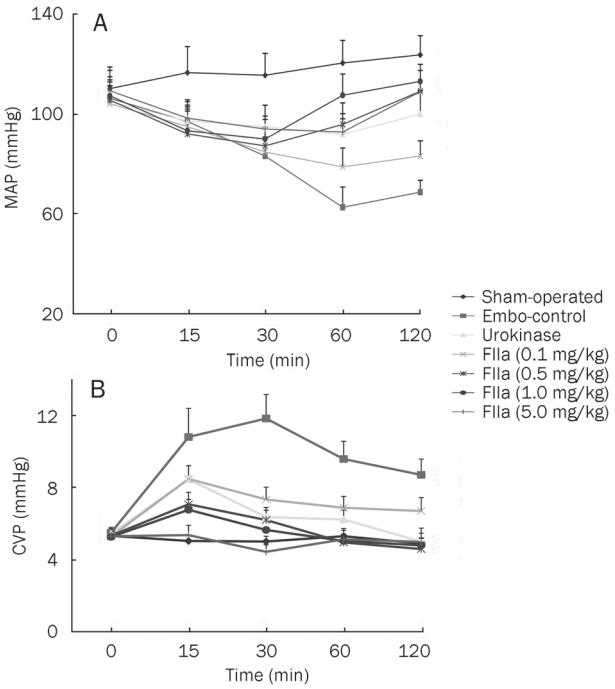

Figure 1. Effects of embolization and thrombolytic agents on mean arterial pressure (MAP, A) and central venous pressure (CVP, B). The data demonstrate that (1) embolization leads to an increase in CVP and a decrease in MAP and (2) FII_a and urokinase consistently ameliorate the hemodynamic derangements.

Thrombolysis effect of FII_a *in vivo*

The *in vivo* thrombolysis effect of FII_a was studied in the rabbit APT model. No change in the thrombi weight was observed in the emboli-control group. The blood clots showed a weight loss of 79.38%±23.72% at 2 h post-infusion time point in the urokinase-treated group (Figure 2). FII_a dose-dependently reduced thrombi weight, which ranged from 53.37%±18.67% for a 0.1 mg/kg dose to 91.36%±7.83% for a 1.0 mg/kg dose (Figure 2). No blood loss was observed in any of the animals treated with FII_a.

Table 1. Thrombolytic characteristics after infusion of urokinase and FII_a in a rabbit APT model. Data were expressed as percentage of the basal value. n=10. Mean±SEM. ^bP<0.05 compared with the sham-operated group. APTT: partial thromboplastin time. PT: prothrombin time.

	Fibrinogen (%)	Plasminogen (%)	APTT (%)	PT (%)	Platelet counts (%)
Sham-operated	101.28±14.27	97.68±20.74	101.36±6.85	99.29±17.84	101.40±10.19
Embo-control	105.37±13.39	103.83±18.65	99.54±16.16	98.48±12.22	100.83±12.61
Urokinase	69.14±26.09^b	180.58±30.96^b	283.12±40.37^b	242.87±37.63^b	59.82±19.07^b
FII_a(0.1 mg/kg)	107.51±20.07	104.48±24.57	97.38±10.31	101.69±11.06	99.52±8.52
FII_a(0.5 mg/kg)	93.41±15.56	109.62±26.74	100.59±9.63	104.19±6.72	93.84±11.93
FII_a(1.0 mg/kg)	89.37±18.92	115.35±24.90	104.62±11.49	103.94±14.27	90.81±13.29
FII_a(5.0 mg/kg)	75.31±24.15^b	143.37±31.42^b	173.80±30.62^b	143.64±25.33^b	70.35±18.98^b

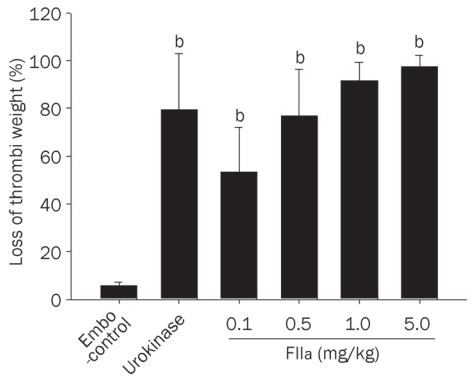

Figure 2. Effect of FII_a on thrombi weight in rabbits (n=10 in each group). Dose-dependent reduction in thrombus weight by FII_a infusion. Data were expressed as mean±SEM. $^bP<0.05$, compared with embo-control.

Pulmonary angiography in the Beagle APT models

Most pulmonary emboli occurred in the lower lobes of the right lung. Serious obstructions occurred in the branches of the right lower lobar pulmonary artery in the embo-control group, following a significant decrease in the perfusion of the right lower lobes of the lung (the reperfusion rate was 0.6%±0.07%, Figure 3). Administration of 1 mg/kg of FII_a resulted in the gradual disappearance of the emboli. Thirty minutes after the infusion of FII_a, a lower level of obstruction was detected in the branches of the lower lobar pulmonary artery, and the reperfusion rate was 70.41%±7.62% (Figure 3). Sixty minutes after the infusion of FII_a, the pulmonary emboli had almost completely disappeared, and the reperfusion rate of the upper to lower lobe was 85.34%±8.42% (Figure 3).

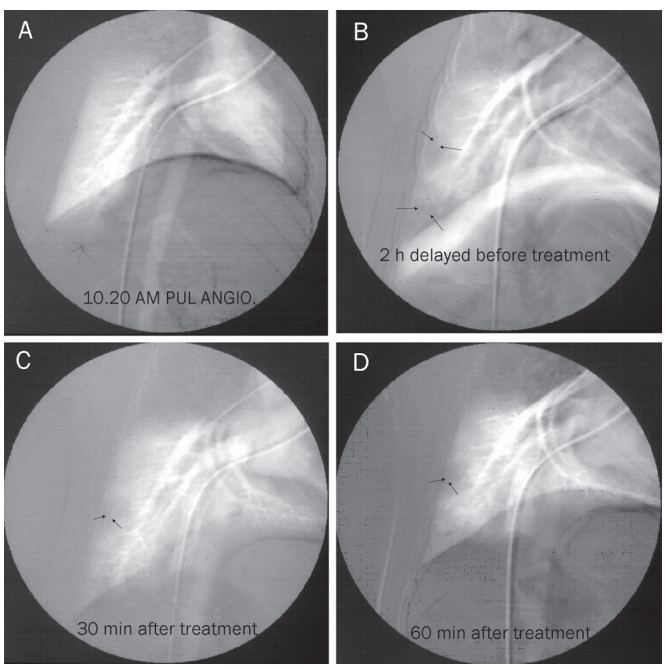

Figure 3. Digital subtraction angiography in APT. Arrows indicate thrombi in the right pulmonary artery. (A) Before pulmonary thromboembolism; (B) Two hours after pulmonary thromboembolism. The right pulmonary artery shows a complete obstruction. (C) FII_a treatment for 30 min. A reduction in obstruction was detected in the lower lobar pulmonary artery branches. (D) FII_a treatment for 60 min. The pulmonary emboli almost completely disappeared.

Discussion

In the present study, we reported that FII_a from *Agkistrodon acutus* venom demonstrated significantly protective properties in APT induced by the injection of preformed blood clots. An improvement in the APT-induced hemodynamic derangements and a reduction in thrombi weight were observed. The angiography evidence in the dog APT model also showed that the pulmonary emboli almost completely disappeared with the infusion of FII_a. In addition, FII_a did not impair the coagulation pathways.

APT can produce severe cardiopulmonary dysfunction that is characterized by pulmonary arterial hypertension, right ventricular failure, and hypoxemia, which is the principal cause of APT-related death[19–22]. In addition, the major adverse effect is attributed to the direct mechanical obstruction of the pulmonary arteries. This evidence suggests that promoting fibrinolysis might be a promising target for therapeutic strategies for APT[23].

In this study, we found that lung embolization resulted in typical changes associated with APT that were characterized by a significant decrease in MAP and a dramatic increase in CVP, which were consistent with the results previously described by Todd *et al*[17]. The angiography evidence in the dog APT model also showed that the pulmonary blood flow was almost completely occluded 2 h after pulmonary embolization.

Using the rabbit model of APT, we found that all doses of FII_a not only significantly attenuated the increase in CVP and the decrease in MAP but also effectively reduced the thrombi weight in the pulmonary artery. Furthermore, the angiography evidence in the dog APT model also showed that the pulmonary emboli almost completely disappeared after a 60-min FII_a infusion, and pulmonary blood flow was almost fully returned to baseline levels. In our previous study[14, 15], we found that fibrin clots were hydrolyzed more efficiently by FII_a than by urokinase *in vitro*. Because FII_a is a snake venom fibrinolytic enzyme, its proteolytic action should involve the mechanism of directly degrading fibrin. Furthermore, FII_a lysed fibrin by direct proteolysis without activating intrinsic plasminogen[24, 25], which resulted in a greater effectiveness than urokinase. These findings suggest that FII_a could be beneficial in improving APT-induced hemodynamic derangements by its direct fibrinolytic effect on thrombi.

Because of the coagulation abnormalities, bleeding is a major complication of thrombolytic therapy. The risk of hemorrhage usually occurs at a site of previous surgery or puncture[26, 27]. As a measure of ongoing coagulation during the infusion of the agents, we determined the fibrinogen concentration, platelet counts, plasminogen activity, PT and APTT.

In this study, the significant changes in these coagulation parameters in the urokinase-treated group indicated that infu-

sion of urokinase impaired the intravascular coagulation in the animals. After a 2-h FII_a infusion (0.1, 0.5, or 1.0 mg/kg), no significant changes in the parameters of coagulation were detected, and no blood loss was observed at the site of infusion. These results suggest that intravascular administration of FII_a did not impair the coagulation system and produced no hemorrhages. FII_a effectively decreased the thrombi weight in a rabbit APT model. Because FII_a does not activate plasminogen, many complex secondary effects, such as platelet activation and fibrinogen degradation, are avoided. The advantages of the plasminogen-independent fibrinolysis induced by FII_a was further demonstrated by the findings of no bleeding in any of the rabbits treated with FII_a in our previous studies[13, 14] and a much wider therapeutic window compared with urokinase.

However, it should be emphasized that FII_a, at its extremely high dose, may result in internal hemorrhaging in some animals. In this study, the values of plasminogen activity, fibrinogen concentration, platelet count, APTT, and PT showed significant changes compared to the respective baseline values in the group with the highest dose of FII_a. Our previous study showed that FII_a influenced blood coagulation by inhibiting the platelet aggregation that was induced by adenosine phosphate and degradation of prothrombin and factor X[13]. Plasminogen provides an important control of fibrinolysis by its degradation of blood coagulation proteins[28]. In addition to its fibrinolytic activity, FII_a is also involved in the degradation of gelatin and collagen, which are the main proteins that compose the vascular basement membrane. Plasminogen also activates collagenases and disrupts the basement membrane barriers[29]. This evidence suggests that extremely high dose of FII_a might stimulate the production of plasminogen *in vivo*, which may be the reason for the impairment of the coagulation pathways. These results suggest that if FII_a is employed in the treatment of APT, it should be utilized in a manner that does not cause systemic activation of the fibrinolytic system. Additional work is needed to further characterize this issue.

In conclusion, FII_a may have protective effects on TAPT by it direct degradation of fibrin clots. These therapeutic effects support the hypothesis that FII_a could be used for reducing thrombi, restoring blood flow in the lung, and improving cardiovascular function. However, we emphasize that the true utility of FII_a in combating APT will require further direct testing in clinical trials.

Acknowledgements

Project was supported by the National Natural Science Foundation of China (No 81000209), the key Project of Chinese Ministry of Education (No 210255), and the Fundamental Research for the Central Universities (No 21609304).

The authors thank Dr Jun XIE and the staff at the Molecular Imaging Lab in the Department of Radiology at the 3rd Affiliated Hospital of Sun Yat-Sen University, Guangzhou, China, for their technical assistance.

Author contribution

Jia-shu CHEN and Guang-mei YAN designed the study; Xi LIN, Xiu-xia LIANG and Peng-xin QIU performed the research; Jian-jun TANG contributed new analytical reagents and tools; and Xi LIN analyzed the data and wrote the paper.

Abbreviations

APT, acute pulmonary thromboembolism; MAP, mean arterial pressure; CVP, central venous pressure; APTT, partial thromboplastin time; PT, prothrombin time; PAI-1, plasminogen activator inhibitor-1.

References

1 Keymel S, Rassaf T, Kelm M. Nitrite in action: a commentary on "Low-dose intravenous nitrite improves hemodynamics in a canine model of acute pulmonary thromboemolism. Free Radic Biol Med 2006; 41: 1750–2.
2 Cushman M, Tsai AW, White RH, Heckbert SR, Rosamond WD, Enright P, *et al*. Deep vein thrombosis and pulmonary embolism in two cohorts: the longitudinal investigation of thromboembolism etiology. Am J Med 2004; 117: 19–25.
3 Goldhaber SZ, Visani L, De Rosa M. Acute pulmonary embolism: clinical outcomes in the International Cooperative Pulmonary Embolism Registry (ICOPER). Lancet 1999; 353: 1386–9.
4 Barritt DW, Jordon SC. Anticoagulant drugs in the treatment of pulmonary embolism: a controlled trial. Lancet 1960; 1: 1309–12.
5 Hull R, Delmore T, Centon E, Hirsh J, Gent M, Sackett D, *et al*. Warfarin sodium versus low-dose heparin in the long-term treatment of venous thrombosis. N Engl J Med 1979; 301: 855–8.
6 Vassalli G, Dichek DA. Gene therapy for arterial thrombosis. Cardiovas Res 1997; 35: 459–69.
7 Goldhaber SZ. Thrombolytic therapy in venous thromboembolism: Clinical trials and current indications. Clin Chest Med 1995; 16: 307–20.
8 Sherry S, Bell WR, Duckert FH, Fletcher AP, Gurewich V, Long DM, *et al*. Thrombolytic therapy in thrombosis: a National Institutes of Health consensus development conference. Ann Intern Med 1980; 93: 141–4.
9 Marder VJ, Sherry S. Thrombolytic therapy: current status (1). N Engl J Med 1988; 318: 1512–20.
10 Marder VJ, Sherry S. Thrombolytic therapy: current status (2). N Engl J Med 1988; 318: 1585–95.
11 Ouriel K. Comparison of safety and efficacy of the various thrombolytic agents. Rev Cardiovasc Med 2002; 3: S17–24.
12 Lou Z, Hou J, Liang X, Chen J, Qiu P, Liu Y, *et al*. Crystal structure of a non-hemorrhagic fibrin (ogen)olytic metalloproteinase complexed with a novel natural tri-peptide inhibitor from venom of *Agkistrodon acutus*. J Struct Biol 2005; 152: 195–203.
13 Liang XX, Zhou YN, Chen JS, Qiu PX, Chen HZ, Sun HH, *et al*. Enzymological characterization of FII_a, a fibrinolytic enzyme from *Agkistrodon acutus* venom. Acta Pharmacol Sin 2005; 26: 1474–8.
14 Liang XX, Chen JS, Zhou YN, Qiu PX, Yan GM. Purification and biochemical characterization of FII_a, a fibrinolytic enzyme from *Agkistrodon acutus* venom. Toxicon 2001; 39: 1133–9.
15 Lin X, Liang XX, Chen JS, Chen Q, Qiu PX, Yan GM. The effect of fibrinolytic enzyme FIIa from *Agkistrodon acutus* venom on disseminated intravascular coagulation in rabbits. Transl Res 2007; 150: 295–302.
16 Chen JS, Liang XX, Qiu PX, Yan GM. Thrombolysis effect with FII_a

from *Agkistrodon acutus* venom in different thrombosis model. Acta Pharmacol Sin 2001; 22: 420–2.
17 Todd MH, Forrest JB, Cragg DB. The effects of aspirin and methysergide, singly and in combination, on systemic haemodynamic responses to pulmonary embolism. Can Anaesth Soc J 1981; 28: 373–80.
18 Dias-Junior CA, Gladwin MT, Tanus-Santos JE. Low-dose intravenous nitrite improves hemodynamics in a canine model of acute pulmonary thromboembolism. Free Radic Biol Med 2006; 41: 1764–70.
19 Gurewich V, Cohen ML, Thomas DP. Humoral factors in massive pulmonary embolism: an experimental study. Am Heart J 1968; 76: 784–94.
20 Daily PO, Griffin A, Blackstone E, Moulder PV. The hemodynamic effects of localized pulmonary embolism. Surg Gynecol Obstet 1966; 123: 765–73.
21 Hyamn AL, Myers WD, Meyer A. The effect of acute pulmonary embolus upon cardiopulmonary hemodynamics. Am Heart J 1964; 67: 313–23.
22 Halmagyi DF, Starzecki B, Horner GJ. Humoral transmission of cardiorespiratory changes in experimental lung embolism. Circ Res 1964; 14: 546–54.
23 Ibrahim SA, Stone RA, Obrosky DS, Geng M, Fine MJ, Aujesky D. Thrombolytic therapy and mortality in patients with acute pulmonary embolism. Arch Intern Med 2008; 168: 2183–90.
24 Ueshima S, Matsuo O. Development of new fibrinolytic agents. Curr Pharm Des 2006; 12: 849–57.
25 Dobrovolsky AB, Titaeva EV. The fibrinolysis system: regulation of activity and physiologic functions of its main components. Biochemistry (Mosc) 2002; 67: 99–108.
26 Stein PD, Matta F. Acute pulmonary embolism. Curr Probl Cardiol 2010; 35: 314–76.
27 Werf FV, Barron HV, Armstrong PW, Granger CB, Berioli S, Barbash G, *et al*. Incidence and predictors of bleeding events after fibrinolytic therapy with fibrin-specific agents. A comparison of TNK-tPA and rt-PA. Eur Heart J 2001; 22: 2253–61.
28 Plow EF, Herren T, Redlitz A, Miles LA, Hoover-Plow JL. The cell biology of the plasminogen system. FASEB J 1995; 9: 939–45.
29 Niedbala MJ, Picarella MS. Tumor necrosis factor induction of endothelial cell urokinase-type plasminogen activator mediated proteolysis of extracellular matrix and its antagonism by gamma-interferon. Blood 1992; 79: 678–87.

Acta Pharmacologica Sinica (2011) 32: 245–252
 1671-4083/11 $32.00
www.nature.com/aps

Original Article

Over-expression of aldehyde dehydrogenase-2 protects against H_2O_2-induced oxidative damage and apoptosis in peripheral blood mononuclear cells

Xiu-ying HU[1, #], Qin FANG[2, #, *], Ji-shi WANG[3, *], Jian-qiong XIE[1], Bai-sheng CHAI[3], Fang-qiong LI[3], Xin CUI[1], Yuan YANG[1]

[1]Department of Hematology and [2]Department of Pharmaceutics, the Affiliated Hospital of Guiyang Medical College, Guiyang 550004, China; [3]School of Pharmaceutics, Guiyang Medical College, Guiyang 550004, China

Aim: To construct an eukaryotic expression vector containing the aldehyde dehydrogenase-2 (ALDH2) gene, and determine whether transfection with the ALDH2 gene can provide protection against hydrogen peroxide-induced oxidative damage, as well as attenuate apoptosis or cell death in human peripheral blood mononuclear cells (PBMCs).
Methods: The ALDH2 gene was cloned from human hepatocytes by RT-PCR. The eukaryotic expression vector containing the gene was constructed and then transfected into PBMCs via liposomes. RT-PCR, indirect immunofluorescence assay, and Western blot were used to evaluate the expression of the transgene in target cells. MTT assay and flow cytometry were used to detect the effects of ALDH2 on PBMCs damaged by hydrogen peroxide (H_2O_2). The level of intracellular reactive oxygen species (ROS) was determined by fluorescence spectrophotometry.
Results: The eukaryotic expression vector pcDNA3.1/myc-His-ALDH2 was successfully constructed and transfected into PBMCs. RT-PCR results showed higher mRNA expression of ALDH2 in the gene-transfected group than in the two control groups (empty vector-transfected group and negative control). Indirect immunofluorescence assay and Western blot indicated distinct higher protein expression of ALDH2 in the gene-transfected group. The cell survival rate against H_2O_2-induced oxidative damage was higher in the ALDH2 gene-transfected group. Moreover, apoptosis rates in gene-transfected PBMCs incubated with 50 and 75 μmol/L H_2O_2 decreased by 7% and 6%, respectively. The generation of intracellular ROS was also markedly downregulated.
Conclusion: ALDH2 gene transfection can protect PBMCs against H_2O_2-induced damage and attenuate apoptosis, accompanied with a downregulation of intracellular ROS. ALDH2 functions as a protector against oxidative stress.

Keywords: aldehyde dehydrogenase-2; oxidative damage; transfection; peripheral blood mononuclear cells; apoptosis

Acta Pharmacologica Sinica (2011) 32: 245–252; doi: 10.1038/aps.2010.203

Introduction

The rapid development of medical and molecular biology techniques has resulted in the rise in importance of and focus on tumor immunotherapy research. In 1989, Komori[1] reported the first successful infusion of IL-2 activated donor lymphocytes after the recurrence of allogeneic hematopoietic stem cell transplantation (HSCT) for acute lymphoblastic leukemia. Since then, adoptive immunotherapy has continued to show challenging and novel application prospects in the treatment of malignant tumors. In recent years, great progress has been made in clinical tests involving adoptive immunotherapy, and various studies on phase I and II clinical trials have been conducted. Immune cells participate in immune response to protect the body during the therapeutic process, but as first-line cells, they are more vulnerable to oxidative damage[2–5]. In different diseases such as renal, cardiovascular, neoplastic, and neurodegenerative illnesses, as well as in aging[6–9], an oxidative stress-induced inflammatory event leading to cellular or tissue injury can be considered a unifying mechanism of injury. Reactive oxygen species (ROS), including hydroxyl radicals, superoxide anions, hydrogen peroxide (H_2O_2), and singlet oxygen, are generated not only in the process of radiotherapy or chemotherapy before HSCT, but also during therapy that uses drugs that cause DNA damage and induce subsequent apoptosis with the generation of ROS[10–12]. Excessive accumulation of ROS can induce oxidative damage to donor or recipient immune cells, weakening the effects of immunotherapy. The protection of immune cells against oxidative damage is, therefore, extremely important to

# These two authors contribute equally to this work.
* To whom correspondence should be addressed.
E-mail fq_fangqin@yahoo.com.cn (Qin FANG);
jswang_yg@yahoo.com (Ji-shi WANG)
Received 2010-01-13 Accepted 2010-07-29

immunotherapy.

At present, many new therapeutic methods are being used in clinical treatments, and a recent strategy involves transferring protective genes in normal immune cells via appropriate vectors to enhance host immunological function against diseases. As a metabolic enzyme of toxic substances, mitochondrial aldehyde dehydrogenase (ALDH2) metabolizes acetaldehyde and plays a major role in the oxidation of acetaldehyde and protection against oxidative injury. It is highly expressed in human liver tissue and lowly expressed in peripheral blood mononuclear cells (PBMCs). It also varies with individual genetic diversity. Some people express inactive ALDH2 for gene mutation. ALDH2 is a nuclear-encoded mitochondrial enzyme that is localized in the mitochondrial matrix, and mitochondria are the major source of ROS. Excessive ROS attacks polyunsaturated fatty acids leading to membrane lipid peroxidation, thereby generating reactive aldehydes, including 4-hydroxy-2-nonenal (4-HNE) and malondialdehyde. ALDH2 provides protection against oxidative damage through the oxidation of exogenous and endogenous aldehydes including 4-HNE, which is the product of lipid peroxidation[13–15]. Thus, ALDH2 gene modification may enhance the anti-oxidative stress capacity of immune cells.

This research aims to determine whether the overexpression of ALDH2 can protect human PBMCs against H_2O_2-induced oxidative damage and attenuate apoptosis. We also investigated the level of ROS in this process. PBMCs are rich in immune cells, their activation and proliferation were studied in this research. This study is a convenient and effective initial foray into investigations on immune cells in gene therapy. Our team previously reported that the resistance to chemotherapeutic agents could be enhanced by transfection with resistant genes in human peripheral blood hematopoietic progenitor cells and PBMCs[16, 17]. In this study, we explored the protective effect of the ALDH2 gene and provide reference for further related research on gene therapy in practical immunotherapy.

Materials and methods

Construction of eukaryotic expression plasmid

Human ALDH2 cDNA (1.5 kb) was synthesized through reverse transcriptase polymerase chain reaction (RT-PCR) with total RNA extracted from normal human hepatocytes. The ALDH2 cDNA was cloned with DNA polymerase (TaKaRa, Japan) into pBS-T vector (TIANGEN, China) and sent to Jinsite Bio Inc (China) for sequencing. The primers used in PCR were ALDH2 forward 5′-GACACGGATCCATGTTGCGCGCTGCCGCCCGCTTCGG-3′ and ALDH2 reverse 5′-GACACGAATTCTTATGAGTTCTTCTGAGGCACTTTGAC-3′. To construct the eukaryotic expression plasmid expressing the ALDH2 gene pcDNA3.1/myc-His, plasmid (Invitrogen, USA) and pBS-T-ALDH2 were digested with restriction endonucleases *EcoR* and *BamH* I, respectively. The refined ALDH2 segments and linearized pcDNA3.1/myc-His were ligated using T_4 DNA ligase with a ratio of 2:1 to construct eukaryotic expression plasmid pcDNA3.1/myc-His-ALDH2 (pcDNA3.1(+)-ALDH2). The eukaryotic expression plasmid was verified by PCR and digestion analysis.

Primary culture and activation of PBMCs

PBMCs from the blood of healthy adult volunteers were isolated using a Ficoll lymphocyte separating liquid, and cultivated in an RPMI-1640 culture medium (Gibco, USA) containing 10% fetal bovine serum in 6-well culture plates at 37 °C, 95% O_2, and 5% CO_2. Phytohemagglutinin (2.5 μg/mL) was added into the culture medium. After 8 h, the cells were moved into fresh medium, into which interleukin-2 (1000 U/mL) was added for activation. The culture medium was replaced with fresh medium 48 h later when the PMBCs were ready for use in the experiments.

Transfection of pcDNA3.1/myc-His-ALDH2 into PBMCs

For eukaryotic expression plasmid transduction, PBMCs were passaged into 6-well plates at a density of 1×10^6 cells/well. When the cells reached 50% confluence (typically on the third day after subculturing), the medium was replaced with 1 mL fresh medium (without serum) containing 8 μL Lipofectamin 2000 transfection reagent (Invitrogen, USA) and 2 μg plasmid DNA. Cells in group 1 were transfected with pcDNA3.1/myc-His-ALDH2, and group 2 with pcDNA3.1/myc-His empty plasmid. Group 3 was used as the negative control group (without plasmid transfection). The medium was replaced with fresh medium after 4 h. Indirect immunofluorescence assay was used to observe the protein expression of ALDH2 after transfection. Transfection rate was calculated at 12, 24, 48, and 72 h according to the observed fluorescence intensity.

RT-PCR analysis

Total RNA was extracted using TRIzol isolation reagent (TaKaRa, Japan), and RT-PCR analysis was performed using a one-step RT-PCR kit (Bio Shinegene Inc., China). β-actin was used as internal control. The primers were actin forward 5′-GCTCGTCGTCGACAACGGCTC-3′ and actin reverse 5′-CAAACATGATCTGGGTCATCTTCTC-3′. RT-PCR analysis was performed at 42 °C for 60 min, 92 °C for 5 min, then at 30 cycles of 94 °C for 50 s, 70.5 °C for 60 s, 72 °C for 60 s, and 72 °C for 10 min. An aliquot (5 μL) from the RT-PCR product was subjected to electrophoresis in 1% agarose gel. The anticipated β-actin PCR product was 353 bp long and ALDH2 was 1576 bp.

Western blot analysis

For Western blot analysis, the cells were washed three times with PBS, homogenized in cell lysis buffer, incubated on ice for 20 min, and then centrifuged for 15 min at 10000×*g*. The aqueous supernatant was collected and quantified using a BCA protein assay kit (Boster, China). Equal amounts (20 μg) of protein extract were loaded and separated by SDS-polyacrylamide gel electrophoresis. After electrophoresis, the proteins on the gel were transferred to polyvinylidene difluoride membranes. The blotted membranes were blocked with 5% skim milk powder in TBS buffer and then probed for 1.5 h

with the ALDH2 monoclonal antibody (1:250; H00000217-M01, Abnova, Chinese Taipei) specific for human cellular ALDH2. After three 10-min washing with TBS-Tween 20 buffer (0.05%), the blots were incubated with a secondary antibody (1:3000; Goat Anti-Mouse IgG-HRP Conjugate secondary antibody, Abnova) for 1.5 h. Antibody binding was visualized using an enhanced chemiluminescence reagent (Santa Cruz, USA) according to the manufacturer's instructions.

Cytotoxicity assay

The cytotoxicity of H_2O_2 to cells in groups 1–3 were examined using the 3-(4,5-dimethylthiazol-2-yl)-2,5-diphenyl tetrazolium bromide (MTT) test. Briefly, cells from the three groups were seeded into a 96-well cell culture plate at a density of 5×10^3 cells/well and incubated overnight. The medium was discarded, and new medium containing 1000.000, 100.000, 10.000, 1.000, 0.100, 0.010, 0.001, and 0 μmol/L H_2O_2 were added into respective wells. Each concentration was tested four times. After 72 h, the medium was discarded and 20 μL of MTT (5 mg/mL) was added to the medium. After another 4 h, the medium was discarded through centrifugation, followed by the addition of DMSO to dissolve the endocellular crystal. *OD* value was measured at 570 nm on a microplate reader (B10 TEK EL×800UV, General Corporation, USA), with 485 nm as reference. Regression analysis was performed with SPSS followed by the calculation of IC_{50} values.

Reactive oxygen species analysis

The measurement of intracellular ROS was based on the ROS-mediated conversion of non-fluorescent dichlorofluorescin diacetate (DCFH-DA) into dichlorofluorescin (DCFH). DCFH is a nonfluorescent compound that is oxidized into fluorescent 2, 7-dichlorofluorescin (DCF) in the presence of oxidants, which can be quantified using a fluorescence spectrophotometer. Briefly, 48 h after transfection, 1×10^6 cells/well on the 6-well plates were harvested after incubation in the presence or absence of H_2O_2 for 8 h, and then replaced with serum-free medium containing 10 μmol/L DCFH-DA for 20 min at 37 °C. The cells were then rinsed three times with PBS. The fluorescence intensity of the cells was measured using a fluorescence spectrophotometer (Cary Elipse, USA).

Flow cytometric analysis of cell apoptosis

Seventy-two hours after transfection, transfection and expression of the transgene in target cells were evaluated and selected in the medium containing different concentrations of H_2O_2. For quantitative analysis of cell apoptosis, 1×10^5 treated cells/tube in 500 μL binding buffer were incubated with Annexin V-FITC (5 μL) and propidium iodide (5 μL) for 5 min at room temperature. The ratio of apoptosis was analyzed by flow cytometry (FCM) (BD FACSCalibur, USA) with CellQuest research software.

Statistical analysis

Each experiment was performed at least three times. All values are expressed as means±SD. Data were collected by the Student's *t*-test using SPSS13.0. $P<0.05$ was considered statistically significant.

Results

Construction of eukaryotic expression vector

Human ALDH2 was cloned from human hepatocytes by RT-PCR. The PCR optimum temperature was 70.5 °C (Figure 1A). The recombinant eukaryotic expression plasmid pcDNA3.1 (+)-ALDH2 was verified by PCR, sequencing, and endonuclease digestion. The sequencing results of recombinant plasmid showed that the cloned gene was identical to the ALDH2 cDNA published in GeneBank (NM_000690, sequence number Q0468). The fragment digested by endonuclease digestion analysis was about 1560 bp and the amplified fragment by PCR confirmation was 1576 bp, as expected (Figure 1B).

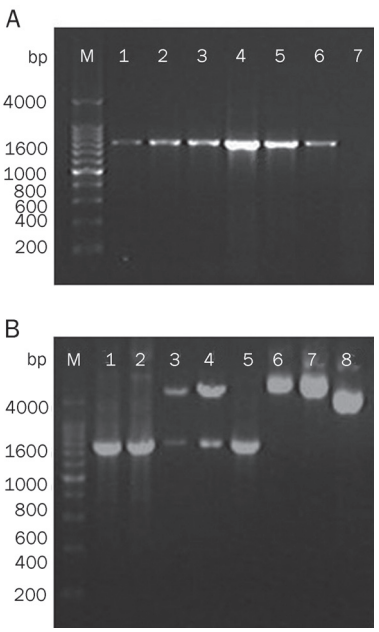

Figure 1. Detection of ALDH2 expression in normal human hepatocytes and recombinated plasmid pcDNA3.1(+)-ALDH2. ALDH2 gene in human hepatocytes was cloned by RT-PCR. (A) Lane M: DNA Marker; Lanes 1–6: RT-PCR-amplified ALDH2 products in different PCR-extending temperatures, Lane 4 was 70.5 °C; Lane 7: negative control; ALDH2 eukaryotic expression vector was verified by PCR and endonuclease digestion; (B) Lane M: DNA marker; Lanes 1, 2: PCR-amplified ALDH2 products (1576 bp) of pcDNA3.1(+)-ALDH2 vectors; Lanes 3, 4: results of endonuclease digestion; Lane 5: PCR-amplified ALDH2 products (1576 bp) of pcDNA3.1(+)-ALDH2 vectors in bacterial liquid; Lane 6: DNA fragment of single enzyme digestion; Lanes 7, 8: circular DNA fragments of pcDNA3.1(+)-ALDH2 and pcDNA3.1(+).

Observation of ALDH2 protein

Creep plates of cultured cells were incubated with an ALDH2 monoclonal antibody and fluorescein isothiocyanate-labeled second antibody. Fluorescence intensity in cells was determined using a fluorescence microscope. ALDH2 proteins expression in group 1 (transgene group) were found 24 h after transfection and became very bright 48 h later (Figure 2). The

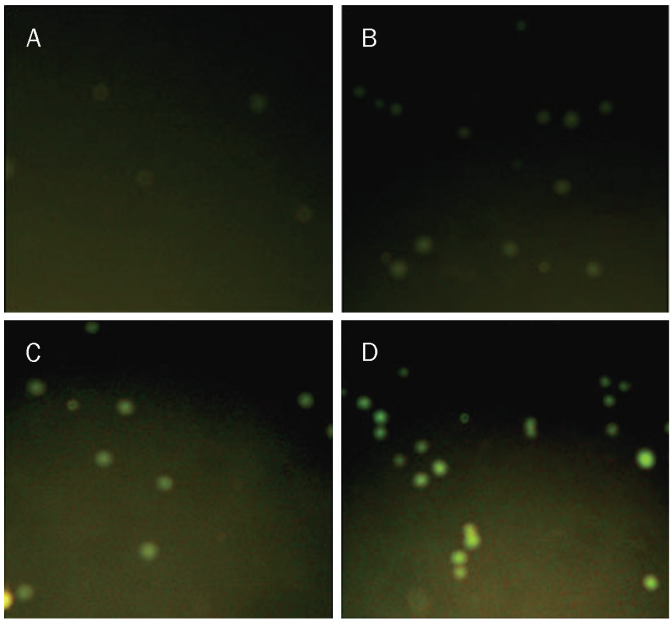

Figure 2. ALDH2 protein expression in PBMCs by indirect immunofluorescence assay. Fluorescence intensity of cells expressing ALDH2 proteins was observed 24 h after transfection. Cells in negative control group at 48 h (A) exhibited weak expression of ALDH2; cells in group 1 (pcDNA3.1(+)-ALDH2 group) at 24 h (B); 48 h (C); and 72 h (D) exhibited considerably stronger fluorescence intensity (P<0.01, n=3). (Original magnification×20 NIKON E5400, F3.9, focal length: 14.5, ISO: 200).

fluorescence remained bright for at least one week. Cells with weak fluorescence intensity was considered the negative control and those with the brightest density were as the positive control. The transfection efficiency was calculated. The transfection efficiency in PBMCs was (33.5±3.5)% at 24 h, (56.6±2.5)% at 48 h, and 100% at 72 h.

Expression of ALDH2 mRNA

The mRNA expression of ALDH2 in group 1 (transfected with pcDNA3.1(+)-ALDH2) was considerably high, but there was no distinct ALDH2 band between groups 2 (transfected with pcDNA3.1/myc-His) and 3 (negative control group) (Figure 3). These results indicate that the transgene PBMCs had a high mRNA expression of ALDH2.

Expression of ALDH2 protein

Results of Western blot analysis demonstrated that the ALDH2-transfected cells in group 1 expressed a very high level of human ALDH2 protein compared with the empty vector-transfected group and the negative control group because the protein strips were distinct in Lane 1, but indistinct in the other two lanes (Figure 4). These results showed higher protein expression of ALDH2 in the gene-transfected group after being transfected for 72 h. PcDNA3.1/myc-His-ALDH2 was successfully expressed in PBMCs. These results indicate that the transfection of recombinant eukaryotic expression plasmid pcDNA3.1/myc-His-ALDH2 was an effective method for inducing overexpression of ALDH2 in cultured PBMCs.

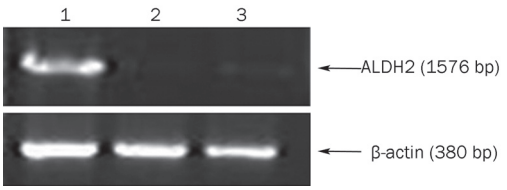

Figure 3. ALDH2 gene transfection induced over-expression of the mRNA of ALDH2 in PBMCs. Products of RT-PCR were analyzed by agarose gel electrophoresis. Lanes 1, 2, 3: RT-PCR amplified ALDH2 and β-actin products from experimental groups 1–3, respectively. β-actin was used as loading control. ALDH2 mRNA expression was considerably increased in cells transfected with pcDNA3.1(+)-ALDH2, compared with that in untransfected cells (P<0.01 *vs* control group, n=3).

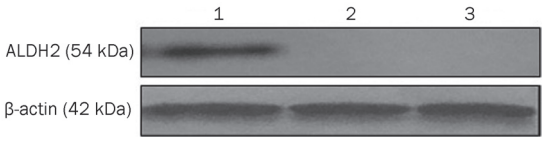

Figure 4. ALDH2 gene transfection induced over-expression of the protein of ALDH2 in PBMCs. ALDH2 protein expressions were detected by Western blot. β-actin was used as loading control. ALDH2 protein expression considerably increased in cells transfected with pcDNA3.1(+)-ALDH2, compared with that in un-transfected cells (P<0.01 *vs* control group, n=3).

Effect of ALDH2 on cultured PBMCs injured by H_2O_2

The relationship between the semilogarithm of H_2O_2 concentration and cell survival rate was determined by the MTT test (Figure 5). The IC_{50} of groups 1, 2, and 3 were obtained using the semilogarithmic regressive equation (calculated with SPSS). The values were 8.833, 2.138, and 1.99 μmol/L, respectively. The semilogarithmic regressive equation of groups 1–3

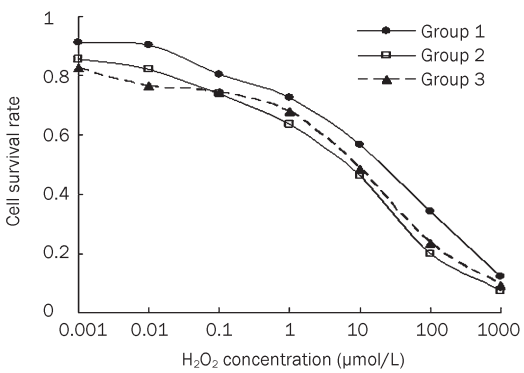

Figure 5. Effect of ALDH2 on cultured PBMCs injured by H_2O_2. Cells were treated with different concentrations of H_2O_2. Semilogarithmic graphs of concentration-survival rate of PBMCs were drawn based on MTT results (group 1: pcDNA3.1(+)-ALDH2 group; group 2: pcDNA3.1 group; group 3: negative control) (P<0.05, n=4).

were y=0.6261–0.1333 lg x, y=0.547–0.1424 lg x, and y=0.5413–0.1381 lg x, respectively. The survival rate data indicated that ALDH2-modified PBMCs (group 1) had a higher tolerance for H_2O_2 than did groups 2 and 3 (P<0.01). There was no significant difference between groups 2 and 3.

Effect of ALDH2 on ROS generation

Treatment with 0, 50, 75, and 100 μmol/L H_2O_2 on PBMCs of the transgene group for 8 h produced a significant decrease in ROS in group 1 compared with that in groups 2 and 3 (P<0.01 or P<0.05; Figure 6A). There was no significant difference between groups 2 and 3 (P>0.05). ALDH2 transfection markedly decreased intracellular ROS generation, indicating that ALDH2 could prevent the increase of ROS generation induced by H_2O_2 at 50, 75, and 100 μmol/L (Figure 6B). ALDH2 transfection could decrease intracellular reactive oxygen species (ROS) generation within a certain concentration.

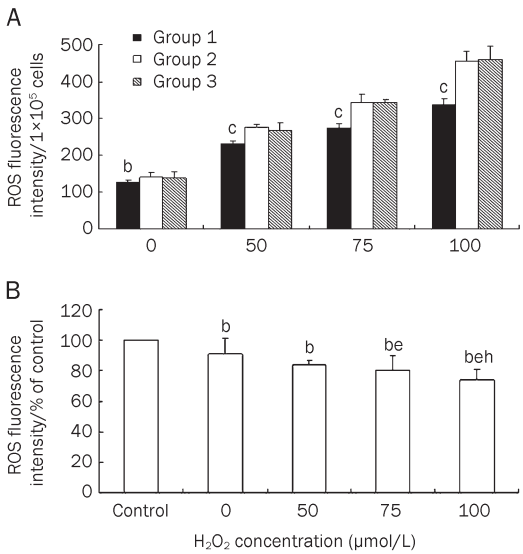

Figure 6. Effect of ALDH2 on the generation of ROS induced by H_2O_2 in PBMCs. Cells were exposed to 0, 50, 75, and 100 μmol/L H_2O_2 for 8 h. n=3. Mean±SD. ^bP<0.05, ^cP<0.01 *vs* control. (A) (group 1: pcDNA3.1(+)-ALDH2 group; group 2: pcDNA3.1 group; group 3: negative control). The percentage of ROS level in the transgene group of control group is shown (B). Relative fluorescence intensities were calculated using group 3 cells as control at different concentrations, and a concentration-dependent decrease of ROS in pcDNA3.1(+)-ALDH2 group is shown. ^bP<0.05 *vs* control. ^eP<0.05 *vs* 0 μmol/L. ^hP<0.05 *vs* 50 μmol/L.

Effect of ALDH2 on H_2O_2-induced apoptosis

Treatment of PBMCs with 0, 50, 75, and 100 μmol/L H_2O_2 for 12 h resulted in cell apoptosis, which can be evaluated by FCM (Figure 7A). Transgene groups treated with H_2O_2, however, showed that ALDH2 could attenuate H_2O_2-induced cell apoptosis within a certain concentration (Figure 7B). ALDH2 had markedly protective effect against H_2O_2-induced (50, 75 μmol/L) apoptosis on PBMCs in group 1 compared with groups 2 and 3 (P<0.05). ALDH2 transfection could protect cells against H_2O_2-induced early and advanced apoptosis at certain concentrations.

Discussion

In this study, we demonstrated that the overexpression of ALDH2 protected PBMCs against oxidative damage and considerably attenuated apoptosis. Oxidative damage could be induced by H_2O_2, and ALDH2 gene transfection enhanced the anti-oxidative effect accompanied with the decreased generation of intracellular ROS in PBMCs.

Adoptive immunotherapy is a new strategy for the treatment of tumors. PBMCs are rich in immune cells, which play a central role in immunotherapy, especially in adoptive immunotherapy. PBMCs are the source of various immune cells, such as natural killer (NK) cells and T lymphocytes. In fact, HSCT is being developed into a type of immunotherapy. Donor $CD4^+$, $CD8^+$, and NK cells have been reported to mediate graft-versus-leukemia effects. Oxidative stress is always induced in different diseases or the pretreatment of radiotherapy and chemotherapy before HSCT. However, immune cells are first subjected to oxidative damage through the generation of redundant ROS[18–24]. Considering the improvements in genetic technology, the use of gene modification appears to be an attractive approach for the protection of immune cells against oxidative damage. We propose that ALDH2 could contribute to the protection of PBMCs against oxidative damage and interpret the mechanism of ALDH2 protection, as well as assist in immune therapy. We chose activated PBMCs, which provide abundant unseparated immune cells from healthy volunteers for the study; however, in clinical applications, we used isolated immune cells such as NK cells, which may have presented some limitations.

First, we cloned the ALDH2 gene from normal human hepatocytes and constructed the eukaryotic expression vector pcDNA3.1/myc-His-ALDH2, which was successfully transfected into PBMCs. The ALDH2 strongly affects alcohol metabolism. Inactive ALDH2 is considered contributory to alcohol flushing, preventing people from developing alcoholism[25–27]. ALDH2 can also protect cells against damage induced by endogenous and exogenous toxic substances. Several reports have suggested that polymorphism ALDH2 genes have a fundamental relationship with colorectal cancer, primary hepatocellular carcinoma, and stomach cancer[28–31]. More important, mitochondrial ALDH2 functions as a protector against oxidative stress[14, 32, 33]. Our subsequent research verified this viewpoint.

As the inductor, H_2O_2 is a central oxygen metabolite during the complete reduction of oxygen to H_2O. It is a biologically important oxidant due to its ability to generate highly reactive and extremely potent hydroxyl radicals[34]. The half life of H_2O_2 is longer than those of other reactive oxygen species; thus, it is typically used to induce oxidative stress *in vitro*[35]. PBMCs are sensitive to H_2O_2-induced oxidative stress. In this study, the treatment of PBMCs with different concentrations of H_2O_2 induced apoptosis in a concentration-dependent manner. ALDH2 overexpression in PBMCs conferred cellular

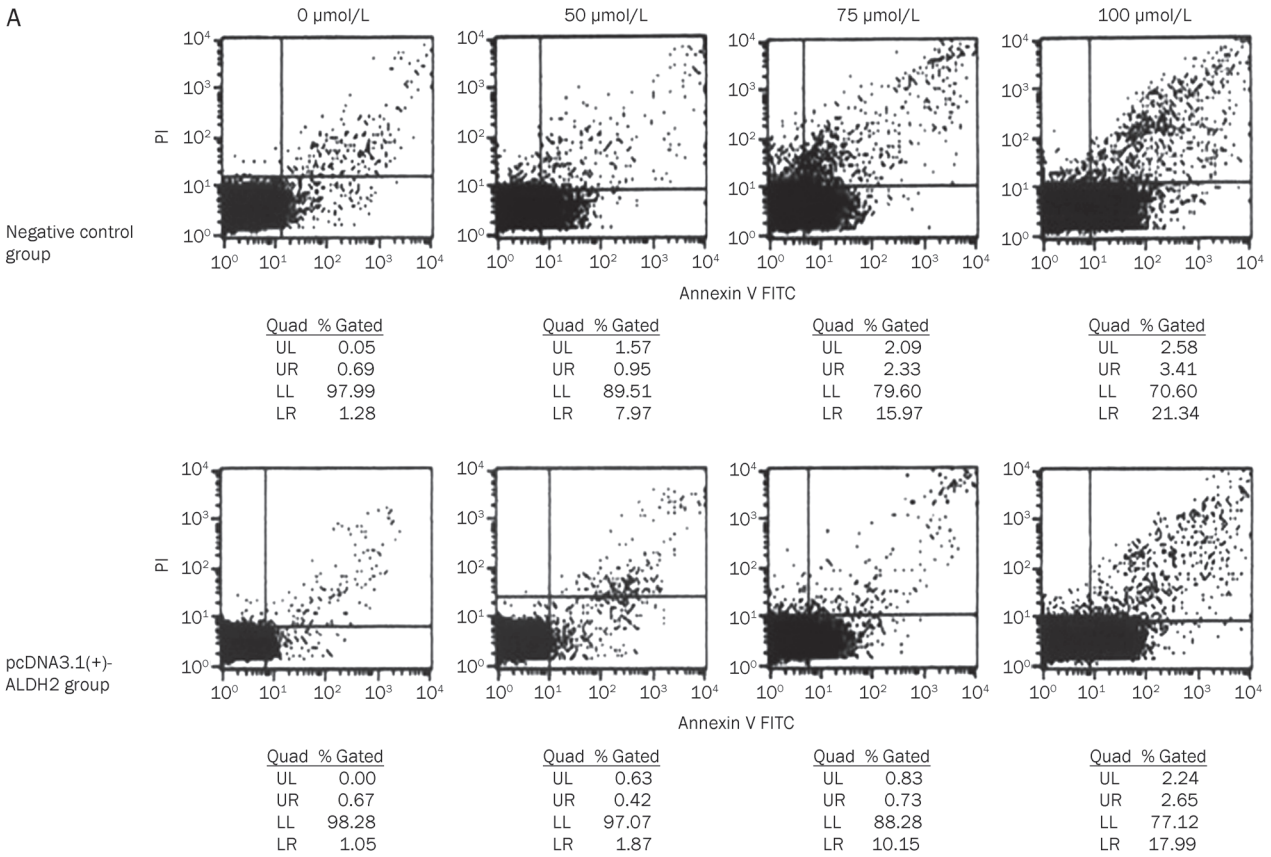

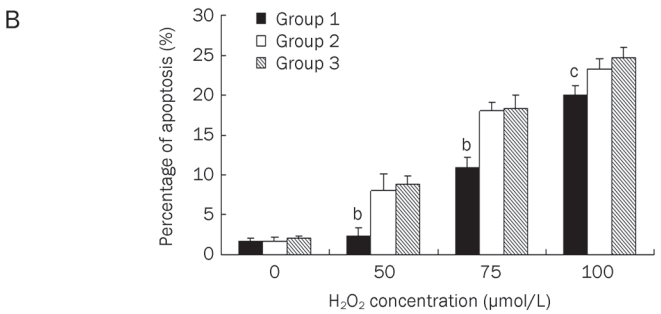

Figure 7. ALDH2 gene transfection reduced cell apoptosis rate induced by H_2O_2. Annexin V and PI FACS analysis showed that early- and advanced-stage apoptotic rates decreased in group 1 (A). Treatment with ALDH2 gene transfection markedly decreased apoptosis compared with the two control groups. n=3. Mean±SD. $^bP<0.05$, $^cP<0.01$ *vs* control. (B) (group 1: pcDNA3.1(+)-ALDH2 group; group 2: pcDNA3.1 group; group 3: negative control).

resistance to H_2O_2 and considerably attenuated hyperoxia-induced cell apoptosis and death. It was proved that ALDH2 could protect PBMCs against H_2O_2-induced oxidative damage and apoptosis. The mechanism of these effects is attributed to the metabolism of 4-HNE and the downregulation of intracellular ROS.

In this study, the ROS production in cultured PBMCs was elevated after H_2O_2 exposure. Overexpression of ALDH2 decreased intracellular ROS production, indicating that ALDH2 might have antioxidant and cytoprotective effects on PBMCs. ROS are the by-products of normal cell metabolism during enzymatic electron-transporting processes, such as mitochondrial respiration, and there is an array of antioxidant systems for maintaining redox balance[36]. Excessive accumulation of ROS, however, can result in the development of oxidative stress. The majority of ROS are produced in mitochondria, resulting in peroxidation of the mitochondrial membrane. The mitochondrial inner membrane is rich in polyunsaturated fatty acids, such as cardiolipin; thus, reactive aldehydes, including 4-HNE, would be easily derived from peroxidated polyunsaturated fatty acids. Thus, the rapid elimination of 4-HNE is necessary in mitochondria. Evidence supports the toxicity of 4-HNE, which results in injury and cell death through both apoptosis and necrosis[37]. ALDH2 plays a major role in the oxidation of aliphatic and aromatic aldehydes, which are exogenous or endogenous, including 4-HNE. This study proved that the decrease in intracellular ROS is involved in the mechanism of protective effects, and mitochondrial ALDH2 plays a major role in the clearance of cytotoxic aldehydes derived from peroxides. Moreover, there may

be other mechanisms related to these protective effects, such as the activation of Akt, AMP-activated protein kinase, and ERK/MAPK and PI3K-Akt pathways. However, further studies are still needed to shed light on these relationships[14, 38].

In summary, this study provides evidence that overexpression of ALDH2 can protect PBMCs against H_2O_2-induced oxidative damage and attenuate apoptosis. Our results also showed that compared with the control cells, the generation of intracellular ROS in gene-transfected cells markedly decreased after ALDH2 transfection. Mitochondrial ALDH2 functions as a protector against oxidative stress in PBMCs. Gene modification focusing on overexpression of ALDH2 and proteins in the immune cells may help elucidate the mechanism of the protective effect of ALDH2, and suggest potential novel gene therapies to assist in immunotherapy.

Acknowledgements

This study was supported by the National Natural Science Foundation of China (No 30460127, 30760276, and 81070444).

Author contribution

Qin FANG, Ji-shi WANG designed the research; Xiu-ying HU performed the research; Jian-qiong XIE, Yuan YANG, Baisheng CHAI, and Xin CUI contributed some reagents and assisted to construct eukaryotic expression vector; Fang-qiong LI assisted to construct Western blot; Qin FANG and Xiu-ying HU analyzed data and wrote the paper.

References

1 Komori T, Sugiyama H, Ogawa H, Oka Y, Miyake S, Soma T, *et al*. Treatment of a patient in a relapse after bone marrow transplantation for acute lymphoblastic leukemia with the systemic administration of allogeneic lymphokine-activated killer cells and recombinant interleukin-2. Eur J Haematol 1989; 43: 184–5.

2 Tricarico M, Rinaldi M, Bonmassar E, Fuggetta MP, Barrera G, Fazio VM. Effect of 4-hydroxynonenal, a product of lipid peroxidation, on natural cell mediated cytotoxicity. Anticancer Res 1999; 19: 5149–54.

3 Schmielau J, Finn O J. Activated granulocytes and granulocyte-derived hydrogen peroxide are the underlying mechanism of suppression of T-cell function in advanced cancer patients. Cancer Res 2001; 61: 4756–60.

4 Mellqvist UH, Hansson M, Brune M, Dahlgren C, Hermodsson S, Hellstrand K. Natural killer cell dysfunction and apoptosis induced by chronic myelogenous leukemia cells: role of reactive oxygen species and regulation by histamine. Blood 2000; 96: 1961–8.

5 Tseng YM, Chen SY, Chen CH, Jin YR, Tsai SM, Chen IJ, *et al*. Effects of alcohol-induced human peripheral blood mononuclear cell (PBMC) pretreated whey protein concentrate (WPC) on oxidative damage. J Agric Food Chem 2008; 56: 8141–7.

6 Kaysen GA, Eiserich JP. The role of oxidative stress-altered lipoprotein structure and function and microinflammation on cardiovascular risk in patients with minor renal dysfunction. J Am Soc Nephrol 2004; 15: 538–48.

7 Kraśniak A, Drozdz M, Pasowicz M, Chmiel G, Kowalczyk-Michałek M, Szumilak D, *et al*. Influence of microinflammation and oxidative stress on atherosclerosis progression and calcifications in cardiovascular system of hemodialyzed patients during two years follow-up. Przegl Lek 2007; 64: 140–7.

8 Mena S, Ortega A, Estrela JM. Oxidative stress in environmental-induced carcinogenesis. Mutat Res 2009; 674: 36–44.

9 Uttara B, Singh AV, Zamboni P, Mahajan RT. Oxidative stress and neurodegenerative diseases: a review of upstream and downstream antioxidant therapeutic options. Curr Neuropharmacol 2009; 7: 65–74.

10 Mizutani H, Tada-Oikawa S, Hiraku Y, Kojima M, Kawanishi S. Mechanism of apoptosis induced by doxorubicin through the generation of hydrogen peroxide. Life Sci 2005; 76: 1439–53.

11 Rosato RR, Almenara JA, Maggio SC, Coe S, Atadja P, Dent P, *et al*. Role of histone deacetylase inhibitor-induced reactive oxygen species and DNA damage in LAQ-824/fludarabine antileukemic interactions. Mol Cancer Ther 2008; 7: 3285–97.

12 Fang J, Nakamura H, Iyer AK. Tumor-targeted induction of oxystress for cancer therapy. J Drug Target 2007;15: 475–86.

13 Li SY, Mark G, Jinhong D. Overexpression of aldehyde dehydrogenase-2 transgene prevents acetaldehyde induced cell injury in human umbilical vein endothelial cells. J Biol Chem 2004; 279: 11244–52.

14 Xu D, Guthrie JR, Mabry S, Sack TM, Truog WE. Mitochondrial aldehyde dehydrogenase attenuates hyperoxia-induced cell death through activation of ERK/MAPK and PI3K-Akt pathways in lung epithelial cells. Am J Physiol Lung Cell Mol Physiol 2006; 291: L966–75.

15 Ohta S, Ohsawa I. Links dysfunction of mitochondria and oxidative stress in the pathogenesis of Alzheimer's disease: on defects in the cytochrome *c* oxidase complex and aldehyde detoxification. J Alzheimers Dis 2006; 9: 155–66.

16 Li DB, Wang JS, Fang Q, Sun HY, Xu W, Li WD. Protective effect of O6-methylguanine-DNA-methyltransferase on mammalian cells. Chin Med J 2007; 120: 714–7.

17 Wang JS, Fang Q, Sun DJ, Chen J, Zhou XL, Lin GW, *et al*. Genetic modification of hematopoietic progenitor cells for combined resistance to 4-hydroperoxycyclophosphamide,vincristine,and daunorubicin. Acta Pharmacol Sin 2001; 22: 949–55.

18 Wu WJ, Pruett SB. Suppression of splenic natural killer cell activity in a mouse model for binge drinking. II. Role of the neuroendocrine system. J Pharmacol Exp Ther 1996; 278: 1331–9.

19 Collier SD, Wu WJ, Pruett SB. Ethanol suppresses NK cell activation by polyinosinic-polycytidylic acid (poly I:C) in female B6C3F1 mice: role of endogenous corticosterone. Alcohol Clin Exp Res 2000; 24: 291–9.

20 Li W, Lidebjer C, Yuan XM, Szymanowski A, Backteman K, Ernerudh J, *et al*. NK cell apoptosis in coronary artery disease: relation to oxidative stress. Atherosclerosis 2008; 199: 65–72.

21 Rinaldi M, Tricarico M, Bonmassar E, Parrella P, Barrera G, Fazio VM. Effect of 4-hydroxynonenal, a product of lipid peroxidation, on NK susceptibility of human K562 target cells. Anticancer Res 1998; 18: 3591–5.

22 Thorén FB, Romero AI, Hermodsson S, Hellstrand K. The CD16-/CD56bright subset of NK cells is resistant to oxidant-induced cell death. J Immunol 2007; 179: 781–5.

23 Carter RH. B cells in health and disease. Mayo Clin Proc 2006; 81: 377–84.

24 Baraldo S, Lokar Oliani K, Turato G, Zuin R, Saetta M. The role of lymphocytes in the pathogenesis of asthma and COPD. Curr Med Chem 2007; 14: 2250–6.

25 Nishiyori A, Shibata A, Ogimoto I, Uchimura N, Egami H, Nakamura J, *et al*. Alcohol drinking frequency is more directly associated with alcohol use disorder than alcohol metabolizing enzymes among male

Japanese. Psychiatry Clin Neurosci 2005; 59: 38–44.
26 Vasiliou V, Pappa A. Polymorphisms of human aldehyde dehydrogenases. Consequences for drug metabolism and disease. Pharmacology 2000; 61: 192–8.
27. Guo R, Zhong L, Ren J. Overexpression of aldehyde dehydrogenase-2 attenuates chronic alcohol exposure-induced apoptosis, change in Akt and Pim signalling in liver. Clin Exp Pharmacol Physiol 2009; 36: 463–8.
28 Gao CM, Takezaki T, Wu JZ, Zhang XM, Cao HX, Ding JH, *et al*. Polymorphisms of alcohol dehydrogenase 2 and aldehyde dehydrogenase 2 and colorectal cancer risk in Chinese males. World J Gastroenterol 2008; 14: 5078–83.
29 Ding J, Li S, Wu J, Gao C, Zhou J, Cao H, *et al*. Alcohol dehydrogenase-2 and aldehyde dehydrogenase-2 genotypes, alcohol drinking and the risk of primary hepatocellular carcinoma in a Chinese population. Asian Pac J Cancer Prev 2008; 9: 31–5.
30 Zhang FF, Hou L, Terry MB, Lissowska J, Morabia A, Chen J, *et al*. Genetic polymorphisms in alcohol metabolism, alcohol intake and the risk of stomach cancer in Warsaw, Poland. Int J Cancer 2007; 121: 2060–4.
31 Ren J, Babcock SA, Li Q, Huff AF, Li SY, Doser TA. Aldehyde dehydrogenase-2 transgene ameliorates chronic alcohol ingestion-induced apoptosis in cerebral cortex. Toxicol Lett 2009; 187: 149–56.
32 Ohta S, Ohsawa I, Kamino K, Ando F, Shimokata H. Mitochondrial ALDH2 deficiency as an oxidative stress. Ann N Y Acad Sci 2004; 1011: 36–44.
33 Ohsawa I, Kamino K, Nagasaka K, Ando F, Niino N, Shimokata H, *et al*. Genetic deficiency of a mitochondrial aldehyde dehydrogenase increases serum lipid peroxides in community-dwelling females. J Hum Genet 2003; 48: 404–9.
34. Clarkson PM, Thompson HS. Antioxidants: what role do they play in physical activity and health. Am J Clin Nutr 2000; 72: 637S–46S.
35 Fatokun AA, Stone TW, Smith RA. Hydrogen peroxide-induced oxidative stress in MC3T3-E1 cells: the effects of glutamate and protection by purines. Bone 2006; 39: 542–51.
36 Ohsawa I, Nishimaki K, Yasuda C, Kamino K, Ohta S. Deficiency in a mitochondrial aldehyde dehydrogenase increases vulnerability to oxidative stress in PC12 cells . J Neurochem 2003; 84: 1110–7.
37 Kakkar P, Singh BK. Mitochondria: a hub of redox activities and cellular distress control. Mol Cell Biochem 2007; 305: 235–53.
38 Ma H, Li J, Gao F, Ren J. Aldehyde dehydrogenase 2 ameliorates acute cardiac toxicity of ethanol: role of protein phosphatase and forkhead transcription factor. J Am Coll Cardiol 2009; 54: 2187–96.

Acta Pharmacologica Sinica (2011) 32: 253–258
 1671-4083/11 $32.00
www.nature.com/aps

Original Article

Over-expression of Gadd45a enhances radiotherapy efficacy in human Tca8113 cell line

Xiao-ying ZHANG[1, 2], Xun QU[3], Cheng-qin WANG[1], Cheng-jun ZHOU[1], Gui-xiang LIU[1], Feng-cai WEI[2], Shan-zhen SUN[1, *]

[1]Department of Pathology, the School of Stomatology, Shandong University, Ji-nan 250012, China; [2]Department of Stomatology, Qilu Hospital, Shandong University, Ji-nan 250012, China; [3]Institute of Basic Medical Sciences, Qilu Hospital, Shandong University, Ji-nan 250012, China

Aim: To investigate the effect of the growth arrest- and DNA damage-inducible *Gadd45a* gene on the radiosensitivity of human tongue squamous cell carcinoma cell line to ionizing radiation (IR).
Methods: Short interfering ribonucleic acid (si-RNA) targeting Gadd45a or an irrelevant mRNA (nonsense si-RNA) was chemically synthesized. The constructed si-RNAs were transfected into Tca8113 cells and Gadd45a expression was determined using quantitative real-time PCR and Western-blot. After 24-h exposure to IR at a dose rate of 4 Gy/min, apoptosis of Tca8113 cells was detected using flow cytometry, and radiosensitivity was measured using MTT assays.
Results: IR apparently increased the expression of Gadd45a at mRNA and protein levels in Tca8113 cells. The effect was efficiently inhibited by transfection with *Gadd45a* si-RNA ($P<0.01$). Furthermore, silencing *Gadd45a* gene significantly increased cell viability and decreased the percentage of apoptotic cells during irradiation, which indicated that IR-induced Gadd45a over-expression could increase the radiosensitivity of Tca8113 cells.
Conclusion: These results indicated that targeting *Gadd45a* may have important therapeutic implications in sensitizing Tca8113 cells to IR.

Keywords: ionizing radiation; Gadd45a; squamous cell carcinoma; Tca8113 cells; apoptosis; RNA interference

Acta Pharmacologica Sinica (2011) 32: 253–258; doi: 10.1038/aps.2010.208

Introduction

Oral squamous cell carcinoma (SCC) is one of the most frequently diagnosed tumors of the head and neck[1, 2]. Despite improvements in treatment, the survival rates of patients with oral SCC have not been significantly improved over the past several decades.

Radiotherapy is one of the most commonly used treatments for cancer patients. The responses of tumor cells to ionizing radiation (IR) are often tissue specific. Some data have confirmed that postoperative radiotherapy (PORT) improved regional control of pathologic N1 neck disease[3]. Identifying molecules and mechanisms that sensitize tumor cells to IR will provide new potential therapeutic strategies for cancer treatment.

The growth arrest- and DNA damage-inducible (*gadd*) 45 gene family, comprising *gadd45α/gadd45a, gadd45β/gadd45b/myd118*, and *gadd45γ/gadd45g/cr6*, is widely expressed in mammalian cells responding to stress stimuli[4]. *Gadd45a* gene was initially isolated from Chinese Hamster Ovarian cells (CHO) treated with ultraviolet radiation[5]. Subsequently, it was found to be induced by a wide spectrum of DNA-damaging agents and growth arrest treatments such as IR[6], methylmethane sulfonate (MMS)[7], growth factor withdrawal[8], hydrogen peroxide[9], hypoxia and many cancer chemotherapeutic drugs[10]. For over one decade, the mechanisms of *Gadd45a* induction have been the focus of study. *Gadd45a* was the first stress-inducible gene determined to be up-regulated by p53 and is also a target for the p53 homologues, p63 and p73[11]. Among p53-regulated genes, *Gadd45a* has been shown to play an important role in DNA damage–induced cell responses. For example, *Gadd45a* deficiency caused defective UV-induced nucleotide excision repair[12]. The embryonic fibroblast cells in *Gadd45a*-null mouse exhibited increased aneuploidy accompanied with abnormal centromere amplification; after exposure to IR, *Gadd45a*-null mice also showed increased carcinogenesis compared with control mice[13]. In addition to p53, BRCA1 and FOXO3a have also been shown to activate *Gadd45a* gene expression[14, 15]. Furthermore, Gadd45a

* To whom correspondence should be addressed.
E-mail leaf_zi@126.com
Received 2010-06-12 Accepted 2010-11-14

is also involved in DNA damage–induced apoptosis. Gadd45a suppresses Ras-induced mammary tumorigenesis by activation of p38 stress signaling and induces apoptosis of HeLa cells by promoting Bim translocation to mitochondria[16, 17]. However, little is known about the role of *Gadd45a* in control of apoptosis in the cell response to IR *in vitro*.

In the present study, we investigated the induction of *Gadd45a* gene expression following irradiation in Tca8113 cells, and assessed its effect on the sensitivity of Tca8113 cells line to IR treatment.

Materials and methods

Cell culture

Tca8113 cell line was purchased from Culture Collection of Chinese Academy of Science (Shanghai, China) and routinely cultured in Dulbecco's modified Eagle's medium (DMEM, Gibco) supplemented with 10% fetal bovine serum (Gibco) at 37 °C in a humidified air atmosphere containing 5% CO_2.

Ionizing radiation (IR)

Tca8113 cells were cultured in six-well plates until 70% confluence and then exposed to IR from a VARIAN clinical 2100C/D linear accelerator (VARIAN, Palo Alto, CA, USA) at a dose rate of 4 Gy/min.

Gene silencing with si-RNA

Tca8113 cells were divided into three groups for transfection: lipofectamine™ 2000 only (mock), nonsense si-RNA or Gadd45a si-RNA. Mock and nonsense si-RNA (Gene Chem, China) were regarded as control groups. Tca8113 cells were planted in six-well plates. The cells reached 40% confluence, and then the media was changed to opti-MEM (Invitrogen, USA). The cells were transfected with the Gadd45a si-RNA or control si-RNA (100 nmol/L) premixed with the lipofectamine™ 2000 (Invitrogen, USA) in Opti-MEM. At 6 h after transfection, the cells were placed in fresh complete medium without penicillin and streptomycin. The sequences of Gadd45a si-RNA and nonsense si-RNA were listed in Table 1.

Table 1. Si-RNA sequences for gene silencing.

Gene name	Si-RNA sequences
Gadd45a	Sense, 5'-3'CACTGATGCAAGGATTACA
	Antisense, 5'-3'TGTAATCCTTGCATCAGTG
Nonsense	Sense, 5'-3'UUCUCCGAACGUGUCACGUtt
	Antisense, 5'-3'ACGUGACACGUUCGGAGAAtt

Quantitative real-time RT-PCR analysis for Gadd45a

Total RNA was extracted from Tca8113 cells using the Trizol (Invitrogen, USA) method as recommended by the manufacturer. The quantity and concentration of the purified RNA were assessed by 260/280 optical density (*OD*) measurements on a spectrophotometer (Biochrom, USA). An equal amount of RNA was reverse transcribed with the First Strand cDNA Synthesis kit (Fermentas, EU). To determine the level of Gadd45a mRNA, real time quantitative PCR analysis was performed with Light Cycler 2.0 (Roche Diagnostics, Switzerland) according to the protocol recommended by TaKaRa SYBR_ Premix Ex Taq™ (TaKaRa, Japan). Thermal cycling parameters were as follows: an initial incubation of 95 °C for 30 s, and then 40 cycles of 95 °C for 5 s and 55 °C for 20 s and 72 °C for 15 s. The Gadd45a mRNA expression level was normalized to the median expression of β-actin. Gene-specific forward (F) and reverse (R) primer sequences for Gadd45a and β-actin were summarized in Table 2.

Table 2. Primer sequences of Gadd45a for quantitative real time RT-PCR.

Gene name	Primer sequences
Gadd45a	F: 5'-CGT TTT GCT GCG AGA ACG AC-3'
	R: 5'-GAA CCC ATT GAT CCA TGT AG-3'
β-actin	F: 5'-AGC GAG CAT CCC CCA AAG TT-3'
	R: 5'-GGG CAC GAA GGC TCA TCA TT-3'

Protein extraction and Western blot analysis

Cellular protein extracts were prepared by homogenization in an ice-cold buffer [50 mmol/L Tris-HCl (pH 7.4), 150 mmol/L NaCl, 1% Triton X-100, 2 mmol/L EDTA (pH 8.0), 2 μg/mL aprotinin, 5 mmol/L dithiothreitol and 0.2 mmol/L phenylmethylsulphonyl fluoride, 1 mmol/L PMSF, 10 μg/mL leupeptin] for 30 min. The lysates were centrifuged at 15000×*g* for 15 min at 4 °C and protein concentrations of the supernatants were determined by BCA protein assay kit (Calbiochem, USA). Equivalent amount of protein (80 μg) was electrophoresed on a 12% polyacrylamide gel and electrotransferred onto Immobilon-P (Millipore). After being blocked with 5% non-fat milk, the membrane was incubated overnight at 4 °C with rabbit polyclonal anti-human Gadd45a antibodies (dilution 1:500, Millipore; 07-1230), then washed and incubated with goat polyclonal anti-rabbit HRP-labeled secondary antibody (Santa Cruz, CA) in TBST (TBS containing 0.05% Tween 20) for 2 h. The bands were detected by enhanced chemiluminescence (ECL). The intensities of acquired bands were measured by computerized image analysis and normalized to tubulin as the internal control.

MTT assays for determination of cellular viability

The antiproliferative effect of Gadd45a gene was evaluated using the MTT assay as described by Azria[18]. Exponentially growing cells were seeded into 96-well plates (6 000/well) and transfected as mentioned above. Tca8113 cells transfected with the Gadd45a si-RNA and the control cells were irradiated in the dose range from 0 to 10 Gy. After 24-h exposure to IR, the viability of the cells was analyzed using MTT colorimetric assay. MTT was a pale yellow tetrazolium salt that produces a dark blue formazan product when incubated with the living

cells. Briefly, 20 μL of 0.5% MTT solution was added to each well and was incubated with the cells for 4 h at 37 °C to allow crystal formation. The medium was decanted and the crystals were dissolved by adding dimethyl sulphoxide (DMSO; 200 μL/well). The absorbance at 490 nm was measured using ELISA Reader (RT-2100C, Rayto, USA). The results were expressed with respect to control values (cells without any treatment). Experiments were repeated three times.

Detection of apoptosis by flow cytometry

Apoptosis rates of the experimental group and the control groups were measured with AnnexinV-FITC kit (BD Biosciences, San Diego, CA, USA) by flow cytometry according to the manufacturer's instructions. At 24 h after radiation exposure to 4 Gy or 10 Gy, the cells were harvested by trypsinization and washed twice with ice-cold PBS and resuspended in binding buffer. A total of 5 μL of Annexin V-FITC and 10 μL of propidium iodide (PI) were added to cell suspensions. After incubation for 15 min at room temperature in the dark, 400 μL of binding buffer was added to the mixture. The cells were analyzed by flow cytometry (Becton Dickinson, USA) and the data were analyzed with WinMDI 2.8 software for calculation of percentage of apoptotic cells.

Statistical analysis

Statistical analysis was performed using SPSS 17.0 version software package for Windows. All values were presented as mean±standard deviation (SD) of replicate samples in single experiments or replicate experiments. The *t* test was used to analyze the data. Differences were considered statistically significant at $P<0.05$.

Results

Basal and IR-induced Gadd45a expression in Tca8113 cells

We initially examined the effect of IR on Gadd45a expression in human Tca8113 cell lines by quantitative real-time RT-PCR and Western blot analysis. Gadd45a induction was assessed by comparing the basal level to that present 24 h following treatment with 4 Gy or 10 Gy IR. As shown in Figure 1A, IR obviously induced Gadd45a mRNA expression compared with the basal level (0.000965±0.00005 *vs* 0.000387±0.00002 and 0.001644±0.000065 *vs* 0.000387±0.00002) in the dose range examined. Consistently, Gadd45a protein level detected by Western blot was also induced by 10 Gy IR ($P=0.0028$) although Gadd45a protein level observed in Tca8113 cells treated with 4 Gy IR had no statistical difference in comparison with the basal level ($P=0.0513$, Figure 1B).

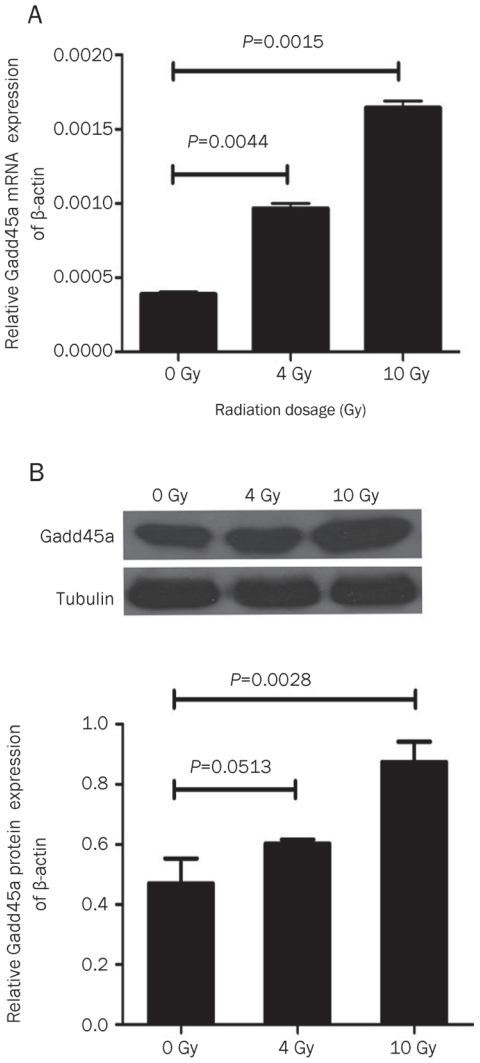

Figure 1. Over-expression of Gadd45a in Tca8113 cells was induced by IR. (A) The level of *Gadd45a* mRNA after 24-h exposure to IR at 4 or 10 Gy was significantly higher than the basal level ($P<0.01$). (B) Over-expression of Gadd45a protein was not significantly induced in Tca8113 cells after exposure to 4 Gy IR ($P=0.0513$), but was markedly induced after exposure to 10 Gy IR ($P=0.0028$). $n=3$. Mean±SD.

Gadd45a si-RNA suppressed the expression of Gadd45a

Quantitative real-time RT-PCR and Western blot were performed to determine whether the expression of Gadd45a mRNA and protein were knocked down by *Gadd45a* siRNA. The levels of *Gadd45a* mRNA and Gadd45a protein in the group transfected with *Gadd45a* si-RNA were significantly decreased compared with the control groups ($P<0.01$), demonstrating that the expression of Gadd45a was effectively restrained by si-RNA (Figure 2). Although Tca8113 cells transfected with Gadd45a si-RNA had an increase in *Gadd45a* mRNA expression following treatment with 10 Gy IR ($P=0.0489$), the level of Gadd45a protein was not markedly elevated ($P=0.0566$).

Gadd45a si-RNA inhibited the radiosensitivity of Tca8113 cells

MTT assays were used to examine the effects of Gadd45a si-RNA on the radiosensitivity of Tca8113 cells. As shown in Figure 3, irradiation resulted in a dose-dependent reduction in cell survival fraction, and the effect was significantly inhibited in the cells transfected with Gadd45a si-RNA compared with nonspecific control cells ($P<0.05$).

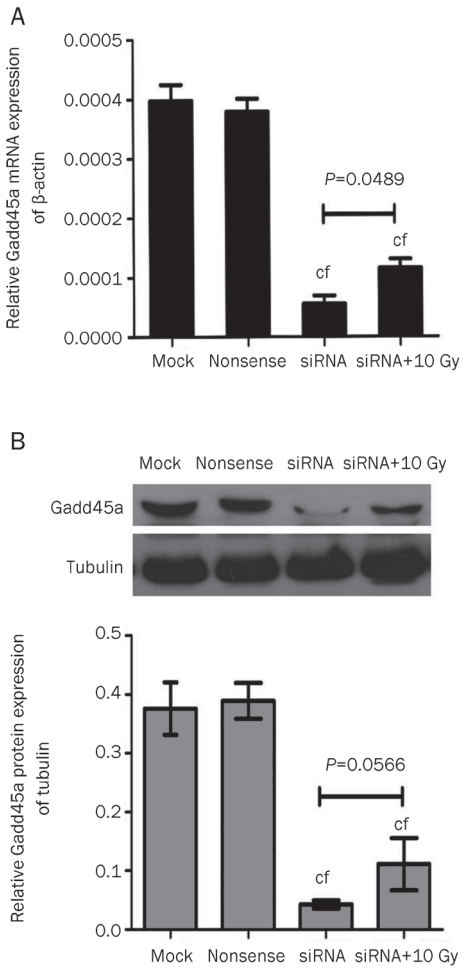

Figure 2. Inhibitive effect of si-RNA on Gadd45a expression in Tca8113 cells. (A) The results of quantitative real-time PCR demonstrated that the expression of Gadd45a mRNA in si-RNA and si-RNA+10 Gy groups was significantly lower than that in the control groups. (B) The expression of Gadd45a protein was apparently inhibited in the Tca8113 cells transfected with Gadd45a si-RNA. n=3. Mean±SD. ^{c}P<0.01 *vs* mock. ^{f}P<0.01 *vs* nonsense.

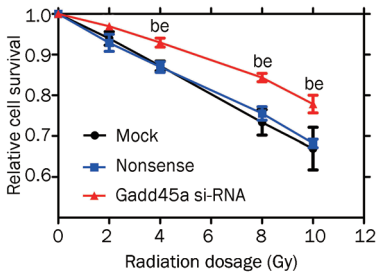

Figure 3. Effect of Gadd45a silencing on the radiosensitivity of Tca8113 cells. Tca8113 cells transfected with the Gadd45a si-RNA and the control cells were seeded into 96-well plates and irradiated in the dose range from 0 to 10 Gy. After 24 h, the viability of the cells was analyzed using MTT assay. When the dose was 4 Gy or more, there was significant difference in the survival level between the cells transfected with Gadd45a si-RNA and the control cells. n=3. Mean±SD. ^{b}P<0.05 *vs* mock. ^{e}P<0.05 *vs* nonsense.

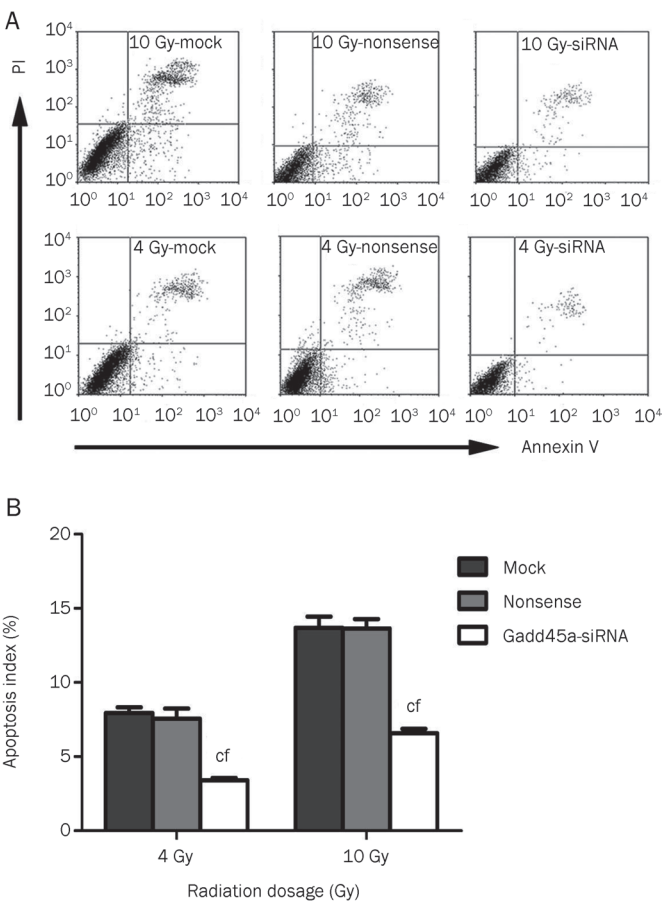

Figure 4. Gadd45a si-RNA reduced the apoptosis of Tca8113 cells after radiotherapy. (A) Tca8113 cells were harvested for apoptosis analysis at 24 h after 4 Gy or 10 Gy IR. Flow cytometry was used to examine the percentage of apoptosis cells. (B) The results of flow cytometry analysis showed that Gadd45a knockdown caused a significant inhibition of apoptosis induced by IR treatment. n=3. Mean±SD. ^{c}P<0.01 *vs* mock. ^{f}P<0.01 *vs* nonsense.

IR-induced over-expression of Gadd45a increased the apoptosis of Tca8113 cells

To determine whether the increased expression of Gadd45a modulated the apoptosis of Tca8113 cells exposed to IR, flow cytometry measurement was used to quantify the percentage of apoptotic cells in the total cell population. After 24-h exposure to 4 or 10 Gy radiation, a significantly lower percentage of apoptotic cells was observed in Tca8113 cells transfected with Gadd45a si-RNA than the other groups (P<0.01, Figure 4).

Discussion

Squamous cell carcinoma (SCC) accounts for more than 90% of malignancies of the oral cavity and oropharynx[19]. Patients with SCC are generally treated with surgery in combination with radiotherapy[20, 21]. However, permanent xerostomia is a common complication of radiation therapy for head and neck

cancer, reducing the patient's quality of life[22]. Therefore, it is essential to develop more effective radiotherapy regimens for oral SCC.

The responses of tumor cells to IR are often closely related to pathway aberrations present in tumors. The *Gadd45a* gene is a member of a group of genes that have been characterized as important players that participate in cellular response to a variety of DNA damage agents[23]. In previous studies, the human Gadd45a has been found to be strongly and rapidly induced by X rays[6, 24]. In the present study, we explored the induction of *Gadd45a* gene in Tca8113 cell line. At 24 h after radiation treatment, the levels of Gadd45a mRNA and protein in Tca8113 cells were markedly up-regulated than the baseline level and graded doses of radiation produced obviously linear increases of *Gadd45a* mRNA in the dose range examined. These results implied that the induction of *Gadd45a* by IR in Tca8113 cells was specific and long-lasting. Similar results have also been shown in human myeloblastic leukemia ML-1 cells[25].

Gadd45a was primarily considered as a pro-apoptotic gene, and has been reported as being able to activate the mitochondrial pathway of apoptosis[26]. It has been reported that knockdown of *Gadd45a* led to increased growth and survival of FDB1 myeloid cells[27]. Moreover, Zhang *et al* found that high level expression of Gadd45a sensitized M1 myeloblastic leukemia and H1299 lung carcinoma cell lines to apoptosis induced by gamma-irradiation[28]. However, inactivation of *Gadd45a* gene has been reported to sensitize transgenic tumor mouse to radiation treatment[29]. In the current study, we further reveal the role of Gadd45a in the response of oral cancer cells to IR treatment using si-RNA. This approach has been used previously in other cell types, and gene silencing of *Gadd45a* led to disruption of functions including its ability to induce apoptosis[30, 31]. We showed that Gadd45a si-RNA specifically repressed Gadd45a expression, and the inhibition reduced cell apoptosis and enhanced proliferation of Tca8113 cells after exposure to radiation. Our results demonstrated that *Gadd45a* inactivation reduced the sensitivity of Tca8113 cells to IR and the high level Gadd45a expression induced by IR might contribute to apoptosis of oral cancer cells. The gene therapy targeting Gadd45a in tumor cells could have important implications for the development of novel strategies in radiotherapy of oral SCC.

In conclusion, the results not only provided a better understanding of the biological function of Gadd45a but also suggested that Gadd45a might be a critical target for enhancing radiosensitivity of oral SCC. Although Gadd45a expression is correlated with the apoptosis induced by IR in Tca8113 cells, further research on the mechanism involved in IR-induced apoptosis is essential for development of therapeutic approaches for oral SCC.

Acknowledgments

This work was supported by grants from National Natural Science Foundations of China (No 81072202 and 30772269). Authors especially thank Prof Yan HOU for her excellent technical assistance.

Author contribution

Xiao-ying ZHANG, Xun QU, Shan-zhen SUN, and Feng-cai WEI designed the research; Xiao-ying ZHANG and Gui-xiang LIU performed research; Cheng-qin WANG and Cheng-jun ZHOU contributed analytic tools; Xiao-ying ZHANG analysed data and wrote the paper.

References

1 Rodrigues VC, Moss SM, Tuomainen H. Oral cancer in the UK: to screen or not to screen. Oral Oncol 1998; 34: 454–65.
2 Greenlee RT, Hill-Harmon MB, Murray T, Thun M. Cancer statistics, 2001. CA Cancer J Clin 2001; 51: 15–36.
3 Jackel MC, Ambrosch P, Christiansen H, Martin A, Steiner W. Value of postoperative radiotherapy in patients with pathologic N1 neck disease. Head Neck 2008; 30: 875–82.
4 Lal A, Gorospe M. Egad, more forms of gene regulation: the gadd45a story. Cell Cycle 2006; 5: 1422–5.
5 Fornace AJ Jr, Alamo I Jr, Hollander MC. DNA damage-inducible transcripts in mammalian cells. Proc Natl Acad Sci USA 1988; 85: 8800–4.
6 Papathanasiou MA, Kerr NC, Robbins JH, McBride OW, Alamo I Jr, Barrett SF, *et al*. Induction by ionizing radiation of the gadd45 gene in cultured human cells: lack of mediation by protein kinase C. Mol Cell Biol 1991; 11: 1009–16.
7 Hollander MC, Alamo I, Jackman J, Wang MG, McBride OW, Fornace AJ Jr. Analysis of the mammalian gadd45 gene and its response to DNA damage. J Biol Chem 1993; 268: 24385–93.
8 Shain SA. Exogenous fibroblast growth factors maintain viability, promote proliferation, and suppress GADD45alpha and GAS6 transcript content of prostate cancer cells genetically modified to lack endogenous FGF-2. Mol Cancer Res 2004; 2: 653–61.
9 Bower JJ, Leonard SS, Chen F, Shi X. As(III) transcriptionally activates the gadd45a gene via the formation of H_2O_2. Free Radic Biol Med 2006; 41: 285–94.
10 Corn PG, El-Deiry WS. Microarray analysis of p53-dependent gene expression in response to hypoxia and DNA damage. Cancer Biol Ther 2007; 6: 1858–66.
11 Rosemary Siafakas A, Richardson DR. Growth arrest and DNA damage-45 alpha (GADD45alpha). Int J Biochem Cell Biol 2009; 41: 986–9.
12 Smith ML, Ford JM, Hollander MC, Bortnick RA, Amundson SA, Seo YR, *et al*. p53-mediated DNA repair responses to UV radiation: studies of mouse cells lacking p53, p21, and/or gadd45 genes. Mol Cell Biol 2000; 20: 3705–14.
13 Hollander MC, Sheikh MS, Bulavin DV, Lundgren K, Augeri-Henmueller L, Shehee R, *et al*. Genomic instability in Gadd45a-deficient mice. Nat Genet 1999; 23: 176–84.
14 Harkin DP, Bean JM, Miklos D, Song YH, Truong VB, Englert C, *et al*. Induction of GADD45 and JNK/SAPK-dependent apoptosis following inducible expression of BRCA1. Cell 1999; 97: 575–86.
15 Tran H, Brunet A, Grenier JM, Datta SR, Fornace AJ Jr, DiStefano PS, *et al*. DNA repair pathway stimulated by the forkhead transcription factor FOXO3a through the Gadd45 protein. Science 2002; 296: 530–4.
16 Tront JS, Hoffman B, Liebermann DA. Gadd45a suppresses Ras-driven mammary tumorigenesis by activation of c-Jun NH_2-terminal kinase and p38 stress signaling resulting in apoptosis and senescence. Cancer Res 2006; 66: 8448–54.
17 Tong T, Ji J, Jin S, Li X, Fan W, Song Y, *et al*. Gadd45a expression induces Bim dissociation from the cytoskeleton and translocation to

mitochondria. Mol Cell Biol 2005; 25: 4488–500.
18 Azria D, Larbouret C, Cunat S, Ozsahin M, Gourgou S, Martineau P, *et al*. Letrozole sensitizes breast cancer cells to ionizing radiation. Breast Cancer Res 2005; 7: R156–63.
19 D'Silva NJ, Ward BB. Tissue biomarkers for diagnosis & management of oral squamous cell carcinoma. Alpha Omegan 2007; 100: 182–9.
20 Palme CE, Gullane PJ, Gilbert RW. Current treatment options in squamous cell carcinoma of the oral cavity. Surg Oncol Clin N Am 2004; 13: 47–70.
21 Jang WI, Wu HG, Park CI, Kim KH, Sung MW, Kim MJ, *et al*. Treatment of patients with clinically lymph node-negative squamous cell carcinoma of the oral cavity. Jpn J Clin Oncol 2008; 38: 395–401.
22 Chambers MS, Garden AS, Kies MS, Martin JW. Radiation-induced xerostomia in patients with head and neck cancer: pathogenesis, impact on quality of life, and management. Head Neck 2004; 26: 796–807.
23 Benjamin CL, Melnikova VO, Ananthaswamy HN. P53 protein and pathogenesis of melanoma and nonmelanoma skin cancer. Adv Exp Med Biol 2008; 624: 265–82.
24 Daino K, Ichimura S, Nenoi M. Early induction of CDKN1A (p21) and GADD45 mRNA by a low dose of ionizing radiation is due to their dose-dependent post-transcriptional regulation. Radiat Res 2002; 157: 478–82.
25 Amundson SA, Lee RA, Koch-Paiz CA, Bittner ML, Meltzer P, Trent JM, *et al*. Differential responses of stress genes to low dose-rate gamma irradiation. Mol Cancer Res 2003; 1: 445–52.
26 Takekawa M, Saito H. A family of stress-inducible GADD45-like proteins mediate activation of the stress-responsive MTK1/MEKK4 MAPKKK. Cell 1998; 95: 521–30.
27 Perugini M, Kok CH, Brown AL, Wilkinson CR, Salerno DG, Young SM, *et al*. Repression of Gadd45alpha by activated FLT3 and GM-CSF receptor mutants contributes to growth, survival and blocked differentiation. Leukemia 2009; 23: 729–38.
28 Zhang W, Hoffman B, Liebermann DA. Ectopic expression of MyD118/Gadd45/CR6 (Gadd45beta/alpha/gamma) sensitizes neoplastic cells to genotoxic stress-induced apoptosis. Int J Oncol 2001; 18: 749–57.
29 Lu X, Yang C, Hill R, Yin C, Hollander MC, Fornace AJ Jr, *et al*. Inactivation of gadd45a sensitizes epithelial cancer cells to ionizing radiation *in vivo* resulting in prolonged survival. Cancer Res 2008; 68: 3579–83.
30 Zerbini LF, Libermann TA. GADD45 deregulation in cancer: frequently methylated tumor suppressors and potential therapeutic targets. Clin Cancer Res 2005; 11: 6409–13.
31 Al-Romaih K, Sadikovic B, Yoshimoto M, Wang Y, Zielenska M, Squire JA. Decitabine-induced demethylation of 5' CpG island in GADD45A leads to apoptosis in osteosarcoma cells. Neoplasia 2008; 10: 471–80.

Acta Pharmacologica Sinica (2011) 32: 259–269

www.nature.com/aps

Original Article

Genome-wide analysis of microRNA and mRNA expression signatures in hydroxycamptothecin-resistant gastric cancer cells

Xue-mei WU[1, 3], Xiang-qiang SHAO[1, 3], Xian-xin MENG[2], Xiao-na ZHANG[2], Li ZHU[1], Shi-xu LIU[1, 3], Jian LIN[1, 3], Hua-sheng XIAO[1, 2, *]

[1]*The Center of Functional Genomics, Key Laboratory of Systems Biology, Shanghai Institutes for Biological Sciences, Chinese Academy of Sciences, Shanghai 200031, China;* [2]*National Engineering Center for Biochip at Shanghai, Shanghai 201203, China;* [3]*Graduate University of Chinese Academy of Sciences, Shanghai 200031, China*

Aim: To investigate the involvement of microRNAs (miRNAs) in intrinsic drug resistance to hydroxycamptothecin (HCPT) of six gastric cancer cell lines (BGC-823, SGC-7901, MGC-803, HGC-27, NCI-N87, and AGS).
Methods: A sulforhodamine B (SRB) assay was used to analyze the sensitivity to HCPT of six gastric cancer cell lines. The miRNA and mRNA expression signatures in HCPT-resistant cell lines were then identified using DNA microarrays. Gene ontology and pathway analysis was conducted using GenMAPP2. A combined analysis was used to explore the relationship between the miRNAs and mRNAs.
Results: The sensitivity to HCPT was significantly different among the six cell lines. In the HCPT-resistant gastric cancer cells, the levels of 25 miRNAs were deregulated, including miR-196a, miR-200 family, miR-338, miR-126, miR-31, miR-98, let-7g, and miR-7. Their target genes were related to cancer development, progression and chemosensitivity. Moreover, 307 genes were differentially expressed in HCPT-resistant cell lines, including apoptosis-related genes (BAX, TIAL1), cell division-related genes (MCM2), cell adhesion- or migration-related genes (TIMP2, VSNL1) and checkpoint genes (RAD1). The combined analysis revealed 78 relation pairs between the miRNAs and mRNAs.
Conclusion: Hierarchical clustering showed that the miRNA and mRNA signatures in our results were informative for discriminating cell lines with different sensitivities to HCPT. However, there was slightly lower correlation between the expression patterns of the miRNA and those of the predicted target transcripts.

Keywords: hydroxycamptothecin (HCPT); gastric cancer; microRNA; signature; drug resistance; gene expression regulation; cluster analysis; messenger RNA

Acta Pharmacologica Sinica (2011) 32: 259–269; doi: 10.1038/aps.2010.204

Introduction

Gastric cancer is the second leading cause of cancer death worldwide and accounts for approximately 10% of newly diagnosed cancers[1]. Camptothecins (CPTs) have been approved for the treatment of various malignancies, including gastric cancer. By binding to the covalent complex formed by Top1 and DNA, CPTs prevent the re-ligation of DNA, which leads to persistent DNA breaks, subsequently inducing cell apoptosis[2]. Clinical data show that the efficiency of CPTs varies between patients, and the resistance mechanism remains to be determined[3]. Previous studies indicated that the resistant phenotype may be the result of inadequate drug accumulation in cancer cells, alterations in the target Top1 and alterations in cellular drug responses including DNA repair and apoptosis[4–6]. Drug transporters that are ATP-dependent, such as P-glycoprotein, multidrug resistance-related protein (MRP) and breast cancer resistance protein (BCRP), were involved in the efflux of CPTs. UDP glucuronosyltransferases, such as UGT1A1, UGT1A3, UGT1A6, and UGT1A9, were associated with the glucuronidation of CPTs, which increased the efflux of this drug. Top1-binding protein nucleolin and small ubiquitin-like modifier (SUMO) could relocalize TOP1, the target of CPTs. The checkpoint genes *ATM*, *MEC1*, *MEC2*, *CHK1*, *RAD9*, *RAD17*, and *ATR* and the DNA repair genes *CSA*, *CSB36*, *RAD6*, *TDP*, *TRF4*, *MSM2*, *MSM3*, *XRCC*, and *PNK1* were related to the repair of DNA damage caused by CPTs. Bax, p53, NF-κB, and survivin participated in the regulation of cell apoptosis induced by CPTs[7–9]. All of these genes have

* To whom correspondence should be addressed.
E-mail huasheng_xiao@shbiochip.com
Received 2010-06-25 Accepted 2010-11-08

been reported to be related to the resistance to CPTs.

MiRNAs are a class of non-coding RNAs that are 21 to 25 nucleotides in length and function as regulators of gene expression. Recently, miRNAs have been identified as oncogenes or tumor suppressors[10, 11], and they have been regarded as potential drug targets[12] due to many of them being located at the fragile sites of chromosomes or cancer-associated genomic regions[13]. Bertino *et al* first introduced the idea of "miRNA pharmacogenomics," which is defined as the study of miRNAs and polymorphisms affecting miRNA function to predict drug response and improve drug efficiency[14]. MiRNA misexpressions or mutations result in a gain or loss of miRNA function and, therefore, a downregulation or upregulation of the target protein, which is involved in the drug response. In previous studies, miR-24, miR-21, let-7a, miR-214, miR-221, miR-222, miR-328, and miR-27a have been reported to be involved in the regulation of chemosensitivity[15]. However, there have been no reports regarding miRNAs and their involvement in the resistance to CPTs of gastric cancer.

To find the miRNAs that are involved in intrinsic resistance to 10-hydroxycamptothecin (HCPT), we conducted a miRNA pharmacogenomics study on HCPT by performing a genome-wide expression profiling of the miRNAs and mRNAs in six different gastric cancer cell lines. Our study provides a resource for integrated chemo-genomic studies that aimed to elucidate the molecular markers for personalized therapy and to understand the mechanisms of HCPT resistance.

Materials and methods

Cell culture

Six human gastric adenocarcinoma cell lines, BGC-823 (low-differentiated human gastric adenocarcinoma cell line), SGC-7901 (moderate-differentiated human gastric adenocarcinoma cell line), MGC-803 (low-differentiated human mucinous gastric carcinoma), HGC-27 (undifferentiated human mucinous gastric carcinoma), NCI-N87 (well-differentiated human carcinoma cell line) and AGS (low-differentiated human gastric adenocarcinoma cell line), were obtained from the Shanghai Institutes for Biological Sciences, Chinese Academy of Sciences, China. The six cell lines were all derived from patients who had received no prior therapy. The cells were cultured in RPMI-1640 medium supplemented with 10% fetal calf serum (Gibco BRL, Grand Island, NY) at 37 °C in 5% CO_2.

SRB assay

Cells were seeded in 96-well plates with 100 μL (5 000 to 10 000 cells/well) for 24 h and then exposed to freshly prepared HCPT (HSFY Pharma, China) at a final concentration that was 0.01, 0.1, 1, 10, and 100 times the human peak plasma concentration for HCPT (1.0 μg/mL). Simultaneously, one plate of each cell line was fixed with TCA. The cells were then incubated for 48 h, and their viability was assessed using the Sulforhodamine B (SRB) assay (Sigma, St Louis, MO). The absorbance at 515 nm (OD_{515}) was read using the automated plate reader. Seven OD_{515} were measured: at time zero (Tz), the growth of control cells (C), and the growth in the presence of the drug at the five concentration levels (Ti). The percentage growth inhibition was calculated as [(Ti–Tz)/(C–Tz)]×100, when Ti>/=Tz; [(Ti–Tz)/Tz]×100, when Ti<Tz. The concentration resulting in a 50% reduction in the net protein increase in control cells during the drug incubation (GI50) was calculated using the percentage growth inhibition curve. All of the experiments were individually performed in triplicate.

Total RNA extraction and quality assessment

The cells were cultured for 24 h and were then collected for total RNA extraction. Total RNA was isolated using the mirVana™ miRNA Isolation Kit (Ambion, Austin, Texas) following the manufacturer's instructions. Then the RNA quantity was determined using Nanodrop1000. The RNA quality was assessed using the Agilent 2100 Bioanalyzer (Agilent, Santa Clara, California). All of the samples were assayed and qualified in triplicate using the miRNA microarray and DNA oligonucleotide microarray.

MiRNA microarray profiling

The input for Agilent's miRNA labeling system was 100 ng total RNA. After dephosphorylation and denaturation, the total RNA was labeled with cyanine 3-pCp and then hybridized to Agilent Human miRNA Microarray V2 using the miRNA Complete Labeling and Hyb Kit (Agilent, Santa Clara, California). After hybridization for 20 h, the slides were then washed using the Gene Expression Wash Buffer Kit (Agilent, Santa Clara, California) and scanned using an Agilent Scanner. The images were processed and analyzed with Agilent Feature Extraction Software.

The raw data were normalized using quantile normalization and then analyzed in GeneSpring GX (zcomSilicon Genetics, Redwood City, CA, USA). Statistical analysis using ANOVA was conducted to compare the differentially expressed miRNAs.

Whole genome gene expression microarray

Gene expression profiles were analyzed using the Affymetrix HG-U133+PM Array Plate (Affymetrix, Santa Clara, CA). Three biological replicates of each cell line were assayed. The probes were labeled, hybridized and scanned according to the manufacturer's instructions. The data were extracted through Expression Console (Affymetrix, Santa Clara, California). Data normalization and analysis were performed in GeneSpring GX software as mentioned above.

Quantitative real-time PCR (qRT-PCR)

For the miRNA, the reverse transcription of RNA was conducted using the miScript Reverse Transcription Kit. The cDNA serves as the template for real-time PCR analysis using a miScript Primer Assay in combination with the miScript SYBR Green PCR Kit (Qiagen, Germany). For the mRNA, the total RNA was reversed transcribed using the OneStep RT-PCR Kit. Then the cDNA served as the template for the real-time PCR analysis using the QuantiTect Primer Assay (Qiagen, Germany). The PCR was conducted using a 7900HT Sequence

Detection System (Applied Biosystems, Austin, TX, USA). All of the reactions were run in triplicate. The relative expression levels of the different miRNAs were calculated based on U6 RNA levels and multiplied by 10^2. The relative expression levels of the mRNAs were calculated based on GAPDH levels and multiplied by 10^2.

Statistical analysis

Each experiment was repeated at least three times. The continuous variables were expressed as the mean values±standard deviations (SD). The Student's *t*-test was used to analyze the different genes between cell lines with different drug sensitivities. A $P<0.05$ was considered statistically significant. All of the statistical analyses, including the normalization of data, choosing the differentially expressed genes and hierarchical clustering, were processed through GeneSpring GX Software.

MiRNAs targets prediction

The target genes of the miRNAs were predicted through miRGen, which incorporates algorithms including TargetScan, miRanda and PicTar (http://www.diana.pcbi.upenn.edu/cgi-bin/miRGen).

Gene ontology and pathway analysis

The gene ontology and pathway analysis was conducted through GenMAPP2 (http://www.genmapp.org/). The permutated *P*-value cutoff was set below 0.05, and the Z-score was set higher than 2.

Results

The growth inhibition effects of HCPT on human gastric cancer cells

Six human gastric cancer cell lines (BGC-823, SGC-7901, MGC-803, HGC-27, NCI-N87, and AGS) were used for the HCPT sensitivity analysis. The SRB assay showed a significant difference in sensitivities among these six cell lines at each concentration of HCPT. The concentration leading to 50% growth inhibition (GI50) was significantly different between the BGC-823 and AGS cell lines (Figure 1A). When exposed to HCPT at 1.0 μg/mL (the human peak plasma concentration), the AGS cells died, while the BGC-823, SGC-7901, MGC-803, HGC-27, and NCI-N87 cell lines displayed 24%, 36%, 65%, 72%, and 90% growth inhibition respectively, compared to the control (Figure 1B). In terms of percentage growth inhibition, there were significant differences ($P<0.05$) among the six cell lines, and they could be sorted according to their sensitivity to HCPT in ascending order: BGC-823, SGC-7901, MGC-803, HGC-27, NCI-N87, and AGS.

MiRNA expression profiling in HCPT-resistant versus HCPT-sensitive gastric cancer cell lines

To investigate the role of miRNAs in intrinsic HCPT resistance, we conducted a comprehensive miRNA expression profiling of the six gastric cancer cell lines using the Agilent Human miRNA Microarray V2.0. This microarray contains 15744 probes representing 723 human miRNAs. After quantile normalization and filtering on flags (present or marginal), 279 miRNAs were selected for further analysis. ANOVA analysis revealed that 137 miRNAs were differentially expressed between the BGC-823 (HCPT-resistant) and AGS (HCPT-sensitive) cell lines with a more than 1.5-fold change ($P<0.05$) (Figure 2A). Further exploration of the other cell lines that had intermediate HCPT sensitivity (SGC-7901, MGC-823, HGC-27, and NCI-N87) revealed 25 miRNAs whose expression levels were also intermediate. Compared with their sensitive counterparts, 12 miRNAs were downregulated and the rest were upregulated in HCPT-resistant gastric cancer cells (Table 1). These results indicated that these 25 miRNAs might play important roles in intrinsic HCPT resistance. Hierarchical cluster analysis based on the expression patterns of these 25 miRNAs accurately separated the HCPT-sensitive cell line from the HCPT-resistant cell lines (Figure 2B).

To validate the miRNA microarray results, 12 deregulated miRNAs were randomly chosen for analysis by qRT-PCR. These miRNAs were miR-196a, miR-365, miR-424, miR-99b,

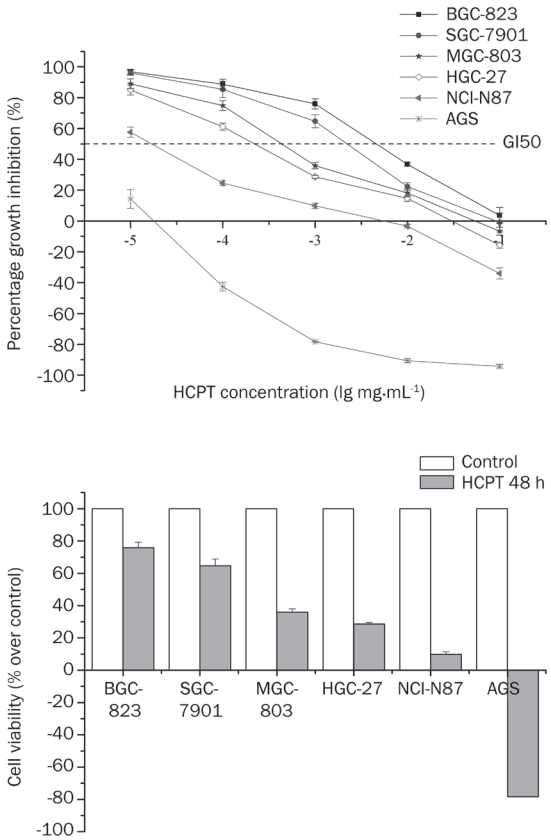

Figure 1. Sensitivity of six gastric cancer cell lines to HCPT. (A) Gastric cancer cells were incubated with HCPT (five different concentrations: 10^{-1}, 10^{-2}, 10^{-3}, 10^{-4}, 10^{-5} mg/mL) for 48 h, and the viability was evaluated as described in the Materials and Methods section. The experiments were performed in triplicate. The six cell lines showed different sensitivities at each HCPT concentration. The concentrations that resulted in 50% growth inhibition (GI50) were significantly different between the cell lines. (B) At the human peak plasma concentration (1.0 μg/mL), the AGS cells experienced cell death, while the other cells proliferated at different rates.

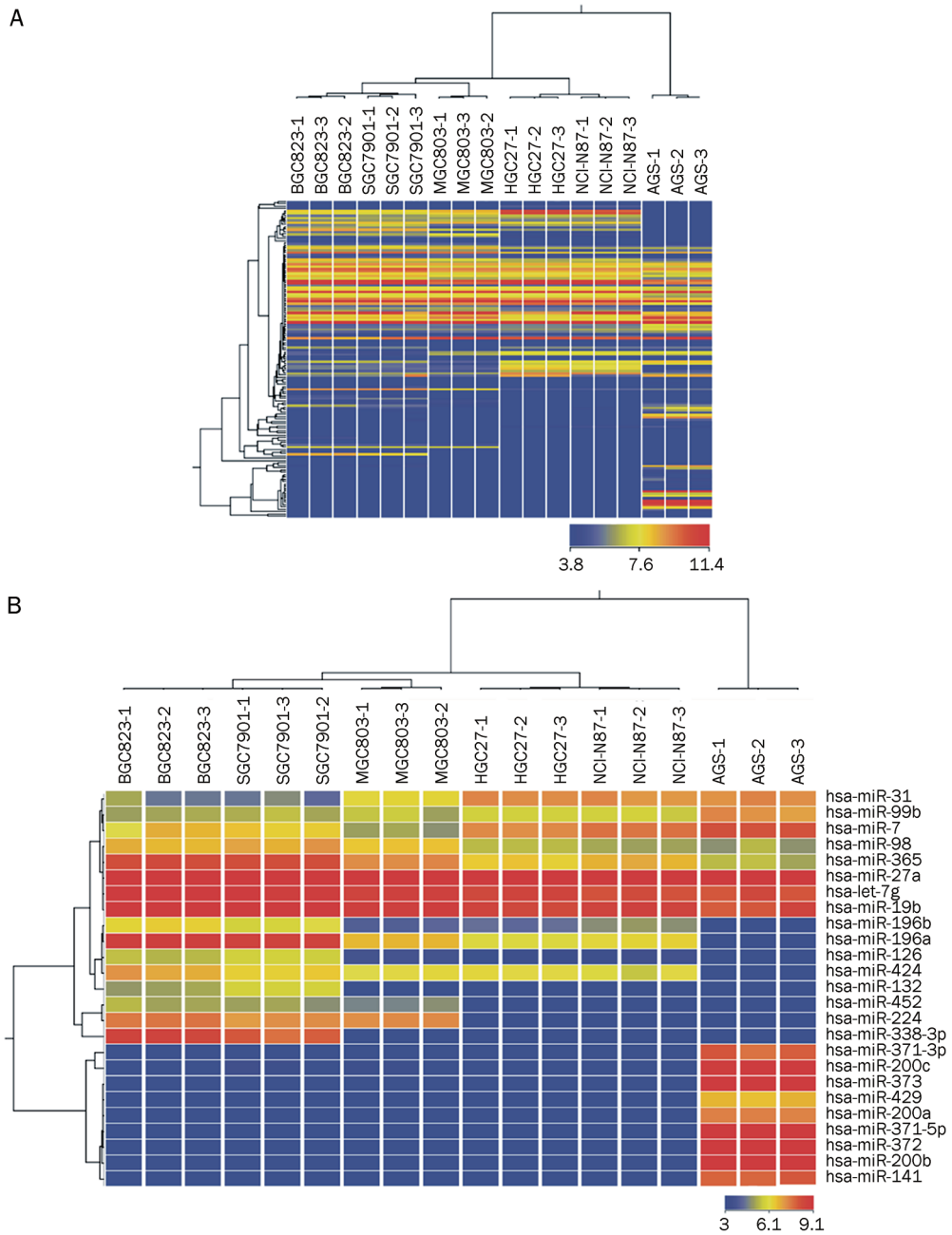

Figure 2. The miRNA expression signature in HCPT-resistant versus HCPT-sensitive gastric cancer cells. The tree was constructed using hierarchical clustering based on the $\log_2$ transformation of the normalized probe signal intensity. (A) The heatmap was based on 137 miRNAs that were differentially expressed between the most resistant cell line BGC-823 and the most sensitive cell line AGS. (B) The heatmap was based on 25 differentially expressed miRNAs, the expressions of which correlated with HCPT sensitivity.

miR-98, miR-224, miR-338-3p, miR-141, miR-200a, miR-200b, miR-372, and miR-373. The qRT-PCR results confirmed the miRNA microarray results (Figure 3). MiR-196a, miR-365, miR-424, miR-99b, and miR-98 were expressed in both the HCPT-sensitive cell lines and the HCPT-resistant cell lines. Cells with higher expression levels of miR-196a, miR-365, miR-424, and miR-98 or lower levels of miR-99b were less sensitive to HCPT. MiR-224 and miR-338-3p were only expressed in HCPT-resistant cells, and miR-141, miR-200a, miR-200b, miR-372, and miR-373 were only expressed in HCPT-sensitive cells. These results indicated that the sensitivity to HCPT of human gastric cancer cell lines may be interfered by the intrinsic expression levels of miRNAs.

Identification of mRNA expression profiles in HCPT-resistant versus HCPT-sensitive gastric cancer cell lines

To explore the impact of gene expression on HCPT sensitivity, we further studied the mRNA expression patterns of these human gastric cancer cell lines using the Affymetrix HG-U133+PM Array Plate. In total, 307 genes were identified as differentially expressed between the HCPT-resistant cell lines and the HCPT-sensitive cell lines. The six cell lines clustered into different groups based on the expression profiles of the 307 genes (Figure 4A). Among these genes, 33 had been reported to be involved in cancer development, cell progression and/or chemoresponse (Figure 4B). Some of the genes are apoptosis-related genes (BAX, TIAL1, TPD52L1, BAG, SP3,

Table 1. miRNAs correlated to intrinsic HCPT resistance in gastric cancer cells.

miRNA	Regulation in resistant cells	Chromosome location
miR-132	Up	17p13.3
miR-224	Up	Xq28
miR-338-3p	Up	17q25.3
miR-452	Up	Xq28
miR-141	Down	12p13.31
miR-200a	Down	1p36.33
miR-200b	Down	1p36.33
miR-200c	Down	12p13.31
miR-371-3p	Down	19q13.41
miR-371-5p	Down	19q13.41
miR-372	Down	19q13.41
miR-373	Down	19q13.41
miR-429	Down	1p36.33
let-7g	Up	3p21.1
miR-126	Up	9q34.3
miR-196a	Up	17q21.32 12q13.13
miR-196b	Up	7p15.2
miR-19b	Up	13q31.3 Xq26.2
miR-27a	Up	19p13.12
miR-31	Down	9p21.3
miR-365	Up	16p13.12 17q11.2
miR-424	Up	Xq26.3
miR-7	Down	9q21.32 15q26.1 19p13.3
miR-98	Up	Xp11.22
miR-99b	Down	19q13.33

Table 2. The miRNA-mRNA regulation pairs.

Regulation in resistant cells	miRNA	Target genes
miRNA up-target down	let-7g	BTG2, VSNL1, MAP4K4, SLC35D2, CHD7, FRAS1, EPHA4, PGM2L1
	has-mir-19b	ADD3, EFNB2, STRN3, GAD1, SPHK2, VPS37B, TP53INP1, PGM2L1, BMPR2
	has-mir-132	BTG2, SOX2
	has-mir-224	SOCS2, JAG1, AMIGO2
	has-mir-338	HIATL1
	has-mir-365	ADD3, KALRN
	has-mir-424	ACTR1A, PSME3, BTG2, EFNB2, PDLIM5, PTPN3, SLC12A2, EPHA1, PIK3R1, ATF7IP2, SEH1L, AXIN2, WDR22, KALRN, PGM2L1
	has-mir-452	EIF2S1
	has-mir-98	BTG2, VSNL1, MAP4K4, SLC35D2, CHD7, FRAS1, EPHA4,PGM2L1
miRNA down-target up	has-mir-200a	OLFM1
	has-mir-200b	MITF, GABARAPL2, SLC38A2, FBXL16, NOG
	has-mir-200c	MITF, GABARAPL2, SLC38A2, FBXL16, NOG
	has-mir-141	OLFM1, GLRX, GABARAPL2, HOXA11, BCOR
	has-mir-429	MITF, PCTK1, GABARAPL2, SLC38A2, FBXL16, NOG, SP3
	has-mir-7	SLC38A2
	has-mir-31	OSBP2
	has-mir-372	SMAD2, SUV39H1
	has-mir-373	SMAD2, SUV39H1

RPS27L, PLSCR3, TP53INP1, *etc*), cell division-related genes (MCM2, *etc*), cell adhesion/migration-related genes (TIMP2, VSNL1, FUT8, TBX3, *etc*) and checkpoint genes (RAD1, *etc*).

To validate the microarray data, nine differentially expressed genes were randomly chosen for qRT-PCR. The results showed that these genes were differentially expressed between different cell lines (Figure 5). Gene ontology and pathway enrichment analysis of these 307 genes demonstrated that two significant pathways ($P<0.05$) were involved: the irinotecan pathway and the IL-3 pathway. The irinotecan pathway is very important for the biotransformation of CPTs, and the IL-3 pathway is related to the proliferation and differentiation of hematopoietic cells. In addition, we examined the focal adhesion pathway and the cell cycle pathway and achieved a *P*-value of 0.1.

Integrated analysis of deregulated miRNAs and mRNAs

MiRNAs modulate gene expression through inducing mRNA degradation or translational repression, or both. Therefore, we further performed an integrated analysis of miRNA and mRNA expression patterns in the six gastric cancer cell lines. The target genes of the 25 deregulated miRNAs were predicted using the intersections of PicTar and TargetScanS in miRgen (http://www.diana.pcbi.upenn.edu/cgi-bin/miRGen) to reduce the chance of false positives. For each deregulated miRNA, 13 to 600 target genes were predicted. As was expected, many known chemoresistant targets were found among the candidates, including CDKN1B (p27), ANXA1 (p35), PDCD4, UGT1A1, TOP1, CYP3A4, ABCG2 (BCRP), CHEK1, TDP1, BCL-2, and SUMO1. The pathways of these predicted target genes were enriched using GenMAPP 2. We also identified 47 biological pathways (permuted *P*-value<0.05), including classical cancer-related pathways (EGFR1, Wnt signaling, MAPK signaling, C-kit receptor, focal adhesion pathways, *etc*); drug metabolism-associated pathways (cytochrome P450, *etc*) and cell apoptosis-related pathways (S1P signaling pathway, *etc*). Fifty percent of these 47 biological pathways had been reported to be implicated in carcinogenesis or chemoresponse (Figure 6A). Moreover, the gene ontology terms of these target genes included cell cycle, cell proliferation, G1/S transition of the mitotic cell cycle, negative regulation of programmed cell death, cell adhesion, positive regulation of cell motility, cell-matrix adhesion and regulation of DNA repair (Figure 6B). These results indicated that the cells were not sensitive to HCPT partially due to their

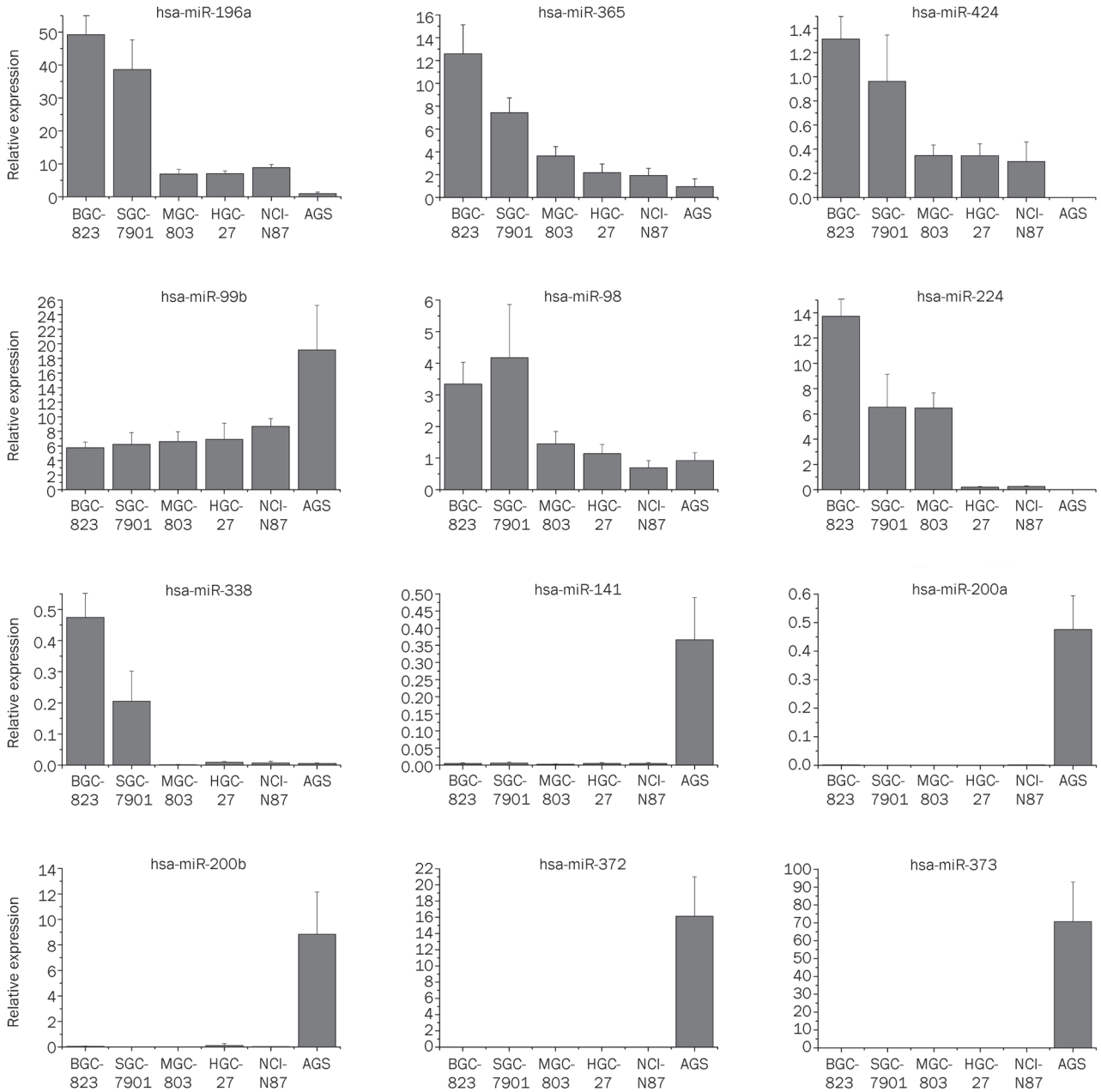

Figure 3. Validation of the differentially expressed miRNAs by real-time PCR. As described in the Materials and Methods, real-time PCR was performed in triplicate, and the relative expression levels of different miRNAs were calculated based on U6 RNA levels and multiplied by 10^2. MiR-196a, -365, -424, -98, -338, and -224 were markedly upregulated in the resistant cells, but not in the sensitive cells, while miR-99b, -141, -200a, -200b, -372, and -373 were markedly downregulated.

increased proliferation, anti-apoptosis and/or migration abilities.

Finally, we deciphered the relationship between the deregulated miRNAs and the mRNAs. Among the 307 differentially expressed mRNAs, 50 genes are the predicted targets of the 25 differential miRNAs, forming 78 relation pairs (Table 2). These 50 genes included tumor suppressors, protein kinases, helicases, histone methyltransferases, transcription factors and proteasome-related proteins. The tumor suppressor gene BTG2, which inhibits proliferation and promotes the apoptosis of gastric cancer cells, was targeted by the highly-expressed miRNAs let-7g, miR-98, and miR-132 in HCPT-resistant cells. Another tumor suppressor gene VSNL1, which inhibits cell migration, was also targeted by let-7g and miR-98. TP53INP1, which promotes TP53 phosphorylation on "Ser-46" and subsequent apoptosis, was predicted to be a target of miR-19b, an upregulated miRNA in HCPT-resistant cells. In addition, we found the components of cancer-related pathways such as SMAD2 and PIK3R1 in the relation pairs. Our systematic analysis revealed that approximately 1.3% of the predicted

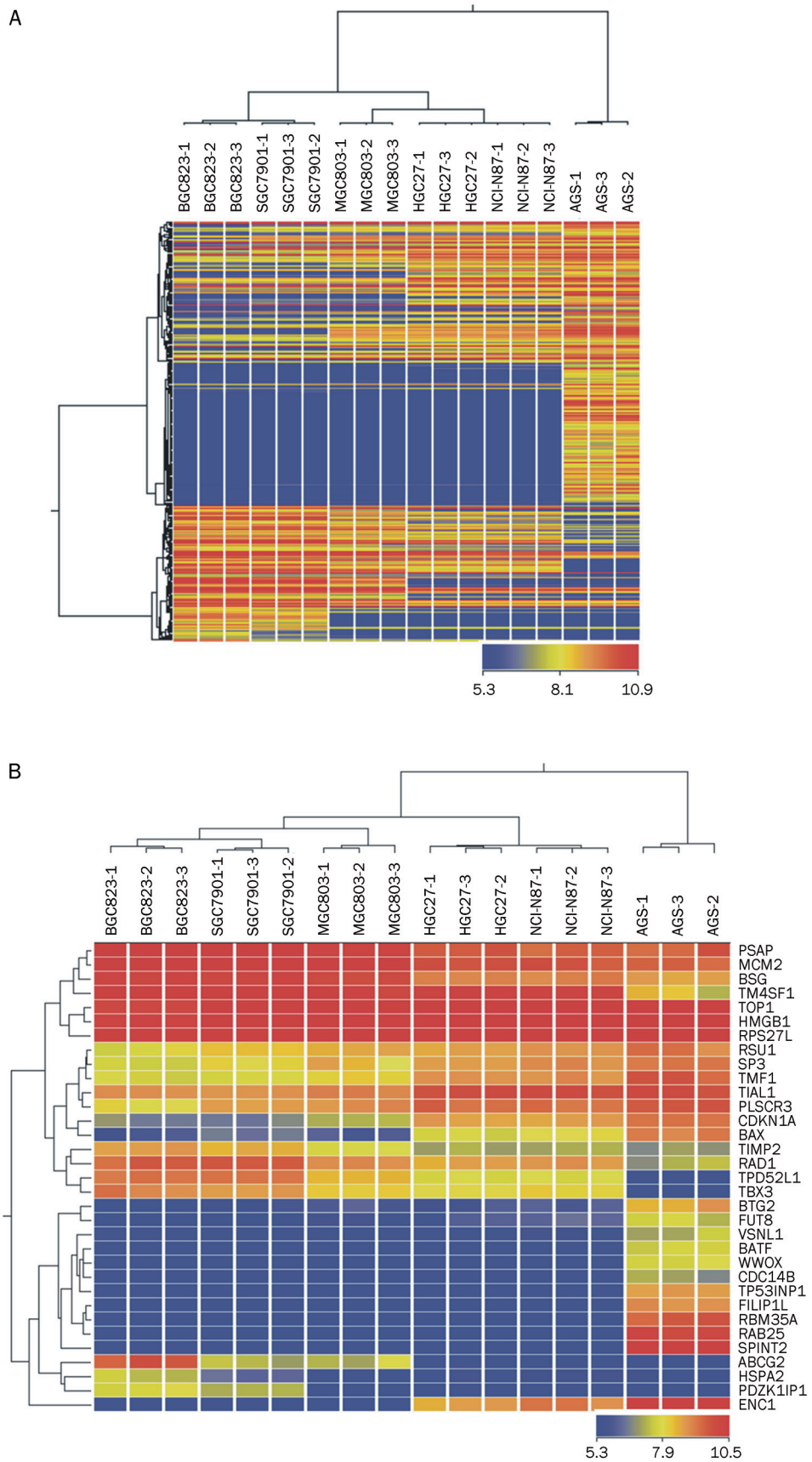

Figure 4. The mRNA expression signatures in HCPT-resistant versus HCPT-sensitive gastric cancer cells. The tree was based on the $\log_2$ transformation of the normalized probe signal intensity using hierarchical clustering. (A) The hierarchical clustering was based on 307 differentially expressed mRNAs whose expression levels were deregulated in HCPT-resistant cell lines. (B) The hierarchical clustering was based on 33 differentially expressed genes that were reported to be involved in cancer progression or chemoresponses.

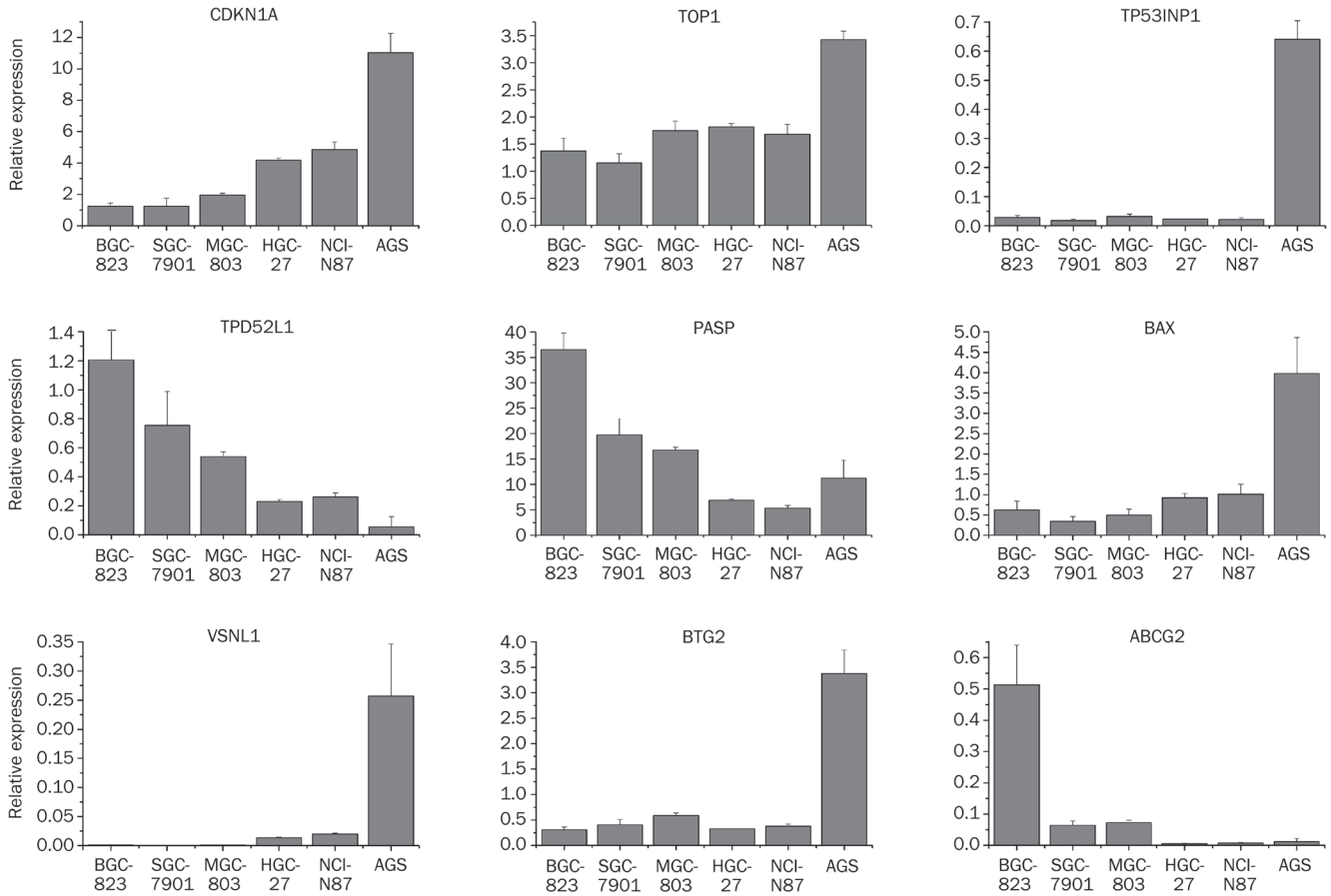

Figure 5. Validation of nine differentially expressed mRNAs. We performed quantitative real-time PCR in triplicate, as described in the Materials and methods, and the relative expression levels of the different mRNAs were calculated based on GAPDH levels and multiplied by 10^2.

miRNA targets formed the reciprocal "up-down" or "down-up" expression relationships with miRNAs. On the one hand, miRNAs modulate gene expression through both mRNA degradation and translational repression mechanisms, and on the other hand, miRNA-mRNA regulatory networks are highly complex.

Discussion

Cancer drug resistance can be classified into acquired and intrinsic resistance. Acquired drug resistance is induced during the process of drug treatment, while intrinsic resistance is the inherent characterization of the original cells before drug treatment. For studying acquired resistance, drug-induced resistant cell lines are used as a model, and the acquired resistance mechanism is determined by comparing the characterization before and after drug treatment. However, for studying intrinsic resistance, untreated original cells are usually used for drug sensitivity assays, and these results indicate the original cell's drug response and give indications for clinical drug treatment. Previous studies of cancer drug resistance have mainly focused on DNA, mRNA and protein levels, including mutations, copy number variations, epigenetic changes at the DNA level and deregulation at the mRNA and protein levels[16]. Different cells appear to achieve the same end result by modulating a definitive number of genes through different mechanisms[17]. Among these mechanisms, miRNA is a newly identified mechanism, and this field is potentially promising. The NCI-60s, a panel of 60 diverse human cancer cell lines established by the National Cancer Institute, have been profiled for their miRNA expression[18]. Using the expression data of the NCI-60 and their corresponding drug sensitivities, miRNA profiles were developed to represent the sensitivities to individual chemotherapeutic agents[19]. However, gastric cancer cell lines were not included in the NCI-60. Therefore, in this study, we examined the role of miRNAs in the intrinsic drug resistance of gastric cancer cell lines. Our results will benefit both the understanding of drug resistance mechanisms and the prediction of clinical drug responses.

First, to explore this new field, we examined the miRNA expression profiles of six gastric cancer cell lines. We identified 25 deregulated miRNAs, and the results were confirmed by qRT-PCR. The miRNA expression pattern was efficient to separate the six cell lines in terms of HCPT sensitivity. Interestingly, some of the deregulated miRNAs were from the same family, and they may produce synergistic effects in mediating the resistant phenotype. Among the 12 downregulated miR-

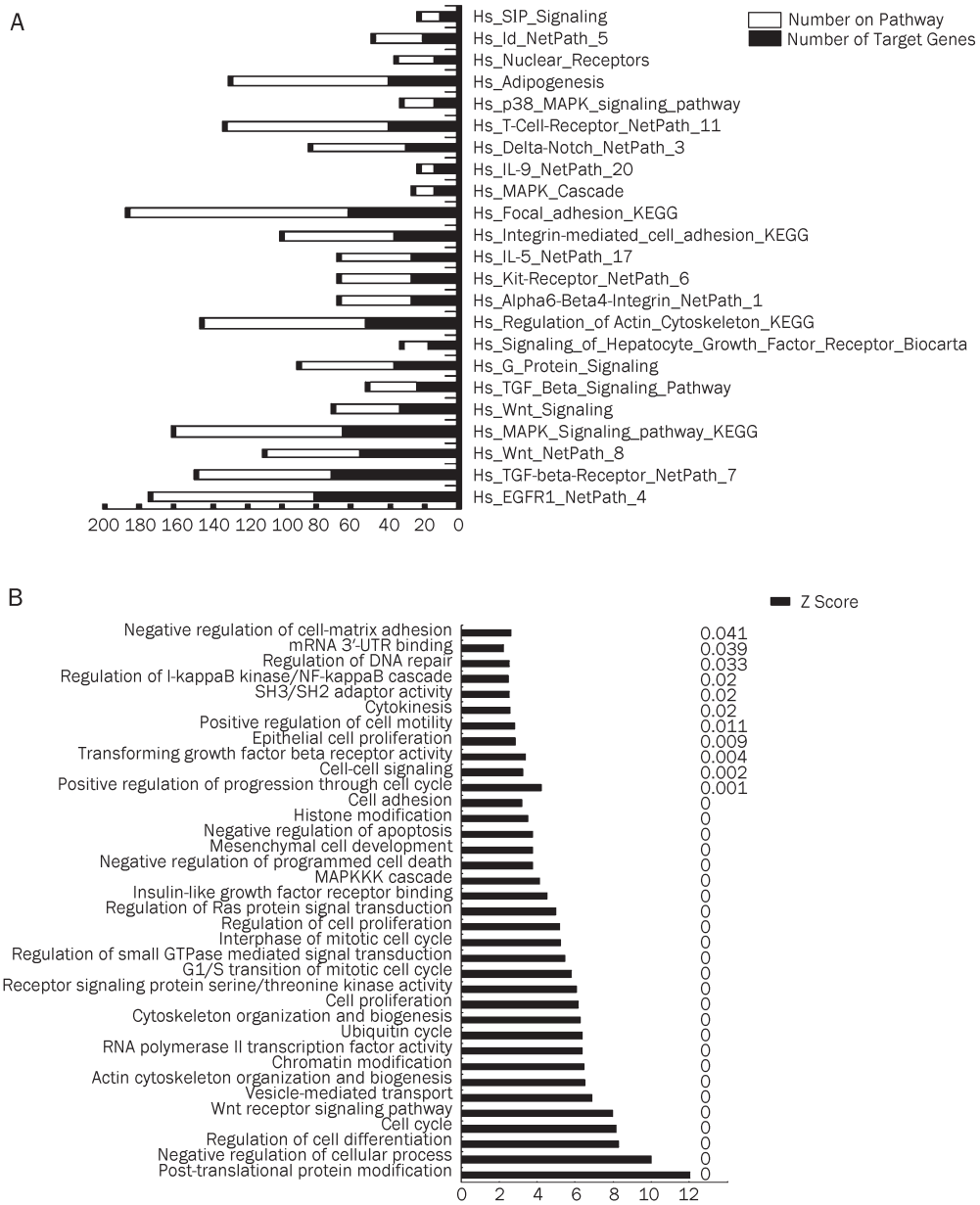

Figure 6. Gene ontology and pathway enrichment of predicted miRNA targets. (A) Significant pathways were enriched by GenMAPP2. The listed pathways are related to cell apoptosis or proliferation and have a *P*-value less than 0.05. The black column represents the number of target genes located in the pathway, while the white column represents the number of total genes located in the pathway. (B) Gene ontology was also enriched by GenMAPP2. The results indicated that these differential miRNAs may regulate genes involved in cell adhesion, cell proliferation and programmed cell death. The Z-score represents the enrichment extent, and the number listed beside each gene ontology term is the *P*-value.

NAs, the miR-200 family was only expressed in the HCPT-sensitive cell line AGS. The miR-200 family inhibits epithelial-mesenchymal transition and cancer cell migration through the direct targeting of E-cadherin transcriptional repressors ZEB1 and ZEB2[20]. In addition, the overexpression of miR-141 in the gastric cancer cell lines was correlated with the inhibition of cell proliferation[21]. MiR-7 inhibits the epidermal growth factor receptor and the Akt pathway in cancer cell lines (lung, breast, and glioblastoma), inducing cell cycle arrest and cell death[22, 23]. MiR-31 inhibits breast cancer metastasis and was shown to be downregulated in gastric cancer tissues[24]. We predicted that the downregulation of these miRNAs could promote cancer cell migration and cell proliferation, thus impairing the HCPT-induced responses. Among the 13 upregulated miRNAs, miR-338 and miR-126 were identified as the signature miRNAs for predicting the survival of gastric cancer patients[25]. MiR-98 and let-7g may play roles in both the apoptotic and cell-proliferation pathways[26], and tumor-suppressor gene FUS1 is a target of miR-98[27]. MiR-196a promotes the oncogenic phenotype of colorectal cancer cells by activating the AKT signaling pathway and promoting cancer cell detachment, migration and invasion[28]. MiR-27a functions as an oncogene in gastric adenocarcinoma by targeting an anti-proliferative protein prohibitin[29], and downregulation of miR-27a could reverse the multidrug resistance of esophageal cancer[30]. The upregulation of these miRNAs may strengthen cell proliferation or reduce apoptosis and therefore render cells insensitive to HCPT. Although no related reports have indicated the involvement of the other deregulated miRNAs in carcinogenesis and chemoresponses, we believe a detailed

study on these miRNAs is warranted.

Gene ontology and pathway enrichment analysis based on the 307 differentially expressed mRNAs revealed only two significant pathways with *P*-values<0.05, including the irinotecan pathway and the IL-3 pathway. In the irinotecan pathway, we found that ABCG2 was downregulated in the HCPT-resistant cell lines; this result was in agreement with a previous report that the ABCG2 protein mediated drug efflux from resistant cells and was directly involved in cellular resistance to SN38 (the active metabolite of irinotecan)[31]. We also found that UGT1A10 and UGT1A6, which catalyze the glucuronidation of SN-38, were only expressed in HCPT-sensitive cell lines; this result disagreed with the putative view that SN-38 glucuronidation could lead to cellular resistance to irinotecans. Therefore, these results indicated that the sensitivity of cells to HCPT was affected by multiple factors that contribute simultaneously.

To study the involvement of miRNA-mediated regulation of gene expression in HCPT resistance, we analyzed whether the 307 genes were the predicted targets of the 25 deregulated miRNAs, and finally, we found 50 genes and 78 relation pairs between them. However, we could not examine the enriched pathways of these 50 genes to analyze them individually. Some of these genes are tumor suppressor genes involved in regulating cancer cell proliferation or apoptosis. Because miRNAs are predicted to target multiple unrelated genes that are not coexpressed and one target gene is predicted to be targeted by multiple miRNAs, it is not surprising that miRNA expression levels do not tend to be strongly correlated with particular target transcripts. This phenomenon was also presented in Blower's study on the NCI-60[18].

This study was based on six gastric cancer cell lines, and we gained some information for intrinsic drug resistance, but more cell lines and clinical samples will need to be analyzed in a future study.

Conclusions

Our study demonstrated that the intracellular levels of miRNAs may interfere the chemoresponses of gastric cancer cells partially due to the regulation of cancer cell proliferation, migration and cell death pathways. Hierarchical clustering based on the expression patterns of 25 miRNAs showed that cell groupings were generally consistent with HCPT sensitivity. The mRNA signature we observed was also informative for discriminating cell lines with different sensitivities to HCPT. In addition, we found a slightly lower correlation between the expression patterns of miRNAs and those of their predicted target transcripts. Our study provides a resource for integrated chemo-genomic studies aimed to elucidate the molecular markers for personalized therapy and to understand the mechanisms of HCPT resistance.

Acknowledgements

This research was supported by grants from the National High-Tech Program "863" (2006AA020704).

Author contribution

Xue-mei WU designed the study, performed the SRB assay, microarray experiments and real-time PCR experiments, analyzed the data and wrote the manuscript. Li ZHU, Xian-xin MENG, and Xiao-na ZHANG performed the microarray experiments and generated the microarray data. Xiang-qiang SHAO, Shi-xu LIU, and Jian LIN performed the miRNA prediction and analysis. Hua-sheng XIAO coordinated the study and reviewed the manuscript. All of the authors have read and approved the final manuscript.

References

1 Crew KD, Neugut AI. Epidemiology of gastric cancer. World J Gastroenterol 2006; 12: 354–62.
2 Liu LF. DNA topoisomerase poisons as antitumor drugs. Annu Rev Biochem 1989; 58: 351–75.
3 Lippert TH, Ruoff HJ, Volm M. Intrinsic and acquired drug resistance in malignant tumors. The main reason for therapeutic failure. Arzneimittelforschung 2008; 58: 261–4.
4 Lage H. An overview of cancer multidrug resistance: a still unsolved problem. Cell Mol Life Sci 2008; 65: 3145–67.
5 Gottesman MM. Mechanisms of cancer drug resistance. Annu Rev Med 2002; 53: 615–27.
6 Mimeault M, Hauke R, Batra SK. Recent advances on the molecular mechanisms involved in the drug resistance of cancer cells and novel targeting therapies. Clin Pharmacol Ther 2008; 83: 673–91.
7 Beretta GL, Perego P, Zunino F. Mechanisms of cellular resistance to camptothecins. Curr Med Chem 2006; 13: 3291–305.
8 Saleem A, Edwards TK, Rasheed Z, Rubin EH. Mechanisms of resistance to camptothecins. Ann N Y Acad Sci 2000; 922: 46–55.
9 Rasheed ZA, Rubin EH. Mechanisms of resistance to topoisomerase I-targeting drugs. Oncogene 2003; 22: 7296–304.
10 Lee YS, Dutta A. MicroRNAs: small but potent oncogenes or tumor suppressors. Curr Opin Investig Drugs 2006; 7: 560–4.
11 Caldas C, Brenton JD. Sizing up miRNAs as cancer genes. Nat Med 2005; 11: 712–4.
12 Sassen S, Miska EA, Caldas C. MicroRNA: implications for cancer. Virchows Arch 2008; 452: 1–10.
13 Calin GA, Sevignani C, Dumitru CD, Hyslop T, Noch E, Yendamuri S, *et al*. Human microRNA genes are frequently located at fragile sites and genomic regions involved in cancers. Proc Natl Acad Sci U S A 2004; 101: 2999–3004.
14 Bertino JR, Banerjee D, Mishra PJ. Pharmacogenomics of microRNA: a miRSNP towards individualized therapy. Pharmacogenomics 2007; 8: 1625–7.
15 Wu XM, Xiao HS. miRNAs modulate the drug response of tumor cells. Sci China C Life Sci 2009; 52: 797–801.
16 Blower PE, Chung JH, Verducci JS, Lin S, Park JK, Dai Z, *et al*. MicroRNAs modulate the chemosensitivity of tumor cells. Mol Cancer Ther 2008; 7: 1–9.
17 Fojo T. Multiple paths to a drug resistance phenotype: mutations, translocations, deletions and amplification of coding genes or promoter regions, epigenetic changes and microRNAs. Drug Resist Updat 2007; 10: 59–67.
18 Blower PE, Verducci JS, Lin S, Zhou J, Chung JH, Dai Z, *et al*. MicroRNA expression profiles for the NCI-60 cancer cell panel. Mol Cancer Ther 2007; 6: 1483–91.
19 Salter KH, Acharya CR, Walters KS, Redman R, Anguiano A, Garman KS, *et al*. An integrated approach to the prediction of

chemotherapeutic response in patients with breast cancer. PLoS ONE 2008; 3: e1908.
20 Korpal M, Lee ES, Hu G, Kang Y. The miR-200 family inhibits epithelial-mesenchymal transition and cancer cell migration by direct targeting of E-cadherin transcriptional repressors ZEB1 and ZEB2. J Biol Chem 2008; 283: 14910–4.
21 Du Y, Xu Y, Ding L, Yao H, Yu H, Zhou T, *et al*. Down-regulation of miR-141 in gastric cancer and its involvement in cell growth. J Gastroenterol 2009; 44: 556–61.
22 Kefas B, Godlewski J, Comeau L, Li Y, Abounader R, Hawkinson M, *et al*. microRNA-7 inhibits the epidermal growth factor receptor and the Akt pathway and is down-regulated in glioblastoma. Cancer Res 2008; 68: 3566–72.
23 Webster RJ, Giles KM, Price KJ, Zhang PM, Mattick JS, Leedman PJ. Regulation of epidermal growth factor receptor signaling in human cancer cells by microRNA-7. J Biol Chem 2009; 284: 5731–41.
24 Zhang Y, Guo J, Li D, Xiao B, Miao Y, Jiang Z, *et al*. Down-regulation of miR-31 expression in gastric cancer tissues and its clinical significance. Med Oncol 2010; 27: 685–9.
25 Li X, Zhang Y, Zhang Y, Ding J, Wu K, Fan D. Survival prediction of gastric cancer by a seven-microRNA signature. Gut 2010; 59: 579–85.
26 Wang Y, Lee CG. MicroRNA and cancer--focus on apoptosis. J Cell Mol Med 2009; 13: 12–23.
27 Du L, Schageman JJ, Subauste MC, Saber B, Hammond SM, Prudkin L, *et al*. miR-93, miR-98, and miR-197 regulate expression of tumor suppressor gene FUS1. Mol Cancer Res 2009; 7: 1234–43.
28 Schimanski CC, Frerichs K, Rahman F, Berger M, Lang H, Galle PR, *et al*. High miR-196a levels promote the oncogenic phenotype of colorectal cancer cells. World J Gastroenterol 2009; 15: 2089–96.
29 Liu T, Tang H, Lang Y, Liu M, Li X. MicroRNA-27a functions as an oncogene in gastric adenocarcinoma by targeting prohibitin. Cancer Lett 2009; 273: 233–42.
30 Zhang H, Li M, Han Y, Hong L, Gong T, Sun L, *et al*. Down-regulation of miR-27a might reverse multidrug resistance of esophageal squamous cell carcinoma. Dig Dis Sci 2010; 55: 2545–51.
31 Candeil L, Gourdier I, Peyron D, Vezzio N, Copois V, Bibeau F, *et al*. ABCG2 overexpression in colon cancer cells resistant to SN38 and in irinotecan-treated metastases. Int J Cancer 2004; 109: 848–54.

Acta Pharmacologica Sinica (2011) 32: 270–278
 1671-4083/11 $32.00
www.nature.com/aps

Original Article

GC-TOF/MS-based metabolomic profiling of estrogen deficiency-induced obesity in ovariectomized rats

Bo MA[1, 2, #], Qi ZHANG[2, #], Guang-ji WANG[1, *], Ji-ye A[1, *], Di WU[3], Ying LIU[2], Bei CAO[1], Lin-sheng LIU[1], Ying-ying HU[2], Yong-lu WANG[2], Ya-ya ZHENG[2]

[1]Key laboratory of drug metabolism and pharmacokinetics, China Pharmaceutical University, Nanjing 210009, People's Republic of China; [2]Nanjing Sino-US Cancer Research Center, School of Pharmaceutical Sciences, Nanjing University of Technology, Nanjing 210009, China; [3]Division of Clinical Pharmacology and Therapeutics, The Children's Hospital of Philadelphia; Kinetic Modeling and Simulation Core, Institute of Translational Medicine and Therapeutics, University of Pennsylvania, Philadelphia, PA 19104, USA

Aim: To explore the alteration of endogenous metabolites and identify potential biomarkers using metabolomic profiling with gas chromatography coupled a time-of-flight mass analyzer (GC/TOF-MS) in a rat model of estrogen-deficiency-induced obesity.
Methods: Twelve female Sprague-Dawley rats six month of age were either sham-operated or ovariectomized (OVX). Rat blood was collected, and serum was analyzed for biomarkers using standard colorimetric methods with commercial assay kits and a metabolomic approach with GC/TOF-MS. The data were analyzed using multivariate statistical techniques.
Results: A high body weight and body mass index inversely correlated with serum estradiol (E2) in the OVX rats compared to the sham rats. Estrogen deficiency also significantly increased serum total cholesterol, triglycerides, and low-density lipoprotein cholesterol. Utilizing GC/TOF-MS-based metabolomic analysis and the partial least-squares discriminant analysis, the OVX samples were discriminated from the shams. Elevated levels of cholesterol, glycerol, glucose, arachidonic acid, glutamic acid, glycine, and cystine and reduced alanine levels were observed. Serum glucose metabolism, energy metabolism, lipid metabolism, and amino acid metabolism were involved in estrogen-deficiency-induced obesity in OVX rats.
Conclusion: The series of potential biomarkers identified in the present study provided fingerprints of rat metabolomic changes during obesity and an overview of multiple metabolic pathways during the progression of obesity involving glucose metabolism, lipid metabolism, and amino acid metabolism.

Keywords: metabolomics; obesity; gas chromatography coupled a time-of-flight mass analyzer; estrogen deficiency

Acta Pharmacologica Sinica (2011) 32: 270–278; doi: 10.1038/aps.2010.196

Introduction

Obesity is a medical condition in which excess body fat has accumulated to such an extent[1] that it becomes linked to several common diseases, including insulin resistance[2], cardiovascular disease[3], stroke[4], and certain cancers[5–8]. Apart from the genetic, environmental, and nutritional factors involved in the occurrence of obesity, endogenous estrogens play an important role in the regulation of body weight and obesity[9, 10]. The decrease in estrogen levels experienced by women after menopause could be associated with an increased risk of obesity and a series of devastating diseases[11, 12]. The relationship between obesity and endogenous estrogen remains unclear. Similar to leptin, estrogens regulate body weight and energy metabolism[13]. Moreover, ovariectomy-induced adiposity is associated with decreased energy expenditure, adipose tissue expansion, and hepatic steatosis[14]. Estrogen receptors alpha and beta play essential roles in controlling the energy metabolism pathways, body fat distribution, and normal body weight.

Estrogen replacement therapy (ERT), the medical administration of estrogen, prevents obesity and estrogen-deficiency-induced complications[15, 16]. In addition, estrogen has favorable effects on the lipid profile, significantly increasing high-density lipoprotein cholesterol (HDL-C) and reducing low-density lipoprotein cholesterol (LDL-C). ERT helps to relieve the cardiovascular diseases caused by obesity by decreasing cardiac mortality, improving endothelial function, and reducing LDL accumulation[17, 18]. However, the safety of ERT is controversial, although appropriate amounts of estrogen

# The first two authors contributed equally to this work.
* To whom correspondence should be addressed.
E-mail zhang_relax@hotmail.com (Guang-ji WANG);
jiye_2005@yahoo.com.cn (Ji-ye A)
Received 2010-08-08 Accepted 2010-10-28

moderate estrogen-deficiency-induced obesity in postmenopausal women. The extensive use of estrogens results in a significant increase in the incidence of breast cancer[19] and ovarian cancer[20] in postmenopausal women. In addition, an increased risk of deep vein thrombosis (DVT)[21] and dementia has been reported when estrogen alone is used in postmenopausal women aged 65 years or older based on data from the Women's Health Initiative (WHI)[22]. Therefore, an understanding of the comprehensive metabolic disorders and metabolic syndromes of estrogen-deficiency-induced obesity has become a topic of interest.

Metabonomics/metabolomics is defined as "the quantitative measurement of the dynamic multiparametric responses of a living system to pathophysiological stimuli or genetic modification"[23]. It is a novel "-omics" discipline that monitors alterations in the levels of endogenous metabolites in response to biological stimuli using modern spectroscopic techniques and statistical approaches[24]. Compared with genomics, transcriptomics, and proteomics, metabolomics profiling can provide a holistic overview and time-dependent snapshots of the physiologic process of endogenous metabolites in cells, tissues, organs, or organisms[25]. As such, metabolomics has been comprehensively applied in physiology, disease, and toxicology research fields[26]. Nuclear magnetic resonance (NMR) spectroscopy[27], liquid chromatography coupled mass spectrometry (LC-MS)[28], gas chromatography coupled mass spectrometry (GC-MS)[29], and Fourier transform mass spectrometry[30] have been successfully used to obtain metabolomic data. GC coupled to a time-of-flight mass analyzer (GC-TOF/MS) provides an improvement over conventional GC-MS analysis due to its high scan rates and the availability of mathematic algorithms to deconvolute closely overlapping peaks. Recent metabolomic approaches utilizing GC-TOF/MS for high-throughput analysis have been successfully applied to the study of hypertension[31], hyperlipemia[32], colon carcinoma, and professional athletes[33] in serum or urine from rat and humans[34]. Therefore, for accuracy and thoroughness, a GC/TOF-MS-based metabolomics approach was implemented to study the biochemical changes in the serum of estrogen-deficiency-induced obesity in female rats in our study. A bilateral ovariectomy was applied to induce estrogen deficiency in female rats. A GC/TOF-MS spectrogram of rat serum was analyzed using a multivariate statistical analysis (MVSA) to differentiate the stages of obesity in OVX rats. The alterations of endogenous metabolites were examined under the conditions of estrogen-deficiency-induced obesity.

Materials and methods

Chemicals and reagents

Myristic-1,2-$^{13}C_2$ acid, 99 atom %^{13}C was used as an internal standard (IS). Methoxyamine hydrochloride (purity 98%), alkane standard solution (C8-C40), and pyridine (>99.8% GC grade) were purchased from Sigma-Aldrich Corporation (St Louis, MO, USA).

N-methyl-*N*-trimethylsilyl-trifluoroacetamide (MSTFA) plus 1% trimethyl chlorosilane (TMCS) were obtained from Fluka (Buchs, Switzerland). Methanol (Merck, Darmstadt, Germany) and *n*-heptane (Tedia, Fairfield, OH, USA) were of high pressure liquid chromatography (HPLC) grade.

Purified water was produced by a Milli-Q system (Millipore, Milford, MA, USA). Kits for total cholesterol (TC), triglyceride (TG), HDL-C and LDL-C were obtained from Nanjing Jiancheng Bioengineering Institute (Nanjing, Jiangsu, China). An ELISA kit for estradiol (E2) was purchased from R&D Systems (Minneapolis, MN, USA).

Animals, surgery and sample preparation

Twelve virgin specific pathogen-free Sprague-Dawley female rats (6 months old, body weight 250±10.0 g) were obtained from the Animal Center of Nanjing Medical University. Rats were housed under controlled conditions (room temperature 22±1°C) with standard solid food and water provided *ad libitum* during the experiment. This study was reviewed and approved by the Animal Ethical Committee of China Pharmaceutical University.

Bilateral ovariectomy (OVX, n=6) or sham operations (sham, n=6) were performed after a seven-day acclimatization. A bilateral (left and right) incision (1–2 cm) that included the skin, muscle, and peritoneum was performed 2 cm below the last rib, and the left and right ovaries were extirpated. For the sham operation, only a small amount of fat around each ovary was extirpated. The rats were provided with standard solid food and deionized water following surgery. Body weights and body mass indexes[36] (BMI, a measurement comparing weight and the height squared) of rats were measured weekly and blood samples were collected on day 0 prior to the operation and at the 3rd and 6th week after bilateral ovariectomy. Serum was immediately separated by centrifugation at 2000×g for 10 min at 4 °C after whole blood was placed for 20 min, and was aliquoted into two parts. One aliquot was used to assay the levels of serum E2 by ELISA and TC, TG, HDL-C, and LDL-C using standard colorimetric methods with commercial kits. The other aliquot was used for GC/TOF-MS analysis. All samples were stored at -80 °C until analysis. All rats were weighed, anesthetized, and bled from the carotid arteries at the end of the experiments 6 weeks post-surgery. Uterine tissues were removed and weighed, and uterus indexes were calculated by dividing the uterus weight by the body weight.

Sample preparation for GC-TOF/MS analysis

Two hundred microliters of methanol containing the internal standard myristic-1,2-$^{13}C_2$ acid (12.5 μg/mL) was added to deproteinize a 50-μL serum sample. After vortex mixing for 5 min and centrifugation at 20000×g for 10 min at 4 °C, 100 μL of supernatant was injected directly into a GC vial and then evaporated to dryness under vacuum. Subsequently, 30 μL of methoxyamine in pyridine (15 mg/mL) was added to the residue and vortexed for 2 min. A methoximation reaction was performed at room temperature for 16 h before trimethylsilylation was performed by the addition of 30 μL MSTFA with 1% TMCS as catalyst for 1 h. Finally, the solution was vortexed for 30 s after methyl myristate in heptane (30 μg/mL),

the external standard, was added to a GC vial for GC-TOF/MS analysis[33–35].

GC-TOF/MS analysis

An Agilent 6980 GC was equipped with an Agilent 7683 Series autosampler (Agilent, Atlanta, GA). Chromatographic separation was performed on a fused-silica capillary column (10 m×0.18 mm ID) chemically bonded with a 0.18 μm DB5-MS stationary phase (J&W Scientific, Folsom, CA, USA). Mass spectra were obtained using a Pegasus III TOF/MS (Leco). The injector temperature and the constant flow rate of carrier gas were controlled at 250 °C at a rate of 1 mL/min with the following parameters: a gradient temperature programming of 70 °C (2.0 min), 70–310 °C linear (35 °C/min), 310 °C (2.0 min); a purge time and flow rate of 60 s at 20 mL/min for 1 min; transfer line temperature and ion source temperature set at 250 °C and 200 °C, respectively; ion source voltage and current of 70 eV and 3.0 mA. The mass spectrometric data were acquired in scan mode over a range of m/z 50–800 at a rate of 20 spectra/s, and the acceleration voltage was turned on at -1650 V with a solvent delay of 170 s.

Data analysis

Automatic peak detection and calculation of the peak area of specific compounds and IS were analyzed by ChromaTOF 2.00 software (Leco). Peaks with signal-to-noise (S/N) ratios lower than 30 were rejected[35]. The retention index for each peak or compound was obtained by comparing its retention time against those of the alkane series (C8-C40). Identification of all of the compounds was performed by comparing their mass spectra and retention indexes with the authentic reference standards and the standards listed in the NIST 2.0 (2005), the Wiley library, and the in-house mass spectra library database established in the Key Laboratory of Drug Metabolism and Pharmacokinetics at China Pharmaceutical University. In addition, potential metabolites were searched using the Human Metabolome Database (http://www.hmdb.ca).

Multivariate statistical analysis (MVSA) was performed using SIMCA-P 11 software (Umetrics, Umea°, Sweden). The data matrix was constructed by GC-TOF/MS responses of each peak as variables with the sample names/IDs as observations in columns and each of the peaks in rows. Subsequently, a principal component analysis (PCA) and a partial least-squares–discriminant analysis (PLS-DA) were used to process the acquired data from the GC-TOF/MS analysis[33].

All data are expressed as means±SD, and statistical analyses were performed using Student's *t*-test for independent two-sample and one-way ANOVA for the comparison of multiple means. $P<0.05$ indicated statistical significance.

Results

Body weight, body mass, and uterine index

Body weight, BMI, and the uterine index were determined; the results are listed in Figure 1A–1C). A significant increase ($P<0.05$) in body weight from the third week post-operation was observed in the OVX group (Figure 1A). Body weight

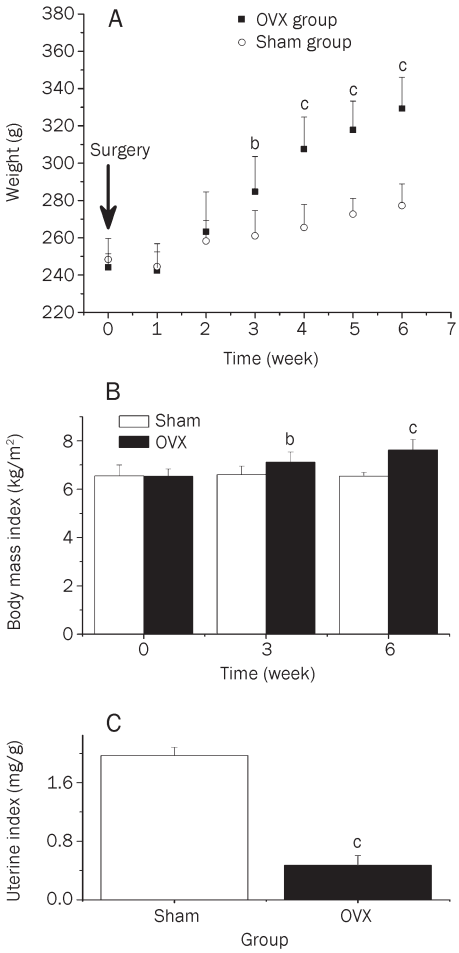

Figure 1. Body weight, body mass index, and uterus index from OVX and the sham rats. (A) Body weight of the rats was recorded weekly during the experiment. (B) Body mass index observed in the pre-surgery and weeks 3 and 6 post-surgery groups. (C) Uterus index. Values with a superscript are significantly different from the sham group ($^bP<0.05$, $^cP<0.01$).

was significantly elevated ($P<0.001$) in the OVX group compared to the sham group in the 4th, 5th, and 6th weeks after surgery. In addition, BMI was significantly increased in the OVX group in the 3rd ($P<0.05$) and 6th ($P<0.001$) weeks compared to the sham group (Figure 1B). Week 6 post-operation, the level of the uterine index was significantly lower ($P<0.001$) than those in the sham group (Figure 1C).

Serum biochemical analysis

As shown in Table 1, serum TC levels in the OVX group in weeks 3 and 6 increased significantly after surgery compared to the sham group ($P<0.05$ and $P<0.01$, respectively). Compared with pre-surgery levels, serum TC ($P<0.001$) and TG ($P<0.05$ and $P<0.001$, respectively) levels were significantly increased in weeks 3 and 6 post-bilateral OVX. Similar to TC and TG, serum LDL-C levels in the OVX group in week 6 post-operation were significantly elevated ($P<0.001$) compared to the sham group and the OVX group prior to surgery. In addition, HDL-C levels in the OVX group observed at weeks 3 and

Table 1. Serum biochemical parameters from the sham group and the OVX group prior to and week 3 and 6 post bilateral ovariectomy. The values represent the means±SD. n=6. [b]P<0.05, [c]P<0.01 *vs* Sham; [e]P<0.05, [f]P<0.01 *vs* the OVX group prior to surgery.

Parameter	Group					
	Sham			OVX		
	Pre-surgery	Week 3 postsurgey	Week 6 postsurgey	Pre-surgery	Week 3 postsurgey	Week 6 postsurgey
TC (mmol/L)	1.48±0.207	1.59±0.252	1.59±0.296	1.51±0.222	2.38±0.347[cf]	3.09±0.460[cf]
TG (mmol/L)	1.06±0.240	1.08±0.232	1.21±0.159	1.02±0.130	1.39±0.162[bf]	1.59±0.216[cf]
HDL-C (mmol/L)	0.85±0.275	0.93±0.227	0.95±0.217	0.86±0.248	0.86±0.190	0.79±0.176
LDL-C (mmol/L)	1.06±0.237	1.14±0.219	1.08±0.230	1.07±0.279	1.34±0.262	2.15±0.499[cf]
E2 (pg/mL)	40.21±10.27	39.32±9.47	38.77±8.32	37.88±8.75	10.72±4.51[cf]	8.65±3.21[cf]

6 post-surgery were slightly reduced but showed no statistical difference compared with the OVX group prior to surgery or with the sham group.

Metabolomic analysis of plasma samples in rats with estrogen-deficiency-induced obesity

The total ion current chromatograms produced by GC-TOF/MS analysis are shown in Figure 2. More than 110 compounds, including amino acids, organic acids, saccharides, and fatty acids, were identified in the metabolomic profiling. In our experiment, the relative standard deviations of the internal standard and the external standard samples were 4.38% and 3.47%, respectively.

PLS-DA was performed on the acquired metabolomic dataset. The PLS-DA score plot for the whole data set categorized serum samples into pre-surgery and weeks 3 and 6 post-surgery in the OVX group (Figure 3A). All of the serum samples in the metabolomic profile of the OVX group (pre-surgery and weeks 3 and 6) were calculated using PLS-DA. Subsequently, a PLS-DA model of two principal components could explain 59.8% of the GC-TOF/MS response variables and predict 72.5% and explain 95.3% according to R^2X, R^2Y, and Q^2Y parameters (R^2X is the percentage of all GC/TOF-MS response variables explained by the model. R^2Y is the percentage of all observation or sample variables explained by the model. Q^2Y is the percentage of all observation or sample variables predicted by the model[33]). The scores are plotted in Figure 3A, in which the x-axis and y-axis are labeled PC1 (the first principal component) and PC2 (the second principal component), respectively. Time-dependent changes of the scores plot in the serum metabolomic profile are obvious in the 2D plane graph. The scores plot shows the samples from rats prior to surgery clustered in the right area of the plot. However, the samples from rats 3 weeks post-surgery are gathered in the top left quadrant of the plot. The samples from rats in week 6 are in the bottom left quadrant of the plot. Our analysis indicated that the stages of estrogen-deficiency-induced obesity could be differentiated clearly between pre-surgery and weeks 3 and 6 post-surgery. Fold changes of endogenous metabolites were further studied by the loadings plot (not shown); the results are shown in Table 2. Cholesterol, glycerol, octadecadienoic acid, 3-hydroxy-butanoic acid, glucose, isoleucine, valine, leucine, and glycine were notably increased in plasma at weeks 3 and 6 post-surgery compared to levels in rats prior to surgery, and glyceraldehyde 3-phosphate, alanine, and arabinofuranose were significantly decreased at weeks 3 and 6 after surgery.

Likewise, a two principal components PLS-DA model was performed between the sham group and the OVX group at week 6 post-surgery. Figure 3B shows the metabolomic movement of both the sham and the OVX groups 6 weeks after bilateral OVX, which could be classified clearly with R^2X: 51.2%, R^2Y: 99.9%, and Q^2Y: 90.7%. In addition, estrogen-deficiency-related modifications of metabolites at different time points are listed in Table 2. The results suggested that estrogen-deficiency-induced obesity greatly affects endogenous

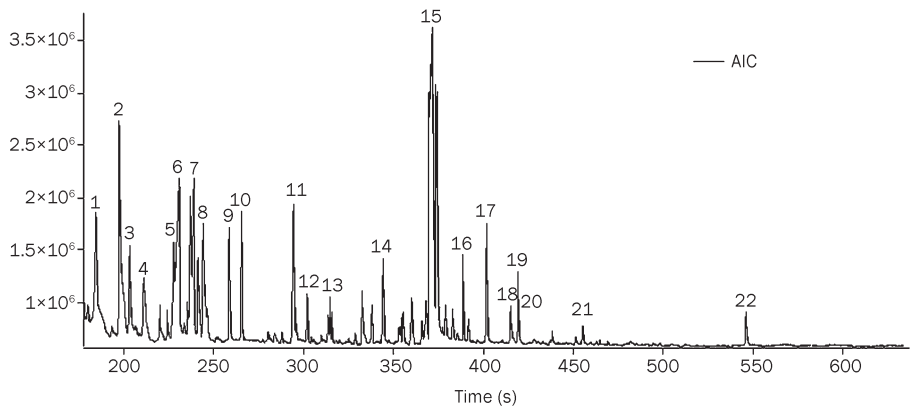

Figure 2. GC-TOF/MS chromatograph of a serum sample obtained from a sham-operated rat. 1, Alanine; 2, Lactic acid; 3, β-Hydroxybutyric acid; 4, Valine; 5, Leucine; 6, Glycerol; 7, Phosphoric acid; 8, Glycine; 9, Isoleucine; 10, Cysteine; 11, Glyceraldehyde 3-phosphate; 12, Creatinine; 13, Glutamic acid; 14, Glutamine; 15, Glucose; 16, Hexadecanoic acid; 17, Uric acid; 18, Oleic acid; 19, Octadecadienoic acid; 20, Octadecanoic acid; 21, Arachidonic acid; 22, Cholesterol.

Table 2. Fold changes of endogenous metabolites detected by GC/TOF-MS. The values represent the means±SD. n=6. [b]P<0.05, [c]P<0.01 *vs* Sham; [e]P<0.05, [f]P<0.01 *vs* in the OVX group prior to surgery.

Metabolites	Retention index	Biological role	Fold change		
			A	B	C
Cholesterol	3170.2	Biomarker of hyperlipidemia	2.10[c]	2.77[c]	2.45[f]
Glycerol	1290.6	An important component of triglycerides and of phospholipids, Galactose metabolism	1.67[c]	2.02[c]	1.34[f]
Octadecadienoic acid	2216.4	An essential fatty acid	2.02[c]	2.02[c]	1.65[f]
Arachidonic acid	2375.2	Precursor of prostaglandins, thromboxanes, and leukotrienes	1.49[c]	1.47[c]	1.25[f]
Oleic acid	2215.3	Saturated fatty acids	2.78[c]	2.33[c]	1.83[f]
Glucose	1935.6	Primary source of energy	1.53[b]	1.24[b]	1.27[e]
Glyceraldehyde-3-phosphate	1547.4	An important metabolic intermediate in both glycolysis and gluconeogenesis	0.57[b]	0.55[b]	0.84[e]
3-Hydroxy-butanoic acid	1172.8	Ketone body, fatty acid biosynthesis	6.38[c]	5.14[c]	2.73[f]
Alanine	1107.5	An important participant and regulator in glucose metabolism	0.89	0.10[c]	0.06[f]
Isoleucine	1305.8	Essential amino acids, stress, energy and muscle metabolism	3.96[c]	4.99[c]	2.20[f]
Valine	1230.8		1.84[c]	2.05[c]	1.56[f]
Leucine	1285.2		1.43[c]	1.87[c]	1.75[f]
Glycine	1347.6	γ-glutamyl cycle	1.46[b]	1.67[c]	1.40[e]
Glutamic acid	1633.5	A key molecule in cellular metabolism, γ-glutamyl cycle	1.12	1.40[c]	1.46[e]

A: Ratio of abundance of endogenous metabolites in serum samples between the week 3 post operation to pre-surgery in OVX group
B: Ratio of abundance of endogenous metabolites in serum samples between the week 6 after operation to pre-surgery in OVX group
C: Ratio of abundance of endogenous metabolites in serum samples between the OVX to the sham group at week 6.

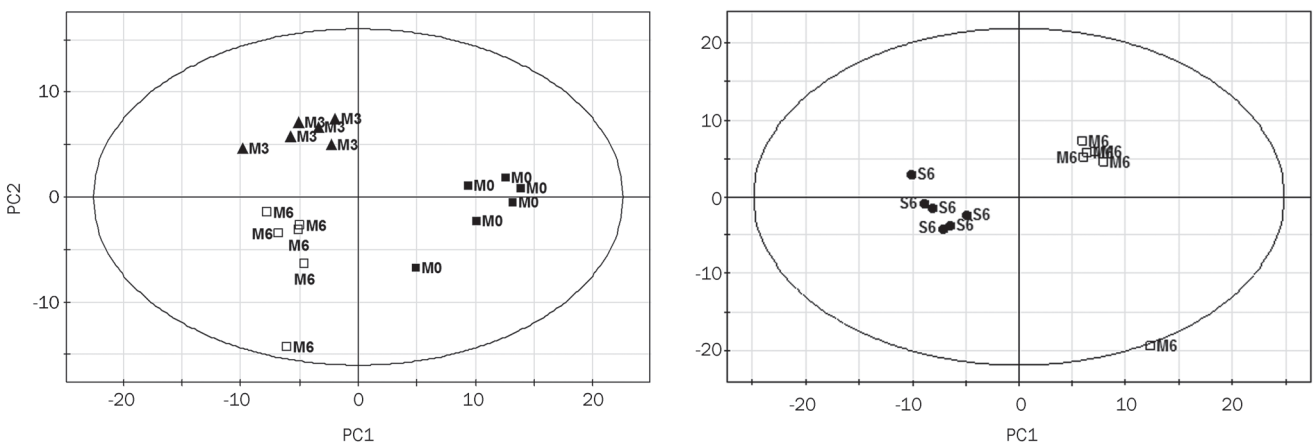

Figure 3. PLS-DA score plots of serum samples. (A) PLS-DA score plots of OVX rats over the whole experiment (pre-surgery, weeks 3 and 6 post-surgery). (B) PLS-DA score plots of OVX rats and sham rats at 6 weeks post-surgery. The x-axis and y-axis are labeled as PC1 (the first principal component) and PC2 (the second principal component), respectively. One data point stands for one subject: ■, OVX rats prior to surgery; □, OVX rats at week 6 post-surgery; ●, sham rats at week 6 post-surgery; ▲, OVX rats at week 3 post-surgery.

metabolite levels compared to the sham group, including a significant increase in the levels of cholesterol, octadecadienoic acid, arachidonic acid, 3-hydroxy-butanoic acid, glutamic acid, glucose, and glycerol and a significant decrease in the levels of glyceraldehyde 3-phosphate, alanine, galactopyranose, and arabinofuranose.

Discussion

Women now, on average, spend more than a third of their life post-menopause. The decline of endogenous estrogen levels, together with physical inactivity, could account for obesity post-menopause, which could lead to an increased risk of cardiovascular diseases (*eg*, high blood pressure, high blood cholesterol, and high triglyceride levels), diabetes, stroke, and depression in postmenopausal women. Bilateral ovariectomy is the gold standard widely used to simulate postmenopausal obesity in female virgin rats[37, 38]. Our results showed that rat weight was significantly elevated in the OVX group compared to the sham group. A higher BMI was observed in estrogen-deficient rats beginning the third week post-surgery despite

similar food consumption between the sham and OVX groups. Body weight and BMI were negatively correlated with levels of estradiol (E2), indicating that the rat model of estrogen-deficiency-induced obesity was successfully established.

However, the mechanisms of increases in body weight and fat content caused by estrogen deficiency remain unclear. It is generally recognized that rapid decrease in E2 secretion can bring about a hypothalamic-pituitary-ovarian (HPO) axis imbalance, which affects insulin, adrenal cortical hormone, growth hormone, and other hormone metabolism and leads to *in vivo* glucose and lipid metabolism disorders. These disorders are likely responsible for the pathogenesis of obesity among postmenopausal women. In addition, significantly elevated levels of TC, TG, and LDL-C and slightly reduced levels of HDL-C in the OVX group caused by estrogen-deficiency-induced obesity could indicate high risk for a series of complications.

Estrogen-deficiency-induced obesity is associated with fat accumulation and excessive intake of energy that break down the balance of energy metabolism (Figure 4). Fats are triesters of glycerol and fatty acids. Using the metabolomic approach, glycerol and fatty acid levels (*eg*, hexadecanoic acid, octadecadienoic acid, oleic acid, and arachidonic acid) were significantly increased in rats with estrogen-deficiency-induced obesity. We presumed that estrogen had a key modulator role in lipid metabolism. Herrero *et al* reported that myocardial fatty acid utilization was higher in women taking estrogens compared to those not receiving estrogens, which might be attributable to the regulation of β-oxidation of fatty acids[39]. It has been reported that mRNA expression and the activity of enzymes including medium-chain acyl coenzyme A dehydrogenase and acetyl CoA oxidase, enzymes with fatty acid β-oxidation, are reduced under estrogen deficiency[40]. Therefore, fatty acid levels may be increased because the estrogen deficiency interferes with the β-oxidation of fatty acids and leads to a reduced decomposition rate of fatty acids. Linoleic acid and essential fatty acids cannot be synthesized by humans and other animals and are only supplied from food components. In our research, linoleic acid was increased 1.4-fold and 1.2-fold compared to pre-surgery levels and to the sham group in the 6th week, respectively. Increased levels of fatty acids might be due to reduced β-oxidation of fatty acids. Moreover, levels of arachidonic acid, a precursor of prostaglandins, thromboxanes, and leukotrienes were elevated in the OVX rats, and arachidonic acid was biosynthesized by linoleic acid catalyzed by a series of enzymes. Therefore, estrogen deficiency might cause a lower rate of β-oxidation of fatty acids and greater biosynthesis of fatty acids. Furthermore, elevated levels of serum glycerol in OVX rats compared to sham rats might be a consequence of self-regulation because obese rats have higher basal lipolytic rates than normal subjects[41].

Likewise, glycolysis is regulated by estrogen and estrogen receptors. Furman *et al* observed that estrogens stimulated the glycolysis process in MCF-7 cells, which could be inhibited by tamoxifen (TAM)[42]. Using metabolomic analysis, the levels of glyceraldehyde 3-phosphate and alanine were significantly decreased in rats with estrogen deficiency. Glyceraldehyde 3-phosphate, an important metabolic intermediate in glycolysis, is bio-synthesized by phosphoglycerate kinase, which catalyzes the conversion of 1,3-bisphosphoglycerate into glyceraldehyde 3-phosphate, which is the first step of ATP production in glycolysis. A decrease in glyceraldehyde 3-phosphate

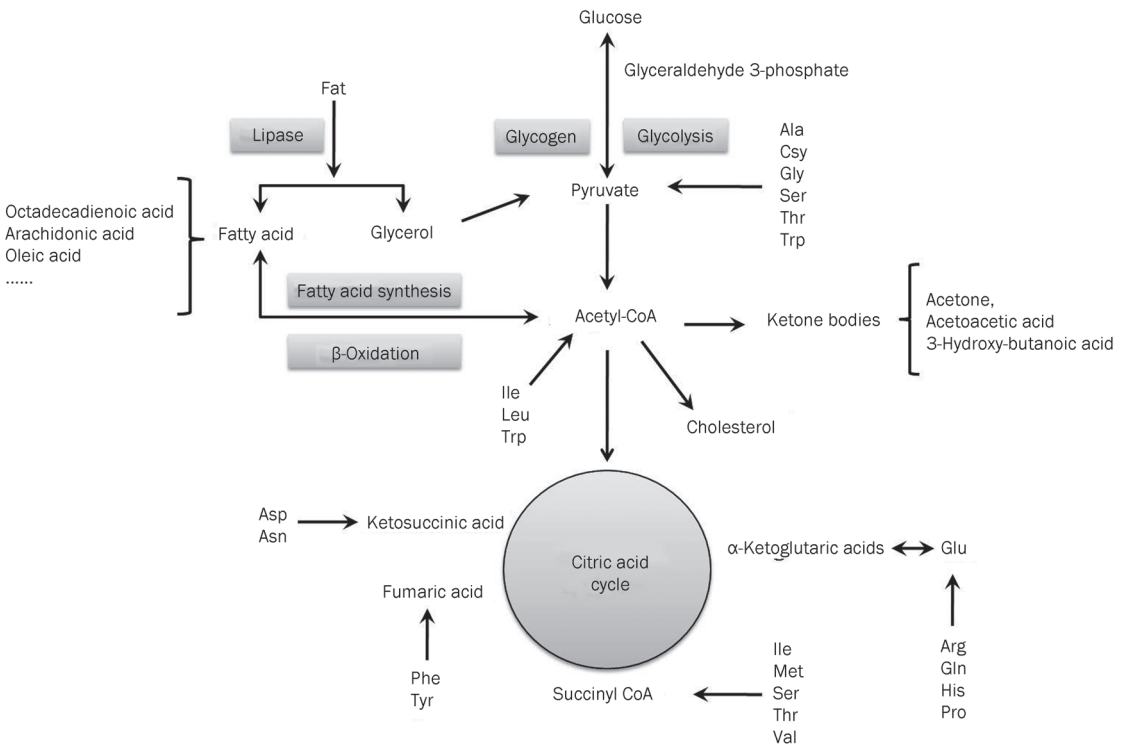

Figure 4. Regulation of glycometabolism, lipid metabolism, and amino acid metabolism by estrogen deficiency (significant difference from the endogenous metabolite is indicated in bold).

suggests that estrogen has an adjustment effect in glycolysis, and an estrogen deficiency could interfere with this process. Similar to glyceraldehyde 3-phosphate, the lower alanine levels found in rats with estrogen deficiency would be indirectly correlated with the glycolysis process because disruption of glycolysis leads to pyruvate insufficiency. Moreover, alanine plays a key role in the glucose-alanine cycle between muscle tissue and the liver; glycolysis in the muscle produces pyruvate, which is further converted to alanine. The results of our study are also suggestive of a modified alanine-glucose cycle. In addition, endogenous estrogen regulates skeletal muscle mass in developing rats. Therefore, estrogen loss can alter skeletal muscle recovery from disuse[43, 44]. As a result, decreased muscle function may also be a reason for the reduction of alanine biosynthesis.

Estrogens are involved in the regulation of not only fatty acid metabolism and glycolysis but also the TCA cycle. The activity of citrate synthase (CS) in skeletal muscle and cerebral blood vessels is enhanced by estrogen therapy in OVX rats[45]. Raben *et al* found that β-hydroxyacyl-CoA dehydrogenase (HADH) and CS levels were 20% lower in formerly obese women[46]. Moreover, pyruvate dehydrogenase, aconitase, and ATP-synthase are regulated by estrogen[47]. Therefore, more precursor acetyl-CoA may enter into the fatty acid, ketone (*eg*, acetoacetate, 3-hydroxy-butanoic acid, and acetone), and cholesterol biosynthesis processes as a result of the TCA cycle being attenuated under estrogen deficiency. As a result of the affected metabolic pathway, high levels of cholesterol and fatty acids were observed in OVX rats, and a marked increase in the levels of 3-hydroxy-butanoic acid was observed in rats with bilateral ovariectomy-induced obesity. Furthermore, glycolysis, the TCA cycle, and insulin would decrease the levels of blood glucose in contrast to gluconeogenesis (the generation of glucose from non-carbohydrates), which could increase the levels of blood glucose. In our study, the levels of blood glucose were slightly elevated during obesity in OVX rats, which might be connected with the subdued glycolysis and TCA cycle caused by estrogen deficiency. Insulin resistance resulting from estrogen deficiency is a known risk factor for type 2 diabetes and leads to the high blood glucose levels observed.

Higher cholesterol levels were found in OVX rats compared to sham rats by metabolomic analysis, which was in agreement with the conventional measurements using commercial kits. High blood cholesterol levels in postmenopausal women are a biom arker of obesity due to ovarian hormone deficiency. Mataumoto *et al* reported that the level of cholesterol 7α-hydroxylase activity, a key enzyme in cholesterol catabolism, was significantly reduced in the liver in OVX rats[48]. Therefore, excessive acetyl-CoA is used for cholesterol synthesis in OVX rats, but the rate of cholesterol degradation is attenuated because of the decrease in 7α-hydroxylase activity. Obviously, the elevated levels of serum cholesterol were a result of a combination of the above two factors.

The branched-chain aliphatic amino acids (BCAAs), including isoleucine, valine, and leucine, are markedly increased after estrogen deficiency. The BCAAs play important roles in protein synthesis, neurotransmitter synthesis, and branched-chain fatty acid synthesis. They cannot be synthesized by the animal itself and must be supplied by the diet. In our study results, serum amino acid levels were elevated in obesity, which is consistent with previous research[49–51]. She *et al*[52] reported that obesity may play a potential role in the regulation of BCAA catabolism. They found that the activities of the BCATm and BCKD enzyme complex, the key enzymes in the first two steps of the BCAAs catabolic pathway, were depressed in obese *ob*/*ob* mice and Zucker rats. Therefore, we presumed that the alternations in BCAA metabolism may contribute to increase in BCAAs in obesity. The γ-glutamyl cycle plays a key role in glutathione synthesis, and the transport system for amino acids and glutamic acid, glycine, and cystine take part in the γ-glutamyl cycle. Higher glutamic acid, glycine, and cystine levels in estrogen-deficiency-induced obesity would influence the γ-glutamyl cycle.

Conclusions

Metabolomic profiling with multivariate statistical analysis combined with conventional measurement kit assays indicated a progression of experimental obesity induced by estrogen deficiency in rats. The series of potential biomarkers identified provide fingerprints of rat metabolomic changes during obesity and an overview of multiple metabolic pathways during the progression of obesity that involves glucose metabolism, lipid metabolism, and amino acid metabolism.

Acknowledgements

This study was supported by a grant from the National Natural Science Foundation of China (Grant No 30873112) and the Six Talent Peek Project of Jiangsu Province (No 07-C-018).

Author contribution

Bo MA and Qi ZHANG have been involved in all phases of this project. Guang-ji WANG designed the research. Ji-ye A analyzed the data, and Di WU revised and wrote the paper. Bei CAO, Ying-ying HU, Lin-sheng LIU were involved in measurements. Ying LIU, Yong-lu WANG, and Ya-ya ZHENG were involved in the animal experiments of the project.

References

1 Haslam DW, James WP. Obesity. Lancet 2005; 366: 1197–209.
2 Ryan AS, Nicklas BJ, Berman DM. Hormone replacement therapy, insulin sensitivity, and abdominal obesity in postmenopausal women. Diabetes Care 2002; 25: 127–33.
3 Burke GL, Bertoni AG, Shea S, Tracy R, Watson KE, Blumenthal RS, *et al*. The impact of obesity on cardiovascular disease risk factors and subclinical vascular disease: the Multi-Ethnic Study of Atherosclerosis. Arch Intern Med 2008; 168: 928–35.
4 Winter Y, Rohrmann S, Linseisen J, Lanczik O, Ringleb PA, Hebebrand J, *et al*. Contribution of obesity and abdominal fat mass to risk of stroke and transient ischemic attacks. Stroke 2008; 39: 3145–51.
5 Kirschner MA, Ertel N, Schneider G. Obesity, hormones, and cancer. Cancer Res 1981; 41: 3711–7.
6 Cleary MP, Grossmann ME, Ray A. Effect of obesity on breast cancer

development. Vet Pathol 2010; 47: 202–13.
7 Cleary MP, Grossmann ME. Minireview: Obesity and breast cancer: the estrogen connection. Endocrinology 2009; 150: 2537–42.
8 Kuhl H. Breast cancer risk in the WHI study: the problem of obesity. Maturitas 2005; 51: 83–97.
9 Balog J. Obesity and estrogen. Am J Obstet Gynecol 1978; 130: 242.
10 de Paz I P, Alameda HC, Olivar RJ. Obesity and menopause. Nutr Hosp 2006; 21: 633–7.
11 Kanaya AM, Vittinghoff E, Shlipak MG, Resnick HE, Visser M, Grady D, *et al*. Association of total and central obesity with mortality in postmenopausal women with coronary heart disease. Am J Epidemiol 2003; 158: 1161–70.
12 Chang CJ, Wu CH, Yao WJ, Yang YC, Wu JS, Lu FH. Relationships of age, menopause and central obesity on cardiovascular disease risk factors in Chinese women. Int J Obes Relat Metab Disord 2000; 24: 1699–704.
13 Gao Q, Horvath TL. Cross-talk between estrogen and leptin signaling in the hypothalamus. Am J Physiol Endocrinol Metab 2008; 294: E817–26.
14 Gomori A, Ishihara A, Ito M, Matsushita H, Ito M, Mashiko S, *et al*. Blockade of MCH1 receptor signalling ameliorates obesity and related hepatic steatosis in ovariectomized mice. Br J Pharmacol 2007; 151: 900–8.
15 Sorensen MB, Rosenfalck AM, Hojgaard L, Ottesen B. Obesity and sarcopenia after menopause are reversed by sex hormone replacement therapy. Obes Res 2001; 9: 622–6.
16 Ryan AS, Nicklas BJ, Berman DM. Hormone replacement therapy, insulin sensitivity, and abdominal obesity in postmenopausal women. Diabetes Care 2002; 25: 127–33.
17 Best PJ, Berger PB, Miller VM, Lerman A. The effect of estrogen replacement therapy on plasma nitric oxide and endothelin-1 levels in postmenopausal women. Ann Intern Med 1998; 128: 285–8.
18 Manolio TA, Furberg CD, Shemanski L, Psaty BM, O'Leary DH, Tracy RP, *et al*. Associations of postmenopausal estrogen use with cardiovascular disease and its risk factors in older women. The CHS Collaborative Research Group. Circulation 1993; 88: 2163–71.
19 Brinton LA, Schairer C. Estrogen replacement therapy and breast cancer risk. Epidemiol Rev 1993; 15: 66–79.
20 Burry K, Cain JM. Estrogen replacement therapy and risk of ovarian cancer in postmenopausal women. JAMA 2002; 288: 2538; author reply 2539.
21 Ambrus JL. Postmenopausal hormone therapy increases risk of deep vein thrombosis and pulmonary embolism. Am J Med 1999; 107: 104.
22 Shumaker SA, Legault C, Kuller L, Rapp SR, Thal L, Lane DS, *et al*. Conjugated equine estrogens and incidence of probable dementia and mild cognitive impairment in postmenopausal women: Women's Health Initiative Memory Study. JAMA 2004; 291: 2947–58.
23 Nicholson JK, Lindon JC, Holmes E. 'Metabonomics': understanding the metabolic responses of living systems to pathophysiological stimuli via multivariate statistical analysis of biological NMR spectroscopic data. Xenobiotica 1999; 29: 1181–9.
24 Nicholson JK, Lindon JC. Systems biology: Metabonomics. Nature 2008; 455: 1054–6.
25 Nicholson JK, Wilson ID. Opinion: understanding 'global' systems biology: metabonomics and the continuum of metabolism. Nat Rev Drug Discov 2003; 2: 668–76.
26 Kaddurah-Daouk R, Kristal BS, Weinshilboum RM. Metabolomics: a global biochemical approach to drug response and disease. Annu Rev Pharmacol Toxicol 2008; 48: 653–83.
27 Saude EJ, Obiefuna IP, Somorjai RL, Ajamian F, Skappak C, Ahmad T, *et al*. Metabolomic biomarkers in a model of asthma exacerbation: urine nuclear magnetic resonance. Am J Respir Crit Care Med 2009; 179: 25–34.
28 Chen C, Gonzalez FJ, Idle JR. LC-MS-based metabolomics in drug metabolism. Drug Metab Rev 2007; 39: 581–97.
29 Zhang Q, Wang GJ, A JY, Wu D, Zhu LL, Ma B, *et al*. Application of GC/MS-based metabonomic profiling in studying the lipid-regulating effects of *Ginkgo biloba* extract on diet-induced hyperlipidemia in rats. Acta Pharmacol Sin 2009; 30: 1674–87.
30 Kamleh MA, Hobani Y, Dow JA, Watson DG. Metabolomic profiling of Drosophila using liquid chromatography Fourier transform mass spectrometry. FEBS Lett 2008; 582: 2916–22.
31 Lu Y, A J, Wang G, Hao H, Huang Q, Yan B, *et al*. Gas chromatography/time-of-flight mass spectrometry based metabonomic approach to differentiating hypertension- and age-related metabolic variation in spontaneously hypertensive rats. Rapid Commun Mass Spectrom 2008; 22: 2882–8.
32 Gu S, A J, Wang G, Zha W, Yan B, Zhang Y, *et al*. Metabonomic profiling of liver metabolites by gas chromatography-mass spectrometry and its application to characterizing hyperlipidemia. Biomed Chromatogr 2010; 24: 245–52.
33 Yan B, A J, Wang G, Lu H, Huang X, Liu Y, *et al*. Metabolomic investigation into variation of endogenous metabolites in professional athletes subject to strength-endurance training. J Appl Physiol 2009; 106: 531–8.
34 Liu L, Aa J, Wang G, Yan B, Zhang Y, Wang X, *et al*. Differences in metabolite profile between blood plasma and serum. Anal Biochem 2010; 406: 105–12.
35 A J, Trygg J, Gullberg J, Johansson AI, Jonsson P, Antti H, *et al*. Extraction and GC/MS analysis of the human blood plasma metabolome. Anal Chem 2005; 77: 8086–94.
36 Novelli EL, Diniz YS, Galhardi CM, Ebaid GM, Rodrigues HG, Mani F, *et al*. Anthropometrical parameters and markers of obesity in rats. Lab Anim 2007; 41: 111–9.
37 Von Diemen V, Trindade EN, Trindade MR. Experimental model to induce obesity in rats. Acta Cir Bras 2006; 21: 425–9.
38 Rogers NH, Perfield JW 2nd, Strissel KJ, Obin MS, Greenberg AS. Reduced energy expenditure and increased inflammation are early events in the development of ovariectomy-induced obesity. Endocrinology 2009; 150: 2161–8.
39 Herrero P, Soto PF, Dence CS, Kisrieva-Ware Z, Delano DA, Peterson LR, *et al*. Impact of hormone replacement on myocardial fatty acid metabolism: potential role of estrogen. J Nucl Cardiol 2005; 12: 574–81.
40 Kamei Y, Suzuki M, Miyazaki H, Tsuboyama-Kasaoka N, Wu J, Ishimi Y, *et al*. Ovariectomy in mice decreases lipid metabolism-related gene expression in adipose tissue and skeletal muscle with increased body fat. J Nutr Sci Vitaminol (Tokyo) 2005; 51: 110–7.
41 Wang Y, Sullivan S, Trujillo M, Lee MJ, Schneider SH, Brolin RE, *et al*. Perilipin expression in human adipose tissues: effects of severe obesity, gender, and depot. Obes Res 2003; 11: 930–6.
42 Furman E, Rushkin E, Margalit R, Bendel P, Degani H. Tamoxifen induced changes in MCF7 human breast cancer: *in vitro* and *in vivo* studies using nuclear magnetic resonance spectroscopy and imaging. J Steroid Biochem Mol Biol 1992; 43: 189–95.
43 McClung JM, Davis JM, Wilson MA, Goldsmith EC, Carson JA. Estrogen status and skeletal muscle recovery from disuse atrophy. J Appl Physiol 2006; 100: 2012–23.
44 Sugiura T, Ito N, Goto K, Naito H, Yoshioka T, Powers SK. Estrogen administration attenuates immobilization-induced skeletal muscle atrophy in male rats. J Physiol Sci 2006; 56: 393–9.

45 Beckett T, Tchernof A, Toth MJ. Effect of ovariectomy and estradiol replacement on skeletal muscle enzyme activity in female rats. Metabolism 2002; 51: 1397–401.
46 Raben A, Mygind E, Astrup A. Lower activity of oxidative key enzymes and smaller fiber areas in skeletal muscle of postobese women. Am J Physiol 1998; 275: E487–94.
47 Nilsen J, Irwin RW, Gallaher TK, Brinton RD. Estradiol *in vivo* regulation of brain mitochondrial proteome. J Neurosci 2007; 27: 14069–77.
48 Mataumoto J, Kishida T, Ebihara K. Sugar beet fiber suppresses ovarian hormone deficiency-induced hypercholesterolemia in rats. Nutr Res 2001; 21: 1519–27.
49 Bagdade JD, Bierman EL, Porte D Jr. Are plasma amino acid levels elevated in obesity. N Engl J Med 1970; 282: 166.
50 Felig P, Marliss E, Cahill GF Jr. Plasma amino acid levels and insulin secretion in obesity. N Engl J Med 1969; 281: 811–6.
51 Leclercq B, Seve B. Influence of adiposity (genetic or hormonal) on the metabolism of amino acids and nutritional responses. Reprod Nutr Dev 1994; 34: 569–82.
52 She P, Van Horn C, Reid T, Hutson SM, Cooney RN, Lynch CJ. Obesity-related elevations in plasma leucine are associated with alterations in enzymes involved in branched-chain amino acid metabolism. Am J Physiol Endocrinol Metab 2007; 293: E1552–63.